DEPARTEMENT DE GEOSCIENCES - GEOGRAPHIE
UNIVERSITE DE FRIBOURG (SUISSE)

Mechanical stability and growth performance of trees

THESE

présentée à la Faculté des Sciences de l'Université de Fribourg (Suisse)
pour l'obtention du grade de *Doctor rerum naturalium*

Tor LUNDSTRÖM

de

Puidoux-Servion (VD, Suisse) et Järfälla (Suède)

Thèse n° 1644

Édition privée

2010

Acceptée par la Faculté des Sciences de l'Université de Fribourg (Suisse)
sur la proposition de :
Dr. Markus Stoffel (directeur de thèse)
Prof. Peter Niemz, Dr. Perry Bartelt, Dr. Luuk Dorren (experts externes)
Prof. Bernard Grobéty (président du jury).

Accepted by the Faculty of Science of the University of Fribourg, Switzerland
on the recommendation of :
Dr. Markus Stoffel (PhD thesis' director)
Prof. Peter Niemz, Dr. Perry Bartelt, Dr. Luuk Dorren (external experts)
Prof. Bernard Grobéty (president of the jury).

Fribourg, le 14 août 2009

The PhD thesis' director:
Directeur de thèse:

Dr. Markus Stoffel

The Dean:
Le Doyen:

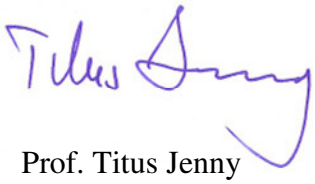

Prof. Titus Jenny

Citation:
Lundström T. 2010: Mechanical stability and growth performance of trees. PhD thesis no. 1644, University of Fribourg, Switzerland

This publication is available online at the University of Fribourg:
http://ethesis.unifr.ch/theses/index.php#Sciences

Table of contents

Abstract

Trees' mechanical stability is essential for the benefits provided by forests including wood and pulp products, specific ecosystems, recreation areas for people, and protection against natural hazards. Since tree growth depends on the environment in which the tree grows, it is possible to influence the mechanical stability of trees and forests. Different forest management strategies affect the tree stability and protection levels differently. It is therefore important to understand how tree growth properties influence tree mechanics and how the environment triggers the tree to grow in a mechanically more or less efficient way. Little information on such influence and triggering phenomena was, however available, to use directly in tree stability science and cause-effect analyses in forest management. Thus the present PhD thesis has the following aims: (1) to provide new allometric relationships for mechanical properties of the main structural elements of the tree, the root-soil system and the stem; (2) to investigate to what extent such properties are influenced by mechanical stress in nature; and (3) to assess the mechanical behavior of the whole tree subject to mechanical stress in nature originating from wind, snow, and/or rockfall. The approach taken was mainly experimental, with a focus on representative species and sites in the Alps. The results are presented in six papers (I-VI) which form the core of this work.

In the first and the second papers, the focus is on the anchorage of the tree, provided by the root-soil system. The investigations include winching tests of conifers and subsequent examinations of the root-soil plate and roots. The five principle findings of the first study are: (1) the anchorage strength M_a was significantly reduced by root rot; (2) M_a did not differ between silver fir (*Abies alba* Mill.) and Norway spruce (*Picea abies* L. Karst.); (3) M_a could be well described by parameters of tree size and weight; (4) the shape of the root-soil plate could be well described by a depth-dependent taper model with an elliptical cross section; and (5) the root growth was preferential in the direction of frequent winds. The focus of the second paper is more on the mechanics of tree anchorage than in the first paper, with two main findings: (1) The resistive anchorage moment, with a maximum value of M_a, depends on the stem base inclination according to a function that could be well described by parameters of tree size and weight for the investigated Norway spruce; and (2) M_a for the Norway spruce on high elevation sites was lower than that growing on low elevation sites. Both studies show that the size of the root-soil plate, and hence size and extension of the roots, is difficult to predict with allometry.

The third and fourth papers focus on the stem of the tree to obtain prediction models of mechanical properties, such as density and bending deformation and resistance, based on properties of radial growth, such as annual ring width, moisture content, and knottiness. In the third paper, this topic is explored in detail for one stem of Norway spruce. Small specimens sawn from different locations in the stem were used to determine the pattern of growth and mechnical properties within the stem, as well as relationships between growth and mechanical properties. The mechanical properties of the stem cross-section were then calculated by considering the annual wood layers as superimposed cylindrical shells with different mechanical properties predicted by the growth properties observed in the wood layers. The quality of the predicted cross-sectional mechanical properties was investigated in the fourth paper for stems of Norway spruce and silver fir. The predictions of stem deformation were precise, whereas those related to stem failure were approximate. In general, all mechanical properties improved with distance from the pith and from the tree top towards the base. The stems investigated can therefore be considered well designed for bending in nature, especially at a mature stage.

The fifth paper is dedicated to the mechanical behavior of the entire tree. The results for the tree elements investigated in the papers I-IV are combined in the detailed analysis of the tree-rock interaction. A new experimental method was used to determine how Norway spruce reacts to and absorbs energy from an impacting rock. When hitting the tree at stem heights frequently observed in the field, the stem governed the tree's reaction and energy absorption. The numerical determination of the reactions and relative energy absorption of different parts of the tree show their relative importance for providing protection against rockfall. The results contribute to further understanding of the tree-rock interaction process. They should therefore help make computer simulations more precise and improve management strategies for rockfall protection forests.

The sixth paper is concerned with the mechanical performance and growth adaptation of the whole tree. The Norway spruce trees investigated in papers I-V grew in environments at different elevations (high and low) with different soils and competitive status. In paper VI their mechanical performance and growth adaptation to different combinations of natural load and tree state were analyzed. The three main findings were: (1) material and geometric non-linearities are important to

consider when analyzing tree deflections and critical loads; (2) the strengths of the stem and the anchorage mutually adapt to the local wind, which acts on the tree crown in the forest canopy; and (3) the radial stem growth follows a mechanically high-performance path because it adapts to the prevailing as well as acute seasonal variations in combinations of tree state, e.g. frozen or unfrozen stems and anchorage, and load, e.g. wind and vertical and lateral snow pressure. Young trees appeared to adapt to such combinations more than older trees.

In conclusion, the six papers together show that: (1) the mechanics of Norway spruce and silver fir can be well predicted by properties of growth and site, and consequently it is possible to predict their reaction and energy absorption in the field; and (2) the mechanical performance of the Norway spruce studied was generally high, which shows that their overall growth had been clearly influenced by mechanical stress specific to the site and tree. The practical implications of these results are that: (1) it is possible to assess the mechanical stability of Norway spruce and silver fir more precisely, and thus evaluate the level of protection against natural hazards offered by the forests in which they occur; and (2) rapid changes in forest structure lead to new load patterns which the trees take time to adapt to. If changes are made too rapidly, there will be increasing risk of tree failure.

Résumé

La stabilité mécanique des arbres joue un rôle prépondérant pour les fonctions offertes par les forêts, tels source première pour les produits à base de bois ou de papier, environnement pour les écosystèmes spécifiques, lieux de récréation pour l'homme et protection contre les dangers naturels. Etant donné que la croissance des arbres dépend des conditions environnementales, il est possible d'influer sur la stabilité mécanique des arbres et des forêts. Différentes stratégies de sylviculture influent sur la stabilité et le niveau de protection de façon diverse. Il est donc important de comprendre comment les caractéristiques de croissances influencent la stabilité mécanique de l'arbre et comment l'environnement déclenche une croissance de l'arbre plus ou moins efficace du point de vue mécanique. Peu d'informations au sujet de cette influence et de ce déclanchement étaient jusqu'à présent disponibles pour une application directe dans l'étude de la stabilité mécanique des arbres et dans l'analyse de cause à effet en sylviculture. Cette thèse recherche donc les buts suivants: (1) fournir de nouvelles relations allométriques pour les propriétés mécaniques des éléments structuraux principaux, à savoir la partie racinaire et le tronc; (2) examiner dans quelle mesure ces propriétés sont influencées par les sollicitations dans la nature; et (3) évaluer le comportement mécanique de l'arbre entier soumis à des sollicitations dans la nature, de vent, de neige, et/ou de chute de pierres. L'approche choisie est essentiellement expérimentale et se concentre sur des espèces et des sites typiques des Alpes. Les résultats sont présentés dans six publications (I-VI) qui forment le noyau de ce travail.

Dans la première et la deuxième publication, l'accent est mis sur l'ancrage, fournit par la partie racinaire de l'arbre. L'étude comprend des essais de tirage au treuil sur des conifères et l'examen subséquent de la motte et des racines. Les cinq principaux constats de la première étude sont: la résistance au moment de flexion de l'ancrage M_a était réduite de façon significative par la pourriture des racines; (2) le M_a du sapin blanc (*Abies alba* Mill.) et de l'épicéa commun (*Picea abies* L. Karst.) n'étaient pas différents; (3) le M_a était bien décrit par les paramètres de grandeur et de poids de l'arbre; (4) la forme de la partie racinaire a bien pu être décrite par un modèle de cône à section elliptique dépendante de la profondeur; et (5) la croissance des racines était prépondérante dans la direction des vents fréquents. Dans la deuxième publication, l'accent est porté plus sur la mécanique de l'ancrage de l'arbre que dans la première, avec deux constats principaux: (1) Le moment résistant de l'ancrage, dont la valeur maximale vaut M_a, dépend de l'inclinaison de la base du tronc et suit une fonction qui pouvait bien être décrite par les paramètres de grandeur et de poids de l'arbre, pour les épicéas examinés; et (2) le M_a des épicéas poussant sur des sites de haute altitude était inférieur à celui des épicéas poussant sur des sites de basse altitude. Les deux études démontrent que la grandeur de la partie racinaire, donc la grandeur et l'extension des racines est difficile à prédire par l'allométrie.

La troisième et la quatrième publication se concentrent sur le tronc de l'arbre pour développer des modèles d'estimation des propriétés mécaniques telles que la densité et la résistance et la déformation en flexion, basés sur des caractéristiques de croissance radiale telles que la largeur des cernes, la teneur en eau et la présence de nœuds. Dans la troisième publication, ce thème est exploré en détail pour un tronc d'épicéa. De petites éprouvettes sciées de différents endroits du tronc ont été employées pour déterminer le schéma spatial des caractéristiques de croissance et des propriétés mécaniques dans le tronc, ainsi que des relations entre les caractéristiques et les propriétés. Les propriétés mécaniques de la section du tronc étaient ensuite calculées en considérant les cernes comme des coques cylindriques superposées avec différentes propriétés mécaniques estimées à l'aide des caractéristiques de croissance observées dans les cernes. La qualité des estimations des propriétés mécaniques de la section a été analysée dans la quatrième publication pour des troncs d'épicéa et de sapin blanc. Les estimations de déformation du tronc en flexion étaient précises, alors que celles associées à la rupture du tronc étaient approximatives. En règle générale, toutes les propriétés mécaniques s'amélioraient relativement à la distance de la moelle et du sommet vers la base. Les troncs examinés, surtout ceux en stade mature, peuvent ainsi être considérés comme bien conçus pour la flexion se produisant dans la nature.

La cinquième publication est dédiée au comportement mécanique de l'arbre entier lors de chute de pierres. Les résultats des différents éléments de l'arbre examinés dans les publications I-IV sont combinés dans une analyse détaillée de l'interaction entre une pierre et le tronc de l'arbre. Une nouvelle méthode expérimentale a été employée pour déterminer comment un épicéa réagit et absorbe de l'énergie lors d'un impact d'une pierre. Quand la pierre heurtait le tronc à des hauteurs fréquemment observées dans la nature, le tronc était la partie de l'arbre qui jouait le rôle majeur dans la réaction et l'absorption d'énergie. La détermination numérique des réactions et de l'absorption relative de l'énergie pour

différentes parties de l'arbre démontre leur capacité respective à fournir une protection contre les chutes de pierres. Les résultats contribuent à une meilleure compréhension du processus d'interaction pierre-arbre. Ils devraient ainsi aider à rendre les simulations par ordinateur plus précises et à améliorer les stratégies de sylviculture pour les forêts de protection.

La sixième publication concerne les performances mécaniques et l'adaptation de croissance de l'arbre entier. Les épicéas examinés dans les publications I-V poussaient à différentes altitudes (haute et basse), dans différents sols et états de compétition. Dans la publication VI leurs performances mécaniques et leur adaptation de croissance selon diverses combinaisons de sollicitations et états d'arbre ont été analysées. Les trois principaux constats étaient: (1) la non-linéarité matérielle et géométrique sont importantes à considérer lors de l'analyse des déflexions et des sollicitations critiques; (2) la résistance du tronc et de l'ancrage s'adaptent de façon réciproque au vent local qui agit sur l'houppier dans la forêt; et (3) la croissance radiale du tronc suit un développement de haute performance mécanique, parce qu'elle s'adapte aux combinaisons prépondérantes ainsi qu'extrêmes des sollicitations et des états de l'arbre, se produisant au cours des saisons et des années, comprenant d'un côté par exemple le vent et le poids et la pression de la neige et de l'autre côté le tronc et la partie racinaire gelés ou non-gelés. Les plus jeunes arbres paraissaient pouvoir mieux s'adapter à ce genre de combinaisons variables que les plus vieux.

En conclusion, les six publications ensemble démontrent que: (1) la mécanique de l'épicéa et du sapin blanc peut être bien estimée sur la base des caractéristiques de croissance et de site, et par conséquent, il est possible de prédire la réaction et l'absorption d'énergie in situ de ces arbres; et que (2) les performances mécaniques de l'épicéa étudié étaient en général élevées, montrant que sa croissance globale a clairement été influencée par les sollicitations mécaniques, spécifiques au site et à l'arbre. Les implications pratiques de ces résultats sont les suivantes: (1) il est possible d'estimer la stabilité mécanique de l'épicéa et du sapin blanc de façon plus précise, et donc d'évaluer le niveau de protection des forêts contre des dangers naturels; et (2) un changement rapide de la structure de forêt implique une nouvelle distribution des sollicitations face à laquelle les arbres nécessitent du temps pour s'adapter. Si les changements se font trop rapidement, le risque de rupture des arbres peut devenir important.

Acknowledgements

Motivation, opportunities and adapted instruments are required to successfully produce results in any type of work, and this PhD thesis was no exception.

My motivation to pursue work in this research area grew towards the end of the Tree stability project at the SLF in Davos (2002-2006) when I realized the potential for additional interesting results. However, I would not have been able to complete this thesis without the encouragement from many people during my two years of PhD-work (2006-2008). Here, I would like to thank especially the following individuals:

Dr. Walter Ammann, Dr. Tobias Jonas, Dr. Martin Jonsson, Dr. Matthias Kalberer, Dr. Martin Schneebeli, Massimiliano Schwarz, Dr. Veronika Stöckli, and Dr. Axel Volkwein (SLF, Davos);

Dr. Perry Bartelt, Dr. Luuk Dorren, Prof. em. Michel Monbaron, Prof. Peter Niemz, and Dr. Markus Stoffel (jury of the thesis);

Dr. Silvia Dingwall, Dr. Raquel González Cuesta, Dr. Ruth Landolt, and Dr. Rozanne Poulson (help with publishing the articles);

Dr. Lionel Dupuy, Dr. John Moore, Dr. Bruce Nicoll, and Dr. François Nicot (helpful non-anonymous reviewers); and

Dr. Fredéric Berger, Dr. Thierry Fourcaud, Prof. Barry Gardiner, Dr. Steve Mitchell, Prof. Bodo Ruck, and Dr. Alexia Stokes (conference organization and animation).

I very much enjoyed working with these people and learning from them on this topic!

I also thank Klaus Alpiger and Urban Paris for letting me work part-time in their engineering office. Their understanding helped me greatly while completing this work.

General introduction

Motivation and scope

Background

Forests fulfill several important purposes. They provide basic and naturally regenerating material for the timber and pulp industries, a living space for animals, insects, and plants, and recreation opportunities for people. Tree roots reinforce the soil and help to stop it eroding. The roots also attenuate variations in water run-off and purify the water contained in the soil (BAFU 2005). The canopy protects the environment at ground level from strong winds, sunlight, and variations in temperature and humidity (Brassel and Brändli 1999). In mountainous regions, forests provide, in addition to these benefits, protection against rockfall, avalanches, landslides, and floods (BAFU 2002b).

Maintaining most of these functions requires an intact forest cover with mechanically stable trees. How stable the trees are will depend on the structure of the forest and hence on its management. The type of forest management policy will in turn depend on how the purposes mentioned above are valued by society (Brang et al. 2006) and how the mechanical stability of the forest is evaluated.

The yearly management costs of all Swiss forests amount to almost half a billion Swiss francs (www.-bafu.admin.ch/wald/01152/01163/index.html?lang=de#-sprungmarke0_7 [accessed October 2008]). The total yearly economic benefits of forests for Switzerland are difficult to quantify due the complex nature of the benefits, but they range from one to several billions of Swiss francs. The value of the protective effect of Swiss forests against natural hazards alone has been estimated as more than 10 billion Swiss francs (BAFU 2002a). Clearly, even a small change in the total benefits forests provide can have a great economic impact. The mechanical stability of trees can positively or negatively contribute to such a change. In areas where forests provide a protection against natural hazards, the level of tree stability will also influence the landscape architecture, land use and risk management.

The mechanical stability of the trees has in the past mostly been evaluated on the basis of statistics, typically as the probability of forest damage for a specific mean wind speed. However, this approach is limited in how much it can explain and predict the effects of forest management and climate change on tree stability. Moreover, it contributes little to the understanding of the physical phenomena involved in the reaction of trees to natural forces. Recent investigations of such phenomena have shed more light on the mechanical stability of trees, especially on tree reactions to wind (e.g. Lohou et al. 2003, Sellier et al. 2008) and tree anchorage (e.g. Dupuy et al. 2005, Nicoll et al. 2006, Fourcaud et al. 2008). These studies have demonstrated that the mechanical stability of trees strongly depends on the region, the local growth conditions, and the species. They have also shown that trees are complex biomechanical structures capable of adapting their cambial growth to external mechanical stress.

The relevance of mechanical tree stability has increased over the last 150 years in Switzerland due to changes in the environment. The forested area has almost doubled and the built environment has increased dramatically, which means the protective effect of forests has become more significant. In Switzerland at present, the built environment is increasing by 1 $m^2 s^{-1}$ (www.bafu.admin-.ch/landschaft/00516/00528/01640/index.html?lang=fr [accessed Oct. 2008]) and the forests are growing by an equivalent of almost half a cubic meter wood material per second (Brassel and Brändli 1999, BAFU 2008). Economic constraints make managers focus on the most important management measures. Moreover, in the future, climate change is likely to lead to more frequent natural hazards of high magnitude involving trees (IPCC 2007, OcCC 2008).

A better understanding of the physical aspects of tree mechanics would help to provide a better basis for the management of forests with respect to their mechanical stability and protective function. We need to know more about the mechanical properties of the root-soil system and the stem, and how these properties depend on growth conditions. Clearly, knowledge is also required about how these elements behave together in a tree as a whole when it interacts with natural forces. Species of particular interest are those which are both subject to natural hazards and are found in settled areas, such as Norway spruce (*Picea abies* L. Karst.), silver fir (*Abies alba* Mill.), and beech (*Fagus sylvatica* L.).

Aims and approach of the study

This PhD thesis contributes to filling the gaps mentioned in the last paragraph, the in the following three ways: (1) by providing new allometric relationships for the mechanical properties of the main structural elements of the tree, the root-soil system and the stem; (2) by investigating to what extent such properties are influenced by mechanical stress in nature; and (3) by assessing the mechanical behavior of the whole tree subject to mechanical stress, originating from wind, snow, and rockfall.

Due to the biomechanical complexity of trees and of forests, the approach taken in this study is mainly experimental. Modeling is used to obtain deeper insights into the experimental results and to help interpret them. To maximize the applicability of the findings, the study trees were selected to be representative for the Alps with respect to tree size, species and growth conditions.

Outline of the study and related projects

Six published research papers form the core of this thesis. Following the convention in a paper thesis, these are preceded by a *General introduction* (the present chapter) and followed by a final chapter with a *Summary discussion and conclusions*. The papers are grouped into six chapters (I to VI). The two first papers (I and II) focus on the tree anchorage, i.e. the root-soil system. The next two papers (III and IV) focus on the tree stem. The last two papers (V and VI) focus on the tree as a whole, and drawing on the findings and methods from the preceding chapters (I-IV). Following the *Summary discussion and conclusions*, there are three *Appendices* describing: (1) the study sites, with the study trees grouped according to study, elevation, plot, and species; (2) Stemtrack, the software tool for detecting stem deflections in tree stability experiments on the basis of digital image analysis; and (3) the results of an unpublished study relating to the stem bending strength of standing trees.

The work for this thesis was undertaken between mid 2006 and mid 2008. It is a scientific follow-up of the project "Tree stability", which was carried out at the Swiss Institute for Snow and Avalanche Research in Davos, from mid 2002 to mid 2006. The tree stability project, which is a combination of the two projects "Rockfor" (QLK5-CT-2000-01302, European Commission) and "Natural hazards and tree stability" ("Naturereignisse und Baumstabilität", ETH, Board of the Swiss Federal Institutes of Technology), included two PhD theses on: (1) Forest management and rockfall (Kalberer 2007); and (2) Energy absorption of trees subject to rockfall (Jonsson 2007). The results presented in the thesis draw on experiments carried out prior to and during the tree stability project, between 2000 and 2005. The analyses for papers I-VI were undertaken between 2006 and 2008.

Elements and phenomena involved in tree stability

Tree stability

In a general context the stability of a body is defined as its "ability to develop forces or moments that restore the original condition when disturbed from a condition of equilibrium or steady motion" (http://www.merriam-webster.com/dictionary/stability [accessed Oct. 2008]). The stability of a tree is relevant for sustainability and can be interpreted as the tree's probability of failure subject to natural influence over time. In tree and forest science, the definition of tree stability includes the mechanical behavior of trees, the forces and pressures acting on trees, the interaction between such actions and trees, and aspects of tree biology and physiology related to tree mechanics. In discussions of "mechanical" tree stability, the tree's mechanics are clearly more in focus than its biology and physiology.

Tree loads in nature

The loads experienced by a tree can be categorized as one of two types. The first type is the loading caused by the tree itself. It includes the weight of the tree, which, for example, makes tree branches bend down, and the self-induced growth stresses within the wood tissue. This load type is permanent, is normally of low magnitude, and can be fairly well predicted. The second type is the loading caused by the environment, such as wind, snow or rockfall. It displays large variations in time, space, and magnitude, and is generally difficult to predict.

Tree structure

The tree can be considered to consist of three major parts with specific physiological functions: (1) the root system, which absorbs water and minerals from the soil for storage and transport to the stem; (2) the stem, which transports the water and minerals to the upper part of the stem and to the crown; and (3) the crown, whose needles (conifers) or leaves (angiosperms) absorb energy (sunlight) and atmospheric CO_2 to produce new wood tissue and atmospheric O_2 (photosynthesis). They also regulate the water balance of the tree through transpiration (http://en.wikipedia.org/wiki/Tree [accessed October 2008]).

The three parts each have their specific structural functions (Fig. 1). The root-soil system (1) provides the anchorage of the tree. It includes the roots and the surrounding soil that contributes significantly to the tree anchorage. For interactions with most environmental loads, the root-soil system corresponds to the uprooted root-soil plate. The stem (2) provides the support for the crown. It ranges from the top of the root-soil system, i.e. at ground level, to the tree top. The crown (3) provides the "sail", "roof", or "mass damper" (James et al. 2006) of the tree. It includes the branches. The crown will influence the mechanical stability of the tree as it interacts with environmental loads like wind, snow, or impacting rocks, but it does not constitute a weak mechanical link in the tree-load interaction, unlike the root-soil system and the stem.

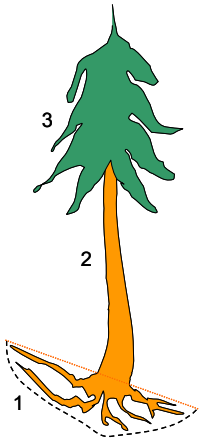

Fig. 1 The three major structural elements of the tree, (1) the root-soil system, 2) the stem, and (3) the crown. A sub-division of these elements may be required depending on the investigation purpose.

The mechanical properties of the tree structure can be divided into two major categories, the material properties and the morphology. They are both governed by the growth of the tree. The mechanical properties of the tree therefore vary in time.

The anatomical properties of the wood in the branches, stem, and roots of conifers display natural genetic variations according to the longitudinal and radial position in the cross section (Trendelenburg and Mayer-Wegelin 1955). Such variations are also influenced by the environment. Typically, the width of the annual rings in the stems of free growing trees increases towards the tree base and the trees have wide and long crowns. Suppressed and dominated trees will develop in the opposite way, and the stems of co-dominant trees a also show a similar tendency (cf. Fig. 2). The pattern tends to be more-or-less distorted by ingrown knots and stem-branch ramifications. The location of knots within the stem corresponds to the timing of the self-pruning of

the tree (Ikonen et al. 2003). As tree growth adjusts to the environment, the stem of a dominated tree will generally produce wood with narrower growth rings, and the branches will have less influence because they drop off (prune) at an early growth stage.

The environment also induces variations in the wood anatomy in the tangential direction due to the branches, reaction wood, and other anomalies. Further, because the water transported in the roots, stem and branches is concentrated in their outer cross-sectional part (sapwood), they all exhibit strong radial and longitudinal differences in wood moisture content. The growth pattern of the stem will also govern its size and taper. The taper of conifer stems in general describes a neiloid at the stem base, i.e. is concave when viewed from the side, and a paraboloid higher up, i.e. with a convex side view. As a result, the growth pattern of the stem will be non-axisymmetric (Trendelenburg and Mayer-Wegelin 1955, Dinwoodie 2000).

Fig. 2 Stem disc cut from height z=1.0 m (left) and from z=21.0 m of a 26 m high, co-dominant Norway spruce growing in Davos (the l-site, Appendix 1, Figures A1-6 and A1-10). The annual rings are narrow at the stem base compared to the tree top and indicate that the tree has been competing for light. The deeply ingrown knots at the stem base (left) indicate a normal early self-pruning here. The top disc (right) was cut between branches and is therefore not affected by the distorted growth pattern close to the stem-branch ramification. The sapwood is about 4 cm thick at z=1.0. At z=21.0 m it occupies the whole cross section.

The anatomical properties and the moisture content of wood govern its mechanical properties (Kollmann 1968, Niemz 1993, Siau 1995). Consequently, the mechanical properties display a heterogeneous pattern in the living tree, as do the anatomical ones. Observations on a local scale for a small wood sample, suggest that mechanical wood properties can be considered to be constant in the radial, tangential and longitudinal directions (anisotropic material). Further, since the differences in the radial and tangential directions are usually small, mechanical wood properties can be simplified and only considered along grain (approximate longitudinal direction) and across grain (approximate radial or tangential direction). The latter simplification, which corresponds to an orthotropic material, is customary in analyses of timber. For the living tree, it is clear that the simplification is only applicable locally, for a given longitudinal, radial, and tangential position in the stem, branch or root, as growth properties (e.g. ring width and knottiness) and taper (neolitic, parabolic) are different depending on position.

The tree is a flexible structure. For lateral loads, three properties contribute to this flexibility. First, the tree stem is flexibly clamped to the ground, meaning that the root-soil system will tilt if it is subject to a rotational moment (e.g. due a lateral force on the stem). Second, the stem and branches are tapered towards the tip. Their bending rigidity therefore decreases exponentially towards the tip. Third, the deformation properties of the wood material in the stem, roots and branches are non-linear functions of the applied load. The displacements therefore increase exponentially with the mechanical stress. Typically, a tree exposed to wind exhibits the three effects in combination (Wood 1995). Here, the crown streamlines and the stem and root-soil system bend. These deformation abilities may be advantageous for the survival of the tree. At the same time, they make the structural behavior of the tree more complex to describe and predict.

Natural loads and trees in interaction

All natural loads likely to act on a tree are dynamic, and they are all exerted by fluids or fluid-granulates (Sovilla et al. 2008) apart from rock impacts. When a fluid acts on the tree with a pressure that varies, the effective load application on the tree will vary according to a chaotic pattern. Clearly, the variations stem from the dynamic nature of the loads as well as the reaction of the tree structure, which deforms and vibrates irregularly, as shown in experiments on tree reactions to winds (e.g. Gardiner 1995, Peltola 1996, Saunderson et al. 1999, Moore and Maguire 2004). The highly dynamic and non-linear nature of the interaction between wind and trees makes it difficult to describe them physically. Therefore, unless the study is of a very specific phenomenon, the analysis and the reproduction of the interaction between trees and loads in nature are usually simplified. Here, the non-linear and dynamic phenomena included in the effective load application on the tree are accounted for using either simple functions or constants in a linear and static approach. Two examples for wind load are: (a) the crown streamlines, thus reducing the effective wind load, according to a simple exponential function of wind speed, where a given increase in speed deforms the crown more in a weak wind than in a strong wind (Rudnicki et al. 2004); and (b) the load amplification due to tree resonance is accounted for using simplified (transfer) functions of the frequency at which the wind load is likely to apply (Saunderson et al. 1999, Sellier et al. 2008).

Mechanical performance of tree growth

When a new wood layer is formed at the periphery of the stem, root or branch cross-section (in the cambium),

the formation process receives signals from the tree. The signals, in the form of variable concentrations of chemical substances (mainly Auxin), transmit information to the cell division activity in the cambium about which wood properties are needed for optimal tree growth (Friml 2003). What is optimal will depend on numerous factors, such as the environmental light, water, nutrition, and temperature, as well as possibly the healing of wounds or combating of biological attacks, the compactness of the ground, and the mechanical stability of the tree.

In addition to this short-term growth adaptation, there is also a potential for trees to evolve and adapt in the long term (Aitken et al. 2008, O'Neill et al. 2008). The natural reproduction of trees (pollination) enables genetic changes to take place. When the trees drop their seed every n^{th} year, a natural selection of optimized reproduction is possible depending on the species and growth conditions. The time horizon is here likely to be hundreds and thousands of years. The seeds may also migrate relatively long distances by wind transport to areas with more suitable growth conditions for the species, which then allows a significantly faster process of environmental adaptation.

The mechanical growth performance of trees measures how well their growth has adapted to environmental loads from a mechanical point of view (Morgan and Cannell 1994, Telewski 2006). This performance is based on the analysis of mechanical tree properties, governed by tree growth and season, and of the effectively applied tree loads, governed by topography, forest structure, tree reaction, and season. The term “tree biomechanics” is commonly used to emphasize the fact that the tree structure adapts through differential growth and thus changes in time according to mechanical stress and growth conditions.

Methods and materials in tree stability

Tree loads in nature

The tree loading caused by tree weight can be considered in the analysis of tree stability if information on tree weight and position are known. To determine the tree position will require inclinometers along the stem, tapes attached to the stem, or some kind of tracking devices like radar, light reflectors or digital images.

Data on the environmental loads susceptible to act on trees are generally obtained in real-time measurements in nature. During recent decades in Switzerland, wind has mainly been measured with anemometers of cup, windmill or sonic type. The properties of avalanche and debris flow have been assessed using digital image series, Doppler radar, optical reflection or pressure captors positioned in the flow (e.g. www.wsl.ch/-forschung/forschungsunits/lawinen/projekte/index_DE [accessed October 2008]). The dynamics of rocks moving down a forested slope have been investigated in the field (Dorren and Berger 2006).

The quality and representativeness of such data for tree stability will depend on the measurement location and on the spatiotemporal resolution of the measurements. The representativeness will also depend on the degree to which the tree and forest influence the load that is effectively applied on the tree. Typically, the wind in the canopy of a mountain forest has a very different flow pattern compared to that of a forest in an open flat area (Raupach 1994, Lo 1995, Morse et al. 2003). Wind measurements relevant to the forest exist (e.g. Mayer 1985, Gardiner 1994) but most wind measuring devices are found in unwooded areas (MeteoSwiss 2006). In addition, winds are, like all natural forces acting on trees, dynamic, and the effective application of the load in time will depend on how the tree behaves during the load application (Lohou et al. 2003). As a consequence *in situ* measurements of wind are often necessary in order to assess the effectively applied wind load on the tree in nature. An adapted design of such measurements requires knowledge about the tree-load interaction. For example, loads applying at crown level do not necessarily need to be recorded at high frequency, unlike loads applying at the stem base. In fact, rapid variations in the tree load application will have little influence on the displacements and stresses at the crown compared to those at the stem base because the crown is more flexible.

In addition to the real-time measurements in the field the properties of environmental tree loads have often been estimated on the basis of post-event observations, such as tree damage, impacts, and deposits left in nature. Finally, reduced-scale experiments (e.g. wind tunnel, inclined bed) provide other ways of estimating the environmental loads likely to act on trees.

Tree structure

The mechanical properties of the tree are either assessed for isolated elements of the tree or for the tree as a whole.

Examples of the first are investigations of the tension strength of roots, the shear strength of the soil, the anchorage strength, which is the maximum resistance to rotational moment of the root-soil system, and the bending elasticity and strength of stem or branch sections. The anchorage strength is obtained in the winching test, which involves pulling the stem of the standing tree sideways with a cable. The other elements are tested in the laboratory according to standard procedures.

Examples of the second are investigations of the swaying properties of the tree (modes, frequencies, damping), and of stem deflections or accelerations due to a lateral force (e.g. winching force or wind pressure) on the standing tree *in situ*. Another example of an assessment for the tree as a whole is the drag coefficient of the tree subject to wind. This test is normally made for small trees clamped at the base and positioned in a wind tunnel.

The tree in interaction with loads in nature

There are three ways to investigate how a tree reacts to loads in nature.

The first is a full-scale investigation *in situ*, with direct real-time tests or observations of past natural events. Here, the latter approach clearly dominates, which is understandable, as direct tests are both time and cost consuming. Observations of past natural events include all potential natural loads on trees, whereas direct tests have been made only for the wind-tree interaction (Gardiner 1995) and for the rock-tree interaction (Dorren and Berger 2006).

The second way to investigate how a tree reacts to environmental loads is using a reduced-scale study. This option will only be as good as the tree, forest and load models used. Such experiments will require *in situ* tests and observations for validation. Reduced-scale investigations of the physical interaction between load and trees have been performed for wind-tree and wind-forest interaction (e.g. Gardiner et al. 1997, Morse et al. 2003).

The third possibility is a computer simulation. Of course, this option will depend on the tree and model data used, and the simulation will need to be validated and the tree-load interaction investigated on a full or reduced scale. Computer simulations have been used, for example, to describe tree reactions to wind (e.g. Saunderson et al. 1999, Sellier et al. 2008).

Mechanical performance of tree growth

Analyzing the biomechanical performance of trees means testing how well their growth has adapted to environmental loads. This can be done by considering trees of different sizes grown under different conditions, or by studying the growth and load history of one or a few specific trees. In either case two types of data are required: the statistical and mechanical properties of the loads that effectively act on the tree, and the (statistical and) mechanical properties of the tree.

Investigations of the biomechanical performance of trees have focused separately on the stem (e.g. Meng et al. 2006) and on the root-soil system (e.g. Stokes et al. 1995). The stem has been analyzed for constancy of bending stress under variable lateral load (e.g. Morgan and Cannell 1994) and the root-soil system for the orientation of root growth in relation to the direction of the prevailing wind or to the slope (e.g. Nicoll and Ray 1996, Chiatante et al. 2002). The resistance of the root-soil system to uprooting has been investigated in relation to soil conditions, the slope, and to the position of the tree in the forest stand (e.g. Ray and Nicoll 1998, Achim et al. 2003, Cucchi et al. 2004).

Mechanical stability and growth performance of trees: knowledge gaps

Tree loads in nature

Tree loading caused by the weight of the crown and the stem has rarely been included in the analysis of the mechanical tree stability. This is probably due to the difficulties of correctly determining the deflection of the tree subject to external loads. Consequently, it is not known to what extent and under which conditions tree loading caused by crown and stem weight is important to consider.

There is some information about natural loads on trees, in particular about, in the order from more to less: wind, snow load (static), rock impact, snow flow (dynamic), and debris flow. The quantity and quality of this information correspond in general to the likelihood that this type of load will cause tree damage (involving load frequency and probability of tree failure). As a consequence, the need for new knowledge is generally about the same for all types of natural tree loads. However, the frequency and magnitude of potential tree loads vary according to the site. For example, infrastructure and settlements of great value maybe subject to infrequent natural hazards of high magnitude, which means considerable risk. If forests provide some protection in such risk situations, it is important to know how the trees will react to particular hazards and to what extent they can reduce the destructive effect of such hazards by slowing them down. In this context information on infrequent tree loads, such as rockfall and snow avalanches, is also of great value. If we know more about how trees react to and protect from particular loads, it will be possible to determine the load and pressure levels for areas in or close to protection forests more precisely.

Tree structure

Several studies have considered tree structure as a whole, including the crown, stem and the root-soil system, in the analysis of the mechanical tree stability. The aim of these studies is to evaluate the general risk of tree failure. Detailed analyses of the mechanical stability of the tree structure as a whole are much less frequent, although they would provide a basis for understanding the processes involved here. Deformation properties of the crown, stem, branches, roots, and the root-soil system have been investigated separately, in more or less detail. However, these properties have not been investigated in combination or compared with respect to the reaction of the entire tree to natural hazards, to assess the importance of different tree elements for tree stability. Such investigations should help to improve the basis for optimal forest management.

Root-soil system

It is important to know the deformation of the root-soil system subject to a rotational moment until failure (e.g. due to a lateral force on the stem) to be able to predict the reactions and energy absorption of a tree subject to any load in nature. Studies have been carried out for Sitka spruce and larch (Coutts 1986, Crook and Ennos 1996). However, the deformation properties of the root-soil system have not been investigated for Norway spruce and have never been parameterized by tree size (allometric descriptions). Further, there seems to be no information for any tree on the deformation of the root-soil system subject to a translational force.

Stem

It is essential to know the deformation of the fresh stem subject to bending to predict the reactions and energy absorption of a tree subject to any load in nature. Deformation of the stem will, just like the deformation of the root-soil system, lead to changes in the structural system of the tree and the applied load. There appears to be no study that describes the stem deformation until failure.

Tree in interaction with loads in nature

Information on the interaction between trees and loads in nature is valuable because it helps us to understand the complex process of load application and hence tree stability, and also provides a better basis for the (simplified) calculation models (cf. Natural loads and trees in interaction, p. 11) used to evaluate hazards and risks. Although progress has been made in describing the tree-wind interaction, the complex nature of the load-tree interaction is still quite unknown. For natural loads other than wind, e.g. rock impact and snow flow, even less is known.

Mechanical performance of tree growth

The adaptation and performance of tree growth in relation to mechanical stress has been investigated separately for the crown, stem, branches, roots, and the root-soil system. The growth performance of the tree as a whole does, however, not seem to have been investigated in detail.

Methods and materials used in this study – a summary

Study trees and sites

The six studies that form the core of this thesis (Table 1) include altogether 136 mature trees (Table 2), composed of 105 Norway spruce (*Picea abies* L. Karst.), 27 silver fir (*Abies alba* Mill.), and four Scots pine (*Pinus sylvestris* L.). The trees were selected to be representative for the forests in the Alps, with respect to tree size, species, vitality, and growth conditions. In addition, the trees were also selected according to the different aims of the six studies (Table 1).

The 136 trees were all growing in Switzerland, with 36 Norway spruce at high elevations (HE, above 1600 m asl) close to Davos, and the remaining 100 trees at low elevations (LE, below 650 m asl) close to Zurich. The trees were located in twelve different plots. The detailed locations of these plots are given in the Appendix 1. The essential characteristics of these plots and of the trees growing there are given in the relevant papers, in chapters I-VI.

Table 1 The focus and purpose of each of the six papers in this thesis (I-VI).

Paper / Chapter No.	Focus of the investigation	
	Tree part	Purpose
I	Anchorage	Resistance, geometry and root growth
II	Anchorage	Mechanical properties
III	Stem	Linking mechanical and growth properties within the stem
IV	Stem	Linking mechanical and growth properties of the stem
V	Tree	Reactions and energy absorption due to a rock impact
VI	Tree	Mechanical performance and growth adaptation

Table 2 Number of trees according to study (paper), species, and site, where LE=low elevation and HE=high elevation. A tree is "new" if it was not investigated in a previous ("prev.") paper.

Paper	All			Norway spruce			Silver fir			Scots pine			LE-site			HE-site		
No.	total	new	prev.	total	new	prev.	total	new	prev.	total	new	prev.	total	new	prev.	total	new	prev.
I	84	84	0	57	57	0	23	23	0	4	4	0	84	84	0	0	0	0
II	66	29	37	66	29	37	0	0	0	0	0	0	45	8	37	21	21	0
III	1	1	0	1	1	0	0	0	0	0	0	0	1	1	0	0	0	0
IV	7	7	0	3	3	0	4	4	0	0	0	0	7	7	0	0	0	0
V	15	15	0	15	15	0	0	0	0	0	0	0	0	0	0	15	15	0
VI	13	0	13	13	0	13	0	0	0	0	0	0	6	0	6	7	0	7
All	136			105			27			4			100			36		

Tree loads

The tree loading caused by tree weight was obtained on the basis of the measured stem and crown weights per meter height of the overturned tree. The loading caused by the environment involved in this thesis are mainly wind, vertical snow load, and rock impact. The wind properties were measured at of one or two Meteo Swiss weather stations as close as possible to the study plot (cf. details in the papers related to wind). In paper VI, the effective winds on the tree crowns were estimated on the basis of (i) literature with specific focus on wind, and (ii) wind profile data from the Seehorn wind tower (Davos). The snow loads used (paper VI) originate from *in situ* measurements and observations made prior to this study close to the study plots (Stadler et al. 1998). The rock impact loads on the tree (paper V) were directly measured. Data on all the three types of loading caused by the environment were completed with *in situ* observations of recent past events in the community of Davos during the period 2002-2006.

Tree structure

A tree was considered to consist of three main structural elements: the crown, stem and anchorage (Fig. 3). The stem was also analyzed according to tree height and radial position in the stem and was therefore subdivided into smaller elements. The dimensions and the deformation properties of these elements were obtained in appropriate *in situ* or laboratory experiments (cf. next sections). The natural swaying properties of a standing tree were obtained by pulling the tree sideways, releasing it, and measuring the acceleration at several stem heights of the freely swaying tree (Jonsson et al. 2007, www.wsl.ch/forschung/forschungsprojekte/tree stability/animation_dynamik.gif [accessed Oct. 2008]).

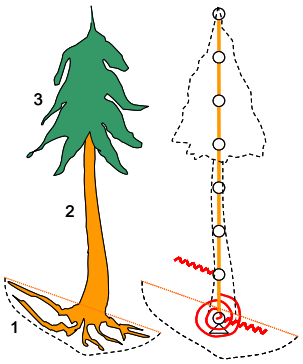

Fig. 3 Division of the tree (1-3, left) into structural elements (right). The deformation properties of the root-soil system (1) are described in the tree model with a rotational and a translational spring (red). The stem (2) is further divided into stem sections (orange elements) with specific bending and shear deformation properties. The radial deformation properties of stem sections are considered with a lateral spring (indicated with a red spring).

Root-soil system

The mechanical properties of the root-soil system were obtained using the winching test (Fig. 4 to Fig. 6). Here, the tree is pulled sideways with a cable attached to the stem, with synchronized records of the pulling force and the position of the tree. The stem position is obtained in two ways: (1) from a computer model of the tree provided with the measured tree weight and dimensions, and constrained with the recorded force and inclination at different stem heights (Jonsson et al. 2007 and paper II), and (2) from a series of digital images where the stem centre line is detected with a piece of software designed for this purpose (Stemtrack, Appendix 2). The deformation of the root-soil system due to a translational force was estimated on the basis of the record obtained in the impact test (paper V and Fig. 12).

Fig. 4 The winching test involved pulling the tree sideways. The records of the pulling force F and of the stem position are made with reference to the stem base in a 3D-coordinate system and to time (t). Records of the stem inclination (a) and digital images help determine the 3D-position (x,y,z) of the stem while pulling, where z is the height and x is the azimuth of the pulling direction.

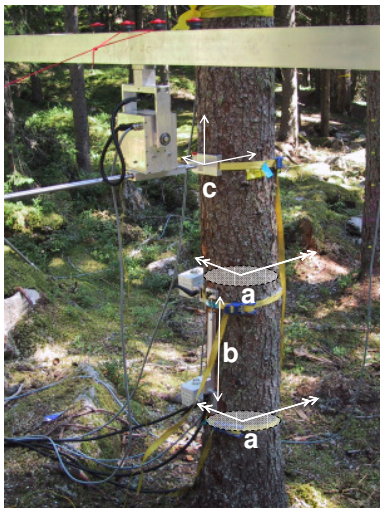

Fig. 5 Detail of the stem base in Fig. 4. Measurements of the stem inclination in 2D (a), the stem elongation (b, one of four measurement points), and the path in 3D of one point fixed to the stem (c).

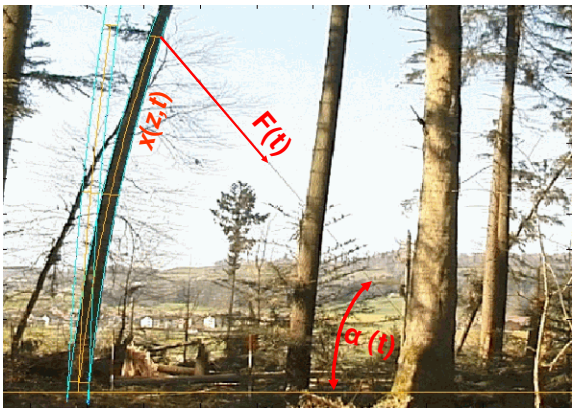

Fig. 6 The stem pulled to the right in the winching test captured in digital images. $x(z,t)$ indicates the stem centre line (curved, fine, yellow lines), $F(t)$ is the pulling force inclined at an angle of α, and t is the time. The stem position in each image is detected on the basis of contrast differences and then referenced to the pulling plane (x,z) using the digital image analysis software Stemtrack (cf. Appendix 2). The blue fine lines defines the left and the right sides of the stem and the yellow its geometric centre. The figure shows the tracked stem position at two time steps. The left three lines refer to an earlier time step than the stem position displayed in the image. To capture the entire tree requires usually two synchronized image series, one from the upper and one from the lower stem. The two series of referenced stem positions merged vertically describe $x(z,t)$ of the entire tree.

Once the tree had overturned, the root-soil system was investigated in more-or-less detail depending on the purpose of the test (Fig. 7). The growth properties analyzed of the roots were in the thesis limited to their size, azimuthal direction of growth and signs of root rot.

Fig. 7 Assessing the root morphology (left) and the shape of the root-soil plate (right) of the overturned root-soil plate, using meters and digital images. The 1.0 m indication (right) applies approximately to the left image as well.

Stem and crown

The stem diameter and bark thickness were measured along the stem of the overturned tree (Fig. 8). The crown extension was measured as the perpendicular distance from the stem centre (Fig. 9). The weight of the stem and crown were obtained for height sections of 1.0 m or shorter (Fig. 10). The mechanical properties of the stem were generally obtained using bending tests in the laboratory (Fig. 11). The applicability of the results from these tests to the standing tree was checked by measuring the stem deflection in winching tests (paper VI). The stiffness for the sideways penetration of a rock front into the stem was obtained experimentally in the laboratory. The experiment is briefly described and animated in: http://www.wsl.ch/forschung/forschungsprojekte/Treestability/local-impact_EN?redir=1& [accessed October 2008].

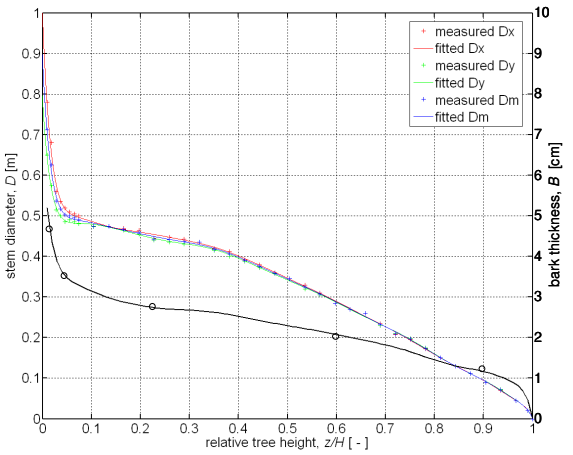

Fig. 8 Example of dimension records of the lying tree: the measured (x) and the fitted (line) stem diameter D over bark in the x-direction (Dx), in the y-direction (Dy), and as the geometric mean (Dm). The black unfilled dots indicate the measured double bark thickness B with a regression line-fit according to Laasasenaho et al. (2005), scaled to fit the measured B at 5% tree height.

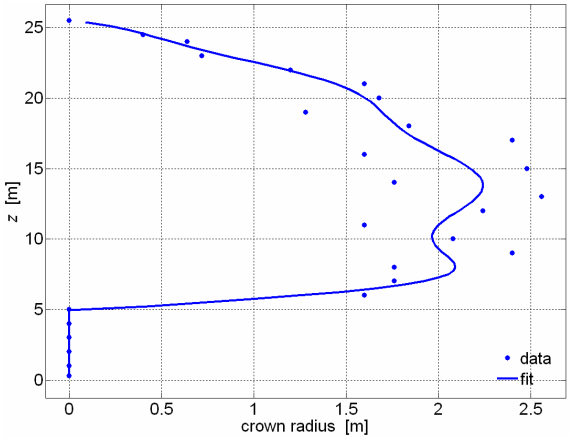

Fig. 9 Example of crown radius according to tree height, with measured data and fitted, continuous curve. Generally, the crown radius was approximated as the geometric mean of the two measured extensions of the crown of the lying tree.

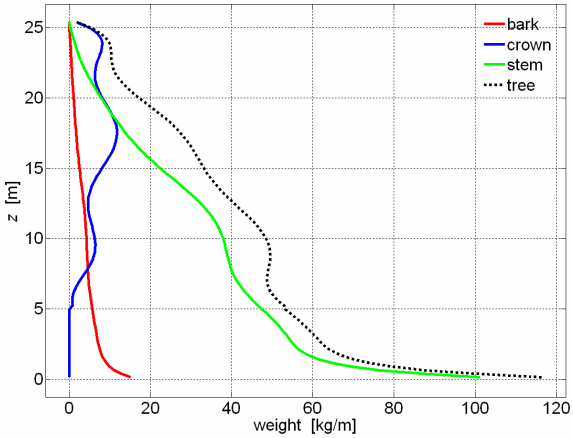

Fig. 10 Example of weight per meter of height for the bark, the stem, the crown and the tree (bark + stem + crown).

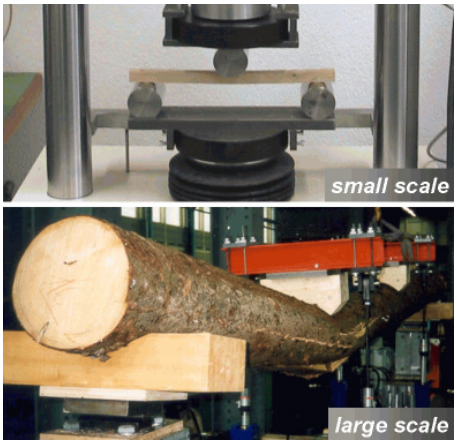

Fig. 11 Bending tests in the laboratory of small-scale samples with rectangular cross sections (top) and of entire stem sections (bottom).

Natural loads and trees in interaction

The dynamic interaction between natural loads and the tree structure was analyzed in the experimental investigation of the tree subjected to an impact from a rock (paper V and example in Fig. 12), and to some extent for the tree subject to wind (paper VI). The previously measured swaying properties of the study trees (Jonsson et al. 2007) helped in the interpretation of the results from studies V and VI.

Fig. 12 Impact trolley (simulated rock, yellow) hits the tree stem. The stem base is colored white with black lines at every percent of stem height to optimize the stem tracking procedure in the image series with the Stemtrack software. Accelerometers are attached to the trolley and to the downhill side of the stem at several heights (cf. details in paper V). Animations of the reactions of the upper and lower part of the tree during the impact event can be viewed in: www.wsl.ch/forschung/-forschungsprojekte/Treestability/insitu-impact_EN?redir=1& [accessed October 2008].

Mechanical performance of tree growth

The morphology and growth properties of the tree measured were interpreted in terms of mechanical properties, and compared to the frequency, magnitude, direction, and location of natural loads. The focus was on how the directions of root growth adapt to the directions of winds (paper I) and how the form and resistance of the main tree elements crown, stem and root-soil system adapt to various lateral loads in nature (paper VI).

Chapter I

Anchorage of mature conifers: resistive turning moment, root-soil plate geometry, and orientation of root growth

Tree Physiology 27, 1217–1227

Anchorage of mature conifers: resistive turning moment, root–soil plate geometry and root growth orientation

TOR LUNDSTRÖM,[1,2] TOBIAS JONAS,[1] VERONIKA STÖCKLI[1] and WALTER AMMANN[1]

[1] *WSL, Swiss Federal Institute for Snow and Avalanche Research SLF, CH-7260 Davos, Switzerland*

[2] *Corresponding author (t.lundstroem@slf.ch)*

Received September 30, 2006; accepted December 12, 2006; published online June 1, 2007

Summary Eighty-four mature Norway spruce (*Picea abies* L. Karst), silver fir (*Abies alba* Mill) and Scots pine (*Pinus sylvestris* L.) trees were winched over to determine the maximum resistive turning moment (M_a) of the root–soil system, the root–soil plate geometry, the azimuthal orientation of root growth, and the occurrence of root rot. The calculation of M_a, based on digital image tracking of stem deflection, accounted not only for the force application and its changing geometry, but also for the weight of the overhanging tree, representing up to 42% of M_a. Root rot reduced M_a significantly and was detected in 25% of the Norway spruce and 5% of the silver fir trees. Excluding trees with root rot, differences in M_a between species were small and insignificant. About 75% of the variance in M_a could be explained by one of the four variables—tree mass, stem mass, stem diameter at breast height squared times tree height, and stem diameter at breast height squared. Among the seven allometric variables assessed above ground, stem diameter at breast height best described the root–soil plate dimensions, but the correlations were weak and the differences between species were insignificant. The shape of the root–soil plate was well described by a depth-dependent taper model with an elliptical cross section. Roots displayed a preferred azimuthal orientation of growth in the axis of prevailing winds, and the direction of frequent weak winds matched the orientation of growth better than that of rare strong winds. The lack of difference in anchorage parameters among species probably reflects the similar belowground growth conditions of the mature trees.

Keywords: allometry, biomechanics, natural hazards, preferential growth, tree structure, winching experiment.

Introduction

The mechanical stability of a forest is challenged by strong winds (e.g., Schiesser et al. 1997). The maximum resistance to turning moment of the root–soil system, denoted by the anchorage strength (M_a), is typically the weakest mechanical link for shallow-rooted trees subjected to strong winds (Papesch et al. 1997, Brassel and Brändli 1999). Values of M_a are commonly obtained in winching experiments (e.g., Coutts 1986, Milne and Blackburn 1989, Crook and Ennos 1996). The moment effectively applied to the root–soil system in such experiments includes the moment due to the winching force and to the weight of the leaning tree. Both factors depend on the position of the stem, which is constantly changing during the winching test.

Almost 40 different series of winching tests have been performed since the sixties (e.g., Fraser 1962, Nicoll et al. 2005). For these tests, a variety of approaches were used to account for changes in the position of the stem, and thus in test geometry, for the calculation of M_a. Overhanging tree weight can amount to between 20 (Peltola 1995, Gardiner et al. 2000) and 70% of M_a (Coutts 1986). Our analysis showed that a change in the geometry of the applied winching force also needs to be considered in the calculation of M_a. When analyzing anchorage mechanics, it is important to know the effective applied and reacting turning moment of the root–soil system because the root–soil system is considered an isolated structural element, or an isolated group of elements, when applying the finite element methods (FEMs). The FEMs are increasingly being applied in the analysis of tree mechanics (Fourcaud et al. 2003*a*, 2003*b*, Dupuy et al. 2005, Yang et al. 2005, Jonsson et al. 2006).

The value of M_a is positively related to the sum of root cross sections at one fixed horizontal distance (e.g., at 0.5 m) from the center line of the stem (Crook and Ennos 1996, Bolenikus 2001), the mass of the woody roots and, to some extent, the size of the root–soil plate and the rooting depth (e.g., Mattheck et al. 1993, Wessolly and Erb 1998, Bolenikus 2001, Meunier et al. 2002). Higher M_a values are found for trees on the edge of a stand than within the stand (Cucchi et al. 2004), and for trees with interlocked root systems (Coutts 1983). The value of M_a depends on soil conditions (Fraser and Gardiner 1967, Moore 2000). Further, M_a is strongly related to tree parameters aboveground (e.g., tree mass, stem mass, stem diameter at breast height and tree height) (e.g., Peltola et al. 2000, Cucchi et al. 2004, Stokes et al. 2005, Nicoll et al. 2006). Winching tests have mostly been conducted on small and young trees because they are usually considered more vulnerable to wind than large trees. Consequently, values of M_a, in combination with below- and aboveground tree parameters, have been determined almost exclusively for small trees.

The size and shape of the overturned root–soil plate indicate

how roots are anchored in the soil and must be known when modeling the mechanics of the root–soil system (Coutts 1983, 1986, Blackwell et al. 1990, Danjon et al. 2005). Various idealized shapes have been used to describe the root–soil plate; however, we were unable to find a three-dimensional description based on experimental data.

Excavations of the root system of young trees show preferential root growth in the direction of the prevailing winds (Stokes et al. 1995, Nicoll and Ray 1996, Mickovski and Ennos 2003*a*, Danjon et al. 2005). The degree of such adaptive growth depends not only on the magnitude and frequency of the prevailing wind, but also on the species and the growth conditions (Nicoll et al. 1995, Coutts et al. 1999). It is possible that mature conifers, like young ones, display a prevailing azimuthal direction of root growth depending on wind load, but, to our knowledge, this has never been demonstrated.

To improve the design of mechanical tree and stand models, we need to better understand the anchorage of large mature trees. Here, we present a novel dataset to test the following hypotheses: (1) in winching tests, stem deflection has a significant influence on the effectively applied M_a; (2) M_a for mature conifers can be predicted with simple allometric relationships; (3) the three-dimensional shape and size of the root–soil plate can be predicted with simple allometric relationships; and (4) mature conifers display preferential root growth in the direction of prevailing winds.

Materials and methods

Trees, stand and site

Eighty-four mature trees were winched over in late spring 2000 on a site close to Zürich, Switzerland (47°14′ N, 8°53′ W) at 460 m a.s.l. The trees included 57 Norway spruces (*Picea abies* L. Karst.), 23 silver firs (*Abies alba* Mill.), and four Scots pines (*Pinus sylvestris* L.), all from the same mixed stand of these species, and some European beech (*Fagus sylvatica* L.) and ash (*Fraxinus excelsior* L.). The forest structure is typical of a managed forest in the Zürich Uplands, the region of the test site. As a result of selective logging, Norway spruce dominates even though it is a natural beech habitat. The density of the mature, single-story stand was about 350 trees ha^{-1}. Although the stand includes local clearings, no test tree grew at the stand edge. Mean cambial age measured at breast height (AGE) of the trees selected for the winching tests was 90 years, the mean tree height (H) was 33 m, and the mean diameter at breast height (DBH) was 46 cm. The distribution of slenderness ($S_n = H/DBH$) was close to normal, with a mean (± SE) of 78 ± 14. The minimum and maximum values were: DBH = 22 and 70 cm, H = 16 and 42 m, AGE = 46 and 154 years and S_n = 51 and 121, respectively. Among the aboveground coniferous tree parameters, only crown length relative to H differed according to species, with lower values for Scots pine (0.32 ± 0.12) than for Norway spruce (0.49 ± 0.13) and silver fir (0.51 ± 0.11).

The study site has a mean annual precipitation of 1100 mm, a mean temperature of 10 °C and a mean annual wind speed of 1.5 m s^{-1}. The predominant winds blow from the W-WSW sector to E-ENE or vice versa (Schmerlikon weather station, 3 km from the test site; MeteoSwiss 2005). During the period 1900–2000, the site was exposed to several severe storms: 300 times > 20 m s^{-1}, 60 times > 25 m s^{-1} and 10 times > 30 m s^{-1} (10-min mean winds; MeteoSwiss 2005). On average and related to the annual harvest, these winds have caused windthrow to 2% and stem breakage to 0.5% of the conifers in the stand, mainly large trees having been affected (Municipal forester, Blöchliger, personal communication, WSL and BUWAL 2001). Soils on the flat test site are medium to deep B-horizons of dystric to gleyic, dystric Cambisols and some Luvisols (taxonomy according to FAO 1998). Throughout the test period, the temperature was above freezing and rainfall was normal for the season.

Test set-up and investigations

The positions of the test trees were first determined with a tachymeter. The trees were then prepared for winching according to a standard test design (e.g., Peltola et al. 2000). A cable was attached at one end to the tree stem at z_a at a relative tree height, $z_{a,rel} = z_a/H$ (Figure 1). For all trees, $z_{a,rel}$ was close to normally distributed between 16 to 67%, averaging 39%. The other cable end was wound up by a tractor-driven winch positioned more than one tree height away from the base of the tree. A digital video camera was positioned to capture the deflection of the tree in the winching direction. Before each winching test, the geometry of the winching and recording set-up was measured relative to the stem base, defining the x-axis to be in the winching direction.

The trees were pulled in the E to ENE direction, i.e., in the axis of the prevailing winds and the expected maximum anchorage moment. As the tree was pulled by the cable, the applied cable force (F) and tree deflection were recorded every second (Figure 1). An MTS force sensor (Type 85081-6100-144 V0000C0, 944860, Messtechnik Schaffhausen, Germany)

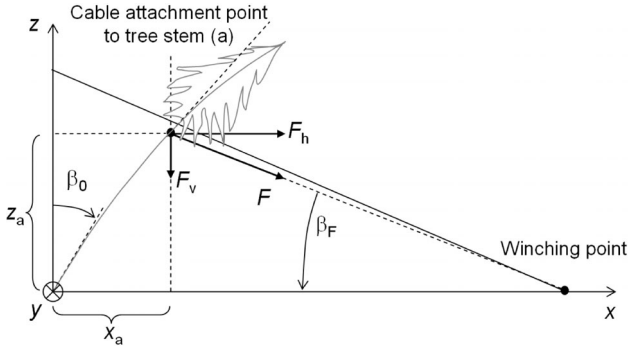

Figure 1. Test set-up for the winching experiments. Abbreviations: β_o, the stem-base inclination; β_F, the angle of cable-force application; z_a and x_a, the height and the horizontal deflections, respectively, for the point a where the cable is attached to the tree stem; and F_h and F_v, the horizontal and vertical components, respectively, of the winching force F. The inclined continuous line between the tractor and the stem indicates the initial position of the winching cable. All angles occur in the vertical plane $y = 0$.

recorded F, while the stem position was tracked with digital photographs taken approximately perpendicular to the pulling direction. The winching rate was an approximately constant 0.10 m s^{-1} until the tree began to fall under its own weight. In a few cases, it was the stem that failed and not the root–soil system, and a second test was performed with the winch attached to the top of the remaining trunk. All winching tests were performed under near windless conditions. Once the tree was uprooted, we recorded the following measurements and observations of the toppled tree.

Root–soil plate We measured dimensions of the root–soil plate, i.e., the height, width and depth of the overturned, truncated root–soil plate and the plate shape (based on digital photographs of the three main profiles, in the planes $y = 0$, $x = 0$ and $z = 0$). Both dimensions and shape refer to the compact soil of the root–soil plate, ignoring single protruding roots. Wetness (visual determination) of the soil material in the root–soil plate and directly beneath it was classified as waterlogged, moist or dry.

Roots We determined the geometrical distribution and diameter of the roots according to azimuth. The visible occurrence of root rot was noted.

Stem Stem diameter was measured at heights of 0.3, 1.3, 3.0 m, and then every 3 m to the top of the tree. Annual ring width was measured in stem discs cut between the tree base and top.

Crown The mass of branches sampled in 1-m height sections from relative crown heights of 1/8, 3/8, 5/8 and 7/8 was measured with the dynamometer.

The complete dataset (1), including the winching experiment and the parameters recorded from the toppled tree, comprised 75 trees: 52 Norway spruces, 20 silver firs and three Scots pines. Excluding trees affected by root rot from dataset (1) resulted in a dataset (1a) with 61 trees. A reduced dataset (2), excluding data related to the resistive anchorage moment, was obtained for 84 trees: 57 Norway spruces, 23 silver firs and four Scots pines. Excluding trees affected by root rot from (2) resulted in a dataset (2a) with 70 trees: 44 Norway spruces, 22 silver firs and four Scots pines. Only four mature Scots pine trees were available for investigations in the test stand. In the analyses, we used dataset 1 for M_a, 1a for stem deflection and 2a for root–soil plate geometry and root growth.

Turning moment of the root–soil system

In analyzing the mechanics of the root–soil system, we refer to the tree coordinates x, y and z. The line described by the center of the stem intersects with the ground level at $(x,y,z) = (0,0,0)$. The winching force causes displacement of the stem in the plane $y = 0$ (Figure 1). To analyze the digital images of stem deflection, we used the software STEMTRACK, which rectifies the images and calculates the deflection of the entire stem in the tree coordinates (x,y,z) for each digital image (every second). The deflection is parameterized by a high-order polynomial $x(z)$. The precision in $x(z)$ depends on the pixel resolution of the image. We used an image resolution of 768 × 576 pixels. If a 30-m high tree is captured entirely in one image, one pixel corresponds to ~10 cm. With a rectification precision of about 4 cm, the rectification accuracy was higher than the pixel resolution. Technical information on STEMTRACK can be accessed at http://www.wsl.ch/forschung/forschungsprojekte/Treestability/Stemtrack.pdf (cited September 28, 2006). All analyses of mechanics and geometry were done with Matlab 7.0 software (MathWorks, USA).

The turning moment applied to the root–soil system (M_o) (Equation 1) was calculated at $(x,y,z) = (0,0,0)$ for every second, from the beginning of the application of the winching force until the tree started to fall under its own weight. From this point, we cannot define values for M_o because our mechanical analysis does not include dynamics and the related forces of inertia. Concerning the point of rotation of the root–soil system, we are aware that it is located at $x > 0$ and presumably $z < 0$, and that $(x,y,z) = (0,0,0)$ is a simplification. Everything belowground is considered as one structural element, namely the "root–soil system," that resists the M_o.

$$M_o = F \cdot \left(z_a \cos\beta_F + x_a \sin\beta_F\right) + \sum_{z=0}^{\text{tree top}} m_{\text{stem}}(z) \cdot g \cdot x(z) + \sum_{\text{crown base}}^{\text{tree top}} m_{\text{branches}}(z) \cdot g \cdot x(z) \quad (1)$$

where the symbols are mostly explained in Figure 1, but $m(z)$ is the mass of the stem and branches, and g is earth gravity (9.82 m s^{-2}). The first term is due to the force application, and the second and third terms are due to gravity. The maximum value of M_o corresponds to the anchorage strength M_a of the tree.

To apply Equation 1, the tree was divided into 100 elements of similar length. Their length was conserved in accordance with the theory of large deflections (e.g., Wood 1995), and the elements diameter and mass of branches m_{branches} (if any) were interpolated (piecewise cubic) from the measured data. The mass of the stem was deduced from the woody stem diameter, bark thickness and the constant moist wood- and bark-bulk density. The bulk density of moist wood was estimated as 825 kg m^{-3}, based on radial growth linked to mass, and that of the bark as 750 kg m^{-3} (Lundström et al. 2007). These estimates are means for all trees and take into consideration the seasonal variations in water content of the stem and the bark (Schmidt-Vogt 1991). The resulting mean bulk density of the stem on bark was 815 kg m^{-3} for a tree of average size, which was used to calculate $m_{\text{stem}}(z)$ for all trees, independent of size.

The contribution to M_o can be divided into three groups, depending on origin: (1) the contribution from F, where only the initial geometry of the winching test is considered; (2) the change in contribution from F caused by the modified geometry, i.e., change in x_a, z_a and β_F (cf. Figure 1); and (3) the contribution from the overhanging tree weight, i.e., gravity. The sum of (1) and (2) is the physically correct contribution from F to M_o, and is thus equal to the first term in Equation 1. To investigate the magnitude of these contributions and to check if the

analysis of M_o (Equation 1) can be simplified, we analyzed the three contributions separately with Equations 2–4, which describe the respective portions of M_o/M_a as:

$$k_{F(ig)} = \frac{F}{M_o}\left(z_a \cos\beta_F + x_a \sin\beta_F\right)_{start} \quad (2)$$

$$k_{geom} = \frac{F}{M_o}\left(z_a \cos\beta_F + x_a \sin\beta_F\right) - k_{F(ig)} \quad (3)$$

$$k_{geom} = \frac{g}{M_o}\left(\sum_{z=0}^{\text{tree top}} m_{stem}(z)\cdot x(z) + \sum_{\text{crown base}}^{\text{tree top}} m_{crown}(z)\cdot x(z)\right) \quad (4)$$

where $k_{F(ig)}$ is the relative contribution to M_o of F, where only the initial geometry ($_{ig}$) of the tree and the winching test set-up are considered; $_{start}$ is the reference to the initial position of the tree and the winching cable; k_{geom} is the relative contribution to M_o caused by the change in the geometry ($_{geom}$) of the winching force application compared with at the start of the test; k_{grav} is the relative contribution to M_o from the overhanging tree mass, i.e., gravity ($_{grav}$); and $k_{F(ig)} + k_{geom} + k_{grav} = M_o/M_a = 1.0$.

Geometry of the root–soil plate

The digital photographs of the root–soil plates revealed that a simple fitting of their shapes, such as a cone or a cylinder, would be imprecise. Therefore, we opted for a shape fitted with an ellipse in the plane, and a depth-dependent taper in width and height (Equation 5, Figure 2), where the shape was assumed to be symmetrical along the *x*- and *y*-axes. This shape-fitting, which was used to calculate the volume of the root–soil plate (V_{plate}; Equation 6), concerns the root–soil plate before truncation, which occurred when the tree overturned. The choice of shape fit was a compromise of small errors and a small number of fitting parameters. Mean errors were evaluated for at least ten measurements, randomly distanced along the profiles in the $x-y$, $x-z$ and $y-z$ planes (Figure 2). The center of the top of the plate corresponds to $(x,y,z) = (0,0,0)$ of the tree.

$$\begin{aligned} z_{R,N} &= \frac{z_R}{\max(z_R)} \\ x_N(z_{R,N},\phi) &= \sin\phi\left(\left(\frac{1-z_{R,N}}{1+z_{R,N}}\right)^{nx} - 1\right) \\ y_N(z_{R,N},\phi) &= \cos\phi\left(\left(\frac{1-z_{R,N}}{1+z_{R,N}}\right)^{ny} - 1\right) \\ x(z_R,\phi) &= x_N(z_{R,N},\phi)\max(x) \\ y(z_R,\phi) &= y_N(z_{R,N},\phi)\max(y) \end{aligned} \quad (5)$$

$$V_{plate} = \pi \int_{z_{R,N}=0}^{z_{R,N}=1} \max\left(x(z_{R,N})\right)\max\left(y(z_{R,N})\right) dz_R \quad (6)$$

where $z_{R,N}$ is the normalized depth of the root–soil plate, in the range 0–1; z_R is the z-coordinate of the plate, in the range $0-\max(z_R)$ (m), where $\max(z_R)$ corresponds to $z = 0$ of the tree above ground; $x(z_R,\phi)$ is the dimension of the plate in the x-direction (half height), in the range $0-\max(x)$ (m); $y(z_R,\phi)$ is the dimension of the plate in the y-direction (half width), in the range $0-\max(y)$ (m); ϕ is the rotational angle around the z-axis, in the range 0–360° (cf. Figure 2C); and nx and ny are the x- and y-taper of the plate, where $nx,ny < 0.8$ describes a pointed (with tap roots), $0.8 < nx,ny < 2.0$ a rounded, and $nx,ny > 2.0$ a rectangular profile (flat plate, mainly horizontal, lateral roots).

Azimuthal distribution of winds and roots

The distribution of roots with a diameter of 1.0 cm and larger was analyzed according to the azimuth angle θ. The summed

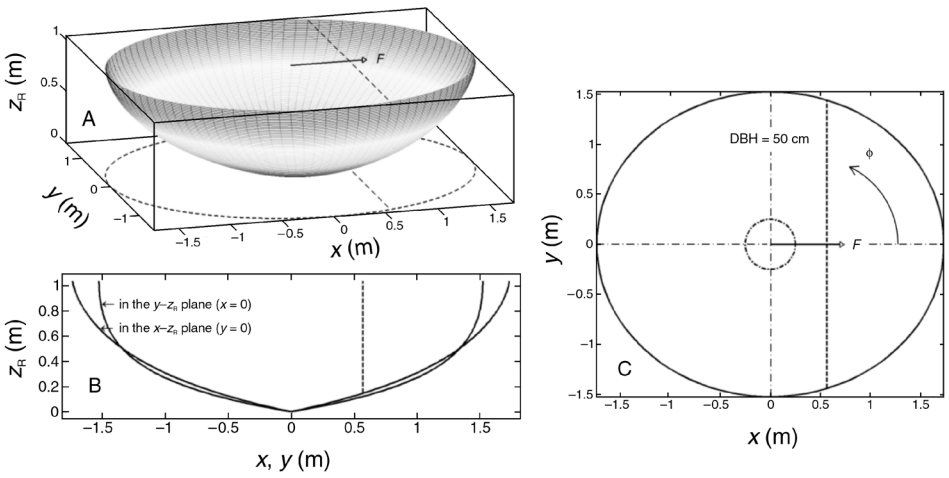

Figure 2. Modeled fit of the root–soil plate in three dimensions (A), with profiles from the side (B) and from above (C). z_R corresponds to the stem centre of the standing tree and x to the stem of the toppled tree, which, in most cases, was also the direction of the winching force (F), and ϕ indicates the rotational angle in the x–y-plane. This example shows a tree with a diameter at breast height (DBH) of 50 cm and x- and y-taper of $nx = 1.4$ (x–z_R-plane) and $ny = 2.0$ (y–z_R-plane), respectively. All straight dashed lines indicate the failure hinge of the root–soil plate at overturning. The remaining, truncated plate is found to the left of this hinge.

cross-sectional area (ΣCSA) of the roots at one fixed radial distance was first determined within 36 azimuthal directions, each having a span of 10° (0 ± 5°, 10 ± 5°…). This radial distance was selected to be slightly less than the mean radius of the root–soil plate (R_{plate}; square root of (max(x))(max(y)); Figure 2) and was consequently different for each tree. The ΣCSA was found to correlate with R_{plate} (cf. Ennos 1993, Bolenikus 2001, Mickovski and Ennos 2003*b*). To compensate for the relative weighting of large trees on ΣCSA(θ), ΣCSA within each azimuthal direction was normalized with R_{plate}, resulting in $\Sigma CSA(\theta)_N$. Thereafter, a mean $\Sigma CSA(\theta)_N$ was calculated for each of the 36 azimuthal directions. These 36 means were finally normalized with the sum of the 36 means, resulting in $CSA_{NN}(\theta)$:

$$CSA_{NN}(\theta) = \frac{CSA_N(\theta)}{\sum_{\theta=0°}^{360°} CSA_N(\theta)} \quad (7)$$

Roots on the truncated, broken-off part of the root–soil plate were in some cases difficult to assess, because the plates were not always completely overturned (i.e., examined upside down). Therefore, out of a total of 70 investigated plates (dataset 1b), CSA close to the plate hinge was obtained from only 17 plates in the azimuth sector WSW ± 30° and from nine plates in the azimuth sector WSW ± 20°. Finally, the preferential root growth across the entire root–soil plate was calculated as the axis of principal orientation of the 36 CSA_{NN} –vectors, as derived from the Least Squares Orthogonal Distance Fitting.

For wind, we analyzed wind vectors (u) and vectors of wind pressure ($P_w(u)$). The wind vectors were 10-min means measured during 1985–1999 at the Schmerlikon weather station (MeteoSwiss 2005). The wind pressure acting on the undeformed crown was defined as $P_w(u) = c(u)u^2\rho/2$, where ρ is air density = 1.17 kg m^{-3}, with the drag coefficient $c(u) = p + (1 - p)e^{\alpha u}$, where $p = 0.18$ and $\alpha = -0.09$ were from the literature (Johnson et al. 1982, Gardiner et al. 2000, Rudnicki et al. 2004). Azimuthal histograms of $P_w(u)$ were calculated for three classes of wind speed: weak (1–6 m s^{-1}), strong (> 6 m s^{-1}), and all wind speeds > 0 m s^{-1} together. The $P_w(u)$-vector values were counted on circle sector "bins," with an opening angle of 5°, resulting in 72 directional bins for the speed range of each wind class. The axis of prevailing wind pressure was derived as for the direction of root growth by using the Least Squares Orthogonal Distance Fitting for all $P_w(u)$-vectors within the three wind-speed classes.

Statistical analysis

The response variables are denoted Y and the explanatory allometric variables X. The Y variables include M_a and the dimensions of the root–soil plate, which were parameterized with the following X variables: DBH, H, total mass of the tree (m_{tree}) and of the stem (m_{stem}), V_{plate}, ΣCSA(θ) for $0 < \theta < 360°$, R_{plate}, radius of the crown's projection on the ground (R_{crown}), crown length relative to H and gradient in stem diameter between 0.3 and 1.3 m tree height. The X variables were selected on the basis of what is easily measurable and on what is commonly used in the literature to enable comparisons with results from published studies.

We first explored the Y variables in multivariate stepwise regression. This analysis yielded regressions of only one significant X, e.g., m_{tree} in the case of M_a. We therefore concentrated on monovariate regressions, including potential combinations and transformations of X variables. The regression equations of M_a were all forced through the origin because a tree with no mass or zero dimensions has an M_a equal to zero. Generally, a regression was considered useful if $R^2 > 0.5$ and a polynomial coefficient was considered meaningful if $P < 0.05$. Significant differences in M_a/X between groups were determined by the Wilcoxon Mann-Whitney Test. This was done for the trees with and without root rot, and with and without stem failure. All differences in allometric relationships between the species were tested similarly.

We use b for regression coefficients, μ for the mean value or the value preceding the standard error (± SE) and SE_N (Y) for the error of predicted value relative to the observed Y value. Levels of significance are denoted as: *, $P < 0.05$; **, $P < 0.01$; ***, $P < 0.001$; and ns, $P > 0.05$.

Results

Influences of stem deflection on the calculated values of M_o and M_a

In all winching experiments, M_o increased first strongly with increasing stem-base inclination (β_o), as expected. The $M_o(\beta_o)$ reached its maximum value, M_a, at a β_o of between 2 and 15°, with a mean value of 5.0° (Figure 3). When this β_o value was exceeded and M_o began to decrease, the roots on the opposite side of the force application were gradually stretched, and, for some trees, these roots even rose vertically in the lateral direction. As these roots failed (in tension, visual observation) at a β_0 between about 20 and 30°, the tree began to fall under its own overhanging weight. The overhanging tree weight (k_{grav}) had an important influence on $M_o(\beta_o)$, whereas the change in geometry of the force application (k_{geom}) during the winching experiment influenced $M_o(\beta_o)$ to a lesser extent (Figure 3).

Overhanging tree weight (k_{grav}; Equation 4) is a result of the overall stem deflection, a combination of stem bending and β_o (Figure 4). Generally, β_o contributed more to k_{grav} than stem bending, apart from a few trees that were winched above half of the tree height. Stem deflection generally increased with winching height and tended to decrease with tree size. The latter resulted from a generally higher β_o at M_a for small trees than for large trees. The minimum value of k_{grav} at M_a was 8% (a silver fir with DBH = 53 cm, $z_{a,start}/H = 0.20$, $\beta_{F,start} = 5°$), the maximum value was 42% (a Norway spruce with DBH = 22 cm, $z_{a,start}/H = 0.55$, $\beta_{F,start} = 25°$), and the mean value of k_{grav} at M_a was 13%.

The value of k_{geom} (Equation 3) increased with larger winching cable angles at the start of the test $\beta_{F,start}$ (Figure 1). The point a where the winching cable was attached to the tree stem

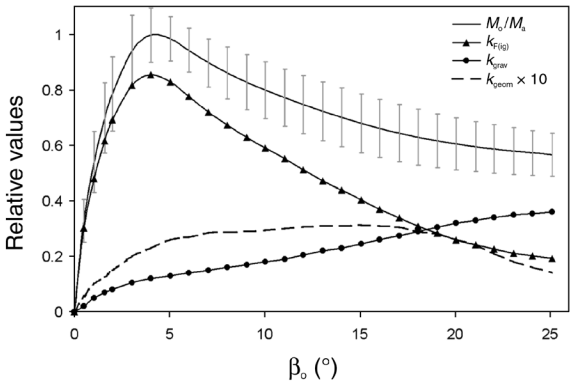

Figure 3. Development of the resistive turning moment of the root–soil system (M_o) with increasing stem-base inclination (β_o) and the relative contributions of the winching force ($k_{F(ig)}$), gravity (k_{grav}) and the geometry of the winching force (k_{geom}) to M_o. When the anchorage strength (M_a) occurs at $\beta_o = 5.0°$, $k_{F(ig)} = 0.84$, $k_{grav} = 0.13$ and $k_{geom} = 0.03$. The curves are the mean values for the investigated trees. Bars indicate the SE of the mean.

described a path, from the test start to M_a, that was close to a circle with a radius equal to the starting winching height ($z_{a,start}$), as shown in Figure 4. Thus, the height coordinate for the force application (z_a) decreased little, whereas the coordinate for the horizontal deflection x_a steadily increased. As a result, the change in β_F from the start of the test to M_a was small, and k_{geom} consequently remained small, even for a $\beta_{F,start}$ value as large as 30°. The minimum value of k_{geom} at M_a was 0% (in general for $\beta_{F,start} < 10°$), the maximum value was 7% (a Norway spruce with DBH = 55 cm $\beta_{F,start} = 29°$), and the mean value of k_{geom} at M_a was 3%.

The value of $k_{F(ig)}$, the part of the actual $M_o(\beta_o)$ that is accounted for if only the initial geometry of the winching test is

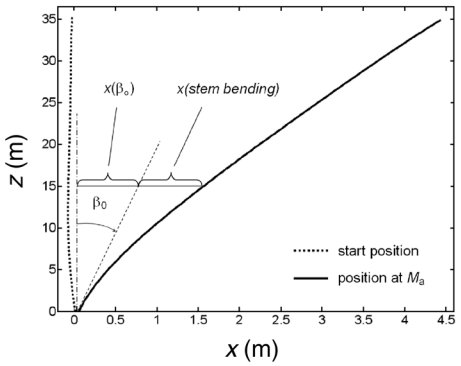

Figure 4. Stem deflection as the applied turning moment of the root–soil system (M_o) reached the anchorage strength (M_a). This silver fir (diameter at breast height = 55 cm, height = 35.2 m), which was not perfectly straight at the start of the test (almost vertical dotted line), was winched at a height of 13.2 m at an angle $\beta_{F,start}$ of 14°. The overhanging tree weight due to stem deflection, originating from the stem-base inclination $x(\beta_o)$ and from stem bending $x(stem\ bending)$, contributes to M_a. The coordinates of the tree top changed little in z value between the test start and M_a: $(z,x)_{start}$ = (35.20 m, –0.01 m), $(z,x)_{M_a}$ = (34.91 m, 4.44 m).

considered in the analysis of $M_o(\beta_o)$, ranged from 1.0 to 0.30. At M_a, the maximum $k_{F(ig)}$ was 0.90, the minimum was 0.53 and the mean value of $k_{F(ig)}$ at M_a was 1 – mean(k_{grav}) – mean(k_{geom}) = 0.84 (Figure 3).

Values of M_a

Among the 75 Norway spruce, silver fir and Scots pine trees, 13 Norway spruces (25%) and one silver fir (5%) had signs of root rot. These 14 diseased trees were growing in two clusters. Although the roots were not badly attacked in any of the trees, the trees with root-rot displayed 21% lower ($P < 0.05$) M_a/X than the trees without root rot. The M_a of all trees with no root rot was, in turn, best correlated with m_{tree}, m_{stem}, DBH^2H and DBH^2 (Table 1). Trees subjected to a second winching test after stem failure in the first test (19 out of 84 trees) displayed no systematic differences in M_a/X.

For the four regression models, there were no significant differences ($P > 0.5$) in M_a/X between species. This is shown in Figure 5, with M_a as a function of DBH^2H. The other three models in Table 1 displayed similar scattering of the M_a data. In Figure 5, we comment on two outliers labeled 1 and 2. The root system of the first outlier (1), a Norway spruce (DBH = 25 cm, $S_n = 121$), was, unlike that of other trees, firmly interlocked with the root–soil system of another close neighbor spruce of DBH = 24 cm, and both trees were overturned together during the winching test. This tree was excluded from all statistical analyses. A very large proportion of the lateral roots of the second outlier (2), also a Norway spruce (DBH = 46 cm, $S_n = 70$), was pulled laterally up above the ground over

Table 1. Statistical data related to models describing the anchorage strength (M_a) = bX (kN m) based on 38 Norway spruces, 19 silver firs and three Scots pines. Only trees without root rot were considered. Abbreviations: m_{tree} and m_{stem} (kg), the total mass of the tree and of the stem, respectively; DBH (m), the stem diameter at breast height; and H (m), the tree height. The models are listed top-down according to the quality (R^2) of the models including all (All) three species.

X	Species	b	SE(p)	SE$_N$(M_a)	R^2
m_{tree}	Spruce	1.25E–1 ***	4.1E–3	0.18	0.76
	Fir	1.20E–1 ***	4.9E–3	0.18	0.82
	Pine	1.23E–1 ***	2.1E–3	0.02	0.98
	All	1.22E–1 ***	2.9E–3	0.17	0.81
m_{stem}	Spruce	1.62E–1 ***	5.5E–3	0.18	0.73
	Fir	1.73E–1 ***	8.3E–3	0.20	0.75
	Pine	1.57E–1 *	1.8E–2	0.14	0.01
	All	1.66E–1 ***	4.5E–3	0.19	0.76
DBH^2H	Spruce	4.19E+1 ***	1.4	0.20	0.76
	Fir	4.15E+1 ***	2.2	0.20	0.71
	Pine	4.18E+1 *	5.1	0.15	–0.14
	All	4.17E+1 ***	1.1	0.20	0.76
DBH^2	Spruce	1.48E+3 ***	5.1E+1	0.20	0.73
	Fir	1.46E+3 ***	8.5E+1	0.21	0.64
	Pine	1.47E+3 *	2.1E+2	0.15	–0.51
	All	1.47E+3 ***	4.3E+1	0.20	0.71

a long distance as the tree turned over.

Characteristics of the root–soil plate

The correlations between dimensions of the root–soil plate and aboveground tree parameters were weak. This also applies to the relationships between width (twice the maximum *y*-value, Figure 2), height (twice the maximum *x*-value) and depth (the maximum *z*-value) of the individual root–soil plates. Consequently, the corresponding regression models provided a poor fit to the data (Table 2). The respective R^2 values were in all cases highest with DBH as the explanatory variable, apart from V_{plate}, which was best described by DBH^2H. The soil in the root–soil plate and directly beneath it was generally dry to slightly moist.

The taper of the root–soil plate *ny* tended to be greater than *nx*, typically *ny* = 2.0 and *nx* = 1.4 (Figure 2). However, the depth taper displayed large variations (SE = 0.8, min = 0.4, max = 3.2) with no obvious pattern. As the root–soil plate fit was adapted to each plate individually, the overall mean errors in profile and volume were small ($SE_N < 0.10$, $SE_N < 0.12$), and mainly caused by departures from the elliptic fit of the cross section (in the *x*–*y* plane). The truncation (broken-off part) of the root–soil plate on the pulling side (positive *x*-side) due to pressure from the tree mass when the tree toppled, was slightly more than half of the maximum *x*-value in this direction (Figures 2B and 2C).

Azimuthal distribution of roots and wind

The directions of root growth and wind display affinities. The preferential axis of the mean distribution of root CSA (Figure 6A) was close to the prevailing axis of wind pressure (Figure 6B). The separate considerations of weak and strong winds show that the root system adapts more to frequent winds of low magnitude than to the less frequent storms, though the differences were small. The azimuthal directions θ for the axis of preferential root growth and wind did not differ with weak winds, whereas with strong and less frequent winds, the difference was 8°. If all magnitudes of winds were considered together, the difference was 4°.

Discussion

Influence of stem deflection on the calculated value of M_a

Stem deflection occurs as a tree is pushed by lateral forces, which may be either artificial (e.g., pulled by a winch) or natural (e.g., wind). In either case, the overhanging tree weight contributes to the effectively applied turning moment of the root–soil system. In addition, the stem deflection that occurs during a winching test typically modifies the geometry of the force application.

Stem deflection results from stem bending and rotation of the root–soil system β_o. We compared our β_o and k_{grav} values with those in the literature (Table 3). Most of the latter values refer, however, to the stem position at maximum force application and not to that at M_a. Our winching experiments showed that both β_o and k_{grav} were up to 25% lower at maximum force application than at M_a. They also showed that k_{grav} increased substantially if *F* was applied above $z_{rel} = 0.5$. It is apparent that both stem-base inclination and stem bending need to be considered when calculating M_a from winching tests. A thorough comparison of $\beta_o(M_a)$ and k_{grav} requires reference to the same type of stem-base moment, i.e., that M_a systematically accounts for the overhanging tree weight. Compared with k_{grav}, k_{geom} is of minor importance in the analysis of the resistive turning moment of the root–soil system. However, under special winching conditions (e.g., for trees winched on a slope), it is possible that k_{geom} becomes more relevant.

Because of the complexity of stem deflection mechanics, it seems impossible to describe the contributions of k_{grav} and k_{geom} to M_a with simple allometric models. Hence, when calculating M_a from winching tests, these contributions need to be determined experimentally. We suggest stem deflection be re-

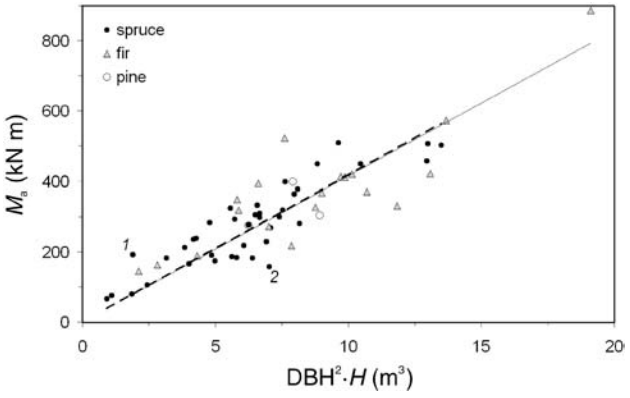

Figure 5. Anchorage strength (M_a) for trees with no root rot plotted against stem diameter at breast height squared times tree height (DBH^2H). The regressions for Norway spruce (fine continuous line), silver fir (hatched line) and Scots pine (not displayed, because it was between those of the Norway spruce and silver fir) are almost identical. Two outliers are indicated (1 and 2).

Table 2. Response variable (*Y*) and explanatory variables (*X*) related to the root–soil plate. All regressions include all 70 Norway spruce, silver fir and Scots pine trees. All regression coefficients (*b*) are significant at $P < 0.001$.

Y	*X*	*b*	SE(*b*)	$SE_N(Y)$	R^2
Width	DBH	5.9	0.19	0.26	0.19
Height	DBH	6.6	0.23	0.30	0.11
Depth	DBH	2.0	0.07	0.35	0.08
R_{plate}	DBH	3.1	0.09	0.24	0.19
V_{plate}[a]	DBH^2H	0.45	0.03	0.53	0.28
Height[b]	Width	1.1	0.04	0.23	0.24
Depth[c]	Width	0.32	0.01	0.38	0.04

[a] Compared with Norway spruce, *b* was 27% larger ($P < 0.05$) for silver fir and 35% larger ($P > 0.05$) for Scots pine.

[b] $b = 1.20$ (Norway spruce); 1.13 (silver fir); 1.29 (Scots pine), but the differences were not significant.

[c] The differences in *b* were negligible (< 3%) between Norway spruce, silver fir and Scots pine.

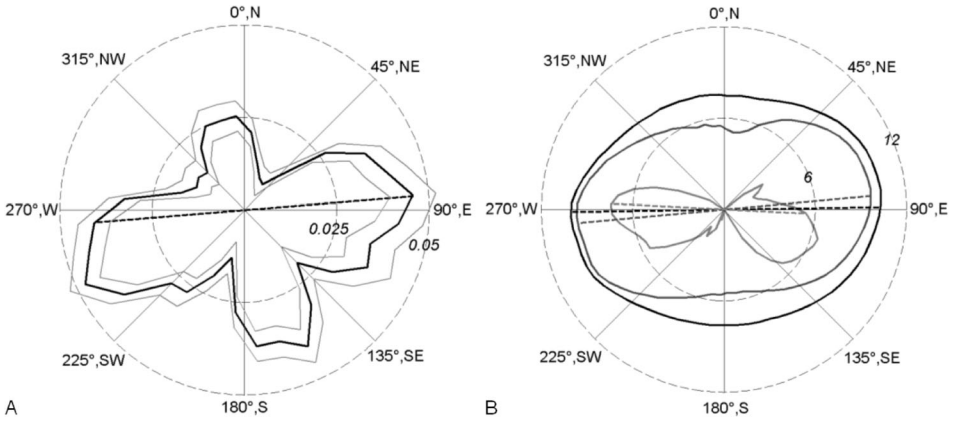

Figure 6. Direction of (A) root growth compared with that of the (B) wind. (A) The average distribution of normalized cross sectional area (CSA) of roots according to azimuth angle (θ) displayed by one circle histogram (continuous black line; gray line is the SE), with the axis of principal orientation of CSA at θ = 265°/85° (black dashed line). (B) The direction of wind pressure on the tree depending on the magnitude of wind speed (u), displayed by three separate circle histograms (continuous lines). The axes of principal orientations of wind pressure are: for all wind data $u > 0$ m s^{-1} (the black and outermost line) at β = 269°/89° (dashed), for low wind-speed data $1 < u < 6$ m s^{-1} (dark gray line) at β = 265°/85°, and for high wind-speed data $u > 6$ m s^{-1} (light gray and innermost line) at β = 273°/93°. The radial graduation corresponds to log(number of data per bin).

Table 3. Comparison of the stem-base inclination (β_o) as the anchorage strength (M_a) is reached and the contribution of the overhanging tree weight (k_{grav}) to M_a. Abbreviations: AGE, mean cambial age measured at breast height; DBH, stem diameter at breast height; and z_{rel}, the relative tree height.

Species	Soil B-Horizon	Forest stand: Density, type	AGE min–max mean (year)	DBH min–max mean (cm)	z_{rel} min–max mean	$\beta_o(M_a)$ min–max mean (°)	k_{grav} min–max mean (%)	Reference
Picea abies *Abies alba* *Pinus sylvestris*	Cambisols, luvisols	350, co-dominant	46–154[1] 90[1]	22–70 46	0.16–0.67 0.39	2–15[2] 5[2]	8–42[2] 13[2]	This study
Picea sitchensis	Shallow peaty gley	co-dominant	34 34	19–23 21	– 0.18	1–10[3,4] 4[3]	– –	Coutts (1983)
Picea sitchensis	Shallow peaty gley	4000 ha^{-1}, co-dominant	35 35	15–27 20	– 0.73	1–10[3,4] 26[2,4]	60–70[2] 67[2]	Coutts (1986)
Picea sitchensis	Shallow peaty gley	4000 ha^{-1}, co-dominant	20–50 –	10–35 –	– –	– –	– 22[3]	Gardiner et al. (2000)
Picea sitchensis	Shallow peaty gley	4000 ha^{-1}, co-dominant	– 40	– 23	– 0.5	– –	– 14[3]	Achim et al. (2003)
Pinus taeda	Fine sand	1000 ha^{-1}	– 30	13–41 –	– 0.5	2–35[1,3] 6[1,3]	– –	Fredericksen et al. (1993)
Pinus sylvestris	Sandy, silty podzol	1000–1800 ha^{-1}	40–100 –	14–23 –	0.3–0.5 –	– –	5–20[3] –	Peltola (1995), Peltola et al. (2000)
Pinus radiata	Shallow, compact gravel	–	10–39 –	23–52 –	0.2–0.4 –	– –	– 9[3]	Papesch et al. (1997)
Pinus pinaster	Sandy podzol	100–1000 ha^{-1}	15–50 –	18–41 –	0.1–0.5 –	– –	4–14[3] 9[3]	Cucchi et al. (2004)

[1] Measured at breast height.
[2] At maximum stem-base moment.
[3] At maximum force application.
[4] Of the root–soil plate, β_o at the stem base ought to be greater because roots deform and bend more easily than the relatively rigid stem base.

corded as a function of stem height, e.g., according to the methods we used.

Allometric predictions of M_a

The M_a was well predicted by either tree mass, stem mass (or stem volume), DBH^2H, or DBH^2 (listed in order of R^2). This is in line with results obtained for Scots pine, Norway spruce and birch (Peltola et al. 2000, Bolenikus 2001), white spruce and balsam fir (Meunier et al. 2002) and silver fir (Stokes et al. 2005). The M_a-model ranking shows that tree anchorage is better adapted to the size of the tree (crown and stem) than to the cross-sectional area at the stem base. Including belowground tree variables (e.g., root CSA or the dimensions of the root–soil plate) in the retained M_a-models of aboveground variables did not improve the quality of the models, in contrast to previous studies on tree anchorage (Papesch et al. 1997, Peltola et al. 2000, Mickovski and Ennos 2003*b*, Cucchi et al. 2004).

For the trees without root rot, we compared our $M_a/(DBH^2H)$ and M_a/m_{stem} data with published values (Table 4). Although our regression coefficients are close to the values in the literature, our coefficients are among the largest. We offer four explanations for this discrepancy: (1) not all studies included k_{grav} and k_{geom}; (2) only our M_a values were derived from winching in the direction of prevailing winds, and were thus likely to be the largest M_a values in terms of azimuth (Danjon et al. 2005); (3) our experiments were conducted on relatively deep and generally well-drained soils; and (4) only our M_a values refer to the tree position at the maximum effective stem-base moment M_a, whereas the M_a values in other studies refer to the position at maximum force application.

The lack of significant differences in M_a/X between Norway spruce and silver fir for trees without root rot is probably associated with local growth conditions: when growing in a mixed stand, both species are limited by similar growth conditions, resulting in a growth response independent of species (Polomski and Kuhn 1998). Therefore, inhibition of root system growth typical of the species is more probable with increasing tree size (Köstler et al. 1968). It is likely that more intensive examinations of local soil and growth conditions would have helped explain more of the overall variations in M_a, and possibly also to explain why no differences were found between the species in the mixed forest. The number of Scots pine trees studied (four) is too low to test whether it differs significantly from silver fir and Norway spruce in any of the anchorage properties studied. Because of root rot, Norway

Table 4. Comparison of M_a-regression coefficients, M_a/m_{stem} and $M_a/(DBH^2H)$. Abbreviations: AGE, mean cambial age measured at breast height; DBH, stem diameter at breast height; M_a, the maximum resistive turning moment; m_{stem}, the mass of the stem; H, tree height; k_{grav}, the relative contribution to M_o from the overhanging tree mass; k_{geom}, the relative contribution to M_o caused by the change in geometry of the winching force application compared with at the start of the test; and M_o, the turning moment applied to the root–soil system.

Species	Soil B-Horizon	Forest stand	AGE (years)	DBH (cm)	M_a/m_{stem} (kN m kg^{-1})	$M_a/(DBH^2H)$ (kN m m^{-3})	Inclusion of k_{grav}; k_{geom}	Reference
Picea abies *Abies alba* *Pinus sylvestris*	Cambisols, luvisols	350 ha^{-1}	46–154	22–70	0.16 0.17 0.16	42 42 42	Yes; Yes	This study
Picea sitchensis	Peaty gley Shallow brown Deep brown	Dense plantation	30	21	0.12 0.17 0.21	–	Yes; Yes	Fraser and Gardiner (1967)
Picea sitchensis	"Free draining brown"	Dense plantation	40	23	0.11[1] 0.10[1] 0.086[1]	–	Yes; Yes	Achim et al. (2003)
Picea sitchensis	Peaty, surface water gley	4000 ha^{-1}	46	32	0.04–0.14[2]	–	No; No	Ray and Nicoll (1998)
Pinus sylvestris	Sandy, silty podzol	1300–1800 ha^{-1}	40–100	14–23	0.13[3]	36	No; Yes	Peltola et al. (2000)
Picea abies	Sandy, silty podzol	1000–1600 ha^{-1}	80–100	16–23	0.11[3]	33	No; Yes	Peltola et al. (2000)
Pinus pinaster	Sandy podzol	100–1000 ha^{-1}	15–50	18–41	–	35[4] 45[4] 40[4]	Yes; Yes	Cucchi et al. (2004)

[1] When pulled down slope/across slope/upslope.
[2] Higher values with deeper water table.
[3] Derived by Gardiner et al. (2000) from the experiments of Peltola et al. (2000).
[4] The regressions were not forced through zero, but the intercept values were small. The three values refer to: trees on soil with a hard pan within the stand; trees on the stand edge; and trees within the stand on soil with no hard pan.

spruce had significantly weaker root–soil anchorage than the other species in the test area.

Shape of the root–soil plate and allometric predictions of its size

The shape of the root–soil plate was well described with a depth-dependent taper model with an elliptical cross section. We compared the performance of this fit to calculate the total plate volume (based on mean values of nx, ny and $\max(x)/\max(y)$) with that of two other fits: a circular-conical shape (Peltola and Kellomäki 1993) and an elliptical cross section, but with a constant profile in depth (Cucchi et al. 2004) similar to the profiles used by Blackwell et al. (1990) and Coutts (1983). Considering the individually fitted plates (Equation 5) as reference volumes, we obtained min/mean/max errors of –25/–5/+70% for the taper model, –110/–40/+10% for the circular-conical fit and +20/+50/+560% for the ellipsoidal fit. Thus, the averaged taper model seems to yield good predictions of shape and volume.

The dimensions of the root–soil plate exhibited larger intra-species differences than interspecies differences, which corresponds with the findings of Brang and Bachofen (2002). The horizontal and vertical plate size was weakly correlated with DBH, similar to the Norway spruce and Scots pine analyzed by Hakkila (1972). The shape and dimensions of the root–soil plate are largely governed by root architecture (Danjon et al. 2005). We therefore believe that the same masking effects described for M_a help explain both the lack of significant differences between species in root–soil plate dimensions and the weak allometric relationships within species.

As the trees toppled, the root–soil plate failed at a distance from the stem center that was less than 50% of the root–soil plate radius in the winching direction ($< 0.5\max(x)$; cf. Figure 2), similar to the $0.4\max(x)$ obtained for Sitka spruce planted close to furrows (Coutts 1983, Ray and Nicoll 1998). The broken-off part of the root–soil plate represented 20–30% of the total (modeled) volume of the root–soil plate of the standing tree.

Azimuthal direction of root growth related to prevailing winds

The distribution of the cross-sectional root area (CSA) was, on average, concentrated in the prevailing wind axis. This confirms the claim that mature trees adapt their root growth to the orientation of prevailing winds, just as do young trees (Nicoll and Ray 1996). The roots seem to adapt their azimuthal CSA more to weak and frequent winds than to rare and heavy storms, although the differences are small. Because maximal M_a is considered to coincide with the axis of preferential orientation of coarse roots (e.g., Coutts 1986, Nicoll and Ray 1996), we consider that our trees were tested in the azimuth of their maximum M_a.

We reached four conclusions from our study. (1) In winching tests, stem bending and the rotation of the root–soil system have a significant influence on the effectively applied M_a. We propose recording stem deflection as a function of tree height when M_a is calculated from winching tests. (2) The M_a for mature conifers can be accurately predicted by monovariate regression with either tree mass, stem mass, DBH^2H or DBH^2. (3) The three-dimensional shape and size of the root–soil plate were weakly correlated with all allometric parameters. (4) Mature conifers showed preferential root growth in the direction of frequent low wind events.

Acknowledgments

We thank the Board of the Swiss Federal Institutes of Technology for financial support as part of the "Tree Stability and Natural Hazards" ("Naturereignisse und Baumstabilität") project, M. Ammann, F. Michel and L. Lorenzato for field assistance, P. Lüscher for soil data, MeteoSwiss for climate data and S. Dingwall for revision of the text.

References

Achim, A., B.C. Nicoll, S. Mochan and B.A. Gardiner. 2003. Wind stability of trees on slopes. *In* Wind Effects on Trees. Eds. B. Ruck, C. Kottmeier, C. Mattheck, C. Quine and G. Wilhelm. University of Karlsruhe, Karlsruhe, Germany, pp 231–237.

Blackwell, P.G., K. Rennolls and M.P. Coutts. 1990. A root anchorage model for shallowly rooted Sitka spruce. Forestry 63:73–92.

Bolenikus, D. 2001. Zur Wurzelausbildung von Fichte (*Picea abies* L. Karst) und Weisstanne (*Abies alba* Mill.) in gleich- und ungleichaltrigen Beständen. Ber. Freiburger Forstl. Forsch. 35:155.

Brang, P. and H. Bachofen. 2002. Kleiner Wurzelballen—grosser Lotharschaden? Inf.bl. Forsch.bereich Wald 11:3.

Brassel, P. and U.-B. Brändli. 1999. Inventaire forestier national Suisse. Résultats du deuxième inventaire 1993–1995. Haupt, Berne, 442 p.

Coutts, M.P. 1983. Root architecture and tree stability. Plant Soil 71:171–188.

Coutts, M.P. 1986. Components of tree stability in Sitka spruce on peaty gley soil. Forestry 59:173–198.

Coutts, M.P., C.C.N. Nielsen and B.C. Nicoll. 1999. The development of symmetry, rigidity and anchorage in the structural root system of conifers. Plant Soil 217:1–15.

Crook, M.J. and A.R. Ennos. 1996. The anchorage mechanics of deep rooted larch, *Larix europea* × *L. japonica*. J. Exp. Bot. 47: 1509–1517.

Cucchi, V., C. Meredieu, A. Stokes, S. Berthier, D. Bert, M. Najar, A. Denis and R. Lastennet. 2004. Root anchorage of inner and edge trees in stands of Maritime pine (*Pinus pinaster* Ait.) growing in different podzolic soil conditions. Trees 18:460–466.

Danjon, F., T. Fourcaud and D. Bert. 2005. Root architecture and wind-firmness of mature *Pinus pinaster*. New Phytol. 168: 387–400.

Dupuy, L., T. Fourcaud and A. Stokes. 2005. A numerical investigation into the influence of soil type and root architecture on tree anchorage. Plant Soil 278:119–134.

Ennos, A.R. 1993. The scaling of root anchorage. J. Theor. Biol. 161:61–75.

FAO. 1998. Soil map of the world. Revised legend. World soil resources report Vol. 60. FAO-Unesco, Food and Agriculture Org. of the United Nations, Rome, 119 p.

Fourcaud, T., F. Blaise, P. Lac, P. Castera and P. de Reffye. 2003*a*. Numerical modeling of shape regulation and growth stresses in trees II. Implementation in the AMAPpara software and simulation of tree growth. Trees 17:31–39.

Fourcaud, T., F. Danjon and L. Dupuy 2003*b*. Numerical analysis of the anchorage of maritime pine trees in connection with root structure. *In* Wind Effects on Trees. Eds. B. Ruck, C. Kottmeier, C. Mattheck, C. Quine and G. Wilhelm. University of Karlsruhe, Karlsruhe, Germany, pp 323–330.

Fraser, A.I. 1962. The soil and roots as factors in tree stability. Forestry 35:117–127.

Fraser, A.I. and J.B.H. Gardiner. 1967. Rooting and stability in Sitka spruce. For. Comm. Bull. Vol. 40. HMSO, London, 28 p.

Fredericksen, T.S., R.L. Hedden and S.A. Williams. 1993. Testing Loblolly-pine wind firmness with simulated wind stress. Can. J. For. Res. 23:1760–1765.

Gardiner, B.A., H. Peltola and S. Kellemäki. 2000. Comparison of two models for predicting the critical wind speeds required to damage coniferous trees. Ecol. Model. 129:1–23.

Hakkila, P. 1972. Mechanized harvesting of stumps and roots. Communicationes Instituti Forestalis Fenniae. Communicationes Instituti Forestalis Fenniae 77:1, Helsinki, 71 p.

Johnson, R.C., G.E. Ramey and D.S. Ohagan. 1982. Wind induced forces on trees. J. Fluids Eng.-Trans. ASME 104:25–30.

Jonsson, M.J., A. Foetzki, M. Kalberer, T. Lundström, W. Ammann and V. Stöckli. 2006. Root–soil rotation stiffness of Norway spruce (*Picea abies* L. Karst) growing on subalpine forested slopes. Plant Soil 285:267–277.

Köstler, J.N., E. Brückner and H. Bibelriether. 1968. Die Wurzeln der Waldbäume. Vol. III. Verlag Paul Parey, Hamburg Berlin, 284 p.

Lundström, T., U. Heiz, M. Stoffel and V. Stöckli. 2007. Fresh wood bending: linking properties of mechanics and growth within the stem. Tree Physiol. 27:1229–1241.

Mattheck, C., K. Bethge and D. Erb. 1993. Failure criteria for trees. Allg. Forst Jagdztg. 164:9–12.

MeteoSwiss. 2005. Climate database. Swiss National Weather Service. http://www.meteoschweiz.ch/web/en/services/data_portal.html.

Meunier, S., J.C. Ruel, G. Laflamme and A. Achim. 2002. Comparative resistance of white spruce and balsam fir to overturning. Can. J. For. Res. 32:642–652.

Mickovski, S.B. and A.R. Ennos. 2003*a*. The effect of unidirectional stem flexing on shoot and root morphology and architecture in young *Pinus sylvestris* trees. Can. J. For. Res. 33:2202–2209.

Mickovski, S.B. and A.R. Ennos. 2003*b*. Anchorage and asymmetry in the root system of *Pinus peuce*. Silva Fenn. 37:161–173.

Milne, R. and P. Blackburn. 1989. The elasticity and vertical distribution of stress within stems of *Picea sitchensis*. Tree Physiol. 5:195–205.

Moore, J.R. 2000. Differences in maximum resistive bending moments of *Pinus radiata* trees grown on a range of soil types. For. Ecol. Manage. 135:63–71.

Nicoll, B.C. and D. Ray. 1996. Adaptive growth of tree root systems in response to wind action and site conditions. Tree Physiol. 16: 891–898.

Nicoll, B.C., E.P. Easton, A.D. Milner, C. Walker and M.P. Coutts. 1995. Wind stability factors in tree selection: distribution of biomass within root systems of Sitka spruce clones. *In* Wind and Trees. Eds. M.P. Coutts and J. Grace. Cambridge University Press, Cambridge, pp 276–292.

Nicoll, B.C., A. Achim, S. Mochan and B.A. Gardiner. 2005. Does steep terrain influence tree stability? A field investigation. Can. J. For. Res. 35:2360–2367.

Nicoll, B.C., B.A. Gardiner, B. Rayner and A.J. Peace. 2006. Anchorage of coniferous trees in relation to species, soil type, and rooting depth. Can. J. For. Res. 36:1871–1883.

Papesch, A.J.G., J.R. Moore and A.E. Hawke. 1997. Mechanical stability of *Pinus radiata* trees at eyrewell forest investigated using static tests. N.Z. J. For. Sci. 27:188–204.

Peltola, H. 1995. Studies on the mechanism of wind-induced damage of Scots pine. Research Notes of the Faculty of Forests 32, University of Joensuu, 28 p.

Peltola, H. and S. Kellomäki. 1993. A mechanistic model for calculating windthrow and stem breakage of Scots pine at stand edge. Silva Fenn. 27:99–111.

Peltola, H., S. Kellomäki, A. Hassinen and M. Granander. 2000. Mechanical stability of Scots pine, Norway spruce and birch: an analysis of tree-pulling experiments in Finland. For. Ecol. Manage. 135:143–153.

Polomski, J. and N. Kuhn. 1998. Wurzelsysteme. Haupt Verlag, Bern, 290 p.

Ray, D. and B.C. Nicoll. 1998. The effect of soil water-table depth on root-plate development and stability of Sitka spruce. Forestry 71:169–182.

Rudnicki, M., S.J. Mitchell and M.D. Novak. 2004. Wind tunnel measurements of crown streamlining and drag relationships for three conifer species. Can. J. For. Res. 34:666–676.

Schiesser, H.H., C. Pfister and J. Bader. 1997. Winter storms in Switzerland north of the Alps 1864/1865-1993/1994. Theor. Appl. Climatol. 58:1–19.

Schmidt-Vogt, H. 1991. Die Fichte: ein Handbuch in zwei Bänden. Waldbau, Ökologie, Urwald, Wirtschaftswald, Ernährung, Düngung, Ausblick Vol. 2/3. Verlag Paul Parey, Hamburg, 781 p.

Stokes, A., A.H. Fitter and M.P. Coutts. 1995. Responses of young trees to wind and shading—effects on root architecture. J. Exp. Bot. 46:1139–1146.

Stokes, A., F. Salin, A.D. Kokutse et al. 2005. Mechanical resistance of different tree species to rockfall in the French Alps. Plant Soil 278:107–117.

Wessolly, L. and M. Erb. 1998. Handbuch der Baumstatik und Baumkontrolle. Patzer, Berlin, 270 p.

Wood, C.J. 1995. Understanding wind forces on trees. *In* Wind and Trees. Eds. M.P. Coutts and J. Grace. Cambridge University Press, Cambridge, pp 133–164.

WSL and BUWAL. 2001. Lothar der Orkan 1999 Ereignisanalyse. Eidg. Forschungsanstalt WSL, Bundesamt für Umwelt, Wald und Landschaft BUWAL, Birmensdorf, Bern, 365 p.

Yang, Y.B., Y.T. Yang and H.H. Su. 2005. Behavior of the tree branches, trunk, and root anchorage by nonlinear finite element analysis. Adv. Struct. Engineer. 8:1–14.

Chapter II

The root-soil system of Norway spruce subjected to turning moment: resistance as a function of rotation

Plant Soil
DOI 10.1007/s11104-007-9386-2

REGULAR ARTICLE

The root–soil system of Norway spruce subjected to turning moment: resistance as a function of rotation

T. Lundström · M. J. Jonsson · M. Kalberer

Received: 27 February 2007 / Accepted: 6 August 2007

Abstract The reactions of trees to wind, rockfall, and snow and debris flow depend largely on how strong and deformable their anchorage in the soil is. Here, the resistive turning moment M of the root–soil system as a function of the rotation ϕ at the stem base plays the major role. $M(\phi)$ describes the behavior of the root–soil system when subject to rotational moment, with the maximum $M(\phi)$ indicating the anchorage strength M_a of the tree. We assessed $M(\phi)$ of 66 Norway spruce (*Picea abies* L. Karst) by pulling them over with a winch. These 45- to 170-year-old trees grew at sites of low and high elevation, with a diameter at breast height DBH=14–69 cm and a height H=9–42 m. $M(\phi)$ displayed a strong nonlinear behavior. M_a was reached at a lower ϕ for large trees than for small trees. Thus overhanging tree weight contributed less to M_a for the large trees. Overturning also occurred at a lower ϕ for the large trees. These observations show that the rotational ductility of the root–soil system is higher for small trees. M_a could be described by four monovariate linear regression equations of tree weight, stem weight, stem volume and $DBH^2 \cdot H$ ($0.80 < R^2 < 0.95$), and ϕ at M_a, ϕ_a, by a power law of $DBH^2 \cdot H$ ($R^2 = 0.85$). We found significantly higher M_a for the low-elevation spruces than for the high-elevation spruces, which were more shallowly anchored, but no significant difference in ϕ_a. The 66 curves of $M(\phi)$, normalized ($_n$) by M_a in M-direction and by ϕ_a in ϕ-direction, yielded one characteristic average curve: $\overline{M}_n(\phi_n)$. Using $\overline{M}_n(\phi_n)$ and the predictions of M_a and ϕ_a, it is shown that $M(\phi)$ and the curves associated with $M(\phi)$ can be predicted with a relative standard error ≤25%. The parameterization of $M(\phi)$ by tree size and weight is novel and provides useful information for predicting with finite-element computer models how trees will react to natural hazards.

Keywords Allometry · Energy absorption capacity · Protective forest · Mechanical modeling · Tree structure · Uprooting process

Abbreviations

Notation	Description (Unit)
b, α	Regression coefficients
DBH	Stem diameter on bark at breast height, i.e. 1.3 m (m)
ϕ	Rotation at the base of the stem due to M (°)

Responsible Editor: Peter J. Gregory.

T. Lundström · M. J. Jonsson · M. Kalberer
WSL, Swiss Federal Institute
for Snow and Avalanche Research SLF,
CH-7260 Davos Dorf, Switzerland

T. Lundström (✉)
Laboratory of Dendrogeomorphology,
University of Fribourg,
1700 Fribourg, Switzerland
e-mail: t.lundstroem@slf.ch

ϕ_a	ϕ at M_a (°)
ϕ_n	ϕ normalized with ϕ_a
ϕ_{OT}	ϕ at which the tree overturns due to M^g only (°)
H	Total tree height (m)
HE, LE	High-elevation site, low-elevation site
κ	Average stem curvature between the stem base and the stem section initially at z_{g0} (m^{-1})
m	Weight (kg)
M	Resistive turning moment of the tree root–soil system (Nm)
M_a	Anchorage strength of the tree, i.e. the maximum M (Nm)
M^F	Contribution of the winching force to M. $M^F=M-M^g$ (Nm)
M^g	Contribution of overhanging weight of stem and crown to M (Nm)
M_n	M normalized with M_a
$\overline{M}_n$	The average $M_n(\phi_n)$-curve
$_n$	Normalized value (as subscript)
$_p$	Predicted value (as subscript)
P	Statistical P-value
R^2	R-squared value of a regression
SE	Standard error, or after±(mean value±SE)
SE_n	Relative standard error=SE divided (normalized) by the estimate itself (-, %)
V	Volume (m^3)
X	Explanatory variable
x, y, z	Cartesian coordinates of the tree: origin at stem base; x=horizontal stem deflection; z=height above origin. (m)
z_{g0}	Height of the tree's centre of gravity. $_0$ refers to the initial tree position (m)

Introduction

Trees are subject to forces from one or several types of natural hazards during their lifetime. Wind affects all trees. Trees in mountain areas may in addition be affected by rockfall, and snow and debris flows, and also naturally protect lower areas against them (Brang et al. 2006). Independent of which of these hazards a tree is exposed to, its reaction to the acting force is a combination of stem deflection and rotation of the root–soil system (Coutts 1986; Crook and Ennos 1996). A sufficiently strong force will cause failure to either the stem or the root–soil system. Observations of trees completely or partly uprooted by strong winds indicate that the root–soil system is a weak link in the transport of forces from the crown to the ground (Brassel and Brändli 1999). Investigations of tree destruction in rockfall couloirs and snow avalanche tracks indicate that loads of this kind may also cause the tree to partially or completely overturn (Gerber and Schnyder 1998; SLF 2000). Irrespective of the action, the anchorage of trees, especially that of the often shallow-rooted Norway spruce (*Picea abies* L. Karst), greatly affects the mechanical stability and protection capacity of trees.

When a root–soil system is subjected to a turning moment, it rotates. It appears that the resistive turning moment of the root–soil system M is a function of the rotational angle, i.e. the stem base inclination ϕ (Coutts 1983). $M(\phi)$ thus describes the rotational behavior of the root–soil system. The curve of $M(\phi)$ is indispensable for modeling the reaction of a tree exposed to winds, rockfall, and snow and debris flows, and thus for predicting the protection capacity of trees, and for assessing potential hazards and risks. In addition, $M(\phi)$ helps us to understand the uprooting process of trees (Coutts 1983), and can therefore be used, in comparative studies, to explain the effects of forest management on tree anchorage.

The maximum value of $M(\phi)$ is commonly called the anchorage strength M_a. The usual method to assess M_a is through winching (e.g. Fraser 1962; Nicoll et al. 2006; Peltola et al. 2000). This experiment can of course also be used to determine $M(\phi)$. Whether the aim is to estimate M_a or $M(\phi)$, a correct analysis needs to take into account the deflection of the tree during the test, because, among other things, the weight of the leaning tree contributes to $M(\phi)$. When M_a is reached, the contribution of the weight can amount to more than 60% (Coutts 1986). If the stem base inclines more than at M_a, it is evident that this proportion increases. Several methods have been developed to assess deflection (Coutts 1986; Hassinen et al. 1998; Lundström et al. 2007).

Despite the frequent use of winching tests to determine M_a, little information on $M(\phi)$ is available with regard to different species, ages and growth conditions. In view of the importance of $M(\phi)$ for

tree stability, this is surprising. Coutts (1983) studied 34-year-old Sitka spruce (*Picea sitchensis* (Bong.) Carr.) that were pulled over with recordings of ϕ and M made simultaneously. This very thorough study of $M(\phi)$ is the only one we found with the inclination measured at the base of the stem from the natural position of the root–soil system up to when it overturned. Crook and Ennos (1996) studied 16-year-old deep-rooted Larch (*Larix europea* × *L-japonica*) pulled at about 20% of tree height, where the inclination was also recorded. Although the inclination was not measured at the base of the stem, this study provides valuable insights into how the resistive moment of the root–soil system develops with increasing inclination of the lower part of the stem, up until when the tree overturns. These two studies show that M increases with increasing ϕ up to M_a and then decreases until there is complete failure and the root–soil system overturns. However, they do not provide us with any parameterized, quantitative description of $M(\phi)$, which is required when modeling trees in finite-element models (FEM).

The aim of the present work was to analyze the uprooting process of Norway spruce, with special attention given to the parameterization of $M(\phi)$, from ϕ=0 to ϕ at tree overturning, using tree and site variables. This involved investigating: (1) the general behavior of the root–soil system, the stem, and $M(\phi)$ during the uprooting in winching tests; and (2) the values and allometric descriptions of M_a and of ϕ_a, i.e. the stem base inclination at M_a. In this paper we show that $M(\phi)$ and the curves associated with it can be well parameterized with aboveground tree parameters and are site dependent.

Materials and methods

Sites, stands and trees

We performed winching tests on 66 mature Norway spruce (*Picea abies* L. Karst.), growing at three different locations in Switzerland. The first location includes six closely situated stands south of Davos, at about 46°46′N, 9°49′W, 1750 m a.s.l.. The second and the third locations are situated close to Zurich, at 47°22′N, 8°28′W, 620 m a.s.l., and 47°14′N, 8°53′W, 460 m a.s.l.. The growth conditions at the two latter locations were similar and our analysis revealed no significant differences between them for the anchorage characteristics studied. In the following we therefore refer to the Davos location as the high-elevation site (HE) and to the two Zurich locations as the low-elevation site (LE). These sites exhibit representative growth conditions, management strategies, tree sizes and ages (Table 1) for the two regions and elevations.

The HE site has an annual mean temperature of +1°C with large diurnal variations, and an annual mean precipitation of 1100 mm. The wind blows generally in the N-S axis with an annual mean and maximum 10-min wind of 2 and 15 m/s (MeteoSwiss 2006). With a slope of about 30°, the site faces W and N. Soils of the shallow B-horizon (0.05 m<soil depth<0.4 m) include dystric Cambisols and Podzols (taxonomy according to FAO 1998) with frequent stones. The site, which is a natural Norway spruce habitat, is also dominated by Norway spruce. The forest had a density of between 500 and 1200 trees per ha before the tests, and had been subjected to little or no forest management for at least a century.

Table 1 Characteristics of the test trees growing at the high elevation site (HE) and at the low elevation site (LE), with minimum, maximum and mean values: DBH=stem diameter at breast height; H=tree height; S=slenderness=H/DBH (m/m); L_c=crown length (m); Age=cambial age measured at breast height; and RW=mean annual ring width at breast height

Site	No. of test trees	DBH (cm)	H (m)	S (–)	L_c/H (%)	Age (years)	RW (mm)
		Min–max					
		Mean					
HE	21	14–49	9.3–29	59–106	35–95	42–271	0.7–2.0
		25	21	86	70	90	1.3
LE	45	19–69	16–42	57–119	15–80	41–152	1.4–3.7
		44	34	80	50	81	2.6

The LE site has an annual mean temperature of +9°C, precipitation of 1150 mm, and the wind blows generally in the SW-NE axis with an annual mean and maximum 10-min wind of 2 and 22 m/s (MeteoSwiss 2006). Its terrain is in general flat. Soils of the B-horizon (0.2 m<soil depth<1.2 m) comprise dystric Cambisols and Luvisols. The site can be characterized as a natural Common beech (*Fagus sylvatica* L.) habitat. Due to selective logging, however, Norway spruce dominates the forest, which, prior to the tests, had a density of between 100 and 350 trees per ha.

During the three months prior to the winching tests and during all tests, the amount of rain was normal to slightly less than normal, the daily mean temperature was above 0°C and the wind conditions were calm (MeteoSwiss 2006 and personal site observations).

Winching tests and investigations

All 66 winching tests were carried out similarly to those described in several previous studies of anchorage strength (e.g. Cucchi et al. 2004; Gardiner 1989; Peltola et al. 2000; Stokes et al. 2005). A cable attached to the stem was pulled by a winch until the tree fell, with simultaneous measurements of force and tree position (Fig. 1). The winching height was in the range 15–67% of tree height, but generally 20±5% (40 trees, 19 at the LE site and all 21 at the HE site). The trees were winched in the direction of the prevailing winds at the LE site and downslope at the HE site, at a rate of between 1 and 10 cm/s. The position of the tree during the test was obtained in one of two ways: (1) from a finite-element model of the tree that was provided with measured tree weight and dimensions, and constrained with recorded force and inclination data measured at 2% relative tree height. Additional inclination data, recorded by inclinometers at 5% and 20% relative heights, were used to position the stem of the model by iteratively changing its structural bending modulus of elasticity, which was set constant for the entire stem (see Jonsson et al. (2006) for further detail); (2) from two series of digital images capturing the lower and the upper part of the tree simultaneously as it was winched. The time step of the image series was adapted to capture the tree top deflection at least every 30 cm. The images were then analyzed with the software tool STEMTRACK, which rectifies the images and calculates the deflection of the entire stem in the tree coordinates (x, y, z) for each digital image (the x-axis in the horizontal direction of winching and of stem deflection, and the z-axis measuring the height above ground). The deflection is parameterized by a high-order polynomial $x(z)$. The precision in $x(z)$ depends on the pixel resolution of the image. We used an image resolution of 768×576 pixels. If a 30-m high tree is captured entirely in one image, one pixel corresponds to ~10 cm. With a rectification precision of about 4 cm, the rectification accuracy was higher than the pixel resolution. For technical information on STEMTRACK, see http://www.wsl.ch/forschung/forschungsunits/lawinen/downloads/Stemtrack.pdf [accessed 6. May 2007]. After each test, the stem diameter and the stem and crown weight were recorded per 1-m sections of height. Among the 45 Norway spruces at the LE site, 37 were investigated previously (Lundström et al. 2007), where the stem weight of each tree was calculated from its on-bark volume and mean bulk density (815 kg/m^3). The annual ring width (RW) was measured with a caliper in stem discs cut close to breast height. The root–soil plate width, depth and height were measured with a meter. On the basis of digital images of the plate, its shape was approximated with an elliptical cross section and depth-dependent

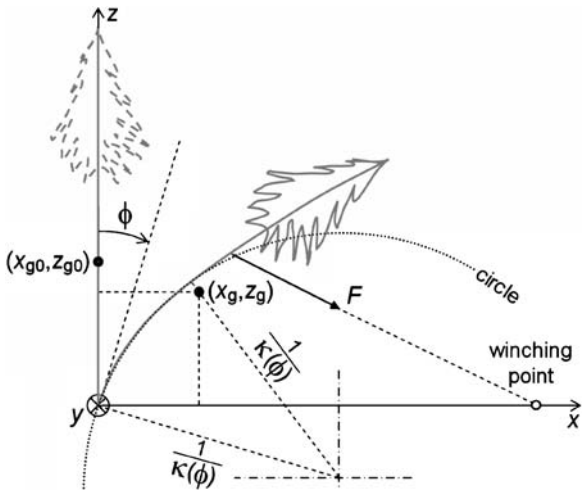

Fig. 1 The winching test. The winching force, F, acts in the x–z plane and causes the tree to deflect in the same plane. The stem deflection is a result of the rotation at the stem base (ϕ) and the stem curvature. Abbreviations used to calculate the predicted contribution of overhanging tree weight to $M(\phi)$ (cf. end of *Mechanical analysis*): (x_g, z_g)=centre of gravity of the tree, initially located at $x=x_{g0}=0$ and $z=z_{g0}$;κ=mean stem curvature between the stem base (x, z)=(0, 0) and the stem section initially located at (x_{g0}, z_{g0})

taper, where single protruding roots and the bent-off part of the plate at the plate hinge are ignored. This parameterization, including results for the LE-site, is reported in detail in Lundström et al. (2007). Details about the test set-ups, measurements, and instruments used are given in Jonsson et al. (2006) and Lundström et al. (2007).

Mechanical analysis

Given the position of the tree and winching cable during the test and the vertical distribution of weight, the effectively applied rotational moment M at the stem base could be computed as a function of the stem-base inclination ϕ (Equation 1)

$$M(\phi) = M^{g}(\phi) + M^{F}(\phi) \quad (1)$$

where $M^{g}(\phi)$ is the stem base moment due to the overhanging weight (^{g}) of the stem and crown and $M^{F}(\phi)$ is due to applied winching force (^{F}). $M^{g}(\phi)$ was calculated as the sum of deflection times weight for 100 equally long stem segments=H/100. $M^{F}(\phi)$ is the vector product of $F(x, z)$ and the coordinates (x, z) for the point where F is applied to the stem, which changes during the test (cf. Fig. 1).

All M:s were calculated between ϕ=0 (the tree in its natural unloaded state) and $\phi=\phi_{OT}$, when the tree began to fall (overturn) due to its own overhanging weight only. Beyond ϕ_{OT}, the tree is not in equilibrium and our static analysis does not apply.

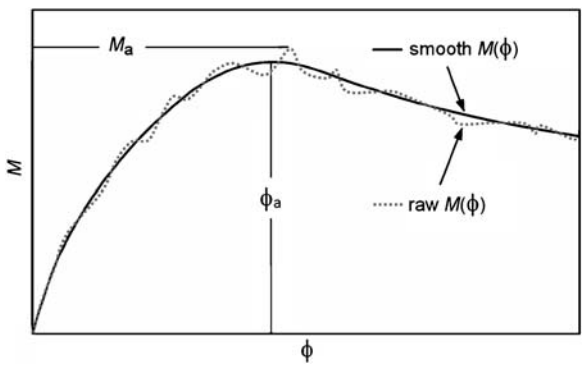

Fig. 2 Schematic description of how parameters were determined from the recorded resistive moment M of the root–soil system as a function of rotation ϕ at the stem base. The maximum M of the raw data (raw $M[\phi]$) corresponds to the anchorage strength M_a and ϕ_a corresponds to the ϕ at the maximum M of the smoothed data (smooth $M[\phi]$)

Knowing $M(\phi)$, the energy absorbed by the root–soil system in rotation $W(\phi)$ could be calculated, as it is represented by the area under the $M(\phi)$-curve (cf. Fig. 2). We determined W_{tot} (W absorbed up to ϕ_{OT}), the anchorage strength M_a (the maximum $M(\phi)$-value), and ϕ_a. Here, ϕ_a refers to the general maximum of the $M(\phi)$-data, which was obtained in three steps, by: (1) estimating ϕ_a from a plot of the raw $M(\phi)$-data; (2) smoothing the raw $M(\phi)$-data, applying a ϕ-smoothing span of 25% of the estimated ϕ_a and using a locally weighted, quadratic, polynomial smooth algorithm (loess, Matlab 7.0, MathWorks, Inc., USA); and (3) determining ϕ_a from the maximum of the smoothed $M(\phi)$-data. The purpose with this smoothening was to bring out the general and thus most significant curve maxima (Fig. 2).

The $M(\phi)$-curve described by the raw data was then normalized ($_n$) for each tree by M_a in the M-direction and by ϕ_a in the ϕ-direction, yielding $M_n=M/M_a$ and $\phi_n=\phi/\phi_a$. The $M_n(\phi_n)$-data of the trees at the two sites were then averaged, and then once again for all trees, to yield the average curve $\overline{M}_n(\phi_n)$ for the HE site, the LE site, and for all trees together. In this averaging, the normalization of ϕ resulted in a denser ϕ-graduation for trees with higher ϕ_a-values. To avoid the $M_n(\phi_n)$-data of these trees being more strongly statistically weighted than trees with low ϕ_a-values at the beginning of the $\overline{M}_n(\phi_n)$ -curve, all $M_n(\phi_n)$ data sets were subjected to interpolation with a ϕ_n-step of 0.01 prior to averaging, using a piecewise cubic polynomial algorithm (pchip, Matlab).

Finally, curves of predicted ($_p$) $M(\phi)$, $M^{g}(\phi)$, $M^{F}(\phi)$, and $W(\phi)$ were calculated. Here, the $M(\phi_p)_p$ was obtained by reversing the normalization described above, i.e. $M_p=M_a(X)\cdot\overline{M}_n$ and $\phi_p=\phi_n\cdot\phi_a(X)$, where X indicates an explanatory variable. To simplify notations from here and on, we use $M(\phi)_p$ for $M(\phi_p)_p$ and similarly for the related predicted curves. The computation of $M^{g}(\phi)_p$ as a function of basic dendrometric variables is more complex. Actually, $M^{g}(\phi)$ depends on how the tree weight is distributed along height z and on the stem curvature that occurs when the tree is winched. Stem curvature, in turn, is influenced by the winching height and angle, as demonstrated in Lundström et al. (2007). With this in mind, we computed $M^{g}(\phi)_p$ from $\overline{M}_n(\phi_n)$ and as a function of

DBH and H, taking into consideration the following (cf. Fig. 1): (1) the weight of the straight and unforced tree concentrated in its centre of gravity, at stem height z_{g0}; (2) a tree height H predicted by DBH, which is to simplify comparisons between trees of different DBH in this paper; the real H should normally be used; (3) only one relative winching height=0.2·H (the most common in our investigations); (4) an average stem curvature κ between the stem base and the point on the stem initially at the height z_{g0}, calculated as a function of ϕ; and (5) an inwards radial shift=(1−sin(β)/β)/κ(ϕ) of the position of the centre of gravity (x_g, z_g) due to the stem curvature during winching, where β=z_{g0}·κ(ϕ). As a consequence, (x_g, z_g) is not situated on the centre line of the stem, but shifted to the winching side during the test. The approximations used in (4) and (5) were based on the observed stem deflections. The calculation of $M^g(\phi)_p$ was then simply the horizontal component of the centre of gravity x_g multiplied by the total weight of the tree. $M^g(\phi)_p$ was also used to calculate $M^F(\phi)_p$=$M(\phi)_p$−$M^g(\phi)_p$, and the ϕ at which the tree is expected to overturn ϕ_{OTp}, i.e. when $M^F(\phi)_p$=0. The curves of $W(\phi)_p$ were obtained by integrating $M(\phi)_p$ with respect to ϕ_p.

Statistical analysis

The statistical, allometric relationships between the targeted response variables, i.e. M_a, ϕ_a, W_{tot}, and the curve $M_n(\phi_n)$, and all the aboveground tree parameters (explanatory variables X) were explored for the HE site, the LE site, and for both sites. This analysis included errors, step-wise multiple regressions and tests for significant differences between the two sites (by adding one fictive term to the two groups, with a value 0 or 1, in the step-wise regressions). The same analysis procedure was used to check how z_{g0}, κ(ϕ), tree and stem weight, and H could be described by the X's. Due to strong correlations between the X's, the step-wise multiple regressions mostly yielded regressions of only one significant X. We therefore concentrated on monovariate regressions, including potential combinations and transformations of the X's. The regression equations of M_a were all forced through the origin as M_a is equal to zero if a tree has no weight or has zero dimensions. To evaluate how exact the predicted curves $M(\phi)_p$, $M^g(\phi)_p$, $M^F(\phi)_p$, and $W(\phi)_p$ were, we compared the predicted and observed values along these curves, and calculated: (1) the relative errors (error/predicted value) within the range $0<\phi<\phi_{OTp}$, for the four curves and all trees; (2) the corresponding relative standard error SE_n for each curve; and finally, (3) the average SE_n, for each of the four curves at the LE site and at the HE site. The SE's were approximately normally distributed for all variables analyzed. The software package S-Plus 2000 (Insightful Corporation, Seattle) was used for all statistical analyses.

Results

General behavior of the root–soil system, the stem, and the $M(\phi)$ during uprooting

During the winching test and the uprooting of the trees, we observed some characteristic patterns of ground deformation, of stem deflection, and of how the resistive stem-base moment M developed with the stem-base inclination ϕ. These patterns depended on the site and tree size.

As the tree was winched, the ground on the winching side of the tree sank, whereas that on the other side rose. The ground movements were especially large where lateral roots emerged from the stem. These movements, perpendicular to the pulling direction, are shown in profile in Fig. 3. The maximum deflection, on the winching as well as on the opposite side, approached the centre of the stem as ϕ increased. On the winching side it was first discerned at a distance of 2 to 3·DBH from the stem centre, and reached 1 to 2·DBH when overturning as the roots and the root-soil plate became very bent at this distance (the "hinge" of the root-soil plate). On the opposite side of the tree, the roots were stretched and failed under traction one after the other. As the tree fell, the lateral roots bent even more on the winching side and the soil failed completely at the hinge. After the test, when the tree was lying down, the root-soil plate was consequently bent-off (i.e. truncated) on the winching side. The root-soil plate of the Norway spruce with shallower roots at the HE site appeared to truncate less than at the LE site, at about 1/2 (HE)

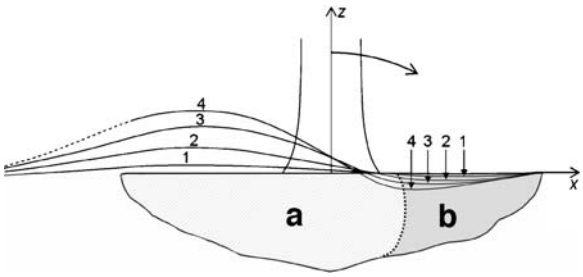

Fig. 3 Example of typical movements of the root-soil plate during uprooting, reconstructed from digital images in the *x*–*z* plane. The continuous lines 1–4 correspond to the profile of the deformed upper surface of the plate, and the dotted line to that of a few roots emerging radially. This Norway spruce grew at the LE site (DBH=39 cm and H=32 m), and started to fall due to the overhanging stem and crown weight just after the deformation reached profile 3. The stem base inclined at 5°, 12°, 23°, and 30° at the profiles 1–4. The numbers 1–4 correspond to the positions of maximum deflection on the winching side (shown with *arrows*) and the opposite side. The profile of the overturned root-soil plate (**a**) is lighter in color than the profile that remained broken off in the ground (**b**)

and 2/3 (LE) of the root-soil plate radius in the pulling axis (x). Coarse lateral roots emerging in the pulling direction lowered the inward radial shift of the maximum ground deflection and the subsequent truncation of the root-soil plate. The shape of the root-soil plate was governed much more by the coarse lateral roots at the HE site than at the LE site and was therefore less symmetric and elliptic in plane. The height (stem centre – top of the plate) and width (the lateral radius) were similar at the HE and the LE site, but the depth (below the stem base) was larger (P<0.001) for the trees at the LE site (Table 2). These dimensions, and the deformations of the root-soil plate during and after the uprooting process, varied by up to 50% and seemed to be mostly governed by the root architecture.

The deflection of the stem and tree originated from the rotation of the root–soil system and the curvature of the stem. Most of the deflection was generally due to the rotation of the root–soil system (cf. Fig. 4a), independent of tree size and site. An inverse relation was observed at large ϕ for a few smaller trees (cf. Fig. 4b), especially when winched high up the stem. Generally, small trees deflected more than large trees.

The root–soil system of small trees maintained their resistance to rotation at higher ϕ-values than larger trees (Fig. 4c,d). As a result, large trees overturned due to the overhanging tree weight at a lower ϕ_{OT} than smaller trees. The minimum ϕ_{OT}=12° was recorded for a Norway spruce with a DBH=67 cm at the LE site, and the maximum ϕ_{OT}=46° for a Norway spruce with a DBH=17 cm at the HE site.

Anchorage strength, M_a

The M_a was strongly correlated with the weight and size of the tree. Four monovariate descriptions of M_a were obtained, which were of almost equal quality (Table 3). For all of them, M_a/X was lower (P<0.001) at the HE site than at the LE site. Figure 5 exemplifies this for M_a as a function of m_{stem} and of $DBH^2 \cdot H$.

The relative contribution of overhanging tree weight to M_a, $M^g(\phi_a)/M_a$, was generally between 10 and 25% for the trees winched at z=0.2·H, but this percentage increased greatly for trees with a DBH<30 cm. For example, it was 68% for the tree in Fig. 4b and d, which is the highest value obtained. The lowest value of 6% was observed for a tree of DBH=64 cm, which is similar to the 7% obtained for the tree in Fig. 4a and c. For all trees winched at 0.2·H, the relation $M^g(\phi_a)/M_a$ at the LE site could be described by $0.374 \cdot (DBH^2 \cdot H)^{-0.552}$ (R^2=0.78) and at the HE site

Table 2 The response variables (Y) root-soil plate width, height, and depth described by the diameter at breast height in simple linear regression, for the trees at the high-elevation (HE) and the low-elevation (LE) site

	LE				HE			
Y	b	SE (b)	SE_n (Y)	R^2	b	SE (b)	SE_n (Y)	R^2
Width	3.0	0.13	0.26	0.22	3.2	0.30	0.45	0.27
Height	3.3	0.15	0.30	0.16	3.7	0.31	0.40	0.30
Depth	2.1	0.10	0.35	0.13	1.1	0.11	0.47	0.24

All regression coefficients b are significant at P<0.001. The width, height, and depth are described in the text and Fig. 3.

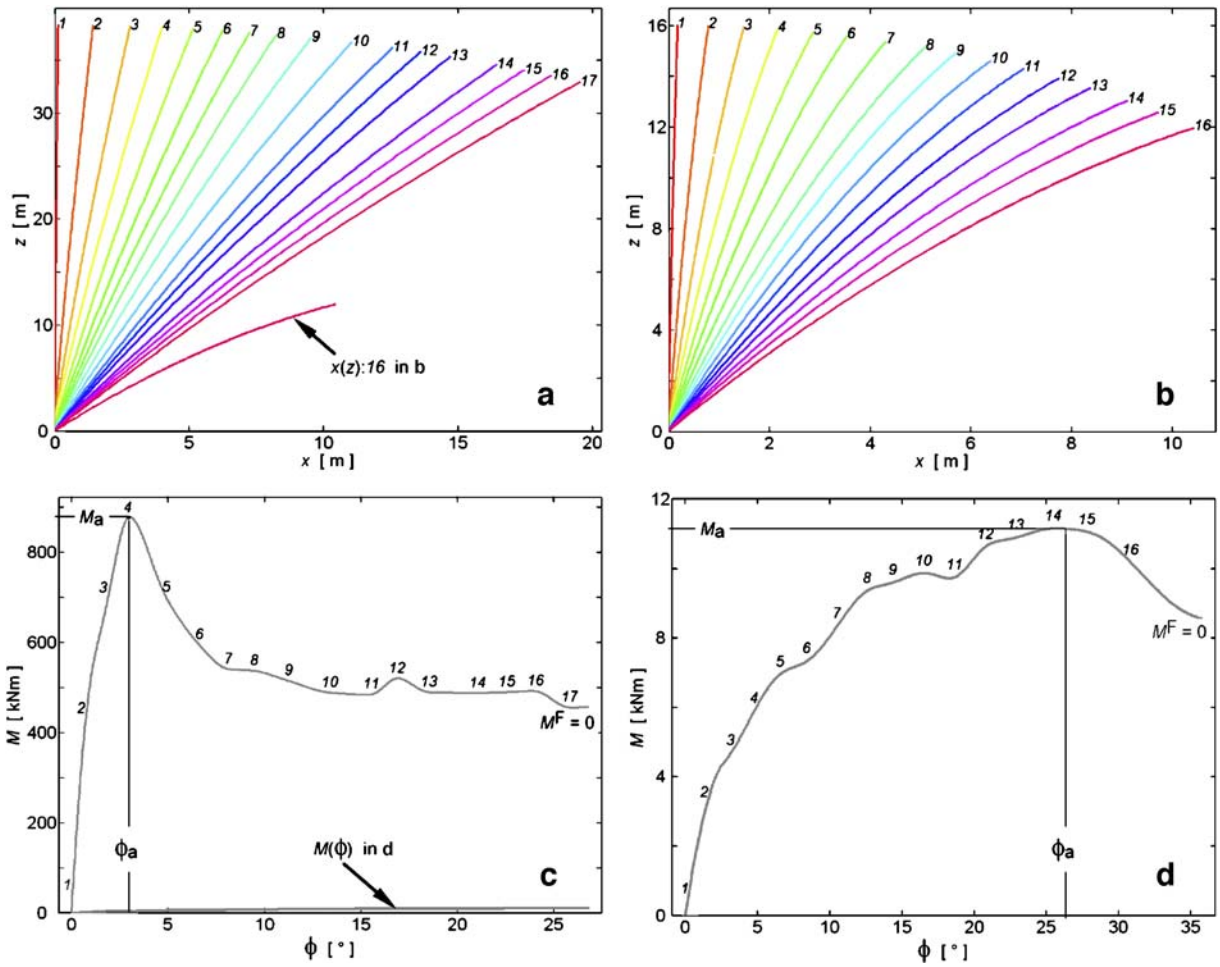

Fig. 4 Stem deflection x according to tree height z, compared to the resistive moment of the root–soil system M until the tree fell, here exemplified by two Norway spruce trees: the largest one (**a** and **c**; DBH=69 cm, H=39 m, LE site) and one of the smallest (**b** and **d**; DBH=16 cm, H=16 m, HE site). The numbers 1–17 (**a** and **c**) and 1–16 (**b** and **d**) refer to the position of the tree stem during the winching test. Both trees were winched at $0.2{\cdot}H$. M^F is the stem-base moment resulting from the applied winching force F. Note that the scales are different in **a** and **b**. To ease scale comparison, **a** and **c** each include one curve from **b** and **d**

by $0.409{\cdot}(\mathrm{DBH}^2{\cdot}H)^{-0.413}$ (R^2=0.81). As only a few trees were winched at heights other than $0.2{\cdot}H$, the effect of winching height on $M^g(\phi_a)/M_a$ could not be efficiently analyzed statistically. However, it appeared, as expected, that $M^g(\phi_a)/M_a$ tended to increase with winching height.

Stem-base inclination, ϕ

The ϕ at M_a is described by the regression model (Eq. 2):

$$\phi_a = b \cdot \left(\mathrm{DBH}^2 \cdot H\right)^{\alpha} \quad (2)$$

where b=11.9±1.0 [°/m$^{3\alpha}$] and α=−0.530±0.027 [−].

The quality (R^2=0.85, $\mathrm{SE_n}(\phi_a)$=0.18) of this model changed little and did not improve if $\mathrm{DBH}^2{\cdot}H$ was replaced with V_{stem}, m_{stem}, or m_{tree}, unlike the models describing M_a. As no significant difference in ϕ_a was found between the LE and HE sites (P=0.26), the final analysis of ϕ_a was made with all the data from both sites taken together (cf. Fig. 6).

In contrast, ϕ at overturning for the trees winched at $0.2{\cdot}H$ was lower (P<0.05) at the HE than at the LE site. At the HE it could be described by $\phi_{OT}=33{\cdot}(\mathrm{DBH}^2{\cdot}H)^{-0.15}$ (R^2=0.72), and at the LE site by $\phi_{OT}=33{\cdot}(\mathrm{DBH}^2{\cdot}H)^{-0.26}$ (R^2=0.76), where the exponent was smaller (P<0.05) for the HE site.

Table 3 Statistical data related to the models describing the anchorage strength $M_a = b \cdot X$ [kNm] (maximum stem-base moment), including 45 Norway spruces from the low-elevation site (LE) and 21 from the high-elevation site (HE)

X	Site	b	SE (b)	SE_n (M_a)	R^2
m_{tree}	LE	1.29E-01	2.4E-03	0.14	0.94
	HE	7.63E-02	2.7E-03	0.15	0.93
m_{stem}	LE	1.57E-01	3.2E-03	0.17	0.93
	HE	9.11E-02	3.6E-03	0.15	0.92
V_{stem}	LE	1.30E+02	2.7E+00	0.16	0.93
	HE	7.46E+01	3.0E+00	0.17	0.92
$DBH^2 \cdot H$	LE	4.37E+01	1.1E+00	0.18	0.90
	HE	2.63E+01	1.6E+00	0.23	0.80

The regressions models are listed top–down according to their quality (R^2) and all b's are significant ($P<0.001$).

m=weight (kg), V=volume (m^3), DBH=stem diameter at breast height (m), H=tree height (m), SE=standard error of mean, and SE_n=relative standard error of mean

Energy absorption

The total energy absorption by the root–soil system in rotation W_{tot} was lower ($P<0.001$) at the HE than at the LE site, as a consequence of the lower M_a. At the LE site, it could be described by $W_{tot}=20.4 \cdot (DBH^2 \cdot H)^{0.79}$ ($R^2=0.77$, $SE_n=0.26$) and $W_{tot}=367 \cdot DBH-65.2$ ($R^2=0.72$). At the HE site, the corresponding descriptions were $W_{tot}=7.47 \cdot (DBH^2 \cdot H)^{0.88}$ ($R^2=0.78$, $SE_n=0.29$) and $W_{tot}=164 \cdot DBH-30.1$ ($R^2=0.72$). The regressions W_{tot}(DBH) were computed so that they could be compared with the results from previous studies (see *Discussion*). The relatively large variations in W_{tot} resulted from variations in ϕ_{OT} and in M_a.

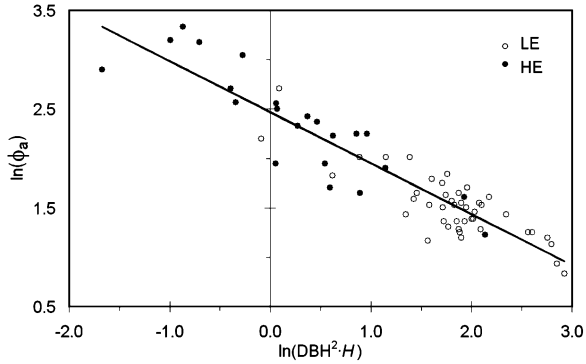

Fig. 6 Stem base inclination ϕ at M_a, as a function of tree size, at the HE site, the LE site, and a regression (Eq. 2) for all trees (*continuous line*). DBH is the diameter at breast height and H the tree height

Normalized $M(\phi)$

The mean curve of the 66 M- and ϕ-normalized $M(\phi)$-curves, $\overline{M}_n(\phi_n)$, can be seen (Fig. 7) to markedly increase up to ϕ_a. Then, after a gradual decrease, it almost stabilizes at $\phi_n \approx 5$. The relative standard error in $\overline{M}_n(\phi_n)$ was on average $SE_n=4.8\%$ for $\phi_n<1$ and $SE_n=8.1\%$ for $\phi_n>1$. The curves of SE_n in Fig. 7 (raw data filtered with a ϕ_n-range=0.25), display a general increase from $\phi_n=1$ (0%) to $\phi_n=8$ (14%). The maximum relative error in $\overline{M}_n(\phi_n)$ belongs to the same tree and was 16% before $\phi_n=1$ and 21% after $\phi_n=1$. It was the result of a mobilization and then a sudden release of the traction forces in the roots on the opposite side of the winching cable, which consequently yielded local maxima and minima in $M(\phi)$. Within the ϕ_n-range with sufficient $M_n(\phi_n)$-values available for both the

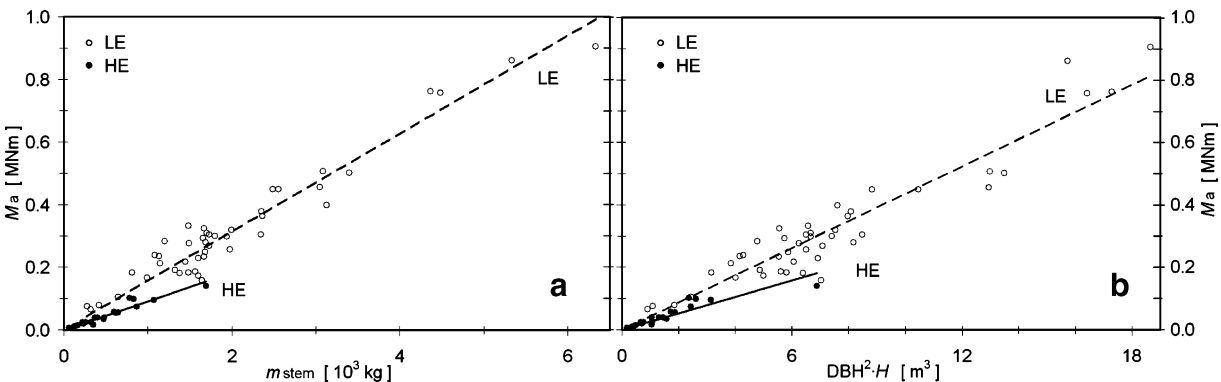

Fig. 5 Anchorage strength M_a of trees from the HE site and the LE site, described by stem weight m_{stem} (**a**) and stem size (**b**). DBH is the diameter at breast height and H the tree height. Characteristics of the four regressions are given in Table 3

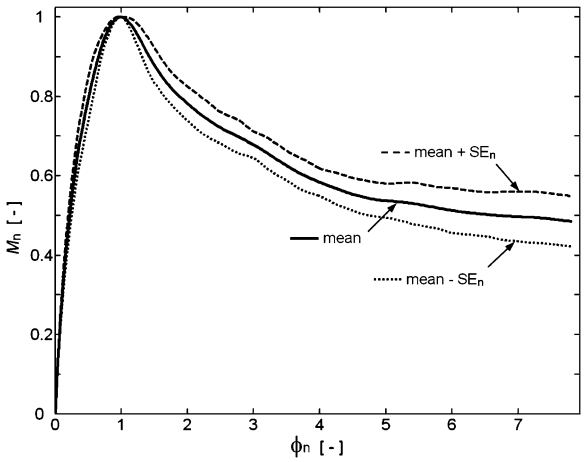

Fig. 7 The $\overline{M}_n(\phi_n)$-curve (*continuous line*), including the upper (*hatch line*) and lower (*dotted line*) limit of the relative standard error $SE_n(\phi_n)$. $\overline{M}_n(\phi_n)$ is the mean of all the 66 recorded resistive turning moments at the stem base M, normalized ($_n$) with M_a, as a function of the rotation ϕ at the base of the stem normalized by ϕ_a

HE and the LE site ($0<\phi_n<4.7$), the differences in $\overline{M}_n(\phi_n)$ were very small and insignificant between the sites. For $\phi_n>5.2$, $\overline{M}_n(\phi_n)$ is based on the $M_n(\phi_n)$-values from the LE site only.

Predictions of $M(\phi)$ and related curves

The curves of predicted ($_p$) M, M^g, M^F, and W as a function of the rotation ϕ at the stem base are presented in Fig. 8 for the LE site. The only information used to produce the curves is $\overline{M}_n(\phi_n)$ (Fig. 7) and DBH, with $M_a(\mathrm{DBH}^2{\cdot}H)$ (Table 3), ϕ_a (Equation 2), and H(DBH). The curves for the HE site have similar shapes (not displayed), apart from three points: (1) their amplitudes are lower, as M_a and to certain extent M^g are lower (the lower M^g result from the lower centre of gravity); (2) M^F turns zero at a slightly higher ϕ as a result of the relatively low M^g; and (3) the DBH-span is more restricted ($14<\mathrm{DBH}<49$ cm) at the HE than at the LE site ($19<\mathrm{DBH}<69$ cm, extrapolated to $15<\mathrm{DBH}<70$ cm in Fig. 8).

Concerning the allometric relationships required to compute $M^g(\phi)_p$, and thus $M^F(\phi)_p=M(\phi)_p-M^g(\phi)_p$, the mean curvature between the stem base and the centre of gravity was described by $\kappa=0.58{\cdot}\phi/\mathrm{DBH}$ (ϕ in °, DBH in m, $R^2=0.88$) and the tree height by $H=60.5{\cdot}\mathrm{DBH}^{0.722}$ ($R^2=0.83$). Both these expressions include all trees, as no significant differences were found between the sites, even if differences were observed DBH-range-wise. The centre of gravity relative to tree height, on the other hand, differed ($P<0.001$) between the sites, with $z_{g0}/H=0.86{\cdot}(\mathrm{DBH}{\cdot}H^2)^{-0.12}$ ($R^2=0.32$) at the LE site, and $z_{g0}/H=0.46{\cdot}(\mathrm{DBH}{\cdot}H^2)^{-0.048}$ ($R^2=0.38$) at the HE site. The total weight of the tree described by $\mathrm{DBH}^2{\cdot}H$ did not vary according to the site. Thus, for all trees included $m_{tree}=338{\cdot}\mathrm{DBH}^2{\cdot}H$ ($R^2=0.95$).

A comparison of Figs. 8a and b shows that M^g/M increases with decreasing tree size, and logically, also with increasing ϕ. Further, Fig. 8c demonstrates that, if a Norway spruce with a DBH=70 cm exceeds a $\phi=21°$, no applied force is required to overturn its root–soil system; the moment due to the overhanging tree weight M^g suffices. Finally, Fig. 8d shows that the root–soil system in rotation is also an effective energy absorber even beyond ϕ_a. When the measured DBH and the H of the trees winched at $0.2{\cdot}H$ were applied to the allometric relationships required for the predicted curves in Fig. 8a–d, we obtained the following average SE_n for the HE and the LE sites, respectively: $M(\phi)_p$, 25% and 21%; $M^g(\phi)_p$, 21% and 22%; $M^F(\phi)_p$, 24% and 20%; and $W(\phi)_p$, 23% and 19%.

Discussion

General behavior of the root–soil system, the stem, and the $M(\phi)$ during uprooting

The inward radial shift in maximum deflection of the ground on the winching side of the tree during uprooting indicates that the centre of rotation of the root-soil plate also shifts towards the stem centre. After a relatively small angle of rotation, this centre was situated close to the centre line of the stem. Therefore, the simplification used for calculating the resistive moment of the root–soil system $M(\phi)$, with the centre of rotation at the intersection between the centre line of the stem and the ground, seems justified. To explain the variations in root-soil plate movements during uprooting would require more detailed measurements of root and soil deformations, along the lines of those described in Coutts (1983). The plate movements we observed with Norway spruce are similar to those recorded with Sitka spruce (e.g. Coutts 1983;

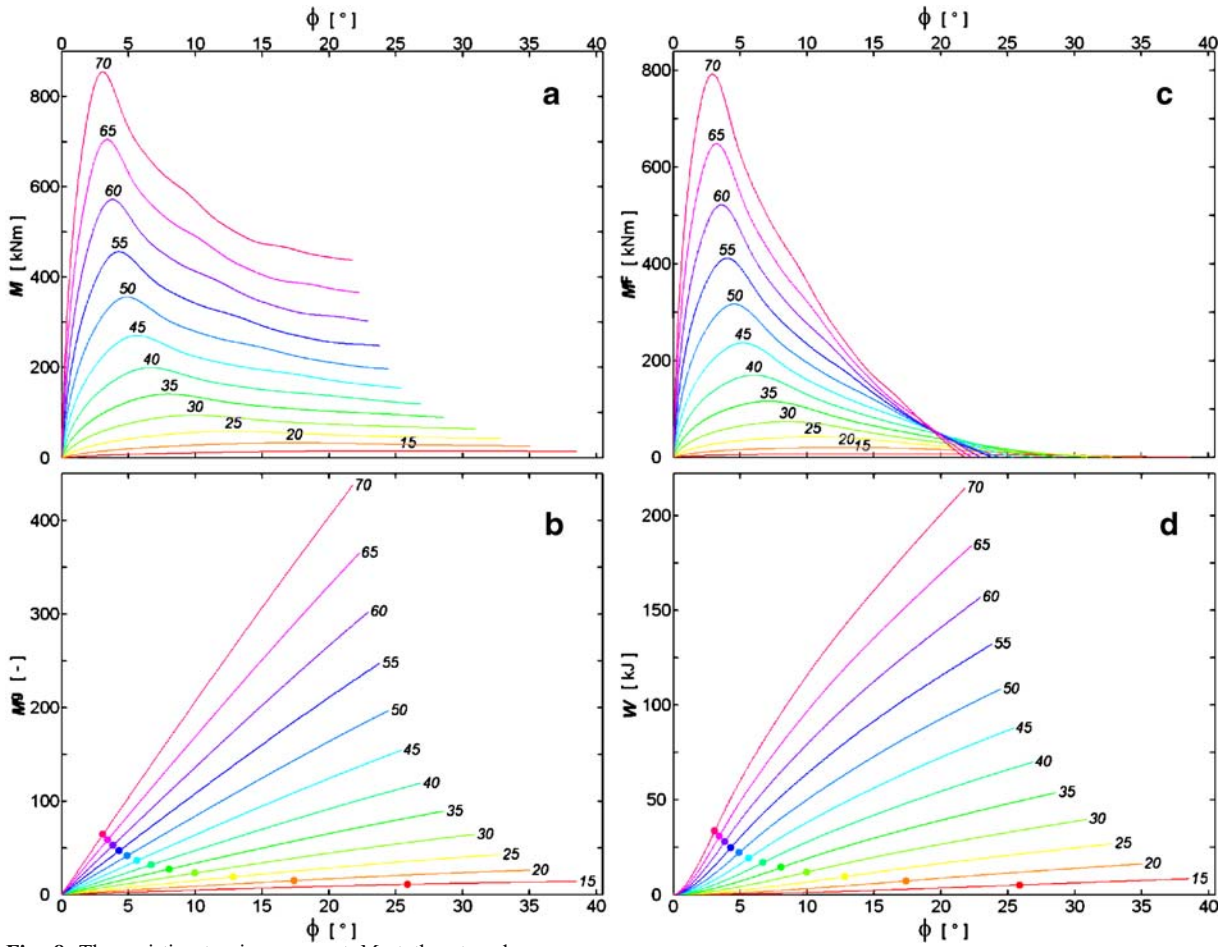

Fig. 8 The resistive turning moment M at the stem base as a function of the rotation ϕ at the stem base (**a**). Stem-base moment due to the overhanging tree weight M^G (**b**) and to the winching force M^F (**c**), and the energy W absorbed by the root-soil system in rotation (**d**). All curves display predicted mean values for 12 Norway spruces on the LE site with a DBH=15, 20, ..., 70 cm, and a predicted H in the range 16–40 m. The maximum $M(\phi)$, i.e. M_a, is indicated by a *dot*. M and W (**a** and **d**) are not dependent on the height of force application, unlike M^G and M^F (**b** and **c**), which both result from a force application at $0.2{\cdot}H$. All curves end at a ϕ, which corresponds to the predicted overturning of the tree, i.e. the ϕ-value where M^F turns zero (**c**)

Ray and Nicoll 1998). Thus it is probable that the root-soil failure mechanisms of the Norway spruce we tested resemble those reported for Sitka spruce. The lower truncation of the root-soil plates at the HE site could be due to a concentration of roots in the upper soil layer and thus a higher radial stiffness of the root–soil compound here, but also to a lower total weight of the root-soil plate and of the tree for the Norway spruces at the HE site. The irregular shape of the root-soil plates at the HE site, due to the presence of some coarse roots, resulted in an approximately modeled plate shape (not shown). The latter plates exhibited, however, cross-sectional elliptical shapes and depth-dependent tapers similar to those at the LE site (cf. Lundström et al. 2007), although the HE-plates were only half as deep as the LE-plates (cf. Table 2).

Our analysis of the mechanical behavior of the 66 Norway spruces indicates that it is important to take the non-linearity of $M(\phi)$ into account if the root–soil system exhibits large M-values. $M>M_a/3$, which corresponds to a stem-base inclination of about $\phi=\phi_a/5$, can in this context be considered large (cf. Figs. 2 and 4). A Norway spruce exceeds this ϕ-threshold (Vanomsen 2006) during storm-force winds when large amplitude swaying occurs. A model tree

with a fully clamped stem base would underestimate its capacity to "follow the flow" and thus its resistance to lateral pressure from, e.g., wind and snow.

The characteristic shape of our $M(\phi)$-curves (Fig. 7) is similar to that modeled for maritime pine (*Pinus pinaster* Ait.) by Fourcaud et al. (2003). It differs, however, from the $M(\phi)$ obtained by Dupuy et al. (2005) for various kinds of root–soil system in that the latter $M(\phi)$ exhibits no positive change in gradient after ϕ_a. Concerning experimentally assessed $M(\phi)$, Crook and Ennos (1996) recorded $M(\phi)$ for deep-rooted larch, although they refer to ϕ as the stem inclination at $0.2{\cdot}H$. To compare our results with theirs, we additionally computed $M(\phi_{0.2H})$ (data not shown). For corresponding tree sizes, we found the curve shapes were similar, but the $M(\phi)$ of our Norway spruce dropped more abruptly after ϕ_a. These differences indicate that the root–soil systems of the deep-rooted larches resist rotation better after ϕ_a than the shallow-rooted Norway spruce we tested.

The $M(\phi)$ of Sitka spruce studied by Coutts (1986) exhibits a two-phase behavior. It is initially relatively stiff and almost ideally elastic. Then, at a small ϕ, it suddenly becomes very deformable and almost ideally plastic at a quasi-constant $M{\approx}M_a$ accompanied by fracturing, until overturning. This $M(\phi)$-behavior resembles that described by Dupuy et al. (2005). Coutts (1986) recorded overturning at ϕ-values comparable to ours, with trees of the same tree size, just after ϕ_a was reached.

It appears that two general, characteristic shapes of $M(\phi)$ exist, the first type being described by Crook and Ennos (1996), Fourcaud et al. (2003), and our data, and the second by Coutts (1986) and Dupuy et al. (2005). However, to explain the existence of the two shapes, we do not have enough information about: (i) the analysis method; (ii) the failure mechanisms and the deformation of the root–soil system while $M(\phi)$ is recorded; and (iii) comparable information on the soil and the root systems. It should be kept in mind in future investigations of $M(\phi)$ that (i)–(iii) should be documented.

Anchorage strength, M_a

The lower M_a at the HE site is probably a result of the shallower root–system there, due to the site having a shallower B-horizon, a shorter vegetation period, and less available nutrition, than the LE site (Köstler et al. 1968; Soethe et al. 2006). The HE site is also exposed to weaker winds. Trees are known to develop their anchorage in response to wind forces (Lundström et al. 2007; Nicoll and Ray 1996). In addition, the trees at the HE site get less light due to the dense stand and the slope (facing E and N), which may inhibit root growth (Polomski and Kuhn 1998). We did not investigate the root architecture of all the trees tested systematically. However, the depth of the root-soil plate was twice as large at the LE than at the HE site, which we interpreted as meaning that the root system at the LE site was more developed, based on the relationships between the size of the root-soil plate and the total root mass for Norway spruce grown on similar soil (Bolenikus 2001). Despite their lower M_a, the HE spruces could be relatively more stable to wind, as they do not grow to be as tall as those at the LE site and have a lower centre of gravity. The HE and the LE spruces were growing in typical conditions for the region and the elevation. The elevation is, at least in the Alps, related to several growth condition parameters (e.g. soil type, depth, moisture, and temperature, slope, management strategies, and tree age). It is likely that Norway spruce trees growing at the same elevations as those in this study, but under different conditions, will exhibit different anchorage characteristics.

Among the four regression models proposed for M_a (Table 3), $M_a(\mathrm{DBH}^2{\cdot}H)$ seems to be the most useful, as it requires only two records of tree size, and no pulling over of the tree. In addition, $\mathrm{DBH}^2{\cdot}H$ is frequently referred to in the literature, which enables comparisons of M_a. Referring to the comparison with other M_a-studies of conifers in Lundström et al. (2007), it appears that the Norway spruces at the LE site exhibit among the highest M_a, whereas the M_a at the HE site is close to the average. However, there are only limited possibilities to compare the M_a obtained in this study with existing data, as most previous studies have focused on smaller and younger trees (e.g. Cucchi et al. 2004; Peltola et al. 2000) and mainly on Sitka spruce (e.g. Achim et al. 2003; Fraser and Gardiner 1967; Ray and Nicoll 1998). Moreover, the regression equations of M_a were not always forced through the origin, and $M^g(\phi)$ was not systematically included in M_a in these studies. We found that $M^g(\phi_a)/M_a$ increases with decreasing tree size by $(\mathrm{DBH}^2{\cdot}H)^{-0.5}$ and can reach 70%, a value that is also reported in Coutts (1986). When modeling mechanical tree

stability, it is probably essential to account for all contributions to the applied moment at the stem base when analyzing $M(\phi)$ as well as its maximum, M_a. This should also enable comparisons between M_a from experiments with different winching heights or tree characteristics.

Stem-base inclination, ϕ

Small trees display greater values of ϕ_a (Equation 2) and ϕ_{OT} than larger trees. This means that small trees have a more deformable root–soil system in rotation. Consequently, small trees are less likely to fail when exposed to wind, snow and debris flow, than large ones as their deflection is more efficient, i.e. they tend to follow the flow rather than opposing it. The stem deflections observed during the winching tests of small trees and the analysis of $M^F(\phi)=M(\phi)-M^g(\phi)$ suggest that, if a force is applied high up the stem to a sufficiently small tree, it may be bent down to the ground without overturning (cf. Fig. 8c, $M_F(\phi=40°$, DBH=15 cm)>0). It would be worth investigating when this occurs, e.g. for which tree sizes, species, and heights of force application, and relating it to the adaptive growth and survival of trees growing in snow avalanche tracks or on extremely windy spots.

Energy absorption

The root–soil system appears to be an effective energy absorber when subject to a rotation caused by e.g. impacting rocks or snow flow. Thanks to the ductility of the root–soil system, the energy $W(\phi)$ absorbed in rotation continues far beyond ϕ_a and even beyond the limit of tree stability. The major part of the total energy absorption capacity actually occurs after M_a is reached. This finding is similar to Crook and Ennos' observation (1996) that the root–soil system of larch maintains resistance to rotations beyond 70°. This has implications for the protection capacity of trees and forests. The root–soil system of a tree subjected to a dynamic loading may experience large rotations without the influence of overhanging tree weight. The effective total energy absorption of the dynamically loaded root–soil system may therefore be substantially larger than that of the statically loaded one.

The $W(\phi)$-values at overturning W_{tot} of our Norway spruces can be compared to the values recorded for the Common beech (Stokes et al. 2005), which also include the contribution of overhanging tree weight to $W(\phi)$. Our LE-site Norway spruces display a similar W_{tot}=367·DBH-65 to their W_{tot}=411·DBH-59, whereas our HE-site spruces had a considerably lower W_{tot}= 164·DBH-30. The difference in W_{tot} between the LE and the HE site is due to the different M_a, which is governed by growth and soil conditions (e.g. Cucchi et al. 2004; Moore 2000). The growth conditions of the Common beech seem similar to that of the HE-site Norway spruce. This confirms the general opinion in forestry that Common beech has a larger W_{tot} (and M_a) than Norway spruce. A scientifically based conclusion would require more systematic data on the growth conditions of the two species. In our study, and also in Stokes et al's (2005), W_{tot} was investigated statically. If the root–soil system is subject to dynamic loading, it may in addition absorb energy related to inertia.

Predictions of $M(\phi)$ and related curves

The differences between the predicted ($_p$) curves $M(\phi)_p$, $M^g(\phi)_p$, $M^F(\phi)_p$, and $W(\phi)_p$ and those actually observed with the 66 trees tested may at first sight appear great. However, this should be seen in the context of the simplifications made and the fact that only three explanatory variables, DBH, H, and site, were used (for the site variable, see the end of the *Anchorage strength* section).

The calculation of $M^g(\phi)_p$ is geometrically inexact because we assume the tree weight to be concentrated in the tree's centre of gravity. However, we estimated this inexactness to produce less than 5% relative error, which must be put in relation to the statistical error of $M^g(\phi)_p$ of about 20%. As the computation of $M^g(\phi)_p$ only requires the $\overline{M}_n(\phi_n)$-curve and the aboveground parameters DBH and H, it is a useful and straightforward way of estimating the contribution of tree weight to $M(\phi)$.

The relative standard errors in predicted curves of 19 to 25% can first be compared to the other relative standard errors obtained in our study, e.g. with the different models of M_a (Table 3). It should also be remembered that the values of $M(\phi)$ and related curves depend on several above- and belowground characteristics of the tree, each exhibiting variations according to the local growth conditions (cf. Blackwell et al. 1990 for belowground related variations in M). Hence, the errors can be considered low and the curves acceptable for further use. To what extent they can be

applied to other sites and trees will not be clear until comparative results are available. Our investigations do, however, indicate that knowing the local M_a (the amplitude of the $M(\phi)$-curve) can help to reduce potential errors in $M(\phi)_p$. If we had not used different M_a in predicting $M(\phi)_p$ for the HE and LE sites, which provide quite different growth conditions, the errors in $M(\phi)_p$ would have been several times greater.

Conclusions and outlook

The behavior of the root–soil system subjected to rotation is decisive for interactions between trees and wind, rockfall, snow avalanches and debris flow. The parameterization of a tree's resistive root-soil moment as a function of its rotation, according to tree size and weight, provides an important basis for predicting such interactions in computer simulations, e.g. for use in assessing hazards and risks. Similar studies with species other than Norway spruce and with different site conditions would be valuable for comparison. Then it should be possible to make better predictions and thus improve scientifically based forest management and optimize ways of providing protection against specific natural hazards.

Acknowledgements We thank the Board of the Swiss Federal Institutes of Technology for funding (*Tree stability and natural hazards*), all people involved in the tree stability project for field assistance, Pierre Vanomsen for valuable collaboration, and Silvia Dingwall for revision of the text.

References

Achim A, Nicoll BC, Mochan S, Gardiner BA (2003) Wind stability of trees on slopes. In: Ruck B, Kottmeier C, Mattheck C, Quine C, Wilhelm G (eds) Wind effects on trees. University of Karlsruhe, Karlsruhe, pp 231–237

Blackwell PG, Rennolls K, Coutts MP (1990) A root anchorage model for shallowly rooted Sitka spruce. Forestry 63:73–92

Bolenikus D (2001) Zur Wurzelausbildung von Fichte (*Picea abies* L. Karst) und Weisstanne (*Abies alba* Mill.) in gleich – und ungleichaltrigen Beständen. Berichte Freiburger Forstliche Forschung 35:155

Brang P, Schönenberger W, Frehner M, Schwitter R, Thormann J-J, Wasser B (2006) Management of protection forests in the European Alps: an overview. Forest Snow Landsc Res 80:23–44

Brassel P, Brändli U-B (1999) Inventaire forestier national suisse. Haupt, Berne, p 442

Coutts MP (1983) Root architecture and tree stability. Plant Soil 71:171–188

Coutts MP (1986) Components of tree stability in Sitka spruce on peaty gley soil. Forestry 59:173–198

Crook MJ, Ennos AR (1996) The anchorage mechanics of deep rooted larch, *Larix europea x L. japonica*. J Exp Bot 47:1509–1517

Cucchi V, Meredieu C, Stokes A, Berthier S, Bert D, Najar M, Denis A, Lastennet R (2004) Root anchorage of inner and edge trees in stands of Maritime pine (*Pinus pinaster* Ait.) growing in different podzolic soil conditions. Trees 18:460–466

Dupuy L, Fourcaud T, Stokes A (2005) A numerical investigation into the influence of soil type and root architecture on tree anchorage. Plant Soil 278:119–134

FAO (1998) Soil map of the world. Revised legend. FAO-UNESCO, Food and Agriculture Org. of the United Nations, Rome, p 119

Fourcaud T, Danjon F, Dupuy L (2003) Numerical analysis of the anchorage of maritime pine trees in connection with root structure. In: Ruck B, Kottmeier C, Mattheck C, Quine C, Wilhelm G (eds) Wind effects on trees. University of Karlsruhe, Karlsruhe, pp 323–330

Fraser AI (1962) The soil and roots as factors in tree stability. Forestry 35(2):117–127

Fraser AI, Gardiner JBH (1967) Rooting and stability in Sitka spruce. HMSO, London, p 28

Gardiner BA (1989) Mechanical characteristics of Sitka spruce. Forestry Commission, Edinburgh, p 11

Gerber W, Schnyder D (1998) Attention, chutes de pierres. Des ouvrages de protection plus efficaces. Arguments de la recherche 14:12–17

Hassinen A, Lemettinen M, Peltola H, Kellomaki B, Gardiner B (1998) A prism-based system for monitoring the swaying of trees under wind loading. Agric For Meteorol 90:187–194

Jonsson MJ, Foetzki A, Kalberer M, Lundström T, Ammann W, Stöckli V (2006) Root-soil rotation stiffness of Norway spruce (*Picea abies* L. Karst) growing on subalpine forested slopes. Plant Soil 285:267–277

Köstler JN, Brückner E, Bibelriether H (1968) Die Wurzeln der Waldbäume. Verlag Paul Parey, Hamburg Berlin, p 284

Lundström T, Jonas T, Stöckli V, Ammann W (2007) Anchorage of mature conifers: resistive turning moment, root-soil plate geometry, and orientation of root growth. Tree Physiol 27:1217–1227

MeteoSwiss (2006) Climate database. Swiss National Weather Service http://www.meteoschweiz.ch/web/en/services/data_portal.html

Moore JR (2000) Differences in maximum resistive bending moments of *Pinus radiata* trees grown on a range of soil types. For Ecol Manag 135:63–71

Nicoll BC, Ray D (1996) Adaptive growth of tree root systems in response to wind action and site conditions. Tree Physiol 16:891–898

Nicoll BC, Gardiner BA, Rayner B, Peace AJ (2006) Anchorage of coniferous trees in relation to species, soil type, and rooting depth. Can J For Res 36:1871–1883

Peltola H, Kellomäki S, Hassinen A, Granander M (2000) Mechanical stability of Scots pine, Norway spruce and

birch: an analysis of tree-pulling experiments in Finland. For Ecol Manag 135:143–153

Polomski J, Kuhn N (1998) Wurzelsysteme. Haupt, Bern Stuttgart Wien, p 290

Ray D, Nicoll BC (1998) The effect of soil water-table depth on root-plate development and stability of Sitka spruce. Forestry 71:169–182

SLF (2000) Der Lawinenwinter 1999: Ereignisanalyse. Eidg. Inst. für Schnee – und Lawinenforsch. (SLF), Davos, p 588

Soethe N, Lehmann J, Engels C (2006) Root morphology and anchorage of six native tree species from a tropical montane forest and an elfin forest in Ecuador. Plant Soil 279:173

Stokes A, Salin F, Kokutse AD, Berthier S, Jeannin H, Mochan S, Dorren L, Kokutse N, Abd Ghani M, Fourcaud T (2005) Mechanical resistance of different tree species to rockfall in the French Alps. Plant Soil 278:107–117

Vanomsen P (2006) Der Einfluss der Durchforstung auf die Verankerung der Fichte hinsichtlich ihrer Sturmresistenz. Monogr. Eidgenössische Technische Hochschule ETH, Zürich, p 248

Chapter III

Fresh-wood bending: linking the mechanical and growth properties of a Norway spruce stem

Tree Physiology 27, 1229–1241

Fresh-wood bending: linking the mechanical and growth properties of a Norway spruce stem†

TOR LUNDSTRÖM,[1–3] URS HEIZ,[1] MARKUS STOFFEL[3] and VERONIKA STÖCKLI[1]

[1] *WSL, Swiss Federal Institute for Snow and Avalanche Research SLF, 7260 Davos Dorf, Switzerland*

[2] *Corresponding author (t.lundstroem@slf.ch)*

[3] *Laboratory of Dendrogeomorphology, University of Fribourg, 1700 Fribourg, Switzerland*

Received September 27, 2006; accepted January 22, 2007; published online June 1, 2007

Summary To provide data and methods for analyzing stem mechanics, we investigated bending, density and growth characteristics of 207 specimens of fresh wood from different heights and radial positions of the stem of one mature Norway spruce (*Picea abies* L. Karst.) tree. From the shape of each stress–strain curve, which was calculated from bending tests that accounted for shear deformation, we determined the modulus of elasticity (MOE), the modulus of rupture (MOR), the completeness of the material, an idealized stress–strain curve and the work involved in bending. In general, all mechanical properties increased with distance from the pith, with values in the ranges of 5.7–18 GPa for MOE, 23–90 MPa for MOR and 370–630 and 430–1100 kg m^{-3} for dry and fresh wood densities, respectively. The first three properties generally decreased with stem height, whereas fresh wood density increased. Multiple regression equations were calculated, relating MOR, MOE and dry wood density to growth properties. We applied these equations to the growth of the entire stem and considered the annual rings as superimposed cylindrical shells, resulting in stem-section values of MOE, MOR and dry and fresh densities as a function of stem height and cambial age. The standing tree exhibits an inner stem structure that is well designed for bending, especially at a mature stage.

Keywords: annual ring width, bending mechanics, bulk density, heartwood, knottiness, latewood, sapwood, stem growth, water content.

Introduction

An important factor determining the stability of trees is the way in which stems bend under the pressure of the wind or when impacted by rock falls or avalanches. To understand and predict how stems bend, information about the material properties of living stems is required. In particular, information is needed concerning the relationships between properties of growth, which are affected by forest management practices, and properties of bending mechanics.

For dry and manufactured wood, the effects of growth on mechanics are relatively well understood, as they are relevant to the wood and paper industry. Research on the effects of thinning regimes, fertilization and genetic plant manipulation on mechanical wood properties has greatly contributed to this knowledge (Kollmann 1968, Schmidt-Vogt 1991, Niemz 1993, Lindstrom 1996, 1997, Saren et al. 2001). In brief, because the properties of tracheids correlate with age and properties of annual rings (Dinwoodie 1961, Fioravanti 2001), the most important variables to consider when estimating the mechanical properties of clear dry wood of conifers are the annual ring width, or the percentage of latewood, and tree age (Deresse and Shepard 1999, Sirviö 2001).

An increase in the water content (u) of fresh wood (abbreviations and their definitions are listed in the Appendix) lowers strength and stiffness, and generally reduces the modulus of elasticity (MOE) and the modulus of rupture (MOR) by a magnitude that depends on dry wood density (Dinwoodie 2000), although low-quality timber seems to be less affected (e.g., fir; Madsen 1975). An increase in u also lowers the longitudinal shear modulus (G) and resistance (τ), which affect MOE and MOR. The negative effect of an increase in u from the usual value of 12% to the point of fiber saturation (about 50%) is, in order of importance: MOR, τ, G and MOE (Kollmann 1968, Green et al. 1999), whereas an increase in u above about 50% has no significant effect on any of these properties. However, high u values affect the bulk density of fresh wood and thus the mass of the living stem. Stem mass has a significant influence on the root–soil moment and the stem stresses in a leaning tree (Neild and Wood 1999), as well as on tree structural dynamics when the stem is subjected to acceleration (Milne 1991, Dorren and Berger 2006). For healthy conifer wood, the change in u that occurs in the transition from sapwood to heartwood as a result of torus closure of tracheids is the only factor that influences the mechanical properties of wood once the differentiation of cambial xylem initials is complete (Siau 1995).

The presence of knots, whether dead or alive, greatly reduces resistance to tension, but does not significantly affect

† *Correction: On Page 1238, Column 2, Line 3, the words "several tenths of a percent …", as originally published, should have read "several tens of percent …". This corrected version of the paper was posted on August 13, 2007.*

compression or shear strength (Kollmann 1968). In timber from *Picea abies* L. Karst. and *Pinus sylvestris* L., knots can lower MOR by up to 75% (Kucera 1973), but their influence on deformation and resistance is lower in intact stems than in sawn-wood products (Green et al. 1999). Kucera (1973) also showed that dead and live knots reduce bending resistance to about the same extent, although the Nordic timber-grading rules (FSS 1997) penalize, to some extent, dead and unsound knots compared with live knots. In general, knots also appear to slightly reduce the MOE of dry wood (Kollmann 1968, Dinwoodie 2000).

The inner-stem structure of Norway spruce displays gradients in annual ring width and percentage of latewood (www.ncdc.noaa.gov/paleo/treering.html). Although a multitude of growth patterns can be found depending on growth conditions, ring width generally decreases and the percentage of latewood increases from the pith toward the bark, with the trends reversing with tree height (Trendelenburg and Mayer-Wegelin 1955). The radial and longitudinal trends in growth pattern are more evident in mature trees, with the exception of suppressed trees (Deresse and Shepard 1999). Water content also exhibits gradients within the stem. In Norway spruce, heartwood water content ranges between 30 and 50%, whereas sapwood displays a season-independent water content that is commonly above 150% in early spring and below 100% in late summer (Trendelenburg and Mayer-Wegelin 1955, Schmidt-Vogt 1991). The presence of knots within the stem results from the self-pruning of dead branches at the crown base. The relative height at which self-pruning occurs increases as trees compete for light, resulting in radial and longitudinal gradients in knot frequency (Ikonen et al. 2003).

Analysis of wood bending includes deformation caused by longitudinal tension, compression and shearing (Newlin and Trayer 1956), and related failure mechanisms. Tests on clear, dry and fresh wood show that elasticity along the grain in tension equals that in compression, but that tension failure stresses are higher than those in compression (Natterer et al. 2000). Because of differences in failure stresses and gradients in the growth pattern and local material heterogeneities, a gradual redistribution of compression, tension and shear stresses occurs as the bending load increases (Kollmann 1968). This redistribution is marked for wood with continuous wood fibers, as was shown in studies of dry logs (Adjanohoun et al. 1998, Natterer et al. 2000). Compared with sawn logs, intact logs have a 10% higher MOE, on average, and a 15–25% higher MOR (Natterer and Sandoz 1997).

Turning living tree stems into dry timber, and especially into clear wood, has several effects on material properties related to bending. The overall goal of this study was to analyze stem mechanics. Specific objectives were to: (1) relate dry and fresh wood density and bending properties of a stem with radial and vertical position in the stem; (2) develop statistical regression models linking the mechanical properties of stem wood with radial growth properties; and (3) apply the regression models based on the data in (1) to the entire stem to determine stem-section values of dry and fresh density, MOE and MOR as a function of height and cambial age.

Materials and methods

Tree and test samples

We investigated bending mechanics, density and growth properties of the fresh stem wood of one mature, co-dominant Norway spruce tree growing at an elevation of 460 m near Zürich in Switzerland, on a dystric Cambisol (FAO 1998), in a mixed forest stand (Lundström et al. 2007). The selected tree was representative of other Norway spruce trees in the stand. Characteristics of the test tree were: diameter at breast height (DBH), 400 mm; cambial age (AGE) at breast height, 100 years; total height (H), 35.0 m; length of the green crown relative to H, 0.42; and bark thickness at breast height relative to DBH, 6%. The tree was straight and apparently healthy.

The test Norway spruce tree was felled in mid-November and the stem transported to the laboratory where it was placed outside on level ground in the shade. The next day, stem diameter and bark thickness were measured at 1-m intervals. The stem was then subjected to five successive cutting steps (cf. Figure 1): (1) three 3-m-long log sections (each comprising log sections T3 + T2 + T1), with their base:top at stem heights of 0.7:3.7, 10.1:13.1 and 19.2:22.2 m, respectively; (2) three shorter log sections (T1, T2, and T3) 0.5, 0.9 and 1.6 m in length, respectively, with the section center at relative stem heights (z_{rel}) = z/H of 0.04 (T3), 0.08 (T2) and 0.10 (T1) of the first 3-m log, 0.31 (T3), 0.35 (T2) and 0.37 (T1) of the second, and 0.57 (T3), 0.61 (T2) and 0.63 (T1) of the third 3-m log; (3) quarter sections (A, B, C and D); (4) planks (I, II, ….VI); and (5) bending specimens, ranging from bark to pith (1, 2, …8).

The bending specimens were 20 × 20 × 360 mm (127 pieces cut from the three log sections denoted T1), 40 × 40 × 720 mm (61, T2) and 80 × 80 × 1440 mm (19, T3), with a total of 113 bending specimens from the heartwood and 94 from the sapwood. The transition between the water-conducting sapwood and the heartwood was set to where there was a steep radial in-

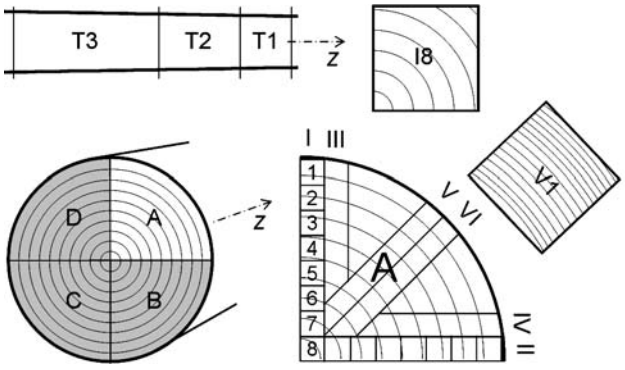

Figure 1. To obtain specimens for bending, each of three 3-m-long logs (top, one 3-m log) cut from the Norway spruce stem was sawn into three shorter sections (T1–3). These shorter sections were then cut into quarter sections (A–D, left), planks (I–VI, right) and finally into bending specimens with square cross sections (1–8, right, with examples shown for bending speciments, I8 and VI). Annual rings are displayed schematically in the cross sections, with light gray circles (left) and circle sectors (right).

crease in water content. Altogether 207 bending specimens were obtained. For each specimen, annual ring width (RW) and percentage of latewood (LW) were measured with a caliper and averaged over the cross section. The specimens were grouped into four categories according to the approximate orientation of the annual rings, with Cut = 1 corresponding to almost straight rings, Cut = 4 to rings resembling a quarter of a circle, and Cut = 2 and 3 to intermediate patterns. This grouping depended on the cutting scheme position of the specimen. For example, the specimens from the inner heartwood were grouped in Category 4, and the ones from the outer sapwood in Category 1 (cf. Figure 1). In addition to the bending specimens, stem discs were cut from z_{rel} = 0.0085 (i.e., at z = 0.30 m), 0.75, 0.90 and 0.99 to analyze radial growth.

Knot frequency was described by a three-number classification. The first number refers to knottiness Q (SIA 2003) of the cross section, which is the ratio between the sum of diameters of knots on the compression- (upper) and tension- (lower) side of the test specimen, along the middle 150 mm of the span, and twice the specimen width. The second and third numbers were calculated accordingly, but refer specifically to the knots on the tension- (t) and the compression- (c) side of the specimen, Q_t and Q_c, respectively. Although most knots were living, no distinction was made between dead and live knots. Because the annual ring curvature was generally small compared with specimen size, the frequently used Knot Area Ratio (KAR, SIA 2003) was less than or equal to 2Q. Wood defects other than knots were not observed among the test specimens.

Tests and investigations

The specimens were tested in 3- and 4-point bending (187 and 20 specimens), according to the German industry code, DIN 52186 (DIN (1992) includes all the mentioned DIN codes), with an exception made for their water content u. For this purpose, we used a hydraulic vertical press D-200-VS 91 connected to a data logger PK-SRG-5000 124 (Walter+Bai AG, Löhningen, Switzerland). The load was applied with a constant deflection rate so that the maximum force was obtained within 90 ± 30 s. With load and deflection sampled at 1 Hz, the tests were continued until complete failure of the specimen occurred. After testing, the wood samples were cut close to the failure zone to analyze u and the dry and fresh wood density ($\rho 0$, ρU) according to DIN 52182 and DIN 52183. To calculate $\rho 0$, we used the dry volume and the wet mass, and corrected for tree volumetric shrinkage with the factor 1.10 (Kollmann 1968). The bending tests and the determinations of u were completed within one day of specimen cutting and one week of tree felling.

Mechanical analysis

All data related to bending mechanics, such as MOE and MOR, were based on the complete curves for bending stress (σ) as a function of bending strain (ε), from no load up to maximum load and then until the load returned to near zero. To obtain these curves, we followed five steps (Table 1) and used Equation 1:

$$E = \frac{F}{s}\left(\frac{C_1}{48I} + C_2\right);\ I = \frac{bh^3}{12}$$
$$C_1 = \frac{1}{2}(2L^3 - 3LL_F{}^2 - L_F{}^3);\ C_1 = L^3 \quad (1)$$
$$C_2 = \beta\left(\frac{E}{G}\right)'\frac{L}{bh}$$

where F is the applied force (N), L, b and h are the length, width and height of the bending specimens (mm), s is the mid-span deflection (Mm), L_F is the distance between support and force application (mm), C_1 is a length factor that equals L^3 in 3-point bending, C_2 is a correction factor for shear deformation, β is a load coefficient that equals 8/27 and 16/81 in 3- and 4-point bending, respectively (Newlin and Trayer 1956), and $(E/G)'$ is an estimated relationship between the elasticity in bending (E) and shear (G) along the grain. For sawn wood of Norway spruce with a density = 400–600 kg m^{-3}, and u = 12%, E/G has a mean of 18 and is about 21 for green wood (u > 50%: Kollmann 1968), which is the value that we adopted for $(E/G)'$. The mass of the bending specimens contributed less than 0.2% to MOR and was therefore omitted from the analysis. Except for the analysis of MOE (Table 1), $\sigma(\varepsilon)$ is used throughout this study.

We also established characteristic $\sigma(\varepsilon)$ curves, where each was the mean stress–strain curve for a specific group of bending specimens. A distinction was made between three groups of mean relative heights 0.10 (1), 0.37 (2) and 0.63 (3), and between two radial ranges, the inner heartwood (IH) and the sapwood (S). The outer heartwood (OH), with properties between the S- and IH-groups, was analyzed only individually. Each of the six groups included between 18 and 32 $\sigma(\varepsilon)$ curves from the small- and medium-sized bending specimens. The

Table 1. Successive steps in the bending mechanics analysis. Abbreviations: σ, bending stress; MOR, modulus of rupture; and MOE, modulus of elasticity.

Step	Description
1	Calculation of σ due to the applied force (DIN 52 186). The maximum σ, independent of type of failure, corresponds to MOR.
2	Calculation of the elasticity in bending (E) due to the applied force (DIN 52 186), corrected for shear deformation (Equation 1).
3	Combination of results from steps 1 and 2 into the bending strain $\varepsilon_E = \sigma/E$ and computation of $\sigma(\varepsilon_E)$. As E is corrected for shear deformation, ε_E is the strain as it would be under pure bending conditions.
4	Definition of MOE as $E(\varepsilon_E)_{0.4MOR}$, the gradient of the straight line between $\sigma(\varepsilon_E) = 0$ and $\sigma(\varepsilon_E) = 0.4MOR$. The initial deformations at supports are not included in the ε_E data.
5	Calculation of $\sigma(\varepsilon)$: ε is the apparent strain from no load until the end of the test, thus with no correction for shear deformation (ε is slightly larger than ε_E).

stress–strain curves obtained were further described with simplified ideal elastic–ideal plastic curves. The break point $(\sigma,\varepsilon) = (\varepsilon_{el\text{-}pl}, MOR \cdot \alpha_{el\text{-}pl})$ between ideal elastic and ideal plastic deformation was conditioned by an equal amount of total work absorbed by the bent member up to $\sigma = MOR$, compared with the original $\sigma(\varepsilon)$ curve.

The absorbed bending work (W) (Equation 2) and the completeness of the material (η) (Equation 3) were both calculated from the load–deflection curve $F(s)$:

$$W = \int_s F(s)ds \tag{2}$$

$$\eta = \frac{W_{MOR}}{F_{max} s_{MOR}} \tag{3}$$

where F_{max} is the maximum applied force (N), s_{MOR} is the value of s at MOR (mm) and W_{MOR} is the work developed up to MOR (N m). The values of total work (W_{tot}) absorbed by the bending specimen during the entire bending test were compared for specimens of the same size. To compare with work absorbed by specimens of other dimensions (e.g., Märki et al. 2005), W_{tot} was divided by the volume (V) of the specimen within the span. For calculations of W/V, only the specimens tested in 3-point bending were included because a larger part of the bending specimen is activated in bending stress in 4-point bending than in 3-point bending, which mobilizes more W/V in 4-point bending. Moreover, work was also expressed in terms of σ integrated with respect to ε, as denoted by $\int\sigma(\varepsilon)\,d\varepsilon$. This number characterizes the material and is independent of the set-up and cross section of the test, just like η. We used Matlab 7.0 (MathWorks) for all mechanics analyses.

Statistical analysis

The statistical relationships within and between the growth characteristics and mechanical properties were explored with S-Plus 2000 (Insightful Corporation). We first applied the pair-wise test between variables to detect their possible transformation and then performed forward and backward stepwise linear regression of the model response variables described by the explanatory variables.

To qualitatively rank the regression models, we used the Akaike Information Criterion AIC (Sakamoto et al. 1986) and the Mallows's Cp statistic (Daniel et al. 1980), where low absolute values of AIC and Cp reflect high quality. The quality of model i was expressed as $AIC_{rel,i} = (1/AIC_i)/(1/AIC_1)$ and $Cp_{rel,i} = (1/Cp_i)/(1/Cp_1)$, where i = 1 is the highest ranked model. We also calculated the R^2 of each model, but as this overestimates the quality of multivariate regression models of correlated variables, it was given third priority in the model ranking. We know of no mathematically correct and straightforward method to calculate the amount of the total variance that each X_j (j = 1, 2,… n – 1, n) explains in a multivariate model of correlated variables (our case). Therefore, to rank the importance of each X_j for its contribution to Y, we used the difference in Cp value between the full, highest ranked model and the model lacking the X_j ("–X_j", Equation 4):

$$+Cp_j = \sum_{j=1}^{n-1} \frac{Cp(Model - X_j) - Cp(Model)}{Cp(Model)} \tag{4}$$

The effect of each X_j on Y was expressed by the standardized regression coefficient of X_j, $\boldsymbol{a_j} = a_j \cdot SE(X_j)/SE(Y)$. Because the investigated mechanical properties were obtained per tested specimen, the growth characteristics needed to be averaged for each bending specimen. For this reason, the large- and medium-sized specimens were less useful for describing the statistical relationships between the properties of growth and mechanics than the small specimens. Consequently, we used only the small specimens.

Application of statistical relationships to the mechanical properties of the entire tree stem

The growth data between pith and bark at seven values of z_{rel} were interpolated radially every millimeter and longitudinally every percent of tree height (piecewise cubic interpolation). The growth data at z_{rel} = 0.10, 0.37 and 0.63 originated from the 188 small- and medium-sized specimens, and those at z_{rel} = 0.0085, 0.75, 0.90 and 0.99 from stem discs sampled at these heights. Data on u were not obtained at the latter heights and originate from neighboring Norway spruce trees with a growth pattern similar to that of our test tree at z_{rel} = 0.10, 0.37 and 0.63 (unpublished SLF). Application of RW, u and Q to the regression equations resulted in $\rho0$, ρU, MOE and MOR within the entire stem. The four mechanical properties were then calculated for the stem section as a function of stem height and AGE at breast height, with the relative distribution of u approximated so as not to vary with AGE (Trendelenburg and Mayer-Wegelin 1955, Schmidt-Vogt 1991).

To calculate $MOE_{section}$ (Equation 5), we used cylindrical shells ranging radially (x, which due to the circular shape, equals r) from pith (j = 1) to bark (j = n) every mm and longitudinally (z) from stem base (i = 1) to tree top (i = 101) every percent of tree height.

$$MOE_{section,i} = \frac{1}{x_n^4} \sum_{j=1}^{n} MOE(x)_{i,j}(x_{i,j+1}^4 - x_{i,j}^4) \tag{5}$$

The calculation of $MOR_{section}$ assumes, in principle, that $\sigma(x)$ as $MOR_{section}$ is reached, is known. In default of this knowledge, and ongoing from the strain–stress distribution of dry timber as its cross section reaches MOR (Kollmann 1968), we used two equations to calculate $MOR_{section}$. The first (Equation 6) applies a linear increase in longitudinal strain from pith to bark, with a gradient governed by the strain at MOR for the cylindrical shell at the radial distance of $\kappa_1 x_n$, where κ_1, is a factor between 0 and 1 (method of linear strain).

$$MOR_{section,i} = \frac{1}{x_n^3} \sum_{j=1}^{n} \sigma(\varepsilon, x, \kappa_1)_{i,j}(x_{i,j+1}^3 - x_{i,j}^3) \tag{6}$$

Unlike this first approach, which requires knowledge of $\sigma(\varepsilon,x)$, the second approach (Equation 7) is simpler. It applies a degree of exploitation $B(\kappa_2)$ of MOR_j, where $B(\kappa_2)$ is an array that increases from 0 to 1 between $x = 0$ and $x = \kappa_2 x_n$ and then remains constant, at a value of 1, between $x = \kappa_2 x_n$ and x_n (method of scaled MOR). Referring, once again, to dry timber, we set both κ_1 and κ_2 equal to 0.85.

$$MOR_{section,i} = \frac{1}{x_n^3}\sum_{j=1}^{n} MOR(x)_{i,j} B(\kappa_2)_{i,j}(x_{i,j+1}^3 - x_{i,j}^3) \quad (7)$$

Finally, the calculations of $\rho 0_{section}$ and $\rho U_{section}$ were simply quadratic summations of dry and fresh wood densities from the pith to the bark (Equation 8).

$$\rho_{section,i} = \frac{1}{x_n^2}\sum_{j=1}^{n} \rho(x)_{i,j}(x_{i,j+1}^2 - x_{i,j}^2) \quad (8)$$

Results

Failure mechanisms and behavior of bending stress–strain

The failure mechanism of the fresh bending specimen started with the wood fibers buckling on the compression side, followed by the fibers tearing apart on the tension side. The latter often occurred close to knots if they were present in the mid-span of the specimen. No signs of shear failure were observed.

The complete $\sigma(\varepsilon)$ curves showed five general features depending on the radial and height position in the stem (Figure 2A and Table 2). First, all bending specimens, independent of height or radial position, displayed a non-negligible remaining resistance beyond the strain at MOR, ε_{MOR}. Second, generally, W_{tot} increased from the IH-wood to the S-wood. Third, W_{tot}, MOE and MOR of the S-wood were almost identical at stem heights 1 and 2, but lower at height 3, and the W_{tot} of the IH-wood decreased with increasing stem height, whereas its MOE and MOR changed little. Fourth, although $\sigma(\varepsilon)$ differed in magnitude depending on height or radial position, $\sigma(\varepsilon)$/MOR curves were similar in shape until ε_{MOR} was reached (Figure 2B). Fifth, beyond ε_{MOR}, $\sigma(\varepsilon)$ displayed a more abrupt drop in the IH-wood compared with the S-wood.

Table 2 shows that MOE and MOR were both about 60% higher and that W_{tot}/V is twice as large for the S-wood than for the IH-wood. It was also apparent that the characteristics of the simplified stress–strain curves were independent of the position within the stem. At the individual specimen level, the IH-wood displayed a step-wise decrease of σ after MOR (Figure 2C). Generally, this stair-case pattern smoothed gradually toward the bark. The SEs of the six mean $\sigma(\varepsilon)$/MOR curves (Figure 2B) were larger after MOR and for the IH-wood than before MOR and the S-wood (Table 2). There was a weak general increase in ε_{MOR} with MOR (Figure 2C and Table 3).

Not accounting for shear deformation in the 3- and 4-point bending tests led to underestimates of MOE of about 11 and 6%, respectively. Apart from this and W_{tot}/V, there were no significant differences in bending properties between the 3- and 4-point bending tests.

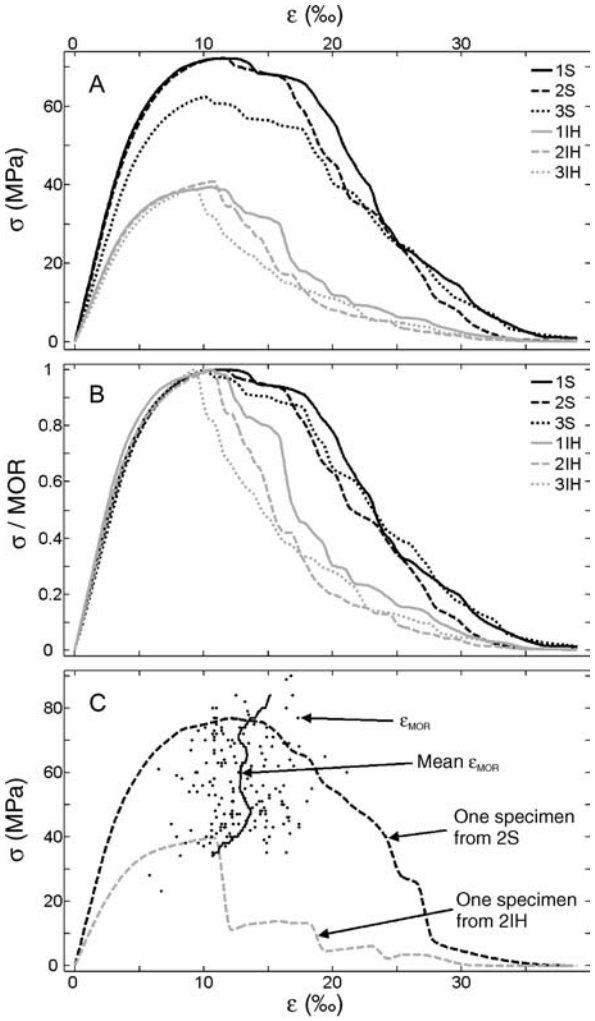

Figure 2. (A) Mean bending stress (σ) as a function of bending strain (ε). (B) IH refers to the inner heartwood, S to the sapwood, and 1, 2 and 3 to relative tree heights 0.10, 0.37 and 0.63, respectively. The $\sigma(\varepsilon)$/modulus of rupture (MOR) curves are similar in shape until the strain reaches MOR (ε_{MOR}), but not when the strain exceeds ε_{MOR}. This is evident in the IH-wood, especially in individual specimens (C). Values of ε_{MOR} (points) tended to increase with MOR (continuous line, mean ε_{MOR} = ε_{MOR} smoothed with the loess algorithm, Matlab).

Growth and mechanics measured across the stem

The measured properties of growth displayed characteristic patterns from the pith to the bark: RW decreased, whereas LW and u generally increased, with values in the range of 0.5–6.5 mm for RW, 0.10–0.71 for LW and 26–145% for u. Knottiness followed a Gaussian curve, with its maxima further from the bark at the stem base than higher up the stem. Values of Q ranged from 0 to 0.9 (apart from one specimen with Q = 1.8) and averaged 0.12. The most obvious dependency on tree

Table 2. Parameters obtained from the curves of bending stress–strain σ(ε) for groups of specimens from different positions in the stem. 1, 2 and 3 denote the relative stem heights 0.10, 0.37 and 0.63, S the sapwood and IH the inner heartwood. For example, 1S refers to the average stress–strain curve for sapwood at the relative height 0.10 and S to the average curve for all sapwood. Abbreviations: MOR, modulus of rupture, and MOE, modulus of elasticity.

Sample group	ε[1]				SE(σ(ε)/MOR)		α_{el-pl}[2] (%)	η[3]	W_{MOR}			MOR (MPa)	MOE (GPa)
	el (‰)	el–pl	MOR	max	<ε_{MOR} (%)	>ε_{MOR}			$\int\sigma(\varepsilon)d\varepsilon$[4] (MPa)	/V[5] (KPa)	/W_{tot}[6] (%)		
1S	2.1	5.0	12	38	2	9	92	72	0.62	71	42	72.9	15.1
2S	2.1	5.2	14	35	4	9	93	74	0.68	77	52	70.4	14.2
3S	2.4	5.6	13	37	2	10	93	71	0.53	61	44	62.9	11.8
S	2.2	5.3	13	37	3	10	92	72	0.61	70	46	68.8	13.7
1IH	2.1	4.8	14	31	8	13	92	76	0.46	63	67	44.5	9.6
2IH	2.2	5.1	14	31	3	10	92	75	0.44	61	76	42.8	8.5
3IH	2.4	5.2	11	31	4	14	90	69	0.31	41	63	40.9	8.0
IH	2.2	5.0	13	31	5	12	91	73	0.40	55	69	42.7	8.7
All	2.2	5.1	13	34	4	11	92	73	0.51	62	57	55.7	11.2

[1] Bending strain at 0.4MOR (el), at the break point for the idealized σ(ε)-curve between ideal elastic and ideal plastic behavior (el–pl), at MOR and as σ returned to a value below 0.5 MPa (max).
[2] Stress level of plasticity for the idealized stress–strain curve, expressed as a fraction of MOR.
[3] Completeness of the material in bending (Equation 3).
[4] Integration of σ(ε) up to MOR, i.e., area under σ(ε) curve.
[5] Work absorbed in bending up to MOR, relative to the volume V within the span of the specimen.
[6] Total work absorbed in bending, i.e., up to ε_{max}.

height was the increase in u. The mechanical properties followed similar patterns to the growth characteristics across and along the stem. All mechanical properties generally increased with distance from the pith, with MOR in the range 23–90 MPa, MOE 5.7–18.1 GPa, W_{tot}/V 35–219 kPa, W_{MOR}/V 20–128 kPa, and ρ0 and ρU in the ranges 370–630 and 430–1100 kg m^{-3}, respectively. Except for W, all general tendencies or means of measured values are shown in Figures 3 and 4.

Relationships between the properties of mechanics and growth

As expected, several of the 13 variables of growth and mechanics were strongly correlated (Table 4). This resulted in regression models for the response variables ρ0, MOR and MOE, with six or less significant variables. Altogether 40 useful models describing ρ0 (9), MOR (20) and MOE (11) were obtained. Nine of these models are described in Tables 5–7.

Among the three response variables, ρ0 was modeled with

Table 3. Regression models for the strain (ε) at the modulus of rupture (MOR), $\varepsilon MOR_i = \sum_{j=1}^{n} a_j X_j$. Variable and intercept coefficients a_j, and standardized variable coefficient $\boldsymbol{a_j}$. The models ($\varepsilon MOR_{1,2}$) and the model variables X_j are listed top down according to the ranking and contribution to the model, respectively. The degrees of freedom are 122. Significance: *, $P < 0.05$; **, $P < 0.01$; and ***, $P < 0.001$.

Model				Variables				
i	AIC_{rel}[1]	Cp_{rel}[1]	R^2	X_j	a_j	SE(a_j)	$\boldsymbol{a_j}$	+Cp_j[2]
1	1.00	1.00	0.50	log(ρ0)	−2.92E−02 ***	2.89E−03	−2.05	0.47
				MOR	3.77E−04 ***	3.78E−05	2.29	0.46
				MOE	−3.25E−07 **	1.01E−07	−0.38	0.04
				z_{rel}	−2.23E−03 **	7.68E−04	−0.20	0.03
				Intercept	1.76E−01 ***	1.61E−02		
2	0.71	0.40	0.30	MOR	1.22E−04 ***	2.25E−05	0.64	0.47
				u	−4.12E−05 ***	7.89E−06	−0.47	0.44
				log(RW)	1.32E−03 *	5.44E−04	0.33	0.07
				Q	−1.59E−03 *	8.42E−04	−0.12	0.03
				Intercept	7.59E−03 ***	1.71E−03		

[1] $AIC_{rel,i} = (1/AIC_i)/(1/AIC_1)$ and $Cp_{rel,i} = (1/Cp_i)/(1/Cp_1)$, where $AIC_1 = -1254$ and $Cp_1 = 3.77E{-}04$ are the criteria of the highest ranked model (εMOR_1) and i = 1, 2 refers to each of the two models.
[2] +Cp_j is the relative contribution of each variable to Cp of the model (Equation 4).

Table 4. Correlation coefficients between variables: modulus of rupture (MOR), modulus of elasticity (MOE), annual ring width (RW), latewood portion (LW), dry wood density (ρ0), water content (u), squared knottiness of the specimen section (Q^2), on the compression (Q_c^2) and on the tension side (Q_t^2) of the specimen, cambial age (AGE) and distance (r) counted from pith toward bark, cutting mode (Cut), describing the annual ring curvature of the sample crosssection, and the relative tree height (z_{rel}).

	MOR	MOE	log(RW)	LW	ρ0	u	Q^2	Q_c^2	Q_t^2	AGE	r	Cut
MOE	0.82											
log(RW)	−0.87	−0.77										
LW	0.84	0.68	−0.77									
ρ0	0.95	0.75	−0.92	0.80								
u	0.63	0.43	−0.74	0.54	0.72							
Q^2	−0.27	−0.27	0.17	−0.18	−0.15	−0.07						
Q_c^2	−0.16	−0.21	0.10	−0.11	−0.07	−0.01	0.79					
Q_t^2	−0.27	−0.21	0.18	−0.18	−0.18	−0.12	0.66	0.07				
AGE	0.88	0.82	−0.84	0.73	0.88	0.50	−0.24	−0.18	−0.20			
r	0.84	0.80	−0.77	0.71	0.79	0.38	−0.30	−0.24	−0.22	0.96		
Cut	−0.58	−0.47	0.52	−0.45	−0.55	−0.33	0.07	−0.03	0.15	−0.61	−0.62	
z_{rel}	−0.11	−0.26	0.00	−0.05	−0.06	0.48	−0.02	0.02	−0.04	−0.35	−0.36	0.23

the highest quality, followed by MOR and then MOE. The variable ρ0 was strongly related to RW and LW (Table 5), and MOR was best described by ρ0 (Table 6). Although Q_t reduced MOR about twice as much as did Q_c, the overall frequency of knots was low, so knottiness contributed little to the quality of the models. The exclusion of ρ0 in the starting set of variables involved log(RW) in the models describing MOR (MOR_{2-4}) because ρ0 and log(RW) were strongly correlated. Excluding ρ0 also suggested models including AGE. However, these models contained additional variables that improved model quality little. Although Cut (= 1, 2, 3 or 4) tended to reduce MOR = –18.9log(Cut) + 67.5 ($R^2 = 0.35$, both coefficients $P < 0.001$), its influence was weak because of the strong correlation with other variables in the multivariate models (Table 4) and the presence of mainly straight annual rings (Cut = 1 or 2). The models describing MOE included log(RW), u and ρ0 (Table 7). Although MOE was also reduced by Q_c ($P = 0.10$), Cut and AGE, their impact on MOE, like that of MOR, was weak (for the same reasons).

Growth and mechanics within the stem

The growth properties interpolated within the entire stem (Figure 3) were applied to the regression models describing mechanical properties within the stem (Figure 4). These two property groups display some general features. For example, the zone between the IH-wood and the S-wood constitutes a transition for all properties of growth and mechanics except for Q. Between $z_{rel} = 0.1$ and 0.5, Q appears to be primarily influenced by the location of the lower part of the crown, changing from $z_{rel} = 0.1$ at AGE = 10 years to $z_{rel} = 0.5$ at 35 years, after which it increased little with height with increasing AGE.

Mechanics of the stem section

All mechanical properties of the stem section (Figure 5) decreased with stem height, except for $\rho U_{section}$, which increased. Within the stem section covered by the crown, $MOR_{section}$, and especially $MOE_{section}$, decreased with increasing height. At the buttressed stem base, the large RW in the outermost stem section reduced $MOR_{section}$ and $MOE_{section}$. At AGE = 100 years at breast height, the section values of MOR (Figure 5B) obtained by the linear strain method (Equation 6) were between 8 and 12% lower than those obtained by the scaled MOR method (Equation 7). These differences, which were largest at the stem base and in the crown, resulted from the different radial

Table 5. Regression models for the dry wood density ($\rho 0_i$). The models ($\rho 0_{1-2}$) and the model variables (X_j) are listed top down according to the ranking and contribution to the model, respectively. The minimum degrees of freedom (for $\rho 0_1$) are 124. Notations and footnotes are further explained in Table 3.

Model				Variables				
i	AIC_{rel}[1]	Cp_{rel}[1]	R^2	X_j	a_j	SE(a_j)	$\boldsymbol{a_j}$	$+Cp_j$[2]
1	1.00	1.00	0.87	log(RW)	−8.59E+01 ***	5.81E+00	−2.06	0.93
				LW	1.48E+02 ***	3.37E+01	0.61	0.07
				Intercept	4.84E+02 ***	1.38E+01		
2	0.99	0.88	0.85	log(RW)	−1.06E+02 ***	3.98E+00		
				Intercept	5.43E+02 ***	3.69E+00		

[1] $AIC_1 = 1222$ and $Cp_1 = 1.104E+05$.

[2] $+Cp_j$ is the relative contribution of each variable to Cp of the model (Equation 4).

Table 6. Regression models for the modulus of rupture (MOR_i). The models (MOR_{1-4}) and the model variables (X_j) are listed in order of their ranking and their contribution to the model, respectively. Minimum degrees of freedom (for MOR_2) are 123. Notations and footnotes are further explained in Table 3.

Model				Variables				
i	AIC_{rel}[1]	Cp_{rel}[1]	R^2	X_j	a_j	SE(a_j)	$\boldsymbol{a_j}$	$+Cp_j$[2]
1	1.00	1.00	0.91	ρ0	1.64E−01 ***	4.81E−03	9.58	0.98
				Q^2	−4.75E+01 ***	9.87E+00	−0.43	0.02
				Intercept	−2.25E+01 ***	2.36E+00		
2	0.90	0.53	0.84	log(RW)	−1.13E+01 ***	1.16E+00	−1.36	0.65
				LW	4.60E+01 ***	6.71E+00	0.96	0.31
				Q_t^2	−3.05E+01 **	1.13E+01	−0.24	0.04
				Intercept	4.82E+01 ***	2.74E+00		
3	0.86	0.39	0.78	log(RW)	−1.73E+01 ***	8.78E−01	−1.78	0.99
				Q_t^2	−3.60E+01 **	1.32E+01	−0.24	0.01
				Intercept	6.64E+01 ***	8.02E−01		
4	0.85	0.38	0.76	log(RW)	−1.77E+01 ***	8.86E−01		
				Intercept	6.63E+01 ***	8.22E−01		

[1] AIC_1 = 732.6 and Cp_1 = 2342.
[2] $+Cp_j$ is the relative contribution of each variable to Cp of the model (Equation 4).

distributions of bending stress (Figure 6). Figures 5A–D show that all section values decreased with AGE, independently of z_{rel}.

Discussion and conclusions

The bending stress–strain curves, σ(ε), obtained for fresh Norway spruce wood differ markedly from those for dry wood of the same species (Kollmann 1968, Märki et al. 2005), the fresh wood being more easily deformed and having a lower MOR. In terms of energy absorption of fresh wood (i.e., area under the σ(ε) curve), these two behaviors have opposite effects. A comparison of the values of energy absorption found in our study with published values for dry wood of Norway spruce undergoing bending (Kollmann 1968, Brauner et al. 2005, Märki et al. 2005) suggests that the two effects are of similar magnitude (a factor of 2). This implies that fresh and dry wood of Norway spruce absorb about the same amount of energy while bending to complete failure. Nevertheless, when analyzing the bending behavior of living tree stems, it is essential to consider the σ(ε) of fresh wood, and not of dry wood.

Most mechanical properties related to the stress–strain curve display a strong gradient in the radial direction because of the gradient in growth properties. The S-wood and the IH-wood (i.e., juvenile wood) form two distinct categories, and the OH-wood provides the transition zone. A similar radial tendency for MOE and MOR, but not for dry wood density, was also recorded by Huang et al. (2005) in logs of red cedar. Compared with S-wood, the IH-wood displays brittle failure, with about 40% lower MOR and MOE and about half of the total energy absorption per volume in bending. This means that S-wood maintains its resistance and energy absorption at

Table 7. Regression models for the modulus of elasticity (MOE_i). The models (MOE_{1-3}) and the model variables (X_j) are listed top down according to the ranking and contribution to the model, respectively. The minimum degrees of freedom (for MOE_1) are 124. Notations and footnotes are further explained in Table 3.

Model				Variables				
i	AIC_{rel}[1]	Cp_{rel}[1]	R^2	X_j	a_j	SE(a_j)	$\boldsymbol{a_j}$	$+Cp_j$[2]
1	1.00	1.00	0.63	log(RW)	−3.86E+03 ***	3.16E+02	−1.61	0.93
				u	−2.50E+01 ***	6.77E+00	−0.49	0.07
				Intercept	1.51E+04 ***	5.66E+02		
2	1.00	0.91	0.59	log(RW)	−3.00E+03 ***	2.08E+02		
				Intercept	1.31E+04 ***	2.24E+02		
3	0.99	0.88	0.57	log(ρ0)	1.26E+04 ***	9.72E+02		
				Intercept	−6.63E+04 ***	5.99E+03		

[1] AIC_1 = 2251 and Cp_1 = 3.642E+08.
[2] $+Cp_j$ is the relative contribution of each variable to Cp of the model (Equation 4).

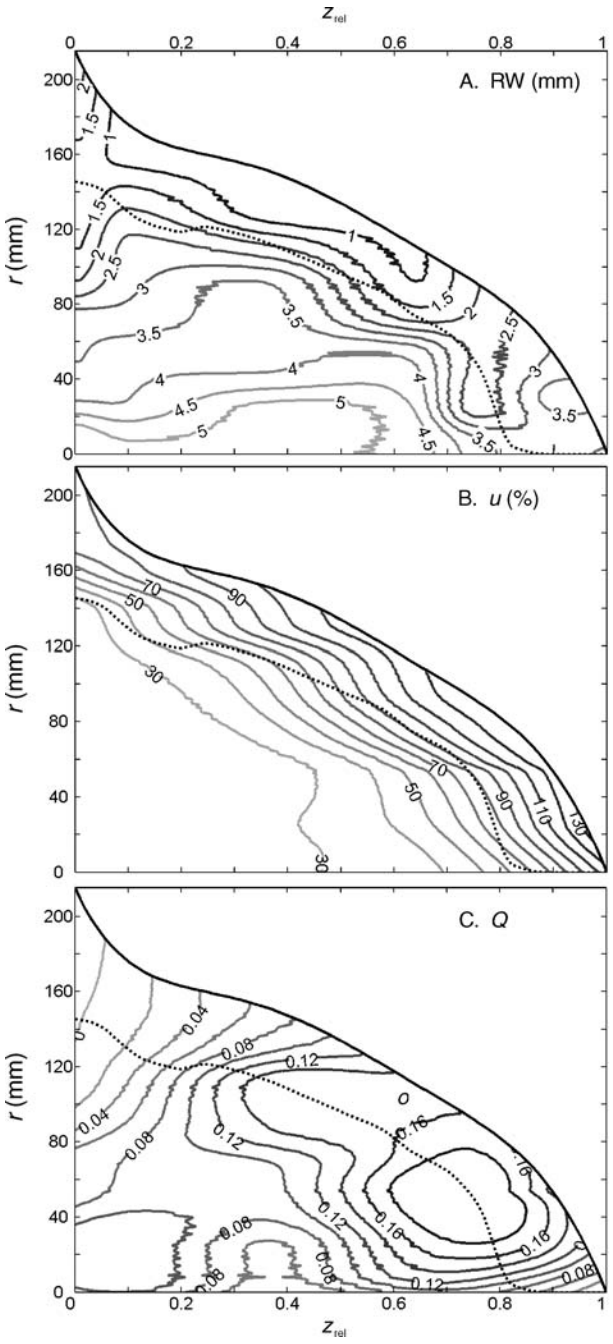

Figure 3. Three growth characteristics of the horizontal stem as functions of stem radius (r) and relative tree height (z_{rel}): (A) annual ring width (RW), (B) wood water content (u) and (C) knottiness (Q). The curved dotted line indicates the border between the heartwood and the sapwood.

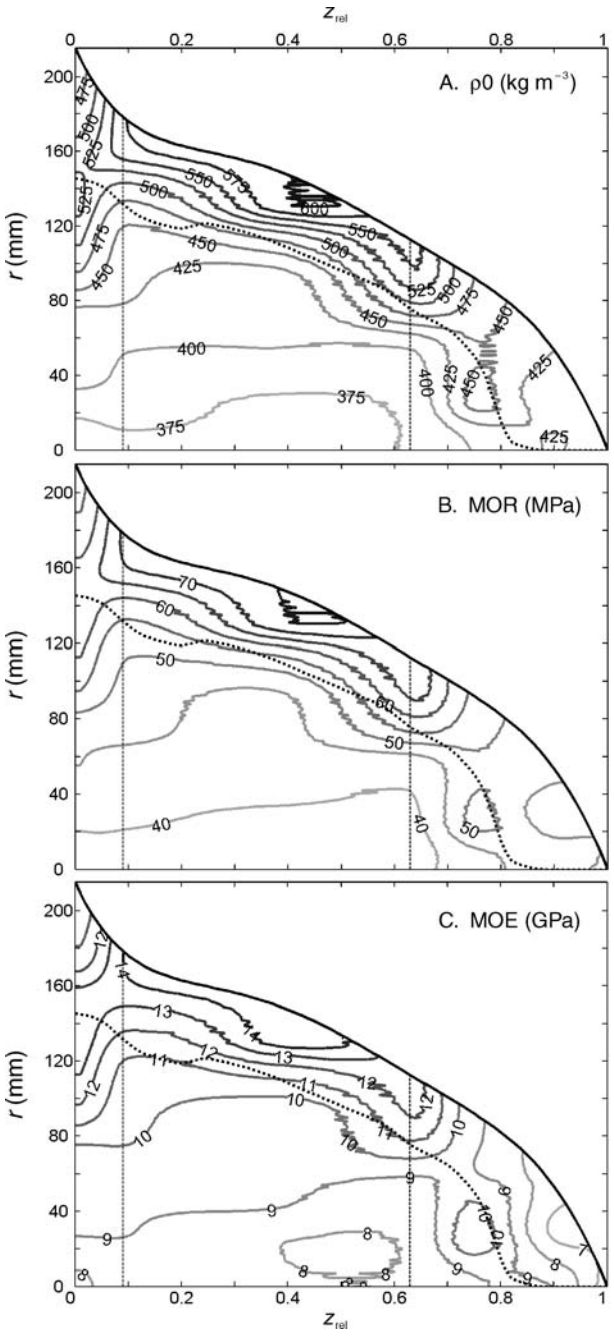

Figure 4. Three mechanical properties of the horizontal stem as a function of stem radius (r) and relative tree height (z_{rel}): (A) dry wood density (ρ0), (B) modulus of rupture (MOR) and (C) modulus of elasticity (MOE). The vertical hatched lines delimit the region for the experimentally obtained mechanical data, and the curved dotted line is the border between the heartwood and the sapwood.

strain values beyond MOR, unlike IH-wood. This difference between S-wood and IH-wood may be a result of a "global effect" found in living stems as well as in the specimens: the cross section of the bending specimen from the S-wood included 10–40 annual rings, and that of the IH-wood only 3–10 rings. The annual rings probably fail one after the other, resulting in a gradual stress redistribution, which may be more abrupt with five annual rings than with 30 rings. The phenomenon may also be associated, in part, with the lower water content of IH-wood compared with S-wood. Nevertheless, the shapes of the $\sigma(\varepsilon)$/MOR curves for IH-wood and S-wood were similar up to MOR (Figure 2B), resulting in similar idealized stress–strain curves and values of completeness, which simpli-

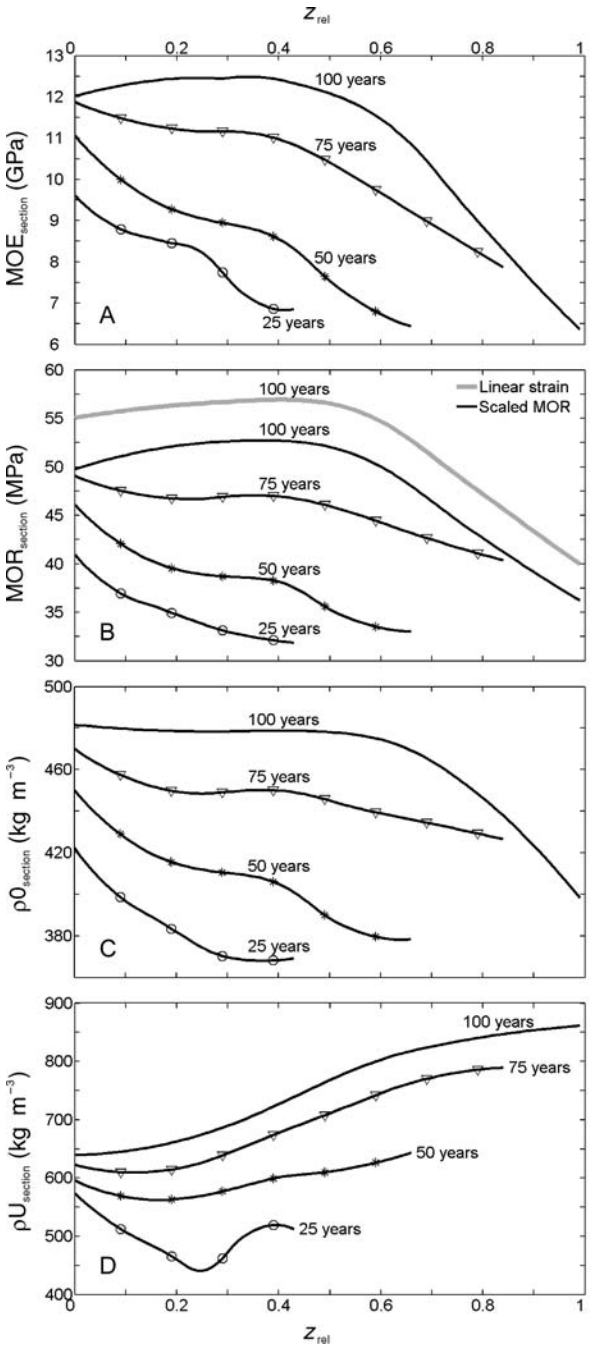

Figure 5. Four mechanical properties of the stem section as functions of relative height (z_{rel}) and cambial age at breast height (years): (A) modulus of elasticity (MOE), (B) modulus of rupture (MOR) calculated by the methods of linear strain and scaled MOR (cf. Figure 6) and (C) dry and (D) fresh wood densities (ρ0 and ρU). Panels A–D are the results from Equations 6–8, smoothed (loess algorithm) using the span = z_{rel}/3. All mechanical properties increase with age, especially MOE and MOR.

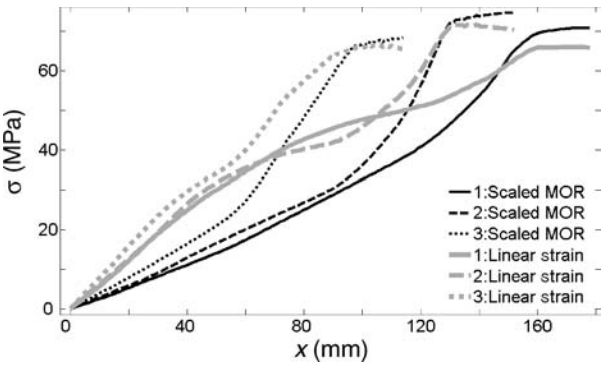

Figure 6. Bending stress (σ) as a function of the distance from pith (x), resulting from the methods based on linear strain (Equation 6) and scaled modulus of rupture (MOR) (Equation 7). Numbers 1, 2 and 3 correspond to relative tree heights 0.10, 0.37 and 0.63. The linear strain method yielded higher bending stress values than the scaled MOR method, except in the outer sapwood.

fies the computation of σ(ε) up to MOR for fresh wood at any radial position on the stem.

Dry wood density was about 40% lower in IH-wood than in S-wood. For fresh wood density, these proportions were roughly inversed because of the water content. Sapwood exhibits variations in water content during the year that can reach several tens of percent (Trendelenburg and Mayer-Wegelin 1955), and these variations affect the fresh wood density of the living tree stem. Our Norway spruce tree was felled in the middle of November when its water content probably approximated the mean annual water content (Schmidt-Vogt 1991). Consequently, the stem section values of fresh density should reflect the annual means.

Comparisons of the mechanical properties of the stem with the literature are relevant only if the growth conditions and properties of radial and apical growth are similar to those of the tested Norway spruce. This applied both to the values within the stem and those obtained for the stem section at cambial ages of 25, 50, 75 and 100 years at breast height. The 100-year-old co-dominant Norway spruce we studied grew in a relatively well drained soil and in competition in a fairly dense stand, and is representative of the whole study stand and of several other sites with similar climatic conditions in and around the Alps (Bräker 1981, Schweingruber 1996) and even worldwide (Core et al. 1979). It is evident that Norway spruce stems with other growth patterns, e.g., trees growing alone, on windy spots, on slopes at the tree line or that are overaged or damaged, will exhibit radial as well as cross-sectional mechanical properties that differ from the properties we observed. For example, Norway spruce trees in the Black Forest grow faster than the Norway spruce tree we investigated and exhibit between 30–40% (Trendelenburg and Mayer-Wegelin 1955) and 5–15% (Brüchert et al. 2000) lower dry wood density at equal cambial ages. For MOE, Brüchert et al. (2000) report 10–30% lower values at the same cambial age, but the MOE distribution within the stem was similar to that in our study tree. We found no published studies on MOR of fresh wood of Norway spruce combined with growth data.

The regression models help to identify growth properties having large effects on MOR, MOE and dry wood density. Our aim was to provide models for stems of a typical Norway

spruce tree. Trees growing under extreme conditions develop special stem wood properties in addition to those considered in this study such as compression wood, spiral or curly grain, callus tissue, traumatic resin ducts and gelatinous tracheids, which all influence wood mechanics (Schweingruber 1996, Mattheck 1998, Dinwoodie 2000). Previous studies have shown that age positively influences mechanical properties (e.g., Sirviö 2001). Nevertheless, old trees with large radii and widely spaced annual rings close to the bark do exist, but multivariate studies of mechanics of fresh wood of old trees are rare. We therefore decided not to present regression models including age or the radial distance from pith, although these variables slightly improved regression quality. The correlations between variables (Table 4) generally confirm previous studies (Kucera 1973, Green et al. 1999, Dinwoodie 2000). The MOE and MOR values predicted by ρ0, RW and Q, with a correction made for u, are comparable with results from previous works (Kollmann 1968, Niemz 1993, Natterer et al. 2000). If we exclude trees with special growth properties, the regression models (Tables 5–7) are likely to be generally applicable to stems of *Picea abies* L. Karst. trees.

The calculated section values of MOR, MOE and wood density (Equations 5–8) indicate that the radial and apical growth of the Norway spruce stem we studied is well designed for bending. The relatively high MOR and MOE values at the base and low values toward the top should provide several advantages for the resistance and stability of the tree, e.g., when it interacts with strong winds. A flexible upper part of the stem prevents the crown from catching wind flow, and the stem-bending resistance is highest where it is most needed, namely at the stem base, where the largest bending stresses occur. The adaptive growth observed in the radial direction of the stem economizes material in that the dense and strong wood is located close to the bark where it most effectively provides resistance and stiffness to the stem section. Although the composite equations require validation (bending of entire logs), they provide a further mechanism of how trees optimize their growth, in addition to what has been found previously (Nicoll and Ray 1996, Mattheck 1998).

The heterogeneity of wood within the stem of Norway spruce and its mechanically optimized inner structure can be accounted for using the relationships and methods presented in this contribution. The methods can be used to analyze the stability and energy dissipation of entire trees and the influence of different thinning regimes on the mechanical properties of the living stem.

Acknowledgments

The authors are indebted to the Board of the Swiss Federal Institutes of Technology for financial support, as part of the "Tree Stability and Natural Hazards" ("Naturereignisse und Baumstabilität") project. We thank Werner Gerber for his precise and successful experimental work and Silvia Dingwall for revising the text.

References

Adjanohoun, G., J.-L. Guillot, J.-D. Lanvin and R. Cholat. 1998. Small roundwood grading by non destructive X-rays and ultrasonic waves methods. 5th World Conference on Timber Engineering. Presses polytechniques et universitaires romandes, Lausanne, Switzerland. Available on the web at http://www.ndt.net/article/v04n11/adjanoh/adjanoh.htm.

Bräker, O.U. 1981. Der Alterstrend bei Jahrringdichten und Jahrringbreiten von Nadelhölzern und sein Ausgleich. Mitt. Forstl. Bundes-Versuchsanst. Wien 142:75–102.

Brauner, M., W. Weinmeister, P. Agner, S. Vospernik and B. Hoesle. 2005. Forest management decision support for evaluating forest protection effects against rockfall. For. Ecol. Manage. 207:75–85.

Brüchert, F., G. Becker and T. Speck. 2000. The mechanics of Norway spruce [*Picea abies* (L.) Karst]: mechanical properties of standing trees from different thinning regimes. For. Ecol. Manage. 135:45–62.

Core, H.A., W.A. Côté and A.C. Day. 1979. Wood: Structure and identification. 2nd Edn. Syracuse University Press, Syracuse, NY, 182 p.

Daniel, D., F.S. Wood and J.W. Gorman. 1980. Fitting equations to data: computer analysis of multifactor data. *In* Probability and Mathematical Statistics. Applied Probability and Statistics Vol. XVIII. 2nd Edn. John Wiley and sons, New York, 458 p.

Deresse, T. and R.K. Shepard. 1999. Wood properties of red pine (*Pinus resinosa* Ait.). CFRU Information Report 42, Dept. of For. Manage., University of Maine, Orono, 17 p.

DIN. 1992. Normen über Holz. Deutsches Institut für Normung. DIN-Taschenbuch Vol.31. 6th Edn. Beuth, Berlin; Köln, 260 p.

Dinwoodie, J.M. 1961. Tracheid and fibre length in timber. A review of literature. Forestry 34:125–144.

Dinwoodie, J.M. 2000. Timber: its nature and behaviour. 2nd Edn. E&FN SPON, London, 257 p.

FAO. 1998. Soil map of the world. Revised legend. World Soil Resources Report Vol. 60. FAO-UNESCO, Rome, 119 p.

Fioravanti, M. 2001. The influence of age and growth factors on microfibril angle of wood. First International Conference of European Society for Wood Mechanics, Lausanne, Switzerland, pp 47–54.

FSS. 1997. Nordic timber-grading rules. Grading rules for pine (*Pinus sylvestris*) and spruce (*Picea abies*) sawn timber. Commercial Grading Based on Evaluation of the Four Sides of Sawn Timber. 2nd Edn. Föreningen Svenska Sågverksmän (FSS)/Suomen Sahateollisuusmiesten Yhdistys (STMY)/Treindustriens Tekniske Forening (TTF), Sweden/Finland/Norway, 80 p.

Green, D.W., J.E. Winandy and D.E. Kretschmann. 1999. Mechanical properties of wood. Department of Agriculture, Forest Service, Madison, WI. Available on on the web at http://www.fpl.fs.fed.us/documnts/fplgtr/fplgtr113/ch04.pdf.

Huang, Y.S., S.S. Chen, L.L. Kuo-Huang and C.M. Lee. 2005. Growth strain in the trunk and branches of *Chamaecyparis formosensis* and its influence on tree form. Tree Physiol. 25: 1119–1126.

Ikonen, V.P., S. Kellomäki and H. Peltola. 2003. Linking tree stem properties of Scots pine (*Pinus sylvestris* L.) to sawn timber properties through simulated sawing. For. Ecol. Manage. 174:251–263.

Kollmann, F.F.P. 1968. Principles of wood science and technology. *In* Solid Wood Vol. 1. Springer-Verlag, Berlin, 592 p.

Kucera, B. 1973. Holzfehler und ihr Einfluss auf die mechanischen Eigenschaften der Fichte und Kiefer. Holztechnologie 14:8–17.

Lindstrom, H. 1996. Basic density of Norway spruce. Part II. Predicted by stem taper, mean growth ring width, and factors related to crown development. Wood Fiber Sci. 28:240–251.

Lindstrom, H. 1997. Fiber length, tracheid diameter, and latewood percentage in Norway spruce: Development from pith outwards. Wood Fiber Sci. 29:21–34.

Lundström, T., T. Jonas, V. Stöckli and W.J. Ammann. 2007. Anchorage of mature conifers: resistive turning moment, root–soil plate geometry, and orientation of root growth. Tree Physiol. 27:1217–1227.

Madsen, B. 1975. Duration of load test for wet lumber in bending. For. Prod. J. 25:33–40.

Märki, C., P. Niemz and D. Mannes. 2005. Vergleichende Untersuchungen zu ausgewählten mechanicshe Eigenschaften von EIbe und Fichte. Schweiz. Z. Forstwes. 3/4:85–91.

Mattheck, C. 1998. Design in nature: learning from trees. Springer-Verlag, Berlin, 276 p.

Milne, R. 1991. Dynamics of swaying of *Picea sitchensis*. Tree Physiol. 9:383–399.

Natterer, J. and J.L. Sandoz. 1997. Construire en bois. Notions de base. Publication IBOIS 97:16. 3rd. Edn. Reprographie Ecole polytechnique fédérale de Lausanne, Lausanne, Switzerland, 198 p.

Natterer, J., J.L. Sandoz and R. Martial. 2000. Construction en bois. Traité de Génie Civil Vol. 13. Presses Polytechniques et Universitaires Romandes, Lausanne, Switzerland, 472 p.

Neild, S.A. and C.J. Wood. 1999. Estimating stem and root-anchorage flexibility in trees. Tree Physiol. 19:141–151.

Newlin, J.A. and G.W. Trayer. 1956. Deflection of beams with special reference to shear deformations. Report 1309, U.S. Department of Agriculture, Forest Service, Madison, WI, 18 p.

Nicoll, B.C. and D. Ray. 1996. Adaptive growth of tree root systems in response to wind action and site conditions. Tree Physiol. 16: 891–898.

Niemz, P. 1993. Physik des Holzes und der Holzwerkstoffe. Holz: Anatomie, Chemie, Physik, Vol. III. DRW-Verlag, Berlin, 247 p.

Sakamoto, Y., M. Ishiguro and G. Kitagawa. 1986. Akaike information criterion statistics, Vol. XIX. KTK Scientific Publishers, Tokyo, 290 p.

Saren, M.P., R. Serimaa, S. Andersson, T. Paakkari, P. Saranpaa and E. Pesonen. 2001. Structural variation of tracheids in Norway spruce (*Picea abies* L. Karst.). J. Struct. Biol. 136:101–109.

Schmidt-Vogt, H. 1991. Die Fichte: ein Handbuch in zwei Bänden. Waldbau, Ökologie, Urwald, Wirtschaftswald, Ernährung, Düngung, Ausblick Vol. 2/3. Verlag Paul Parey, Hamburg, 781 p.

Schweingruber, F.H. 1996. Tree rings and environment. Dendroecology. Haupt Verlag, Bern, 609 p.

SIA. 2003. Timber structures—supplementary specifications. 265/1, Schweizerischer Ingenieur—und Architektenverein (SIA), Zurich, 27 p.

Siau, J.F. 1995. Wood: Influence of moisture on physical properties. Department of Wood Science and Forest Products, Virginia Polytechnic Institute and State University, Keene, NY, 227 p.

Sirviö, J. 2001. The effects of age and growth rate on wood basic density in Scots pine and Norway spruce. First International Conference of European Society for Wood Mechanics, Lausanne, Switzerland, pp 13–22.

Trendelenburg, R. and H. Mayer-Wegelin. 1955. Das Holz als Rohstoff. 2nd Edn. J.F. Lehmanns Verlag, München, 541 p.

Appendix

Table A1. List of symbols and notations and their definitions and units used in the study.

Symbol/Notation	Description	Unit
* , **, ***	Levels of significance for $P < 0.05$, $P < 0.01$ and $P < 0.001$	–
a; $\boldsymbol{a}$	Variable and intercept coefficients; standardized variable coefficient (cf. Statistical analysis)	–
AGE	Cambial age counted from pith	Years
AIC; Cp	Statistical indices of quality of regression models and variables (cf. Statistical analysis)	–
Cut	Parameter describing the annual ring curvature within the cross section of specimens (cf. Figure 1)	–
DBH	Stem diameter on bark at breast height, i.e. 1.3 m	m
E	Secant modulus of elasticity due to pure bending = σ/ε_E	MPa
ε; ε_E	Apparent bending strain (simply "bending strain"); ε without the contribution from shear deformation	–
ε_{el}; ε_{MOR}; ε_{max}	ε as σ reaches 0.4MOR (defined limit of elasticity); reaches MOR; and returns to 0.5 Mpa	–
$\varepsilon_{el\text{-}pl}$, $\alpha_{el\text{-}pl}$	The ideal elastic-ideal plastic $\sigma(\varepsilon)$-curve has a break point at $\varepsilon = \varepsilon_{el\text{-}pl}$ and $\sigma = \alpha_{el\text{-}pl}$MOR	–
F; F_{max}	Applied force when testing bending specimens; maximum applied F	N
G	Shear modulus in the z-direction, i.e. along fibers	MPa
H	Total tree height	m
η	Completeness of the material in bending (cf. Equation 3)	–
L, b, h; L_F	Length, width and height of the bending specimen; distance between support and force application	mm
LW	Late wood portion = width of late wood/RW	–
MOE; $MOE_{section}$	Modulus of elasticity = the secant modulus of $\sigma(\varepsilon)$ as 0.4MOR is reached; MOE of stem section	GPa
MOR; $MOR_{section}$	Modulus of rupture = maximum value of $\sigma(\varepsilon)$; MOR of stem section	MPa
$\int \sigma(\varepsilon) d\varepsilon$	Integration of $\sigma(\varepsilon)$ up to MOR, i.e. area under $\sigma(\varepsilon)$-curve	MPa
Q, Q_t, Q_c	Knottiness of the specimen cross-section, on the tension (t) and on the compression (c) side	–
r	The radial coordinate of the stem section, ranging from pith to bark	mm
$\rho 0$, ρU	Density of oven-dry and of fresh wood	kg m^{-3}
RW	Annual ring width	mm
σ	Bending stress	MPa
s; s_{MOR}	Mid-span deflection when testing bending specimens; s at MOR	mm
S; IH	Sapwood; inner heartwood	–
SE; R^2; P	Standard error; R-squared value of a regression; P-value of significance	–

Table A1 Con't. List of symbols and notations and their definitions and units used in the study.

Symbol/Notation	Description	Unit
τ, τ_{max}	Shear stress and resistance in the z-direction	MPa
u	Wood water content = mass of water/oven-dry mass	%
V	Volume of bending specimen within the bending span	m^3
W, W_{MOR}, W_{tot}	Work absorbed in bending, at MOR and at ε_{max}	N m
x, z	Cartesian coordinates of the standing tree stem: z is the height above stem base and $x = 0$ in the pith	mm, m
X; Y	Explanatory variable; response variable	–
z_{rel}	Relative height above stem base = z/H	–

Chapter IV

Fresh-stem bending of silver fir and Norway spruce

Tree Physiology 28, 355–366

Fresh-stem bending of silver fir and Norway spruce

TOR LUNDSTRÖM,[1–3] MARKUS STOFFEL[2] and VERONIKA STÖCKLI[1]

[1] *WSL, Swiss Federal Institute for Snow and Avalanche Research SLF, 7260 Davos Dorf, Switzerland*

[2] *Laboratory of Dendrogeomorphology, University of Fribourg, 1700 Fribourg, Switzerland*

[3] *Corresponding author (t.lundstroem@slf.ch)*

Received May 15, 2007; accepted July 24, 2007; published online January 2, 2008

Summary The bending and growth characteristics of large fresh stems from four silver fir (*Abies alba* Mill.) and three Norway spruce (*Picea abies* (L.) Karst.) trees were studied. Twenty logs taken from different stem heights were subjected to four-point bending tests. From the bending test records, we calculated stress–strain curves, which accounted for detailed log taper, shear deformation and self weight. From these curves we determined, among other parameters, the modulus of elasticity (MOE), the modulus of rupture (MOR) and the work absorbed in bending (W). No significant differences were found between species for the wood properties examined. Values of MOE, MOR and W generally decreased with stem height, with MOR in the range of 43 to 59 MPa and MOE ranging from 10.6 to 15.6 GPa. These MOE values are twice or more those reported for stems of young Sitka spruce (*Picea sitchensis* (Bong.) Carr.) trees. Based on the radial growth properties measured in discs from the logs, we calculated predicted values of MOE and MOR for the stem cross section. The predictions of MOE were precise, whereas those of MOR were approximate because of a complex combination of different failure mechanisms. Methods to test and calculate MOE, MOR and W for the stems of living trees are discussed with the aim of improving analyses of tree biomechanics and assessments of forest stability protection.

Keywords: Abies alba, energy absorption, experiment, fresh wood, model validation, nonlinear behavior, Picea abies.

Introduction

Stem bending is an important factor determining tree stability. It occurs as a tree interacts with wind or is subjected to rock impacts or avalanches. The mechanical processes involved during bending and failure of tree stems remain, however, largely unexplored.

Bending stress as a function of bending strain describes how a material behaves while bending, and this function includes several important bending characteristics. For example, the modulus of rupture (MOR) is the maximum value of bending stress, the modulus of elasticity (MOE) represents the secant-modulus of the stress–strain curve, and the work absorbed in bending (W) is proportional to the area under the stress–strain curve. How a stem bends thus depends on its geometry and mechanical properties, which in turn are influenced by radial stem growth processes reflected in annual ring width and knottiness.

The effects of stem growth on the bending properties of dry and sawn wood have been well established by the wood and timber industry. In contrast, how growth affects the mechanical properties of fresh wood, especially of intact tree stems, is less well known (Lundström et al. 2007). The structure of wood in the stem is anisotropic and heterogeneous, with variation in stiffness and strength properties (Trendelenburg and Mayer-Wegelin 1955, Green et al. 1999). Because lumber is sawn in such a way as to minimize heterogeneity in mechanical properties within a piece, we can expect a more complex distribution of stresses during the bending of an entire fresh stem than of dry and sawn wood, and thus different bending stress–strain behaviors. Tests of fresh logs of young Sitka spruce (*Picea sitchensis* (Bong.) Carr.) growing in plantations in Scotland (Cannell and Morgan 1987) with an MOE of about 8 GPa show that cambial age positively influences the cross-sectional MOE. For intact stems of older trees, however, there seems to be no information on MOE or on stem bending in general.

Differences among Norway spruce (*Picea abies* (L.) Karst.) and silver fir (*Abies alba* Mill.) in mechanical bending properties of dry timber are related to growth patterns, not species (Trendelenburg and Mayer-Wegelin 1955, Kucera and Gfeller 1994). To assess possible differences in mechanical properties between these species, data are required on the properties of radial growth that have a significant influence on tested mechanical values.

When tree stems in nature are subject to bending, they react with a combination of mechanisms and modes of failure (e.g., Mattheck and Breloer 1994). Diverse behavior makes it difficult to predict the consequences of stem bending. In static bending tests in the laboratory, shearing or torsion can be limited or accounted for. The shear strain can be calculated (e.g., Newlin and Trayer 1956) and the torsion avoided by selecting straight and round test logs. Independently of how the bending properties of intact stems are tested, a detailed description of stem taper under bark is required, because the determination of MOE, MOR and W depends on measured woody stem diame-

ter in the fourth, third and second power, respectively. It is difficult to predict these properties, because little is known about how the cross-sectional bending stress develops with increasing strain, even for dry and clear wood (Adjanohoun et al. 1998, Dinwoodie 2000).

To assess how mature fresh stems bend and to relate this bending to properties of radial growth, we carried out static, four-point bending tests on 20 logs of silver fir and Norway spruce taken from different stem heights and analyzed radial growth in the laboratory. We present novel data relating to the bending stress–strain of the stem and results from performance tests of models that predict stem bending based on properties of radial stem growth.

Materials and methods

Trees and logs

The stems analyzed for their bending and cross-sectional growth were cut from three large Norway spruce (*P. abies*) and four large silver fir (*A. alba*) trees. These trees grew in a mixed, single-story forest stand of Norway spruce, silver fir, Scots pine (*Pinus sylvestris* L.) and common beech (*Fagus sylvatica* L.) on nearly flat ground. The stand is located on the Swiss Plateau (47°14′ N, 8°53′ W, 460 m a.s.l.) and was previously studied by Lundström et al. (2007). The seven test trees were codominant or dominant in relation to their neighboring trees, straight in stature and apparently healthy. Their bark thickness at breast height relative to the woody stem radius at this height was 6 ± 1%. Further tree data are given in Table 1. Symbols used in this paper are summarized in Table A1.

The trees were felled in mid-November. Before the stems were transported to the laboratory, the stem base was removed to minimize taper, and the upper crown was removed to avoid irregular stem growth due to branching. In the laboratory, the stems were cut into two, three or four sections, depending on the total stem length, resulting in 11 silver fir and nine Norway spruce logs. We measured log length, log diameter at five points along the log axis and mean bark thickness at both ends. Cross sections of the logs were almost perfectly circular. The 20 logs originated from stem heights of between 1.0 and 26.8 m (Table 2).

Table 1. Properties of the four silver fir (*Abies alba*) and three Norway spruce (*Picea abies*) trees subjected to bending tests: AGE = cambial age measured at 1.3 m stem height; H = total tree height; DBH = diameter at breast height; S = slenderness = H/DBH; and L_{cr} = crown length, measured from lowest green branches to top of tree.

Tree	AGE (years)	H (m)	DBH (mm)	S	L_{cr}/H
Silver fir					
1	80	35.0	410	85	0.42
2	75	31.0	400	78	0.40
3	105	33.0	440	75	0.42
4	95	31.5	420	75	0.42
Norway spruce					
5	100	35.0	420	83	0.43
6	80	37.0	415	89	0.43
7	100	31.5	420	75	0.35

Bending tests

One week passed between tree falling and log testing, during which time the stems were kept outside in the shade, fully supported on the ground, to prevent loss of humidity. The fresh logs were subjected to four-point bending tests according to the German industry code, DIN 52186 (DIN 1992), with an exception made for their higher water content. The test geometry followed the European code EN 408 (CEN 2003), with a total span of 5.92 m for logs from Stem heights 1 and 2 (Table 2) and 4.80 m for logs from Stem heights 3 and 4, and a distance between the two symmetrically applied forces of 2.15 and 1.42 m, respectively. The test equipment comprised Parker Hannifin hydraulic cylinders 8201-5500-H021A (HYDREL, Romanshorn, Switzerland) and displacement sensors TK-100-E-2 (PRECISOR Messtechnik, Munich, Germany), and data were acquired at 1 Hz with a Darwin DA 100 (YOKOGAWA Electric, Tokyo, Japan) controller. To avoid local de-

Table 2. Dimensions and height positions of Logs 1–4 of each silver fir (*Abies alba*) and Norway spruce (*Picea abies*) test tree: L_{tot} = total log length; D_c = log diameter at its center; and z_c/H = height of log center relative to total tree height. Log numbers 1–4 are found at Stem heights 1–4, respectively, which refer to ranges of z_c/H.

Tree	Log 1			Log 2			Log 3			Log 4		
	L_{tot} (m)	D_c (mm)	z_c/H	L_{tot} (m)	D_c (mm)	z_c/H	L_{tot} (m)	D_c (mm)	z_c/H	L_{tot} (m)	D_c (mm)	z_c/H
Silver fir												
1	6.85	319	0.19	6.96	288	0.41	5.55	254	0.56	–	–	–
2	6.96	322	0.14	6.90	282	0.40	5.55	242	0.57	–	–	–
3	6.89	353	0.15	7.08	319	0.38	5.57	279	0.54	–	–	–
4	6.15	320	0.26	6.12	273	0.50	–	–	–	–	–	–
Norway spruce												
5	6.45	340	0.13	7.08	307	0.34	5.60	276	0.49	–	–	–
6	6.92	332	0.16	6.95	295	0.37	5.45	254	0.53	5.50	217	0.65
7	6.94	334	0.16	6.96	285	0.38	–	–	–	–	–	–

formation and concentration of stresses perpendicular to the wood grain, each log was placed on a 250-mm-thick, cylindrically sawn veneer board positioned on an articulated joint on each support. For the same reason, both points of load application were provided with cylindrical "gloves" and additional rubber inlays. The load was applied at a constant deflection rate, so that the maximum force was obtained within 120 ± 30 s. The tests were then continued until the logs failed. The load records could be followed until the load returned close to zero. In contrast, the stem deflection could not be recorded (only visually estimated) until the log fell apart, because of the restricted measuring range of the displacement sensors. However, this has no practical implications for the parameters that are the focus of this study.

Growth properties of log cross sections

After the bending tests, 150-mm-long cross sections were cut close to the failure zone of the logs and annual ring width (RW) and knottiness (Q) from pith to bark were measured with a caliper (Figure 1). Based on SIA (2003), we defined Q at the radius from the pith (r) as an eighth of the summed surface area of knots (A_{knots}) intersecting with the 150-mm-long cylinder:

$$Q(r) = \tfrac{1}{8} A_{knots} \in \underbrace{\int_{z-75}^{z+75} \int_{\phi=0}^{2\pi} r\,\phi\, d\phi\, dz}_{\text{cylinder}} \quad (1)$$

where ϕ is the rotation around the z-axis and z is in mm. For comparison, the frequently used knot area ratio (KAR; SIA 2003) applied to our logs approximately equals the mean of $Q(0 \le r \le D_0/2)$, where D_0 is stem diameter under bark. The woody stem discs were weighed to determine disc density.

Water content (u) was not measured in the radial direction and only coarsely in the longitudinal direction (one stem disc per log). We therefore adopted the same distribution for u in the relative radial and longitudinal directions as for the Norway spruce stem growing in the same stand studied by Lundström et al. (2007), and verified that this assumption was correct based on measured disc density. The sapwood and heartwood extensions (Figure 1), which are used only as an approximate description of the radial positions, were estimated on the basis of RW(r) and the RW(r) and $u(r)$ measurements by Lundström et al. (2007). Bark density at testing was an estimated 600 kg m^{-3} (USDA 1972, Schmidt-Vogt 1991).

Analysis

In the analysis of mechanics, we refer to tree coordinates z and x, where z is along the stem with $z = 0$ at the stem base of the standing tree and x is in the direction of deflection with $x = 0$ at the stem center. We also refer to some calculation algorithms that are included in the Matlab 7.0 (MathWorks) software package.

When analyzing the bending behavior of logs, we accounted for log taper, self weight and deflection due to shear forces. The taper of each stem (Table 2) was first given a continuous description with a polynomial fit $D(z)$ based on the diameters measured along the stem. Each fit was then reduced for bark thickness $b(z)$, i.e., $D_0(z) = D(z) - 2b(z)$, where $b(z)$ is a polynomial based on relative bark thickness at breast height, as described by Laasasenaho et al. (2005), which was verified with the bark measurements at each log end.

The bending properties of the logs were characterized based on curves of bending stress (σ) as a function of the bending strain (ε), from zero load to failure. To obtain the $\sigma(\varepsilon)$ curves, we followed seven calculation steps (Table 3) and used two equations (Equations 2 and 3):

$$\begin{aligned} \sigma &= \sigma_F + \sigma_g \\ \sigma_F &= \frac{F D_{0c}}{8 I_{0c}}(L - L_F); \qquad I_{0c} = \tfrac{1}{64}\pi D_{0c}^{\,4} \\ \sigma_g &= \frac{m g D_{0c} L}{16 I_{0c}}; \qquad m = \rho_w V_0 + \rho_b V_b \end{aligned} \quad (2)$$

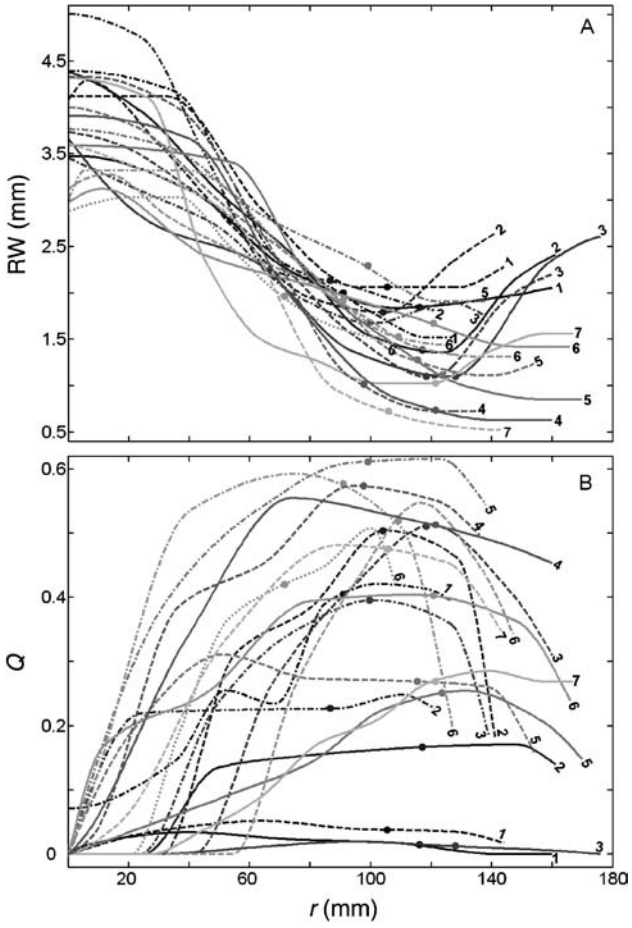

Figure 1. (A) Annual ring width (RW) and (B) knottiness (Q) as functions of radial distance from the pith (r) of logs from silver fir (*Abies alba*) and Norway spruce (*Picea abies*) trees. Each log is identified by tree number (1–7) and linetype: solid = Log 1; dashed = Log 2; dash-dotted = Log 3; and dotted = Log 4. Filled circles indicate approximate locations of heartwood–sapwood borders.

Table 3. Successive steps in analyzing the properties of the bending mechanics of tested logs.

Step	Description
1	Calculation of bending stress (σ; Equation 2), including contributions from applied force and log weight. Maximum σ, independent of type of failure, corresponds to MOR.
2	Calculation of the elasticity in bending E_F (Equation 3; DIN 52 186) due to the applied force F, accounting for shear deformation and detailed log taper.
3	Combination of Steps 1 and 2 into the bending strain $\varepsilon_F = \sigma_F/E_F$ and $E_F(\varepsilon_F)$. As E_F is elasticity in bending corrected for shear deformation, ε_F is bending strain as it would be under pure bending conditions.
4	Calculation of bending strain due to weight of the log: $\varepsilon_g = \sigma_g/E_{0.4F_{max}}$, where $E_{0.4F_{max}}$ is E_F at 40% of maximum F.
5	Concatenation of $(\varepsilon,\sigma) = (0,0)$, (ε_g,σ_g) and (ε_F,σ_F), into the array $\sigma(\varepsilon_E)$, where $E(\varepsilon_E)$ is the corresponding elasticity in pure bending.
6	Definition of MOE as $E(\varepsilon_E)_{0.4MOR}$, i.e., the gradient of the straight line between $\sigma(\varepsilon_E) = 0$ and $\sigma(\varepsilon_E) = 0.4MOR$, and in addition, as $E(\varepsilon_E)_{LIN}$, the gradient for the visually estimated first linear part of $\sigma(\varepsilon_E)$.
7	Computation of $\sigma(\varepsilon)$, where ε is apparent strain, from $\varepsilon = 0$ until the end of the test, with no correction for shear deformation (ε is slightly greater than ε_E). Apart from the analysis of MOE (Step 6), $\sigma(\varepsilon)$ is used throughout the study.

where σ_F is bending stress due to the applied force (F), σ_g is bending stress due to the weight of the log (mg), subscript c refers to the center of the log, I_{0c} is moment of inertia about the log center excluding bark, L is log span (distance between the two supports), L_F is the distance between the two points of load application, m is mass of the log within the span reduced for overhang at the two log ends, g is earth gravity, ρ_w and ρ_b are the bulk densities of fresh wood and bark, respectively, and V is total volume within the span reduced for overhang of the two log ends; and:

$$\begin{aligned} E_F &= \frac{F}{s}\left(\frac{C_1}{48 I_{0c}} + C_2\right) \\ C_1 &= \tfrac{1}{2}(2L^3 - 3L{L_F}^2 - {L_F}^3) \\ C_2 &= \beta\left(\frac{E(z)}{G(z)}\right)' \frac{L}{A_0(1+\tfrac{1}{2}KL)} \end{aligned} \tag{3}$$

where E_F is explained in Table 3, C_1 is a length factor, C_2 is a correction factor for shear deformation and measured difference in diameter under bark (0) between the thin end (1) and the thick end (2) of the log at the supports, with $KL = (D_{02} - D_{01})/D_{01}$ (Cannell and Morgan 1987), β is a load coefficient, which equals 16/81 in four-point bending (Newlin and Trayer 1956), and $(E(z)/G(z))'$ is an estimated ($'$) relationship between the elasticity in bending E and shear G along the grain of the cross section. This relationship depends primarily on the value of E/G at the stem heights where the largest bending strain (in the outermost stem) and shearing strain (in the stem center) occur. Both E and G of fresh wood are correlated with RW (Kollmann 1968, Lundström et al. 2007). For the stems tested, RW in the outermost stem decreased with z, but RW in the stem center remained nearly constant with z, suggesting $(E(z)/G(z))'$ decreases with z. We therefore estimated $G(z)$ in the heartwood and $E(z)$ in the sapwood on the basis of $RW(x,z)$ and adopted $(E(z)/G(z))' = 25 - 0.07z/H$ for all the logs. The contribution of bark to the bending resistance of the log was ignored, because both the shear resistance of the bark-to-wood layer and the shear and bending strength of bark are much lower than the corresponding values of the underlying wood for hardwood species (Einspahr et al. 1984). We believe that these orders of magnitude apply to the softwood species tested. To explore the influence of differences in diameter at the thin and thick log ends and of shear deformation on the calculated MOE values (cf. Table 3), E_F was calculated by setting K and C_2, respectively (Equation 3), equal to zero.

Idealized stress–strain curves were calculated for each bending test, and characteristic bending stress–strain curves were established for the lowest three logs. "Idealized" as used here means that the stress–strain curve includes one ideal elastic and one ideal plastic deformation, and "characteristic" refers to the mean stress–strain curve of the group according to height or species. For details on the calculation methods, see Lundström et al. (2007).

Shear stress as a function of radial distance from the pith and position along the log ($\tau(x,z)$) was calculated as:

$$\tau(x,z) = \frac{4T(z)}{3A_0(z)}\sqrt{1-\left(\frac{x}{\frac{1}{2}D_0(z)}\right)^2} \tag{4}$$

where $T = dM/dz$ is the transverse force along the log (commonly called the shear force), occasioned by the applied forces and the weight of the log, A_0 is the cross-sectional area of the log and $0 < x < D_0/2$. This equation is a simplification, because it assumes the shearing elasticity (G) is constant across the log section. The shear strength ($\tau_{max}(x,z)$; Equation 5) was estimated according to Kollmann (1968) and Dinwoodie (2000) on the basis of the dry wood density ($\rho_0(x,z)$; Equation 6) calculated according to Lundström et al. (2007):

$$\tau_{max}(x,z) = a_1\rho_0(x,z) + a_2 \tag{5}$$

$$\rho_0(x,z) = a_1\log\big(\mathrm{RW}(x,z)\big) + a_2 \tag{6}$$

where $\vec{a} = [0.019\ \ -4.9]$ in Equation 5 and $\vec{a} = [543\ \ -106]$ in Equation 6.

The work absorbed by the logs in bending up to MOR (W_{MOR}) was calculated from the load-deflection curve $F(s)$ as:

$$W_{\mathrm{MOR}} = \tfrac{1}{2} F_g s_g + \int_{s_g}^{s_{\mathrm{MOR}}} F(s)\, ds; \qquad F_g = \tfrac{5}{8} mg \tag{7}$$

where s_g is the initial deflection at mid-span due to the linear load caused by the log weight, s_{MOR} is the total deflection at mid-span at MOR and F_g is the concentrated (fictive) force that causes the same deflection as the log weight. Here, s_g is calculated using MOE.

The numerical values of W_{MOR} were first compared among the logs by dividing their W_{MOR} by the woody volume of the log within the bending span (V_0). General comparisons of W_{MOR} or W_{MOR}/V_0 obtained by this method assume normalized test set-ups, e.g., three-point bending of a beam of a square section according to DIN (1992). Because this was not the case, we: (1) define work as the integral of the stress–strain curve of the tested section, $\int \sigma(\varepsilon)\, d\varepsilon$; and (2) calculate work absorbed by a bent member based on $\int \sigma(\varepsilon)\, d\varepsilon$ according to the methods in the Appendix. The results for W_{MOR} from Equation 7 and from (2) were compared. The work-related material-property completeness (η) was also calculated from the $F(s)$-curve:

$$\eta = \frac{W_{F_{\max}}}{(F_g + F_{\max}) s_{F_{\max}}} \tag{8}$$

where $F_{\max}$ is the maximum applied force, $W_{F_{\max}}$ is the work absorbed by logs in bending due to $F_{\max}$, $s_{F_{\max}}$ is the mid-span deflection due to $F_{\max}$, and $\eta = 1.0$ and 0.5 characterize materials with ideal-plastic and ideal-elastic stress–strain behaviors, respectively.

Experimental values of MOE and MOR of the mid-span cross sections were compared with the calculated predicted values, as proposed by Lundström et al. (2007). These calculated values are obtained in two steps.

In Step 1, reference is made to one cylindrical shell of the cross section in the log mid-span, located at stem height z (cf. Table 2) and at radial position j, where j ranges from pith ($j = 1$) to bark ($j = n$) every 1 mm. The measured data of radial growth are first interpolated radially every mm and then attributed to this shell, of which $\mathrm{MOE}(z)_j$ and $\mathrm{MOR}(z)_j$ are computed as regressions:

$$\mathrm{MOE}(z)_j = a_1 \log\left(\mathrm{RW}(z)_j\right) + a_2 u(z)_j + a_3 \tag{9}$$

$$\mathrm{MOR}(z)_j = a_1 \log\left(\mathrm{RW}(z)_j\right) + a_2 Q(z)_j^2 + a_3 \tag{10}$$

where $\bar{a}$ = [–5860 –25.0 15100] in Equation 9 and $\bar{a}$ = [–17.3 –36.0 66.4] in Equation 10. The standardized regression coefficients, which indicate the impact of each explanatory variable on the response variable, are $\bar{\boldsymbol{a}}$ = [–1.61 –0.49] and $\bar{\boldsymbol{a}}$ = [–1.78 –0.24], respectively, where, for example, $\boldsymbol{a}_2 = a_2 \mathrm{SE}(u)/\mathrm{SE}(\mathrm{MOE})$ for the regression coefficient of u in Equation 9.

In Step 2, values of $\mathrm{MOE}(z)_j$ and $\mathrm{MOR}(z)_j$ obtained in Step 1 are superposed radially, cylindrical shell by shell (j) to form the log section. For MOE, this is described as:

$$\mathrm{MOE}(z)_{\mathrm{sect}} = \frac{\gamma_{\mathrm{MOE}}}{x_n(z)^4} \sum_{j=1}^{n} \mathrm{MOE}(z)_j \left(x(z)_{j+1}^4 - x(z)_j^4\right) \tag{11}$$

where subscript "sect" is used to distinguish from subscript "j", the value of each shell and $x = r$, because of the circular log shape. The calculation of $\mathrm{MOR}_{\mathrm{sect}}$ assumes, in principle, that we know the distribution of bending stress across the stem section, $\sigma(x)$, when $\mathrm{MOR}_{\mathrm{sect}}$ is reached. In the absence of this information, and based on $\sigma(x)$ of dry timber as its cross section reaches MOR (Kollmann 1968), we use two approaches (linear strain method and scaled MOR method) to calculate $\mathrm{MOR}_{\mathrm{sect}}$. The linear strain method applies a linear increase in ε from pith to bark, with a gradient governed by ε at MOR for the cylindrical shell at a radial distance of $\kappa_1 x_n$, where κ_1 is a factor between 0 and 1:

$$\mathrm{MOR}(z)_{\mathrm{sect}} = \frac{\gamma_{\mathrm{MOR},1}}{x_n(z)^3} \sum_{j=1}^{n} \sigma(\varepsilon, x(z), \kappa_1)_j \left(x(z)_{j+1}^3 - x(z)_j^3\right) \tag{12}$$

In our study, $\sigma(\varepsilon,x)$ in Equation 12 is the the average curve for Norway spruce and silver fir. The scaled MOR method simply applies a scaling of MOR:

$$\mathrm{MOR}(z)_{\mathrm{sect}} = \frac{\gamma_{\mathrm{MOR},2}}{x_n(z)^3} \sum_{j=1}^{n} \mathrm{MOR}(z,x)_j B(\kappa_2) \left(x(z)_{j+1}^3 - x(z)_j^3\right) \tag{13}$$

where $B(\kappa_2)$ is the degree of exploitation of MOR_j, represented as an array of n elements that increases from 0 to 1 between $x = 0$ and $x = \kappa_2 x_n$ and then remains constant, at a value of 1, between $x = \kappa_2 x_n$ and x_n. Parameters κ_1 and κ_2 thus govern the degree of plasticity of the outer part of the woody stem section.

In applying Equations 11–13 as linear regression models versus the experimental data for MOR and MOE for all the logs, the best fits yielded the values of parameters γ_{MOE}, $\gamma_{\mathrm{MOR},1}$, $\gamma_{\mathrm{MOR},2}$, κ_1 and κ_2. The regression coefficients of Equations 9 and 10 were checked, except for a_2 in Equation 9, by fitting them with the measured RW(r), $Q(r)$, MOE and MOR of the 20 logs in unconstrained nonlinear optimization (Matlab) and setting all $\gamma = 1.0$. The significance of the new coefficients was verified with the S-Plus 2000 software program (Insightful, Seattle, WA).

Results

Failure mechanisms and stress–strain curve characteristics

Bending failure usually began with buckling of the outermost wood fibers on the compression side of the log, followed by the outermost wood fibers on the tension side tearing apart (Table 4). The logs from the lower part of the Norway spruce trees, however, broke suddenly in the outer heartwood as a result of longitudinal shearing. For the three logs that did not fail

completely, i.e., fall apart, the applied force remained almost constant between half and maximum deflection, ending with a slight decrease.

The curves of bending stress–strain of the 20 logs were similar, with a quasi ideal-elastic first part to about two-thirds of MOR, from where the deformation increased significantly (Figure 2A). Close examination showed that both MOE and MOR generally decreased with stem height (Figures 2B and 3). Norway spruce logs were slightly stiffer but slightly weaker than silver fir logs (Figure 2C, Table 5). A comparison of the shapes of individual stress–strain curves (Figure 2A) and the types of failure (Table 4) revealed no obvious pattern. When MOE was defined as the first linear part of the stress–strain curve ($E(\varepsilon_E)_{LIN}$) instead of as 0.4MOR ($E(\varepsilon_E)_{0.4MOR}$), MOE was overestimated by 2.2%, on average, but the difference varied between 14% and −9.5%. When MOR was reached, the calculated shear stress $\tau(z,x)$ (Equation 4) was well below the estimated shear strength $\tau_{max}(z,x)$ (Equations 5 and 6) in the outer heartwood (Figure 4). Their ratio $\tau(z,x)/\tau_{max}(z,x)$ was highest in the pith at the thinner end of the log. Higher maximum ratios were generally found for logs from the lower part of the stem (e.g., 0.74 for Log 1 of Tree 7) than from the higher part of the stem (e.g., 0.34 for Log 4 of Tree 6). There was a trend of increasing MOR with increasing MOE, but the correlation was weak ($R = 0.30$).

The idealized stress–strain curves (example in Figure 2C) and η (cf. Equation 8) display some general tendencies. Averaged per tree height, mean $\varepsilon_{el\text{-}pl}$ and mean ε_{MOR} were 10% higher for silver fir than for Norway spruce, whereas mean $\alpha_{el\text{-}pl}$ and mean η differed by less than 1% between species. These variables increased with tree height, except for $\varepsilon_{el\text{-}pl}$, which remained nearly constant. Further, $\alpha_{el\text{-}pl}$ was equal to $0.28\eta + 0.73$ ($R^2 = 0.75$) for all logs combined. Although differences in mean values of the bending parameters were found between silver fir and Norway spruce, and according to stem height, none were significant (Table 6).

Table 4. Subsequent failure mechanisms (separated by a slash) observed during bending tests of 20 logs of silver fir (*Abies alba*) and Norway spruce (*Picea abies*). Failure mechanisms: c = wood fibers buckling on the compression side of the log; t = wood fibers tearing apart on the tension side; and s = longitudinal-cylindrical shearing. Listed are the clearly visible and significant mechanisms (naturally, the s-mechanism initiates within a brief moment of c- and t-failure).

Tree	Log 1	Log 2	Log 3	Log 4
Silver fir				
1	c[1]	t	c[1]	–
2	c / t	c / t	c / t	–
3	c / t	c / t	c / t	–
4	c / t	c[1]	–	–
Norway spruce				
5	s	c / s	c / t	–
6	s	t	c / t	c / t
7	s	c / s	–	–

[1] No complete failure.

The work absorbed by the mid-span of the log, in terms of $\int\sigma(\varepsilon)\,d\varepsilon$, the integral of stress as a function of apparent strain up to MOR, averaged 0.25 N mm^{-2} (min = 0.21, max = 0.30 and SE = 0.02 N mm^{-2}). The W_{MOR} calculated as bending stress integrated over the log volume (cf. Appendix) differed from the actual W_{MOR} absorbed, i.e., Fs. The detailed method (Equations A1, A2 and A4) yielded, on average, 1% smaller W_{MOR}, with relative standard, minimum and maximum errors of 4, −9 and 6%, respectively. Overly low values were calculated for logs from the lower part of the stem, whereas overly high values were calculated for logs originating from the upper part of the stem. The approximate method (Equations A3 and A4) yielded, on average, 4% larger W_{MOR}, with relative standard, minimum and maximum errors of 4, −1 and 15%, re-

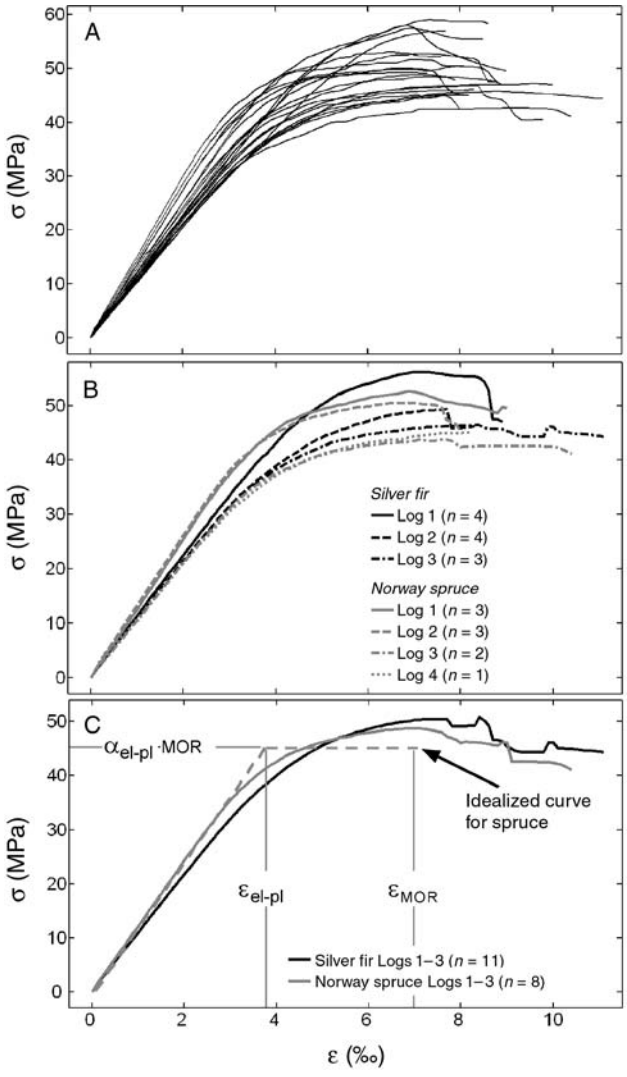

Figure 2. (A) Bending stress (σ) as a function of bending strain (ε) for all 20 logs from silver fir (*Abies alba*) and Norway spruce (*Picea abies*) trees. Mean $\sigma(\varepsilon)$ for logs grouped by (B) height and species and (C) by species. The idealized stress–strain curve in (C) is ideally elastic up to a percentage $\alpha_{el\text{-}pl}$ of the modulus of rupture (MOR), and ideally plastic between $\varepsilon_{el\text{-}pl}$ and ε_{MOR}.

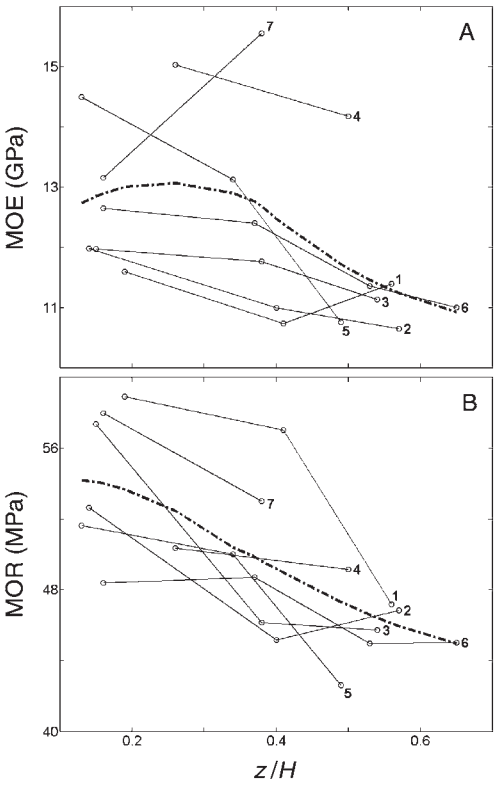

Figure 3. (A) Modulus of elasticity (MOE) and (B) modulus of rupture (MOR) of cross sections from silver fir (*Abies alba*) and Norway spruce (*Picea abies*) Trees 1–7 according to relative tree height = z/H (see Table 5 for numerical data). Dash-dot lines are smoothed averages of all trees (span = 95% of z/H range).

spectively, and a similar, but less clear, error distribution with stem height. When the detailed method was applied to a (fictive) three-point bending test of a beam with a square cross section and the same stress–strain curve data and in-span volume as our logs, W_{MOR}, and thus also W_{MOR}/V_0, were on average 20% smaller than the recorded W_{MOR}. The ratio W_{MOR}/V_0 ranged from 32 to 56, averaging 42 kN m m^{-3} (SE = 5 kN m

Table 5. Bending modulus of rupture (MOR) and modulus of elasticity (MOE) for Logs 1–4 of each silver fir (*Abies alba*) and Norway spruce (*Picea abies*) tree. The MOE is defined at 0.4MOR.

Tree	MOR (MPa)				MOE (GPa)			
	1	2	3	4	1	2	3	4
Silver fir								
1	58.9	57.0	47.2	–	11.6	10.7	11.4	–
2	52.7	45.2	46.9	–	12.0	11.0	10.6	–
3	57.4	46.2	45.8	–	12.0	11.8	11.1	–
Norway spruce								
4	50.4	49.2	–	–	15.0	14.2	–	–
5	51.6	50.0	42.6	–	14.5	13.1	10.8	–
6	48.4	48.7	45.0	45.0	12.6	12.4	11.4	11.0
7	58.0	53.0	–	–	13.2	15.6	–	–

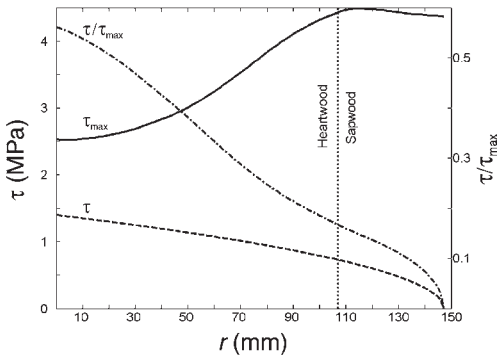

Figure 4. Shear stress (τ), shear resistance (τ_{max}) and their ratio as functions of radial distance from pith (r) in logs of silver fir (*Abies alba*) and Norway spruce (*Picea abies*) trees. Means are shown for all logs as MOR was reached and for the stem cross section where the highest ratios were found (below location of force application at the thinner side of the log). Shear failure occurred in the outer heartwood, i.e., about $60 < r < 100$ mm.

m^{-3}), otherwise expressed as $W_{MOR} = 42V_0$ (W_{MOR} in kN m, V_0 in m^3) ($R^2 = 0.90$).

Influences of analytical method on MOE, MOR and energy absorption

Approximation of the stem taper under bark as a truncated cone between the large- and small-end diameters of a log would yield non-negligible errors in diameter at the center of the log, especially in logs from the stem base where the curvature is strong. For all test trees, these errors were at the most 23, –6, –5 and –7 mm for Logs 1–4, respectively. The truncated cone approximation therefore resulted in relative errors in calculated values of MOE of –23, 8, 8 and 14%, and of MOR of –18, 6, 6 and 10% for Logs 1–4, respectively. The influence of the differences in diameter at the thin and the thick log ends (*KL*) on MOE was, however, low. Because *KL* was low for the tested logs (≤ 0.05), it reduced MOE by less than 0.13%. When shear deflections were considered (Equation 3), MOE increased by 3.3–7.4%. The self weight of the logs contributed, on average, 1.3% to MOR, but naturally did not contribute to MOE, because the addition of self weight does not change the initial slope of the stress–strain curve. The error in energy absorption, in terms of $\int\sigma(\varepsilon)\,d\varepsilon$, was at most –14%, when ignoring the precise stem taper and log weight.

Predictions of MOE and MOR

Because no significant differences in MOE or MOR were found between silver fir and Norway spruce, the prediction models were evaluated for all logs combined. Generally, MOE of the log section was well predicted by the models (Equations 9 and 11), unlike MOR (Equations 10, 12 and 13). The beneficial effect of the intact stem compared with separate cylindrical shells amounted to 6% for MOE. For MOR, this effect amounted to 0% when calculated with the linear strain method, and 9% when calculated with the scaled MOR method. The corresponding regression coefficients were

Table 6. Characteristics of the bending stress–strain and load-deflection curves for Logs 1–4 of each silver fir (*Abies alba*) and Norway spruce (*Picea abies*) tree. Abbreviations: ε_{el}, strain at 0.4MOR; $\varepsilon_{el\text{-}pl}$, strain at the break point between ideal elastic and ideal plastic bending; ε_{MOR}, strain at maximum load; $\alpha_{el\text{-}pl}$, proportion of MOR at plasticity; η, completeness of the material in bending (Equation 8); and MOR, modulus of rupture.

Tree	ε_{el} (‰)				$\varepsilon_{el\text{-}pl}$ (‰)				ε_{MOR} (‰)				$\alpha_{el\text{-}pl}$ (%)				η (%)			
	1	2	3	4	1	2	3	4	1	2	3	4	1	2	3	4	1	2	3	4
Silver fir																				
1	2.0	2.1	1.7	–	4.6	4.8	3.9	–	7.0	7.4	9.2	–	90	90	95	–	61	62	75	–
2	1.8	1.6	1.8	–	4.0	3.8	4.1	–	6.7	7.4	8.1	–	92	92	93	–	65	69	70	–
3	1.9	1.6	1.6	–	4.4	3.7	3.8	–	6.5	7.9	8.4	–	91	95	92	–	61	73	72	–
4	1.3	1.4	–	–	3.2	3.3	–	–	7.5	6.2	–	–	94	94	–	–	75	70	–	–
Norway spruce																				
5	1.4	1.5	1.6	–	3.3	3.6	3.7	–	6.6	6.6	8.5	–	92	94	94	–	71	69	74	–
6	1.5	1.6	1.6	1.6	3.5	3.6	3.7	3.7	6.9	6.6	6.6	7.9	92	92	92	92	69	68	68	71
7	1.8	1.4	–	–	4.0	3.2	–	–	6.5	6.3	–	–	91	92	–	–	64	70	–	–

$\gamma_{MOE} = 1.06$ ($R^2 = 0.93$, SE(MOE) = 0.16 GPa; cf. Equation 11), $\gamma_{MOR,1} = 1.00$ and $\kappa_1 = 0.90$ ($R^2 = 0.39$, SE(MOR) = 4.2 MPa; cf. Equation 12), and $\gamma_{MOR,2} = 1.09$ and $\kappa_2 = 0.85$ ($R^2 = 0.26$, SE(MOR) = 4.6 MPa; cf. Equation 13). When the measured cross-sectional modules were refitted with the measured RW(r) and $Q(r)$, we obtained the following statistical data for MOE: $\bar{a}$ = [–4098 –22.3 15749], $\bar{\boldsymbol{a}}$ = [–0.49 –0.25], R^2 = 0.95, SE(MOE) = 0.11 GPa; and for MOR: $\bar{a}$ = [–6.88 –45.2 68.2], $\bar{\boldsymbol{a}}$ = [–0.26 –0.89], $R^2 = 0.64$, SE(MOR) = 2.9 MPa, when using the scaled MOR method, $\gamma_{MOR,2} = 1.0$, and κ_2 = 0.85; and $\bar{\boldsymbol{a}}$ = [–0.35 –0.79], $R^2 = 0.64$, when refitting with the linear strain method, $\gamma_{MOR,1} = 1.00$, and $\kappa_1 = 0.90$. All $\bar{a}$ coefficients were highly significant ($P < 0.005$) except a_1 of MOR (P = 0.01). The initial and refitted regression models of MOE were similar, but measured MOR was more strongly influenced by $Q(r)$ than was predicted by Equation 9.

The predictions demonstrate a change in cross-sectional MOE with stem size and cambial age (Figures 5A and 5B): from a younger (0–25 years) to an older (> 60 years) stage, MOE increases by up to 60% for individual sections and by 35% on average. This trend is also apparent for MOR(z,r) predicted with the initial regression model but is less clear for the refitted model (Figure 5C). For both models, this increasing trend in MOR(z,r) with radius, was stronger in the lower stem. In the higher part, it was nonexistent for the initial model and slightly negative for the refitted model. Figure 5, which includes all logs and thus all stem heights admixed, shows that differences in MOE(z,r) and MOR(z,r) were greater among trees at the same height than among stem heights.

Discussion

Failure mechanisms and stress–strain curve characteristics

Fifteen of the 20 logs tested failed in the same way as sawn wood. The remaining five logs, from the lower part of Norway spruce trees broke because of longitudinal shearing apparently in the outer heartwood. The reasons for this difference in mode of breakage are unclear. The calculated maximum shear stresses were well below the estimated shear strengths (Figure 4). We postulate that there were local unobserved differences in radial growth properties, implying that local, strong radial gradients in strength and stiffness initiate slip along the grain, resulting in shear stresses that exceed the local shear strength. Heartwood fulfills an important function (cf. Stokes et al. 2001) in transmitting forces perpendicular to the stem into stress along the grain in the sapwood, which has a large capacity to absorb such stress. This function may, however, constitute a weak mechanical link, as found in 25% of our tests. It will be challenging to determine under what conditions this transmission function of heartwood is optimized.

We found no literature on the shape of the bending stress–strain curves of fresh tree stems. The curve shapes for the two species studied here were similar. This may have a natural explanation. Both species had similar annual ring widths and knottiness, both of which significantly influence the mechanical properties of bending (cf. Equations 9 and 10). Based on a comparison of the shapes of our bending stress–strain curves with those obtained from square specimens from the fresh heartwood and sapwood of Norway spruce (Lundström et al. 2007), it appears that the strain values are generally about 40% lower for the logs than for square specimens. It is probable that this difference is associated with the greater knottiness of the test logs, but it may also reflect an inherent behavior of the intact stem while bending.

Several important mechanical properties related to bending can be deduced from the stress–strain curves. The cross-sectional MOE values of the 90-year-old dominant and codominant Norway spruce test trees are: 50% higher than those of dominant Norway spruce of half the age at the same relative stem height (Brüchert et al. 2000); 70% higher than those of Sitka spruce of a third the age and with about the same dry stem bulk density (Cannell and Morgan 1987); and two to six times higher than those of 22-year-old Sitka spruce (Milne and Blackburn 1989). It is unlikely that the different methods of assessing stress and strain in the stem are the only reasons for these considerable differences. The stem normally produces stiffer wood at a mature stage, especially in the lower stem,

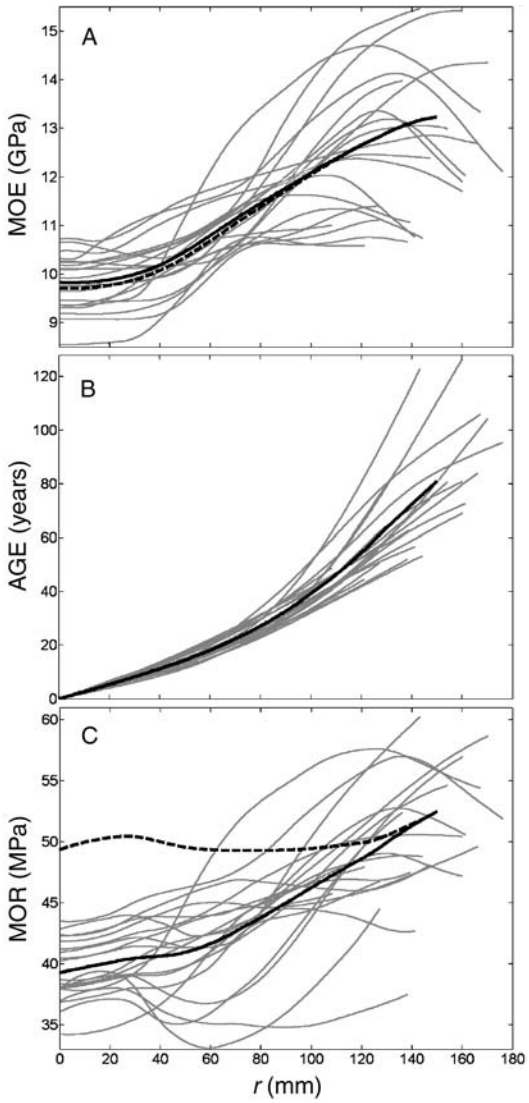

Figure 5. Modeled changes in (A) modulus of elasticity (MOE) and (C) modulus of rupture (MOR) of the cross section, with stem radius (r) and (B) cambial age at 1.3 m stem height (AGE). (A and C) Gray lines show the predicted MOE and MOR for all 20 logs (Equations 9–10 with the initial regression coefficients); solid black lines are means up to $r = 150$ mm, resulting from the initial coefficients; and dashed black lines are means resulting from the refitted coefficients. (B) Gray lines represent individual logs, and the black line is the mean.

which then influences the overall stiffness of the stem (cf. Figures 3A and 5A; Lundström et al. (2007)).

The cross-sectional MOR values can be compared with the mean value of 55 MPa obtained at a stem height of 2.5 m for 73, 100-year-old, Scots pine trees, which had grown more slowly at latitude 61° N in Sweden than our test trees (S. Brüzelius, Rundvirke Poles AB, personal communication). The logs we tested displayed a greater decrease in MOR with tree height (Figure 3B) than found by Lundström et al. (2007). This difference may be associated with a comparatively greater increase in knottiness in the outer part of the stem above a relative tree height of 0.3 among the logs we studied.

There have been few studies on W_{MOR} for fresh intact stems. Expressing W_{MOR} in terms of $\int\sigma(\varepsilon)\,d\varepsilon$ facilitates comparisons of W_{MOR}, because comparisons of W_{MOR} calculated as load times deflection assume an identical geometry of load application and cross section. We found that W_{MOR} was 20% lower in the three-point than in the four-point bending tests, as a result of the smaller stem volume subjected to stress in the former. If $\int\sigma(\varepsilon)\,d\varepsilon$ and bending moment along the log are known, the work effectively absorbed by a log, or any type of member subject to bending, can also be calculated (Equations A1–A4). In our case, W_{MOR} calculated by the detailed $\int\sigma(\varepsilon)\,d\varepsilon$-method (Equations A1, A2 and A4) yielded relatively small errors compared with the work effectively absorbed, i.e., the measured force times deflection. Thus, this method appears useful for estimating work absorbed by a tree stem subject to bending. The errors in calculated W_{MOR} may arise because of differences between the actual (not exactly known) and the assumed: (1) cross-sectional distribution of bending or shearing stress with stem height; and (2) bending moment along the log. The approximate $\int\sigma(\varepsilon)\,d\varepsilon$-method (Equations 16 and 17) also appears useful, although it tends to overestimate the absorbed energy, because the radial difference in MOR is not considered. The mean value of $\int\sigma(\varepsilon)\,d\varepsilon$ up to MOR of the logs (0.25 N mm^{-2}) is lower than the values of 0.40 and 0.61 N mm^{-2} obtained for specimens from the heartwood and sapwood of fresh Norway spruce by Lundström et al. (2007). This difference is due to the compressed stress–strain curves in the strain direction for the logs, as discussed previously. It is clear that intact stems and sawn wood display different behaviors while bending. It is also apparent that the bending properties of living stems largely depend on the growth conditions experienced by the tree. The growth pattern of the Norway spruce and silver fir stems in our study is representative of other sites with similar climatic conditions in and around the Alps (Schweingruber 1996). However, stems of the same species grown under different conditions will exhibit different bending properties to those observed here.

Influences of test and analysis methods

Stem bending stress and strain can be assessed and interpreted in various ways. In laboratory tests, such as four-point, three-point and cantilever bending, curves of bending stress–strain can be obtained for stem sections taken from different tree heights under controlled and close to standardized conditions (DIN 2000, BSI 2001, CEN 2003). A drawback is that the longitudinal growth stresses within the stem of a standing tree (Fourcaud et al. 2003, Huang et al. 2005) are released when the tree is felled. However, these stresses represent only a few percent of the stem bending resistance for Norway spruce and silver fir (Dinwoodie 2000), and the internal growth stresses may, at least theoretically, be superimposed on the bending stress obtained in the laboratory test. The stress– strain of the stem while bending can also be assessed in situ, by pulling the stem of a standing tree sideways (cf. Milne and Blackburn 1989), but it may then be more difficult to precisely assess strains and load application along the stem. For any test used, our investigations show that a precise measurement of stem

taper is especially important. Otherwise errors of more than 20% may arise in the calculated stress–strain and the derived bending properties, making comparisons of results from different investigations less meaningful (cf. Morgan and Cannell 1994). In addition to bending, the stem of a standing tree can occasionally be subject to torsion (e.g., if the crown is asymmetric) and length forces that may impair the bending capacity of the stem. Torsion is, however, rare, and length forces are of low magnitude (Mayer 1985, Amtmann 1986), so neither were considered in this study.

Predictions of cross-sectional MOE and MOR

The method used for predicting MOE appears to be robust. The predictions of MOR were only approximate because of several failure mechanisms that are difficult to predict. The small differences in error between the two methods of predicting MOR (Equations 12 and 13) are irrelevant in the context of the study, but Equation 13 has the advantage of being simpler. The MOR(r) values predicted with the initial and with the refitted regression coefficient differed. Although it is not evident which method best predicts MOR(r), the tested MOR($r = D_0/2$) is predicted better with the refitted version. The method to obtain the regression coefficients of the refitted version statistically weights the RW and Q in the outermost part of the stem cross section heavily. Also, the prediction using the initial regression coefficients is statistically stronger for the mean of MOR(r) than for individual MOR(r)s because of the statistical effect of linear transformation. The increasing trend in this initial mean MOR(r) with radius, and thus with the cambial age, as well as the strong correlations between MOE and MOR for wood in general (Kollmann 1968) suggest that MOR should increase with cambial age, similarly to MOE. For better predictions of cross-sectional MOR, we need to know more about the stem-bending failure mechanisms in trees differing in age and radial stem growth properties.

Acknowledgments

We are indebted to the Board of the Swiss Federal Institutes of Technology for financial support for this work, conducted within the project "Tree Stability and Natural Hazards." We thank the Institute of Structural Engineering at the ETHZ for the use of their laboratory, Hanspeter Arm for his precise experimental work, and Silvia Dingwall for revision of the text.

References

Adjanohoun, G., J.-L. Guillot, J.-D. Lanvin and R. Cholat. 1998. Small roundwood grading by nondestructive x-rays and ultrasonic waves methods. 5th World Conf. on Timber Engineering. Presses Polytechniques et Universitaires Romandes, Lausanne, Switzerland. www.ndt.net/article/v04n11/adjanoh/adjanoh.htm.

Amtmann, R., 1986. Dynamische Windbelastung von Nadelbäumen. Forstl. Forsch. Ber. 74:215.

Brüchert, F., G. Becker and T. Speck. 2000. The mechanics of Norway spruce (*Picea abies* (L.) Karst): mechanical properties of standing trees from different thinning regimes. For. Ecol. Manage. 135:45–62.

BSI. 2001. Timber poles for overhead lines—test methods—determination of modulus of elasticity, bending strength, density and moisture content. BS EN 12509 2001. BSI, London, 14 p.

Cannell, M.G.R. and J. Morgan. 1987. Young's modulus of sections of living branches and tree trunks. Tree Physiol. 3:355–364.

CEN. 2003. EN 408: Timber structures—structural and glued laminated timber—determination of some physical and mechanical properties. Brussels, 12 p.

DIN. 1992. Normen über Holz. Deutsches Institut für Normung. DIN-Taschenbuch Vol. 31. 6th Edn. Beuth, Berlin, Köln, 260 p.

DIN. 2000. Normen über Holz. Deutsches Institut für Normung. DIN-Taschenbuch Vol. 31. 7th Edn. Beuth, Berlin, Köln, 597 p.

Dinwoodie, J.M. 2000. Timber: its nature and behaviour. 2nd Edn. E&FN SPON, London, 257 p.

Einspahr, D.W., R.H. Vaneperen and M.L. Fiscus. 1984. Morphological and bark strength characteristics important to wood–bark adhesion in hardwoods. Wood Fiber Sci. 16:339–348.

Fourcaud, T., F. Blaise, P. Lac, P. Castera and P. de Reffye. 2003. Numerical modeling of shape regulation and growth stresses in trees II. Implementation in the AMAPpara software and simulation of tree growth. Trees 17:31–39.

Green, D.W., J.E. Winandy and D.E. Kretschmann. 1999. Mechanical properties of wood. USDA For. Serv., Forest Products Lab., Madison, WI. www.fpl.fs.fed.us/documnts/fplgtr/fplgtr113/ch04.pdf.

Huang, Y.S., S.S. Chen, L.L. Kuo-Huang and C.M. Lee. 2005. Growth strain in the trunk and branches of *Chamaecyparis formosensis* and its influence on tree form. Tree Physiol. 25:1119–1126.

Kollmann, F.F.P. 1968. Principles of wood science and technology. Solid wood. Vol. 1. Springer-Verlag, Berlin, 592 p.

Kucera, L.J. and B. Gfeller. 1994. Einheimische und fremdländische Nutzhölzer. Professur Holzwissenschaften, ETHZ, Zurich, 144 p.

Laasasenaho, J., T. Melkas and S. Alden. 2005. Modeling bark thickness of *Picea abies* with taper curves. For. Ecol. Manage. 206: 35–47.

Lundström, T., U. Heiz, M. Stoffel and V. Stöckli. 2007. Fresh-wood bending: linking the mechanical and growth properties of a Norway spruce stem. Tree Physiol. 27:1229–1241.

Mattheck, C. and H. Breloer. 1994. The body language of trees: a handbook for failure analysis. HMSO, London, 240 p.

Mayer, H. 1985. Baumschwingungen und Sturmgefährdung des Waldes. Universität München, Meteorologisches Institut, München, 51, 247 p.

Milne, R. and P. Blackburn. 1989. The elasticity and vertical distribution of stress within stems of *Picea sitchensis*. Tree Physiol. 5: 195–205.

Morgan, J. and M.G.R. Cannell. 1994. Shape of tree stems—a reexamination of the uniform stress hypothesis. Tree Physiol. 14:49–62.

Newlin, J.A. and G.W. Trayer. 1956. Deflection of beams with special reference to shear deformations. USDA For. Serv., Forest Products Lab., Report 1309, Madison, WI, 18 p.

Schmidt-Vogt, H. 1991. Die Fichte: ein Handbuch in zwei Bänden. Waldbau, Ökologie, Urwald, Wirtschaftswald, Ernährung, Düngung, Ausblick Vol. 2/3. Verlag Paul Parey, Hamburg und Berlin, 781 p.

Schweingruber, F.H. 1996. Tree rings and environment. Dendroecology. Haupt, Bern, 609 p.

SIA. 2003. Timber structures—supplementary specifications. Schweizerischer Ingenieur- und Architektenverein (SIA), Zurich, 265/1, 27 p.

Stokes, A., T. Fourcaud and S. Berthier. 2001. How trees stand up and fall down: tree resistance to wind, or strange things that happen under stress. Int. Conf. Tree Structure and Mechanics, Savannah, GA, pp 21–37.

Trendelenburg, R. and H. Mayer-Wegelin. 1955. Das Holz als Rohstoff. 2nd Edn. J.F. Lehmanns Verlag, Munich, 541 p.

USDA. 1972. The moisture content and specific gravity of the bark and wood of northern pulpwood species. USDA For. Serv., North Central Forest Exp. Stn., Minnesota, Res. Note NC-141, 3 p.

Appendix

Table A1. List of symbols and notations and their definitions and units used in the study.

Symbol/Notation	Description	Unit
AGE	Cambial age counted from pith	year
D, D_0; $_{1, 2, c}$	Stem diameter on and under bark; reference to thin and thick log end and to log centre	mm, m
A_0	Cross-sectional area of woody log	mm^2, m^2
E; E_F	Secant modulus of elasticity due to pure bending, i.e., elasticity corrected for shear deformation = σ/ε_E; $E_F = \sigma_F/\varepsilon_F$	GPa
ε; ε_E; ε_F	Apparent bending strain (simply "bending strain"); ε corrected for shear deformation; ε due to F and corrected for shear deformation	–
ε_{el}; ε_{MOR}	ε as σ reaches: 0.4MOR (defined limit of elasticity); and MOR	–
$\varepsilon_{el\text{-}pl}$, $\alpha_{el\text{-}pl}$	The ideal elastic–ideal plastic $\sigma(\varepsilon)$-curve has a break point at $\varepsilon = \varepsilon_{el\text{-}pl}$ and $\sigma = \alpha_{el\text{-}pl}$MOR	–
F; F_{max}; F_g	Applied force in bending test; maximum applied F; concentrated (fictive) force causing same deflection as log weight	N
g; $_g$	Earth gravity; reference to own weight	$m\ s^{-2}$
G	Shear modulus in the z-direction, i.e., along fibers	MPa
γ_{MOE}; $\gamma_{MOR,1}$; $\gamma_{MOR,2}$	Coefficients accounting for the beneficial effect on MOE and MOR of intact logs compared to sawn wood (cf. Equations 11–13)	–
η	Completeness of the material in bending (cf. Equation 8)	–
H	Total tree height	m
K	Log taper = $(D_{02} - D_{01})/(D_{01}L)$	m^{-1}
κ_1; κ_2	Coefficients of plastification (cf. Equations 12 and 13)	–
L_{tot}; L; L_F	Test log length (total; in-span); and distance between support and force application	mm, m
MOE	Modulus of elasticity = the secant modulus of $\sigma(\varepsilon)$ as 0.4MOR is reached	GPa
MOR	Modulus of rupture = maximum value of $\sigma(\varepsilon)$	MPa
$\int\sigma(\varepsilon)d\varepsilon$	Integration of $\sigma(\varepsilon)$ up to σ = MOR, i.e., area under $\sigma(\varepsilon)$-curve	MPa
Q; $Q(r)$	Knottiness: of the stem cross section; and at the radial distance (r) from the pith (cf. Equation 1)	–
r; r_0	Radial coordinate of the stem, ranging from the stem center ($r = 0$) to the bark ($r = r_0$)	mm, m
ρ_w, ρ_b; ρ_0	Density of fresh wood and of bark; calculated dry wood density	$kg\ m^{-3}$
RW	Annual ring width	mm
σ; σ_F; σ_g	Bending stress; σ due to F; σ due to weight of log	MPa
I_{0c}	Moment of inertia about the log center	mm^4, m^4
s; $s_{F_{max}}$; s_g	Mid-span deflection of log; s at F_{max}; s due to weight of log	mm, m
τ, τ_{max}	Shear stress and resistance in z-direction	MPa
u	Wood moisture content = mass of water/oven-dry mass	%
V_0	Volume of woody log within the bending span	m^3
W; W_{MOR}; $W_{F_{max}}$	Work absorbed in bending; W at MOR; W due to F_{max}	N m
x, y, z	Cartesian coordinates of standing tree stem: z is height above stem base; and x is in the direction of deflection, $x = 0$ at stem center	mm, m
ϕ	Rotation around z-axis	rad

Work absorbed in bending, based on bending stress as a function of bending strain

The total work absorbed by a member subjected to bending can be expressed as the sum of energies absorbed by the small volume elements of the member. Below, this is exemplified at two levels of detail for the round logs that we tested.

The bending work absorbed within an infinitesimally thin slice of the middle cross section of the log (i.e., the test section) can be expressed as:

$$\frac{dW}{dz'}(z'_{test})_{sect} = \int_{-r_0}^{r_0}\left(\int_0^{\varepsilon(x)}\sigma(\varepsilon,x)\,d\varepsilon\right)C(x)\underbrace{2y(x)\,dx}_{dA_y(x)} \qquad (A1)$$

where: $0 < z' < L$ is the coordinate along the log subjected to bending and $z'_{test} = L/2$; r_0 is the radius of the middle of the woody log; $\sigma(\varepsilon,x)$ is the bending stress as a function of bending strain and distance from the log centre; $dA_y(x)$ is an area segment of the cross section (cf. Figure A1) with an infinitesi-

mal height dx, so that the strain occasioned by the bending can be assumed to be constant within the segment; and $C(x)$ is a coefficient that accounts for the radial gradient in MOR across the circular log:

$$C(x) = \frac{\sum_{i=1}^{n} dA_{xy}(x)_i \, \mathrm{MOR}(x)_i}{dA_y(x) \, \mathrm{MOR}_{\mathrm{sect}}} \gamma_{\mathrm{MOR}} \quad \text{(A2)}$$

where γ_{MOR} = 1.09 or 1.00 (found in this study), depending on

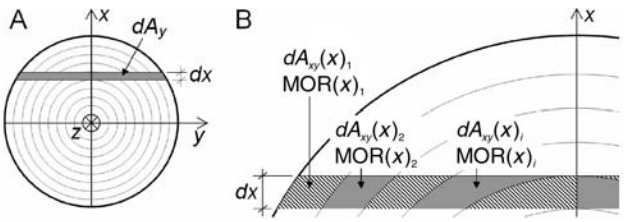

Figure A1. (A) Log cross section with schematic, enlarged annual year rings. Axes: z is the height above the stem base, and y the axis of applied bending moment in the tests, which causes deflections in the x-direction. (B) Enlargement of the upper left part of (A). Modulus of rupture (MOR) of each area element dA_y is calculated (Equation 15) on the basis of $\mathrm{MOR}(x)_i$ of finite area elements $dA_{xy}(x)_i$.

the x-wise distribution of bending stress (Equation 12 or 13). The other notations are explained in Figure A1B. If the distribution of bending stress across the section is approximated as triangular, then Equation A1 simplifies to:

$$\frac{dW}{dz'}(z'_{\mathrm{test}})_{\mathrm{sect}} = \tfrac{1}{4}\pi r_0^2 \int_0^{\varepsilon(r_0)} \sigma(\varepsilon)\, d\varepsilon \quad \text{(A3)}$$

This seems justified if: (1) the bending remains elastic, or at least, does not cause bending strain larger than that at MOR (cf. Table 6); and (2) the variation in $\mathrm{MOR}(r)$ is low. The work absorption along the log is proportional to the applied bending moment $M(z')$, which is obtained from basic mechanics. Therefore, the total bending work W absorbed by the log can be expressed as:

$$W = \int_0^L \frac{dW}{dz}(z'_{\mathrm{test}})_{\mathrm{sect}} \frac{M(z')}{M(z'_{\mathrm{test}})} dz' \quad \text{(A4)}$$

Consequently, the total work absorbed by a log can be calculated if data are available on: (1) the curve of the bending stress–strain, which may or may not be linear, of one stem section; (2) the shape or radius of this cross section; (3) the radial variation of MOR across the section; and (4) the applied bending moment along the log.

Chapter V

Reactions and energy absorption of trees subject to rockfall: a detailed assessment using a new experimental method

Tree Physiology 29, 345–359
doi:10.1093/treephys/tpn030

Reactions and energy absorption of trees subject to rockfall: a detailed assessment using a new experimental method

TOR LUNDSTRÖM,[1,2,3] MARTIN J. JONSSON,[1] AXEL VOLKWEIN[1] and MARKUS STOFFEL[3]

[1] *WSL, Swiss Federal Institute for Snow and Avalanche Research SLF, CH-7260 Davos, Switzerland*

[2] *Corresponding author (t.lundstroem@slf.ch)*

[3] *Laboratory of Dendrogeomorphology, University of Fribourg, 1700 Fribourg, Switzerland*

Received August 15, 2008; accepted October 20, 2008; published online December 23, 2008

Summary A new method for investigating the detailed reaction and the energy absorption of trees during a rock impact was developed and applied to 15 subalpine Norway spruce (*Picea abies* L. Karst) trees. A wedge-shaped trolley, guided by prestressed steel wires, was mounted on a forested slope to simulate a falling rock. The trolley accelerates down the wires and hits a tree at a preselected stem height with variable energies. The tree displacements and accelerations during the impact were recorded to determine reactions and energy absorption for the stem, root–soil system, crown and the entire tree. Trees absorbed the kinetic energy of the trolley rapidly by mobilizing strain and inertia forces close to the impact location in the stem and the root–soil system. This energy was then gradually dissipated all over the tree through permanent deformations and damping. The stem assimilated more energy than the root–soil system. The tree's energy absorption capacity was limited by stem-bending stresses at impact height, by shear stresses at the stem base and by lack of resistance of the root–soil anchorage. It was positively and exponentially related to stem diameter at breast height and negatively related to impact height. The field experiment enabled a physical description of how a tree reacts to a rock impact and highlighted the most important and critical components of the tree for its energy absorption. Such descriptions should help make computer simulations of rock–forest interrelations more precise and thus improve management strategies to ensure that forests can provide protection against rockfall.

Keywords: biomechanics, dynamics, energy balance, finite-element tree model, spatiotemporal analysis, stem deflection.

Introduction

Mountain forests provide a form of natural protection against falling rocks. Although rockfall models are commonly used to predict the trajectory, kinetic energy and run-out distance of the rocks (Zinggeler et al. 1991, Dorren and Seijmonsbergen 2003), less empirical information about the phenomenon of rock impact on trees is available (Mizuyama and Narita 1988, Dorren and Berger 2006). To determine the protective capacity of forests and to develop effective forest management strategies, it is essential to understand the mechanical processes of the tree–rock interaction. This understanding provides a basis for defining the forest parameters affecting the energy absorption of trees and the extent to which such parameters can be modified by human intervention.

A kinematical description of a falling rock moving through a mountain forest is complex. Rocks have a wide variety of shapes and forms, making it difficult to predict the center of mass and moments of inertia accurately. Falling rocks tend to rotate around the smaller inertia axis, contacting the ground in a jumping and sliding motion (Azzoni and Defreitas 1995). These factors reduce the rotational energy of the rock. In the field, this energy is negligible (Dorren and Berger 2006), unlike observations in the laboratory (Chau et al. 2002, Heidenreich and Labiouse 2004). Typical translational velocities are in the order of 10–30 m s^{-1} (Krummenacher and Keusen 1997). Recent investigations of rockfall scars on tree stems (Perret et al. 2004, Stoffel et al. 2006) indicate that impact heights of 1.2 ± 0.5 m are common. Experiments with rocks thrown down a forested slope (Dorren and Berger 2006) indicate that the kinetic rock energy is absorbed by the entire tree (root–soil anchorage, stem and crown). This energy absorption is, as for any structure subject to heavy dynamic loading, related to inertia, reversible and permanent deformation, friction and damping. The latter three terms describe dissipation of energy, i.e., how the energy changes form (e.g., into heat). Energy absorption, a generic name for energy uptake, is a sine qua non for energy dissipation. The focus of this paper is therefore on energy absorption.

From a mechanical point of view, trees are highly complex. Their anisotropically organized structure depends on

growth conditions (Brüchert et al. 2000, Polomski and Kuhn 2001). Because of these natural variations, it is difficult to predict the reaction of a tree to a rock impact, and trees can be expected to absorb energy in different ways and in varying amounts. Energy absorption due to deformation depends on mechanical properties, e.g., how stress develops with strain. For coniferous wood, the stress–strain time course is strain-rate dependent (Bragov and Lomunov 1997). Strain rates above 5 and 100 s^{-1} yield relatively higher stress perpendicular and parallel to the wood fiber, respectively (Murray 2003). Some of the mechanical properties of tree components likely to play important roles in the rock–tree interaction have been described, e.g., the bending of the stem (Lundström et al. 2008*b*) and of the root–soil system (Lundström et al. 2007*b*). However, how these components behave and how they interact during a rock impact on the tree have been largely unexplored.

To better understand the interaction between an impacting rock and a tree, a new experimental method was developed to explore: (1) How a tree reacts to a rock impact? (2) How the kinetic energy of the rock is absorbed in the tree? (3) How much energy a tree can assimilate without falling over? The method included investigating living trees in the forest, carrying out full-scale rock–tree impact tests and analyzing the field records with a simplified finite-element tree model. In this study, the method was applied to 15 subalpine Norway spruce trees.

Materials and methods

Test trees

Fifteen Norway spruce (*Picea abies* L. Karst) trees were selected as being representative of protective forests in the Alps, in terms of tree size and growth conditions (Table 1). All trees appeared healthy, except Tree A7 that had some rot in the center of the stem along its base. All the 15 trees grew in two closely situated subalpine forests near Davos, Switzerland, with Site A at 46°47′N, 9°48′W and 1770 m a.s.l. and Site B at 46°47′N, 9°50′W and 1680 m a.s.l. The ground of Site A faces ESE with a slope of 30°. It has a shallow B-horizon (5–35 cm) of dystric Cambisol (taxonomy according to FAO 1998) with frequent stones. The ground of Site B faces NNW with a slope of 35°. Its B-horizon is also a dystric Cambisol, but it is less shallow (10–40 cm) and has less frequent stones. Mean stocking density was 500 trees ha^{-1} in both stands. Rocks falling through the forests of the study area generally have low kinetic energy (< 100 kJ) and mass (< 1000 kg). The periods before and during the tests in summer 2003 and 2004 were slightly warmer and drier than normal (+12 versus +10 °C and 110 versus 120 mm $month^{-1}$). Further relevant site climate data are presented in Lundström et al. (2008*a*). Symbols used in this paper are summarized in the Appendix (Table A1).

Table 1. Tree characteristics relevant to this study: DBH = diameter at breast height, i.e., at stem height z = 1.3 m; H = tree height; L_c = crown length; m_{tree} = total aboveground tree mass; Age = cambial age; RW = annual ring width, where $_i$ refers to the mean of the inner 75% radial part of the stem cross section and $_o$ to the mean of the remaining outer radial part; ρ_w = stem bulk density; σ_{max} = bending strength (also called modulus of rupture); MOE = bending elasticity (or modulus of elasticity); τ_{max} = shearing strength and G = shearing elasticity.

Site and tree no.	DBH (m)	H (m)	L_c/H (–)	m_{tree} (kg)	Age[1] (years)	RW_i[1] (mm)	RW_o[1] (mm)	ρ_w[1] (kg m^{-3})	σ_{max}[1] (MPa)	MOE[1] (GPa)	τ_{max}[1] (MPa)	G[1] (MPa)
A1	0.35	26	0.53	950	125	2.1	1.4	830	57.8	11.8	2.6	530
A2	0.48	33	0.88	2430	218	1.9	1.2	850	49.0	12.8	2.7	540
A3	0.44	30	0.92	1970	193	1.5	0.9	880	44.4	14.5	3.0	580
A4	0.58	35	0.83	2820	272	0.9	0.6	930	57.1	17.0	3.7	670
A5	0.43	28	0.78	1480	184	1.1	0.9	870	54.6	14.5	3.5	630
A6	0.22	21	0.76	360	110	1.5	0.7	880	59.7	16.5	3.1	590
A7	0.38	23	0.66	1180	132	1.8	1.3	840	54.2	12.3	2.8	550
A8	0.35	26	0.80	910	116	1.6	1.2	830	53.3	12.8	3.0	580
A9	0.50	35	0.80	2770	273	1.3	1.3	880	49.0	12.3	3.2	600
A10	0.51	32	0.88	2720	271	0.9	1.2	900	46.5	12.8	3.8	670
B1	0.40	31	0.78	1640	170	1.5	1.2	850	51.2	12.8	3.0	580
B2	0.39	34	0.56	1600	175	1.7	0.8	860	61.6	15.3	2.9	570
B3	0.49	33	0.49	2030	221	1.7	0.8	870	63.1	15.3	2.9	570
B4	0.43	32	0.47	1620	179	1.3	1.0	860	60.5	13.9	3.3	610
B5	0.43	32	0.78	1820	174	1.4	1.1	860	50.0	13.3	3.1	590

[1] Value of the fresh stem section at z = 2 m.

Test procedure

Each test tree was investigated before and after the destructive impact experiment (Table 2). In the impact experiment (Step 4, Table 2), the rock was simulated with a wedge-front-shaped trolley (Figure 1A), guided by two steel wires on each side of the test tree (Figure 1B), prestressed with about 50 kN between two groups of trees. The trolley front is made of solid steel with a rough surface, representing a coefficient of kinetic friction of 0.3 against green wood (determined experimentally in the laboratory). Deposits of rocks originating from rockfall in the region of Davos were investigated to determine a typical rock edge. This was found to be right-angled, but slightly rounded, so the trolley front edge was designed with an angle of 90°, and rounded-off at a 20 mm radius. The trolley mass is adjustable from 292 to 892 kg with 50 and 100 kg concrete blocks positioned behind the front. The wire positions can be adjusted in height and sideways with steel supports on the lower and the upper wire ends. A third wire is attached to the back of the trolley to winch it up the wires to the starting position with a jeep driven on a forest road. There, it is released and accelerated down the wires to impact the test tree. The vertical drop that determines the impact speed and the mass of the trolley was adjusted to the energy required to make the tree just fall over. This energy was estimated on the basis of previous tests, data from the investigation Steps 1–3 (Table 2) and displacement-based simulations with the tree model used for the impact analysis (cf. section entitled *Tree model and its mechanical properties*). The highest achievable kinetic energy depends on the wire length and slope angle. With a maximum effective wire length of 55 m (for practical reasons) and a mean slope of 30°, this energy is about 250 kJ. A steel wire protection net was mounted on the lower side of the tree in case the trolley was not stopped by the tree.

Data acquisition of the impact test

Ten accelerometers (ABM-25-4-20, AMOS Sensoren & Meßtechnik, Mannheim, Germany) and four digital video cameras (two Sony DCR-TRV900E, Sony Corp., Tokyo, Japan, and two Redlake MotionScope-PCI, Roper Industries Inc., Duluth, GA) were connected to a data logger (DAQPad-6052E, NI Corp., Austin, TX). To minimize the influence of magnetic fields and temperature changes, all 14 devices were supplied with current. The data logger was connected by a firewire (IEE394) to a laptop computer that controlled and synchronized the measuring devices using a LabView-program (NI Corp.). On the trolley, two accelerometers measured in the vertical plane ($y = 0$) (Figure 1A): one in the direction of the wire (x') and one perpendicular to it (z'), both with a range of ± 500 m s^{-2}. Eight accelerometers were positioned on the downhill side of the stem at relative tree heights of 2% (x/y; $\pm 500/200$ m s^{-2}), 7% (x; ± 500 m s^{-2}), 20% (x; ± 200 m s^{-2}), 35% (x; ± 200 m s^{-2}), 53% (x; ± 100 m s^{-2}) and 75% (x/y; $\pm 100/50$ m s^{-2}), where x and y

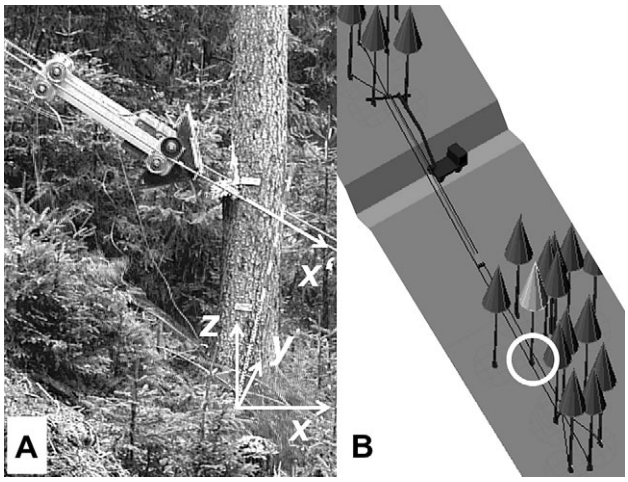

Figure 1. (A) The trolley, pictured shortly after impact with the test tree, is guided by four wheels on each side that grip the prestressed steel wires. (B) The trolley runs down the steel wires, which are mounted between two groups of trees, to impact the tree (circled).

Table 2. Successive steps for investigating trees subject to rock impact. The methods or data sources used are given in parentheses.

Step	Description
1	Characterization of the tree: species, DBH, estimated H (with clipper, measuring tape and hypsometer), vitality (optically), soil type (data bank or in situ sample)
2	Swaying test: determination of natural swaying frequencies and damping (Jonsson et al. 2007)
3	Winching test: determination of the initial rotational stiffness of the root–soil system (Jonsson et al. 2006)
4	Destructive impact test. If this test does not make the tree fall, the entire tree is winched down
5	Measurements of the lying tree: the geometry and mass of the stem and the crown (Lundström et al. 2008*a*) and the dimensions and shape of the root–soil plate (Lundström et al. 2007*a*)
6	Laboratory investigations of stem and soil samples: determination of the annual ring width RW, knottiness and stem bulk density ρ_w in stem disks from close below and above the impact height, and at least four additional stem heights above it (Lundström et al. 2008*b*); determination of the bulk density, moisture content and granulometry of the soil in the root–soil plate (according to standard procedures)
7	Laboratory tests of the local penetration of a rock front into the fully supported stem, thus with no stem-bending. The test setup, which uses the same impact trolley as in Step 4, is described in: http://www.wsl.ch/forschung/forschungsprojekte/Treestability/local-impact_EN [accessed July 9, 2008]

indicate their measurement directions. All accelerometers sampled at a rate of 10 kHz. Records in the *y*-direction were made to verify that the energy analysis was restricted to the *x*–*z*-plane. Two cameras filmed the lower part of the tree with a frequency of 25 (Sony) and 250 Hz (Redlake), respectively. The latter also detected the impact velocity of the trolley. The two remaining cameras film the upper part of the tree with the same frequencies. The data logger was triggered to start sampling accelerations and images as the trolley passed a photocell (Polifemo, Microgate, Italy) positioned some meters above the test tree.

Displacement analysis of the impact test

The displacements in time of the tree and the trolley, in the *x*- and *y*-directions, were detected from the 250 Hz video image series (480 × 420 pixels). For this detection, two software programs were used: (1) WinAnalyse (DEL Imaging Systems, LLC, Cheshire, CT), which allows point-tracking, with automatic descriptions of displacements, velocities and accelerations, but which does not account for the geometrical and the optical image distortion and (2) Stemtrack, especially developed for detecting tree deflections with high precision. It describes stem deflection with polynomials of stem height and time $x(z, t)$ and takes the image distortion fully into account. If a 30-m high tree is captured entirely in two 250 Hz-images merged vertically, the precision in stem deflection is about 5 cm (cf. Lundström et al. 2007*a*). For technical information, see http://www.wsl.ch/forschung/forschungsunits/lawinen/downloads/Stemtrack.pdf [accessed July 9, 2008]. WinAnalyse analyzed the local penetration of the trolley front into the stem and Stemtrack analyzed the deflections of the entire tree stem. Here, the deflections detected from the picture series filmed with the lower and the upper cameras were merged. To increase the number of deflection estimates in time, i.e., to obtain stem deflections between those detected with Stemtrack, the recorded accelerations were integrated twice according to Newmark's linear acceleration method (Chopra 1995). The latter high-frequency deflections (10 kHz) were forced to coincide with the deflections of Stemtrack (250 Hz) at the same time step. Deflections obtained on the basis of acceleration records only would be erroneous because of the accumulated errors resulting from the dynamical drift and offset of the sensors. The 25 Hz series (768 × 576 pixels) were analyzed in the same way as the 250 Hz series and provided a control function of every 10th image from the 250 Hz series.

A precise description of the stem deflections and deformations of the root–soil system during the impact is essential to accurately determine the tree's reaction and energy absorption. The following description has proved to be precise and practical:

$$x(z,t) = a_n(t) \cdot z^n + a_{n-1}(t) \cdot z^{n-1} \cdot \ldots \cdot a_1(t) \cdot z^1 + a_0(t), \quad (1)$$

where $x(z, t)$ is the cylindrical center of the stem, describing a line from the stem base to the tree top (Figure 3A); $a(t)$ is a polynomial coefficient at time t and superscript n is a

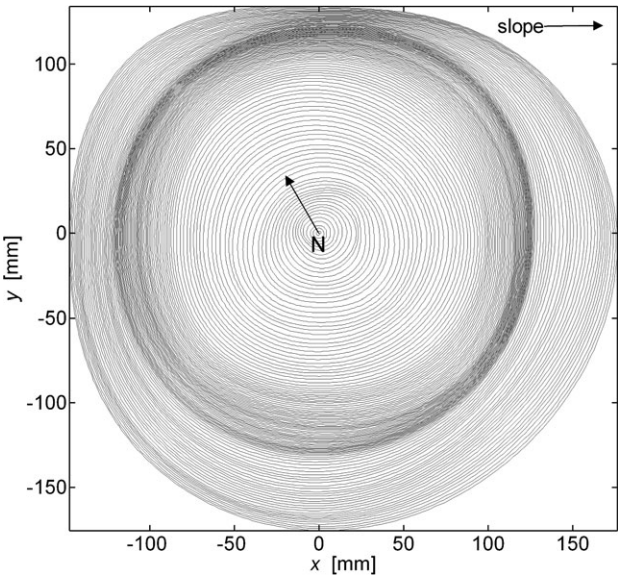

Figure 2. Digitized stem disk with annual rings sampled at a stem height of 2.0 m from Tree A8. The *x*-axis (to the right in the figure) corresponds to the slope and impact direction and faces ESE. The preferential azimuthal stem growth is found in the orientations facing the slope and the south. N (in the pith) indicates the north.

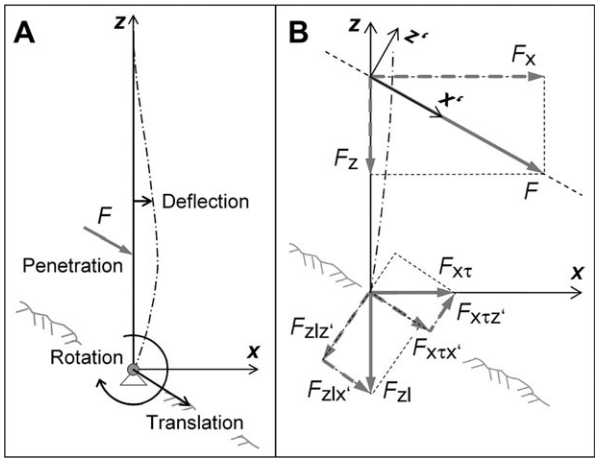

Figure 3. (A) Simplified model of the tree used to analyze the tree reaction and the energy absorption caused by stem deflection, local penetration of the trolley front into the stem, and rotation and translation of the root–soil system. (B) Decomposition of the force F applied by the trolley to the stem into vector components. Abbreviations: τ denotes the transverse (shear) forces; l denotes the longitudinal (compressive or tension) forces effectively transmitted by the stem to the ground; $F_{x\tau x'}$ and $F_{x\tau z'}$ are components of $F_{x\tau}$; and $F_{zlx'}$ and $F_{zlz'}$ are components of F_{zl}. The magnitudes of $F_{x\tau}$ and F_{zl} depend on how intensively the energy is absorbed by the stem.

polynomial degree, so that the stem deflection, and thus the tree reaction, is reproduced accurately. During the short time interval of energy absorption analyzed, the vertical stem deflections are small compared with the lateral stem deflections and are therefore neglected. To facilitate the analysis, the initial positions for x and y are set to 0. The stem line thus intersects the ground at (x, y, z) = (0, 0, 0), from where it describes a vertical up to the top of the tree. The location of the center of rotation of the root–soil system approximates (x, y, z) = (0, 0, 0) (cf. Lundström et al. 2007*b*). Consequently, the rotation of the root–soil system equals the rotation at the stem base (z = 0). The last polynomial term, $a_0(t)$, divided by the cosine of the slope angle, describes the translation of the root–soil system in the slope direction, and $a_1(t)$ describes its rotation (i.e., the stem-base inclination) as a function of time. The strain rate for the roots is estimated from the time courses of a_0 and a_1, and considering that an equivalent root length of at least 0.5 m is subjected to strain. All second derivatives of Eq. (1) with respect to t describe accelerations. The second derivative of Eq. (1) with respect to z describes the stem curvature and the third derivative describes the change in this curvature. The two derivates are related to the bending strain in the outermost wood fiber and to the mean shear strain of the cross section, ε and γ, respectively:

$$\varepsilon(z) = \frac{D(z)}{2} \cdot \frac{\mathrm{d}^2 x}{\mathrm{d}z^2};$$
$$\gamma(z) = \frac{\mathrm{MOE}(z) \cdot I(z)}{G(z) \cdot A_S(z)} \cdot \frac{\mathrm{d}^3 x}{\mathrm{d}z^3}, \quad (2)$$

where $D(z) = D_1(z) - B(z)$ is stem diameter under bark, $D_1(z)$ is stem diameter on bark, $B(z)$ is double bark thickness, MOE(z) is the bending modulus of elasticity, $I(z) = \pi(D(z)^4/64)$ is the cross-sectional moment of inertia, $G(z)$ is the shear modulus of elasticity, $A_s(z) = A(z)/1.1$ is the effective shear area of the actual cross-sectional area, $A(z) = \pi(D(z)^2/4)$. The strain rates of stem-bending and shear are determined by analyzing the time course of Eq. (2).

Tree model and its mechanical properties

To analyze the reaction and the energy absorption of the tested tree on impact, a simplified finite-element model of the test tree was coded in Matlab 7.0 (MathWorks, Inc., Natick, MA). The model consists of 100 equally long beam elements (of Timoshenko type, cf. Cook et al. 2002), with the lowermost element flexibly clamped to the ground. The elements are attributed mechanical properties on the basis of Steps 1, 3 and 5–7 in Table 2 and the values in Table 1, with all geometrical properties and density as polynomials of height. The tree model is similar to that described by Lundström et al. (2008*a*), with three exceptions: no geometrical nonlinear effects are considered; the maximum resistive turning moment of the root–soil system $M^0{}_{\max}$ is predicted (according to Lundström et al. 2007*b*) and the stem-bending is simplified (according to Lundström et al. 2008*b*). The pure bending stress σ is thus ideally elastic from the bending strain $\varepsilon = 0$ to $\varepsilon = \varepsilon_1 = 0.91\ \sigma_{\max}(z)/\mathrm{MOE}(z)$, and then ideally plastic from ε_1 to the bending failure at $\varepsilon = 2.4\varepsilon_1$, with the actual $\sigma_{\max}$ occurring at $\varepsilon = 2.0\varepsilon_1$ (see Tables 1 and A1 for symbol explanations). The bending shear stress γ has its respective shear strain limits $\gamma_1 = 0.91\gamma_{\max}(z)/G(z)$ and $1.4\gamma_1$ (Wessolly and Erb 1998, Dinwoodie 2000). The $\sigma_{\max}(z)$ and MOE(z) of the model tree is each defined by a spline (cubic spline interpolation, Matlab) covering $0 < z < H$, calculated (according to Lundström et al. 2008*b*) on the basis of the annual ring width (RW) and the knottiness in the stem disks sampled from the tree.

Some of the trees tested displayed fairly asymmetrically grown stems (Figure 2). Therefore a comparison was made between the bending properties calculated for symmetrical (geometric mean) and asymmetrical (actual) stem disks sampled at z = 2.0 m. The cross section was divided into circle segments with the thickness of one annual ring and an opening angle of 1°, and MOE and $\sigma_{\max}$ were calculated in all bending azimuths (0–359°) on the basis of Lundström et al. (2008*b*) and the parallel-axis theorem. The difference between the asymmetric and symmetric disks was at the most 3% for MOE and 2% for $\sigma_{\max}$. Calculated on the same basis for the two related geometrical properties I and the section modulus $2(I/D)$, the corresponding differences were at most 13% and 8%, respectively. These four differences averaged for all trees were about a third as great. Because these discrepancies have little influence on the aims of our study, the analysis was simplified by considering all bending properties to be independent of azimuth. Finally, the properties of growth in the stem center varied little with height. Therefore, $G(z)$ and $\tau_{\max}(z)$ were approximated and treated as constants (Table 1), estimating $\tau_{\max}$ according to Lundström et al. (2008*b*) and $G = 118\tau_{\max} + 400$ (MPa) (Kollmann 1968).

Energy analysis of the impact test

To determine how the energy applied by the impact trolley is absorbed by the tree over time and space, the energy balance for the trolley–tree interaction was considered, applying the equation of motion of an inelastic system (Clough and Penzien 1993). Here, all the relevant forces and stresses acting in the system (Figure 3A) were multiplied by their displacements, computed for every time step (set to 1 ms) from the first contact between the trolley and the tree stem (t = 0) until the intensity of the tree's energy absorption reaches a value close to zero, i.e., during the period T_{abs}. The energy intensity (J s^{-1} or W) applied by the trolley to the tree is:

$$\mathrm{d}W_{\mathrm{app}} = -m_{\mathrm{trolley}} \cdot \left(\frac{\mathrm{d}^2 x'}{\mathrm{d}t^2} \cdot \mathrm{d}x' + \frac{\mathrm{d}^2 x'}{\mathrm{d}t^2} \cdot \mathrm{d}z' \right), \quad (3)$$

Table 3. Groups of energy absorption phenomena of the tree, their descriptions and corresponding equation (Eq.).

Group	Description	Eq.
I	Deformation of stem in bending, through	4
Ia	pure bending in the elastic domain	
Ib	pure bending in the plastic domain	
Ic	longitudinal shearing in the elastic domain	
Id	longitudinal shearing in the plastic domain	
II	Inertia of stem in x-wise deflection	5
III	Deformation of stem by local penetration[1]	6
IV	Deformation of root–soil system in rotation	7
V	Inertia of root–soil system in rotation	8
VI	Deformation of root–soil system in translation	9
VII	Inertia of root–soil system in translation	10
VIII	Diverse losses	–

[1] Penetration by the trolley front (simulated rock edge) into the stem.

where m_{trolley} is the total mass of the trolley and x' and z' are displacements of the trolley's center of gravity (Figure 3B). Equation (3) assumes that the energy absorbed z'-wise is used to deform the tree and not to push the wires, i.e., that the wedge front does not just slip down on the tree stem in the z'-direction.

The way the tree structure absorbs $\mathrm{d}W_{\text{app}}$ was categorized into eight groups of absorption phenomena (I–VIII, Table 3), which are incorporated in the code for the tree model. When provided with records of displacements and accelerations (Eq. (1)), the code calculates the energy intensity $\mathrm{d}W$ and the energy absorption W for each phenomenon and for the entire tree, where W is $\mathrm{d}W$ integrated with respect to time. The energy absorbed by the tree through damping can be ignored for the impact event, because T_{abs} is short compared with the first vibration frequencies of the tree structure (Clough and Penzien 1993). In contrast, the elastic strains and inertia forces need to be considered in the energy analysis during T_{abs}, although the related energies will, after T_{abs}, dissipate in damping or plastic strain throughout the tree. The energy intensities, $\mathrm{d}W$, for each of the eight phenomena are described below.

Energy is required to deform the stem in bending (I, Table 3). In the elastic domain (Ia and Ic), this is described by Sundström (1998), and is reproduced here slightly rearranged

$$\begin{aligned} \mathrm{d}W &= W(t+\mathrm{d}t) - W(t); \\ W(t) &= \underbrace{\frac{1}{8}\cdot\int_{z=0}^{H} \mathrm{MOE}(z)\cdot A(z)\cdot \varepsilon(z,t)^2\cdot \mathrm{d}z}_{\text{bending}} \\ &\quad + \underbrace{\frac{1}{2}\cdot\int_{z=0}^{H} G(z)\cdot A_{\mathrm{S}}(z)\cdot \gamma(z,t)^2\cdot \mathrm{d}z}_{\text{shearing}}, \end{aligned} \tag{4}$$

where the bending and shear strains ε and γ are obtained from Eq. (2). In the plastic domain (Ib and Id), $\mathrm{d}W$ is independent of the ε- and γ-values. Therefore, the energy intensities per strain increment $\mathrm{d}W/\mathrm{d}\varepsilon$ for Ib and Id are equal to those for Ia and Ic at $\varepsilon = \varepsilon_1$ and $\gamma = \gamma_1$, respectively. The image series are again useful to verify that the stem section has not been broken off before the defined failure limits ($\varepsilon = 2.4\varepsilon_1$ or $\gamma = 1.4\gamma_1$) are exceeded. If necessary, the factors (2.4 and 1.4) are corrected to suit the failure mechanisms observed in the image series. No correction was required for the Norway spruce trees that we tested.

Energy is required to accelerate the stem because of its inertia (II, Table 3). For the x-ways deflection, this is described as:

$$\mathrm{d}W = \frac{\pi}{4}\cdot\int_{0}^{H} D_1(z)^2\cdot\rho_{\mathrm{w}}(z)\cdot\frac{\mathrm{d}^2x}{\mathrm{d}t^2}(z)\cdot\mathrm{d}x(z)\cdot\mathrm{d}z. \tag{5}$$

Energy is absorbed and dissipated by the woody stem as the trolley front (simulated rock edge) penetrates it and crushes the wood fibers (III, Table 3):

$$\mathrm{d}W = k_{\mathrm{p}}\cdot x_{\mathrm{p}}\cdot\mathrm{d}x_{\mathrm{p}};\quad k_{\mathrm{p}} = a_{\mathrm{p}}\cdot D_1(z), \tag{6}$$

where k_{p} is penetration stiffness, $a_{\mathrm{p}} = 10\ \mathrm{N\ mm^{-2}}$ is a regression coefficient obtained experimentally (Step 7, Table 2) for 25 stems of Norway spruce from the test plot, x_{p} is penetration depth into the woody stem and $k_{\mathrm{p}}{\cdot}x_{\mathrm{p}}$ is penetration force. The value of k_{p} also includes the flattening of the stem caused by the high cross-sectional pressure in the impact direction. The sign of $\mathrm{d}W$ turns negative by the end of the trolley front–stem contact because of reflected elastic strain energy.

Energy, related to deformation, gravity and friction, is required to rotate the root–soil system (IV, Table 3):

$$\mathrm{d}W = M^0(\phi)\cdot\mathrm{d}\phi, \tag{7}$$

where $M^0(\phi)$ is the curve describing the resistive turning moment of the root–soil system as a function of the stem-base inclination ϕ, predicted with m_{tree}, DBH and H (Lundström et al. 2007*b*), and ϕ equals $\mathrm{d}x/\mathrm{d}z$ ($z = 0$) (Eq. (1)). The beginning of the calculated $M^0(\phi)$-curve is compared with the curve measured for $0° < \phi < 2.5°$ in investigation no. 3 (Step 3, Table 2). If the difference is significant, the calculated $M^0(\phi)$ is rescaled in the M^0- or ϕ-direction, or both, to fit the measured $M^0(\phi)$. Rescaling was unnecessary for the Norway spruce trees that we tested.

Energy is required to accelerate the root–soil system in rotation because of its inertia (V, Table 3):

$$\begin{aligned} \mathrm{d}W &= J\cdot\frac{\mathrm{d}^2\phi}{\mathrm{d}t^2}\cdot\mathrm{d}\phi; \\ J &= \sum_{\substack{i=1\\ V_{\text{part}}}}^{i=n}\left(J(z_i) + m_i\cdot z_i^2\right), \end{aligned} \tag{8}$$

where $d^2\phi/dt^2$ is the angular acceleration of the root–soil plate and J describes its mass moment of inertia, $J(z_i)$ is the J for the rotation around the axis $(x, z) = (0, z_i)$, of a horizontal, elliptical root–soil plate slice of thickness $z_{i+1} - z_i$, located at a distance z_i from $(x, y, z) = (0, 0, 0)$, with a mass m_i calculated from the bulk density ρ_s of the root–soil plate. The root–soil plate shape is modeled with an elliptical cross section and a depth-dependent taper. The part bent-off at the root–soil plate hinge is ignored (cf. the illustration in Lundström et al. 2007*a*). For all Norway spruce trees tested, ρ_s was estimated to be 1500 kg m^{-3} based on a soil density = 1900 kg m^{-3}, a root density = 700 kg m^{-3} and an assumed volume mix of soil (67%) and roots (33%) in the root–soil plate, similar to that for mature Norway spruce trees growing on mineral soils (Hakkila 1972). Because the root diameter decreases from the root–soil plate center outward, the root–soil plate stiffness decreases radially. Therefore, as estimated from series of digital images, only 70% of the entire volume of the root–soil plate V is considered to effectively contribute to its inertia during the impact. The 'participating' volume of the root–soil plate (V_{part}) is thus obtained by multiplying the height, width and depth of V by $0.7^{1/3}$.

The energy required to deform the root–soil system in translation (VI, Table 3) is:

$$dW = \frac{k_t}{\cos(\beta_s)} \cdot dx, \quad (9)$$

where k_t represents the (unknown) translational deformation stiffness of the root–soil plate and β_s is the slope at the location of the tree. A hypothesis supported by tests is that k_t is independent of x and is equivalent to a force of shear-friction type (unit Newton). The magnitude of k_t is the difference between W_{app0} and W (I to VI + VIII) divided by the translational deformation of the root–soil plate at the end of T_{abs}.

Energy is required to accelerate the root–soil system in translation due to inertia (VII, Table 3):

$$dW = \frac{V_{part} \cdot \rho_s}{\cos^2(\beta_s)} \cdot \frac{d^2x}{dt^2} \cdot dx. \quad (10)$$

Finally, the energy attributed to the group of energy absorption phenomena entitled 'Diverse losses' (VIII, Table 3) includes some minor energy quantities absorbed during T_{abs} through subsidiary phenomena not considered in the other groups. Principally, three observations from the test series help interpret this group: (1) The impact force involves a vertical component directed downward along the stem (Figure 3B) toward the root–soil system, to which the vertical structure of the stem base–root system reacts elastically and plastically. The x- and z-wise projections of Eq. (3) are used to analyze this feature, whose energy absorption is entirely attributed to the stem. (2) Because of the deflection at impact height, a downward displacement of the stem above impact height occurs. This displacement, which first accelerates and then decelerates, absorbs some energy due to inertia. (3) The simplified stress–strain relationships used for bending (cf. *Tree model and its mechanical properties*) will imply some fluctuations in time of the energy absorbed in Group VIII.

Energy absorption capacity of the tree

The energy absorption capacity, W_{cap}, of the tree is reached when the weakest component, i.e., either the stem or the root–soil system, in the transport of forces from the impact trolley to the ground fails (cf. Figure 3). To determine when and where during the impact this weak mechanical link occurs, observations were made on three levels (Table 4). From these, W_{cap} can be obtained, provided that the total kinetic energy of the trolley W_{app0} exceeds W_{cap}. If, however, W_{app0} falls below W_{cap}, the mechanical behavior of the tree that was tested needs to be extrapolated. Here, experimental experience has shown that the energy absorption related to phenomenon I (I, Table 3) is useful, because this energy in most cases dominates W_{cap} among the phenomena I–VIII, and the resistance related to phenomenon I governs the total possible energy uptake of the tree. Therefore, W_{app0} is multiplied by a factor equal to: the area under the defined $\sigma(\varepsilon)$-curve, between $\varepsilon = 0$ and $2.4\varepsilon_1$ divided by the area under the $\sigma(\varepsilon)$-curve between $\varepsilon = 0$ and the maximum measured ε. For example, with a stem deflection that yields (Eq. (2)) a maximum measured $\varepsilon = 2\varepsilon_1 = (1.4 + 0.6)\varepsilon_1$, the factor equals $(1.4/2 + 1.0)/$

Table 4. Observations relating to specific groups of energy involved in the trolley–tree interaction which help quantify the energy absorption capacity W_{cap} of the tree.

No.	Energy group: observation and interpretation
1	Energy intensity applied by the trolley in the x'-direction (Eq. (3)): an abrupt drop in this intensity to a value close to zero indicates a sudden low resistance offered by the tree to the impact loading, and the point of absorption capacity
2	Stem-bending (I): the measured maximum bending strain $\varepsilon(z, t)$ along the stem is compared to the stress–strain curves defined for bending (cf. *Tree model and its mechanical properties*). W_{cap} is reached at complete stem failure, i.e., when $\varepsilon(z, t) > 2.4\varepsilon_1(z, t)$. Stem failure is not caused by $\gamma(z, t) > 1.4\gamma_1(z, t)$ alone, but it sets off greater $\varepsilon(z, t)$
3	Root–soil rotation (IV): the measured stem-base rotation $\phi(t)$ is compared to the predicted $M^0(\phi)$ of the tree (Eq. (7)). The W_{cap} is reached when $\phi(t) > \phi(M^0{}_{max})$

(1.4/2 + 0.6) = 1.31. If, exceptionally, little stem curvature but large stem-base rotation occurs during the impact, the up-scaling factor is based on (3) in Table 4 in analogy with the $\sigma(\varepsilon)$-curve. Regardless of whether W_{app0} exceeds or falls below W_{cap}, the series of digital images are essential in assessing stem deflections and qualitatively surveying the interaction between the trolley front (simulated rock) and the heterogeneous tree structure.

Results

Tree reaction to the impact: general

The trolley hit the stems of the 15 test trees under somewhat different conditions (Table 5). The overall tree reactions during the impact, however, were similar in many ways. The trolley front crushed the wood fibers locally and pushed the stem down slope. This push bent the stem and also caused the root–soil system to rotate and translate. The trolley was rapidly stopped as a result of the absorption of its energy by the tree, but the tree reactions continued for a long time. The impact excited several different vibrational modes in the tree, causing transverse waves to propagate toward the tree top along the stem (Figure 4A). Above a certain tree height (about 12 m; Figure 4A), the energy contained in such a wave increased deflection of the stem, because stem diameter decreases with height, and thus stem rigidity and mass also decrease. Consequently, the strains and stresses associated with stem-bending increased. Close to the tree top, these strains and stresses exceeded the wood-failure limits, resulting in one or several stem failures. About 0.2 s after the predominant transverse wave had snapped the stem, the first natural swaying frequency of the tree dominated its motion. Then one of the following scenarios occurred: (1) the swaying was gradually damped out and the tree remained standing; (2) the stem broke off at impact location and the tree part above this height fell; or (3) the root–soil system failed (in rotation and translation) and the entire tree fell, including the root–soil plate. Scenarios 2 and 3 occurred a few seconds after the first contact between the trolley and the tree stem. The types of tree failure observed are listed in Table 5.

The stem deflections during the trolley–stem interactions for all of the tested trees were accurately described by a ninth degree polynomial (Eq. (1)) or higher. The high polynomial degrees were required to describe the curvature of the lowermost and the uppermost stem, and thus the strains and stresses there. The highest strain rates for the stem and the root system occurred shortly after $t = 0$ ms. For the stem in shear, tension and compression, the strain rates never exceeded 1 s^{-1}, and for the roots subjected to rotation and translation, they were even lower. Thus, the influence of strain rates on the stress–strain curve for the stem and on the turning moment for the root–soil system can be ignored.

Tree reaction and energy absorption: detail

Among the 15 trees tested, Tree A8 displayed typical reactions and energy absorptions. For this reason, and to demonstrate the method, the results for Tree A8 are presented in detail. On the basis of the stem deflections over time (Figure 4A and C), some significant tree reactions were identified: (1) the predicted shear failure of the stem ($\gamma = 1.4\gamma_1$) was reached at the stem base when (t, z, x) = (21 ms, 1.8 m, 120 mm); (2) the predicted bending failure of the stem ($\varepsilon = 2.4\varepsilon_1$) was reached at $z = 2.1$ m

Table 5. Data for the trolley and observations of tree failures resulting from the impact test. Abbreviations: m = mass; v = speed; z = height on the tree; β = angle to the horizontal; $_0$ refers to time zero, i.e., the first contact between the trolley front and the stem of the test tree; W_{app0} = kinetic energy of the trolley; x_{pr} = the remaining maximum depth of the local penetration of the trolley front into the woody tree stem; R = root–soil system; S = stem and R/S = predominantly R.

Site and tree no.	Trolley						Tree	
	m (kg)	v_0 (m/s)	z_0 (m)	z_0/H (%)	β_0 (°)	W_{app0} (kJ)	x_{pr} (mm)	Failure type
A1	692	17.7	0.83	3.2	27	108	68	R
A2	692	18.4	1.10	3.3	27	118	60	S
A3	692	19.5	0.72	2.4	30	131	75	R
A4	792	20.0	0.95	2.8	26	158	56	R/S
A5	792	18.5	1.20	4.3	26	135	50	R
A6	492	5.7	1.20	5.8	26	8	20	S
A7	492	13.7	1.16	5.0	29	46	35	S
A8	592	13.3	1.36	5.3	28	52	44	S
A9	792	17.7	1.40	4.1	30	124	50	R/S
A10	792	20.7	1.48	4.6	27	170	70	S
B1	892	15.8	1.85	5.9	32	111	28	S
B2	892	17.5	0.70	2.1	33	136	75	R/S
B3	592	22.0	0.90	2.7	33	143	68	S
B4	492	21.5	1.80	5.6	33	113	35	S
B5	492	19.8	0.95	3.0	35	96	40	S

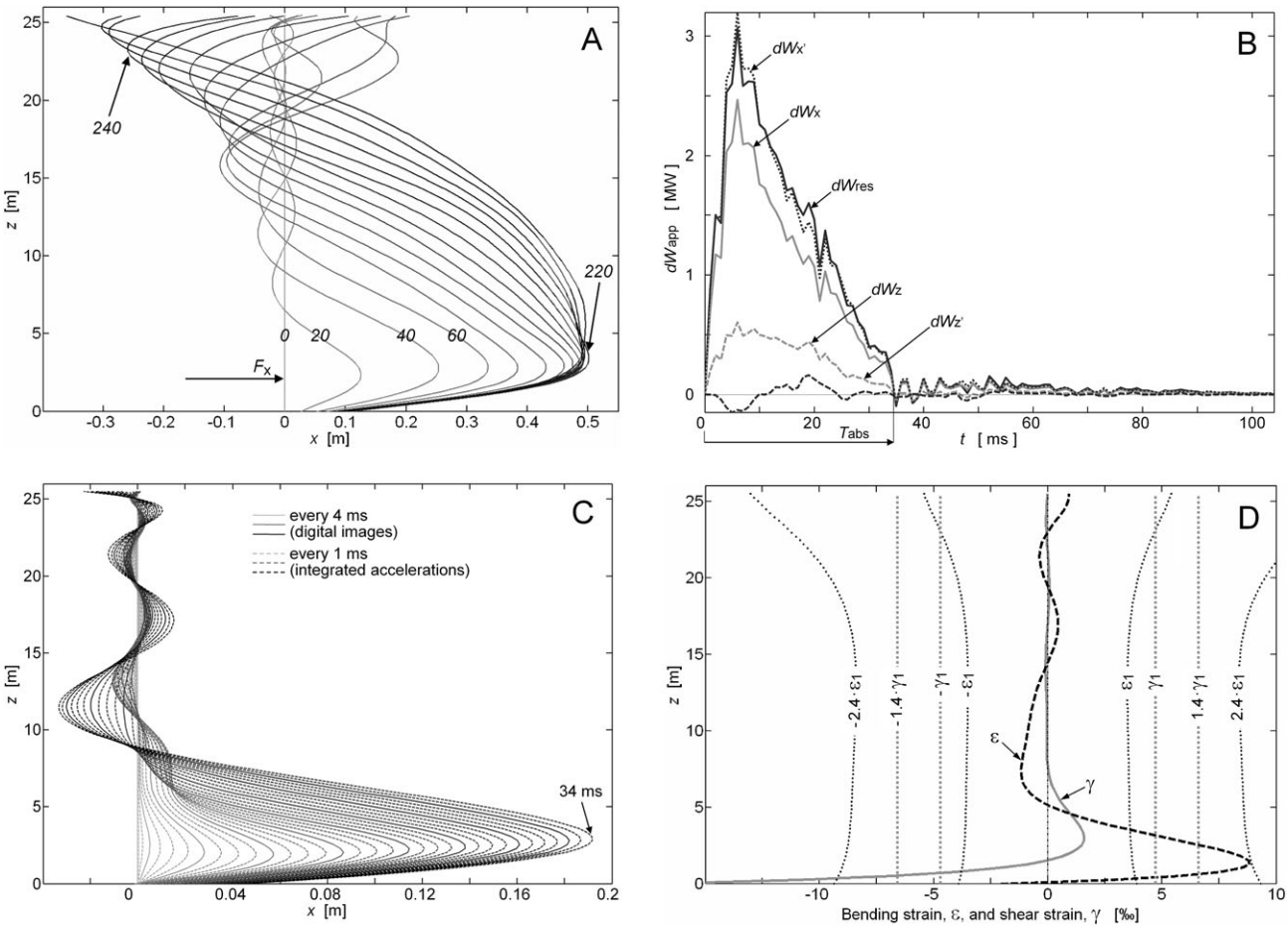

Figure 4. (A) Dependence of stem deflections x on height z and time t = 0, 20, 40, …, 300 ms, where t = 0 is the time of the first contact between the force F applied by the trolley on the stem. Down slope is to the right. At t = 220 ms and maximum x = 500 mm, the trolley and the stem at impact height started to go backwards, in negative x'- and x-directions. (B) Energy intensity dW applied by the trolley to the tree. Abbreviations: dW_{res} is the vectorial sum of the intensities along and perpendicular to the trolley $dW_{x'}$ and $dW_{z'}$, respectively; and dW_x and dW_z are the resulting intensities across and along the stem (cf. Figure 3B). The period of energy absorption T_{abs} lasts from t = 0 to t = 34 ms as dW_{res} declines to a value close to zero. (C) Stem deflections during T_{abs} obtained from high-speed digital images (every 4 ms); completed with double integrated acceleration records (every 1 ms). (D) Stem strains at t = 34 ms, with the limits of plastification ($\pm\varepsilon_1$ and $\pm\gamma_1$) and of failure ($\pm 2.4\varepsilon_1$ and $\pm 1.4\gamma_1$). The stem had just reached the limit of bending failure at impact height, and shear failure was surpassed at the stem base. After t = 34 ms, ε and γ greatly increased along the upper part of the stem, and at t = 160 ms they both exhibited an hourglass shape similar to the ± 2.4 ε_1-curves. The width of this hourglass increased with time at the tree top and exceeded the 2.4 ε_1-limit at (z, t) = (22.1 m, 240 ms) (cf. A).

when (t, z, x) = (34 ms, 2.1 m, 190 mm) (cf. Figure 4D), which was at the same time as the rotation of the root–soil system was 5.4° and its translation was 45 mm; (3) the predicted (M^0_{max}, ϕ) = (69 kNm, 6.3°) was reached when (t, z, x) = (45 ms, 2.2 m, 240 mm); (4) the maximum stem deflection was reached when (t, z, x) = (220 ms, 2.9 m, 500 mm), which was at the same time as the maximum rotation and translation of the root–soil system (9.0° and 85 mm) and (5) at t = 240 ms and z = 22.1 m (cf. Figure 4A), a transverse wave snapped the stem, because the bending strain was about 0.010.

Tree A8 fell on impact during the test, indicating that the kinetic energy applied by the trolley exceeded the energy absorption capacity of the tree. The latter could thus be determined from the energy intensity (dW_{res}) applied by the trolley to the tree and the development of the bending and shear stresses over time (nos. 1 and 2 in Table 4). At t = 34 ms, dW_{res} reached a value close to zero (Figure 4B, based on Eq. (3)). This was due to the low rate of deceleration of the trolley because the tree no longer offered much resistance to the moving trolley at t = 34 ms. The low resistance was caused by stem-bending failure at impact height and to stem shear failure at the stem base, resulting from the excessive bending and shear stresses, respectively (Figure 4D). The latter became evident when the stem was sawn into sections after the impact experiment and the wood fell apart longitudinally and cylindrically along the inner annual rings. By t = 34 ms, the trolley had trans-

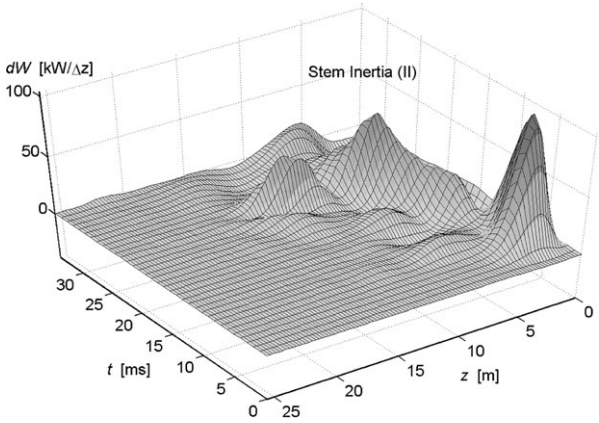

Figure 5. Energy absorption as a function of time and tree height $dW(t, z)$ for the stem and crown due to their x-wise acceleration (inertia). Abbreviations: $\Delta z = 25.5$ cm corresponds to 1% of the total tree height; negative dW-values indicate stem deceleration. For this tree (A8), the peak intensity of 110 kW/Δz occurred just below impact height, at stem height $z = 1.5$ m and time $t = 6$ ms. The energy absorption due to stem-bending (I) was distributed analogously.

mitted 96% (50 kJ) of its initial kinetic energy (52 kJ) to the tree. The absorption capacity W_{cap} of the tree was thus 50 kJ, which was exceeded by $52 - 50 = 2$ kJ or 4%. Until $t = 34$ ms, $> 99.5\%$ of the energy had been absorbed by the tree in the x–z-plane and $< 0.5\%$ in the y-direction.

How W_{cap} was assimilated by the tree becomes apparent when observing its energy absorption in different dimensions: (1) according to time and height, for individual phenomena (Figure 5); (2) according to time, for several phenomena (Figure 6); or (3) according to phenomenon, as relative parts of W_{cap} (Table 6). For Tree A8, W_{cap} was dominated by the stem's capacity to absorb energy (Figure 6). The energy absorption by the stem was principally a result of bending in the plastic domain, but the energy absorbed in shear deformation caused by bending cannot be ignored (Figure 6B). Energy absorption by the root–soil system was temporarily dominated by inertia energy, but energy absorption due to strain dominated toward the end of T_{abs} (Figure 6C). The energy absorbed through 'Diverse losses' (VIII, Figure 6D) equaled the energy 'Applied' minus 'Tree' (Figure 6A) minus 'VI' (Figure 6C), and was $50.0 - 46.3 - 2.5 = 1.2$ kJ at $t = 34$ ms. The bending of branches, caused by transverse waves along the upper stem, occurred mainly after T_{abs} and could therefore be neglected in the analysis of W_{cap}.

If the total aboveground energy absorption (I–IV) is analyzed according to height, $< 5\%$ of the absorption in Tree A8 occurred above $z = 9.0$ m (Figure 7), i.e., in the upper two-thirds of the tree. Thus, only the lower third of the stem contributed to the energy absorption capacity of the tree. Analyzed in time, the above- and the belowground energy absorption displayed a general and steady increase during

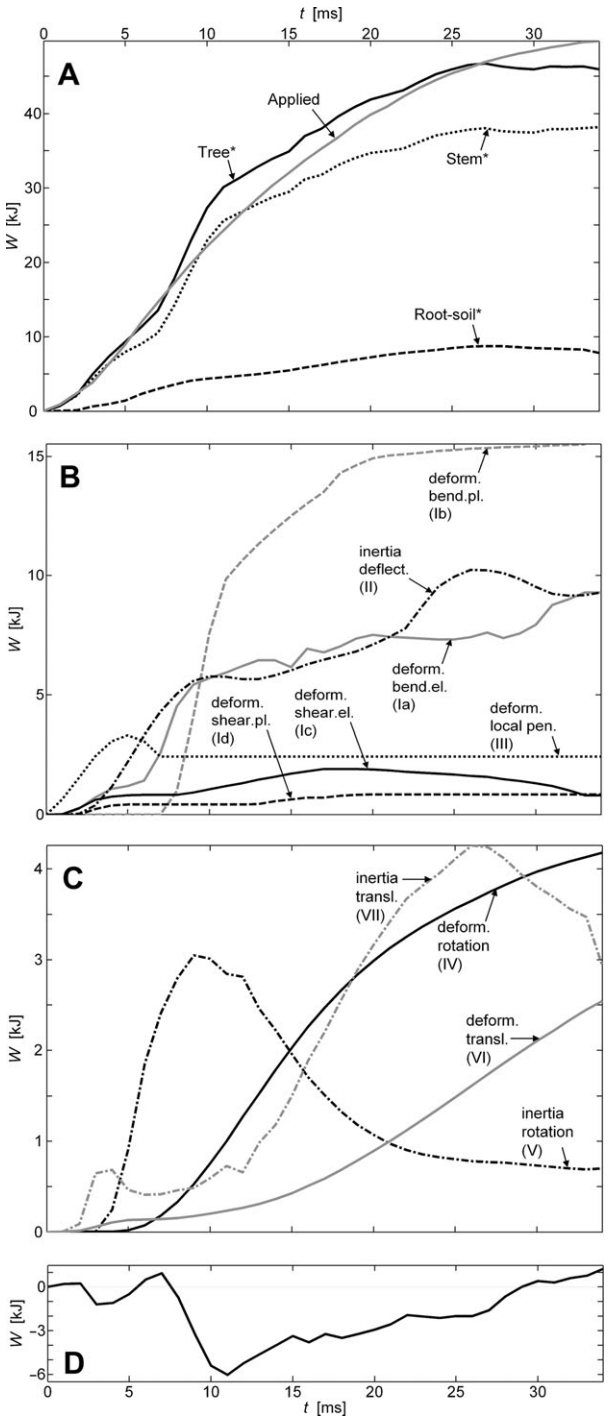

Figure 6. Energy intensities accumulated over time $W(t)$ in Tree A8. (A) The $W(t)$ applied by the trolley and $W(t)$ absorbed by the entire tree, the stem and the root–soil system without (*) considering the energy absorption phenomena VI and VIII. (B) The $W(t)$ for the stem in detail, where el. = elastic and pl. = plastic. (C) The $W(t)$ for the root–soil system in detail. (D) The $W(t)$ for 'Diverse losses' (VIII) (abbreviations are explained in Table 3).

the impact event (Figure 8), contributing 79% and 21%, respectively, of the energy capacity of the tree W_{cap} at $t = 34$ ms.

Table 6. Relative contributions of groups of energy absorption phenomena (I–VIII) to the energy absorption capacity W_{cap} of the tree, the relative contributions of the crown and stem (above ground) and the root–soil system (below ground), the absolute values of W_{cap}, and its ratio to the total energy applied by the impact trolley to the tree W_{app0}. The last row shows mean values for all trees.

Site and tree no.	Stem			Root–soil system				Tree	Total			
	Deform. bending I (%)	Inertia deflect. II (%)	Deform. local pen. III (%)	Deform. rotation IV (%)	Inertia rotation V (%)	Deform. transl. VI (%)	Inertia transl. VII (%)	Diverse losses VIII (%)	Above ground (%)	Below ground (%)	W_{cap} (kJ)	$\frac{W_{cap}}{W_{app0}}(-)$
A1	49	8	6	12	4	10	9	3	65	35	90	1.2
A2	53	14	6	9	3	9	6	1	74	26	131	0.9
A3	43	10	11	11	3	10	8	4	67	33	169	0.78
A4	48	10	7	10	6	9	8	2	67	33	226	0.7
A5	56	16	3	9	4	4	5	3	77	23	129	1.05
A6	50	20	6	12	1	5	3	3	78	22	11	0.75
A7	55	13	5	11	3	7	6	2	74	26	54	0.85
A8	53	19	5	8	1	5	6	2	78	22	50	1.04
A9	59	14	4	8	2	5	5	3	79	21	137	0.9
A10	56	14	5	12	3	4	3	2	77	23	162	1.05
B1	60	22	1	13	1	0	0	3	84	16	96	1.15
B2	50	13	7	7	2	12	9	2	71	29	128	1.06
B3	53	12	7	13	3	6	5	2	73	27	159	0.9
B4	63	18	1	15	1	1	0	1	83	17	98	1.16
B5	51	16	4	13	3	5	4	3	73	27	139	0.69
All	53[1]	15	5	11	3	6	5	2	75	25	119	0.94

[1] On average, composed of 19% pure elastic bending (Ia), 31% plastic bending (Ib), 1.6% elastic shearing (Ic) and 1.7% plastic shearing (Id).

Energy absorption of the trees: summary

The energy absorption in time and space occurred generally in a similar way for all 15 trees. The vertical distribution of energy, however, was influenced by the relative impact height z_0/H. The magnitude of absorption for the different phenomena (I–VII) depended on z_0/H in a linear or logarithmic way. The correlations (R) between z_0/H and the relative energy absorption (Table 6) for the absorption groups were: aboveground, $R = 0.79$; I, $R = 0.66$; II, $R = 0.79$; III, $R = -0.71$; IV, $R = 0.32$; V, $R = -0.52$; VI, $R = -0.78$ and VII, $R = -0.75$. Clearly, the trees absorbed more energy above- than belowground if the impact occurred above a stem height of 0.70 m. Low relative impact height shifted the absorption from the stem (and crown) toward the root–soil system. The kinetic energy of the trolley exceeded W_{cap} for seven test trees and was below W_{cap} for the other eight trees (Table 6). For all trees, the translational stiffness of the root–soil system (cf. Eq. (9)) was best described by $k_t = 1.53 \times 10^6 \mathrm{DBH}^3$ ($R^2 = 0.52$).

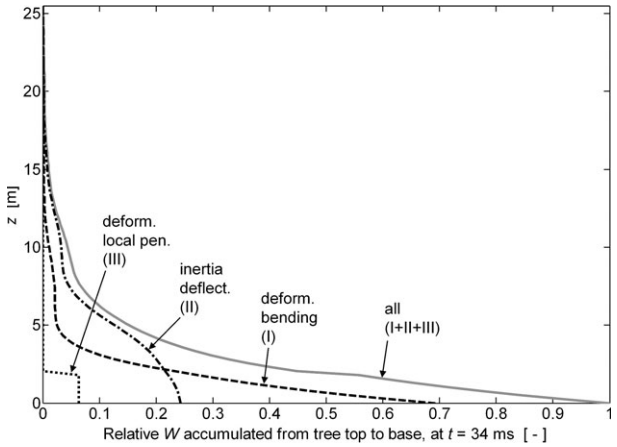

Figure 7. Height-wise (z) energy absorption by the stem of Tree A8 at the end of T_{abs}, i.e., at $t = 34$ ms, including local penetration of the trolley front into the woody stem (III), inertia due to x-wise acceleration of stem and branches (II) and stem-bending (I). The x-graduation is the energy accumulated z-wise, starting at the tree top and ending at the stem base, divided by the total energy (I + II + III) absorbed at $t = 34$ ms.

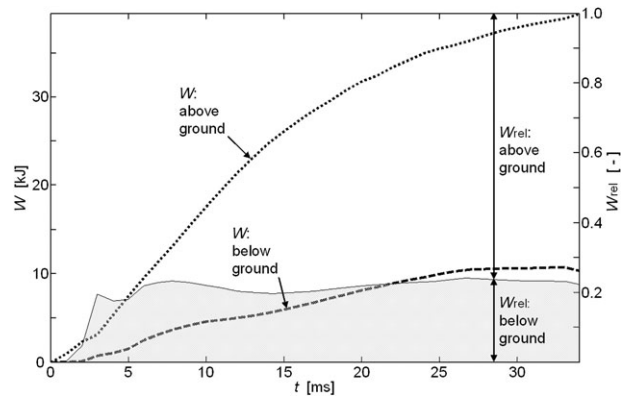

Figure 8. Development over time t of the tree's absolute energy absorption W above- and belowground for Tree A8, and the respective energy absorptions relative to the sum of the absolute values, W_{rel}.

On the basis of the tree characteristics (Table 1) and W_{cap} (Table 6) of the tested tree, the predicted energy capacity of tree $W_{cap,p}$ could be well described with four models (Table 7). If the models of $W_{cap,p}$ described by DBH^{α} (nos. 2 and 4) were optimized for a low standard error $\mathrm{SE}(Y_i - Y_{pi})$, instead of a high R^2, the exponent took the value $\alpha = 2.16$. Changing the exponent value in Model 1 did not improve its quality. For identical DBH and z_0/H, the W_{cap} of trees at Site A was on average 5% lower than the W_{cap} of trees at Site B (Figure 9), but the difference was statistically insignificant ($P = 0.37$). Tree A7, which had signs of rot in the center of the stem base, had a W_{cap} 30% lower than that predicted by Model 1.

Discussion

Our analysis of trees impacted by simulated rockfalls combines and makes use of: (1) information on the mechanical properties of tree components, such as the stem and the root–soil system subject to bending (Lundström et al. 2007*b*, 2008*b*); (2) a simplified tree model built from such components and (3) stem deflections in time assessed from digital images. The method provides results in sufficient detail to understand how a tree reacts and absorbs energy during a rock impact, which were the two main aims of the study. The third objective was to explore the energy absorption capacity W_{cap} of the tree. Here, the energy of the trolley W_{app0} should ideally exceed the energy absorption capacity W_{cap} of the tree by a few percent, to avoid extrapolation of the tree's mechanical behavior, where W_{cap} can be predicted statistically (e.g., Table 7) or mechanically (tree model). If only W_{cap} is required, W_{app0} should exceed W_{cap} with a larger margin, and attention should be paid to the additional inertia forces induced.

Tree mechanical properties contributed to uncertainty with respect to all three aims of our study. Minimizing this uncertainty requires detailed investigations of the tree before and after the impact experiment (cf. Table 2). Less information is known about how the root–soil system deforms in translation, even after this study. To improve the impact experiment, we suggest filming the trolley–tree interaction at a higher image frequency than that in our study with at least the same pixel resolution. Other full-scale experiments for exploring the tree–rockfall interaction have been used at a more coarse level of detail (Dorren and Berger 2006) or described rather briefly (Mizuyama and Narita 1988), making it difficult to compare methods.

Our observations confirm the complex behavior of a tree during a rock impact. Nevertheless, the mechanical behavior of the tree is logical and includes no strange or unex-

Table 7. Four regression models describing the energy absorption capacity W_{cap} of the tree. Abbreviations: Y = response variable (kJ); subscript p refers to predicted value; X = explanatory variable (basic unit is m); ln(b) = intercept, in the de-logarithmic model as $W_{cap} = b \cdot DBH^{a1}$; a = regression coefficient; $\boldsymbol{a}$ = standardized regression coefficient and $|\boldsymbol{a_1}/\boldsymbol{a_2}|$ = the impact of the first model variable X_1 on Y_i relative to the impact of the second variable X_2 on Y_i. Values of Y_i and X_j are listed top down according to their ranking (R^2) and contribution ($|\boldsymbol{a_j}|$) to the model, respectively. Significance: *, $P < 0.05$; **, $P < 0.01$ and ***, $P < 0.001$.

Model					Variables				
i	Y_i	SE(Y_i)	SE($Y_i - Y_{pi}$)	R^2	X_j	a_j	$\boldsymbol{a_j}$	$\lvert\boldsymbol{a_1}/\boldsymbol{a_2}\rvert$	SE(X_j)
1	W_{cap}	14.0	17.3	0.90	DBH^2	9.02E + 02***	4.53	3.15	0.070
					DBH^2(z_0/H)	−7.15E + 03**	−1.44	–	0.003
2	ln(W_{cap})	0.191	0.269	0.88	ln(DBH)	3.01E + 00***	3.63	–	0.229
					ln(b)	7.25E + 00***	–	–	–
3	W_{cap}	14.0	20.6	0.87	DBH^2	7.72E + 02***	3.87	6.38	0.070
					z_0	−2.39E + 01*	−0.61	–	0.355
4	W_{cap}	14.0	23.5	0.81	DBH^2	6.40E + 02***	3.21	–	0.070

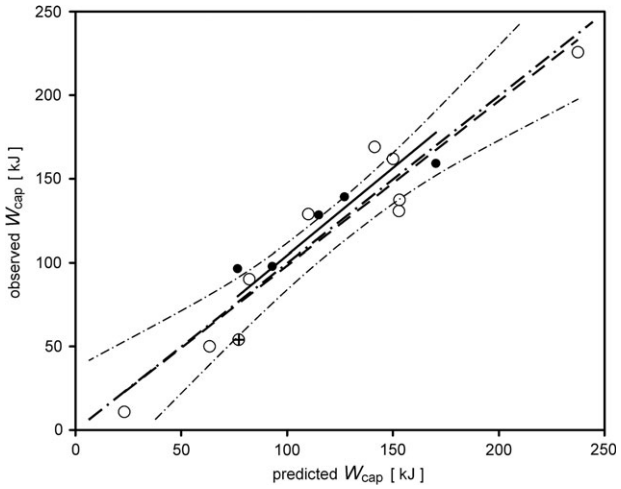

Figure 9. Observed energy absorption capacity W_{cap} plotted against the predicted W_{cap} for the ten Norway spruce trees at Site A (unfilled dots) and the five trees at Site B (filled dots) with linear regressions (continuous and dash lines, respectively). The dash-dot lines show the linear regression (heavy) and the bounds for a 95% confidence interval (fine) for all 15 trees. The tree with rot in the center of the stem base (A7) is indicated with a '+' in the circle.

pected phenomena. Because our impact experiment was labor-intensive, it would be worthwhile attempting to simulate rock–tree interactions with computer models, provided that the mechanical properties of the tree components involved in the major energy absorption phenomena (I–VII) are sufficiently well known. For this purpose, a suitable method to assess the translational deformation properties of the tree anchorage would be of great value. Additional full-scale tests are needed to calibrate phenomena that are not investigated in this work, such as other impact speeds and different impact shapes. A combination of in situ and computer experiments with tree–rock interactions should help increase the precision of estimates of how much protection forests can provide against rockfall and thus improve management strategies.

A tree's energy absorption capacity W_{cap} is effectively a combination of several phenomena. For all the Norway spruce trees tested, W_{cap} was largely dominated by the energy absorption in the stem (Table 6) and in general was restricted by bending stresses at the impact location (Figure 4D). When a tree is subject to typical impact heights under natural conditions (above 1.0 m in our study, Perret et al. 2004), the stem is decisive because it mobilizes much of the energy absorbed and it provides the weakest link in the transport of the impact force to the ground. Stem diameter has the greatest impact on W_{cap}, whereas the bending strengths and density of the stem are less relevant. The root–soil anchorage seems to provide the weakest link only if the tree is impacted at a low stem height and if it grows in a shallow soil (Table 5). The trees that are more firmly anchored than the trees that we tested would mobilize more energy absorption in the root–soil system when impacted at a low stem height. As a consequence of the stiffer stem base, more energy would also be absorbed through the local stem penetration of the rock front. It is, however, improbable that this penetration would be a limiting factor for the tree's capacity to absorb energy, similar to stem-bending (cf. Figure 4D and Table 5), unless the impacting rock edge is sharp enough to crosscut the stem.

We defined the energy absorption capacity W_{cap} of a tree as the maximum kinetic energy a tree can withstand without falling over. Provided that the tree recovers from the impact after a while, it can still continue to fulfil its protection function. If the tree falls, the energy absorption capacity is higher, because more of the energy related to the strain and inertia of the stem and of the root–soil system can be mobilized. The energy dissipation for *Abies alba* (Mill.) with a DBH = 0.40 m when completely destroyed by a rock was estimated (Dorren and Berger 2006) to be about 160 kJ. The corresponding W_{cap} of the *P. abies* in our study was about 100 kJ. It is likely that this 60 kJ difference is partly because the *A. alba* tree was better anchored than the *P. abies* tree that we tested. The difference in energy absorption for the root–soil system subject to rotation was about 50% (Stokes et al. 2005, Lundström et al. 2007*b*).

When selecting a prediction model for the energy absorption capacity of a tree, one should consider not only the statistical behavior of the linear regression model, but also the expected mechanical behavior of the tree–rock interaction. The strain and inertia energies absorbed in the stem are proportional to the woody stem diameter to the second and the third power, respectively, and the energy absorbed in the root–soil system subject to rotation is proportional to the DBH to the third power. How these energies are mobilized will depend on the height, speed and angle of the rock impact. This was taken into account for the models in Table 7, as far as the available data allowed. Whether the four models are valid beyond the range for which they were tested ($0.2 < \text{DBH} < 0.6$ m and $z_0/H < 0.1$) is uncertain. What is striking is that the models including z_0 yield negative W_{cap} values for high impacts. This is understandable because the relationship between W_{cap} and z_0/H is logarithmic (Jonsson 2007) and not linear. It will be difficult to find a general allometric model that can precisely predict the energy absorption along the whole stem. However, trees clearly have a significant braking effect on falling rocks, and this study has contributed to our understanding of this effect. The findings should contribute to more precise rock–forest interaction models, thus improving the basis for managing protection forests.

Acknowledgments

The authors are indebted to the European Commission for funding the project 'Rockfor' (QLK5-CT-2000-01302) and to the Board of the Swiss Federal Institutes of Technology for funding the project Natural Hazards and Tree Stability (Naturereignisse und Baumstabilität). Thanks are also due to Bruno Fritschi for help with the metrology, to Matthias Kalberer, Holger Simon and the other people involved in the field work for assisting with the experiments, and to Silvia Dingwall for revision of the text.

References

Azzoni, A. and M.H. Defreitas. 1995. Experimentally gained parameters, decisive for rock fall analysis. Rock Mech. Rock Eng. 28:111–124.

Bragov, A. and A.K. Lomunov. 1997. Dynamic properties of some wood species. J. Phys. IV 7:487–492.

Brüchert, F., G. Becker and T. Speck. 2000. The mechanics of Norway spruce [*Picea abies* (L.) Karst]: mechanical properties of standing trees from different thinning regimes. For. Ecol. Manag. 135:45–62.

Chau, K.T., R.H.C. Wong and J.J. Wu. 2002. Coefficient of restitution and rotational motions of rockfall impacts. Intl. J. Rock Mech. Min. Sci. 39:69–77.

Chopra, A.K. 1995. Dynamics of structures: theory and applications to earthquake engineering. Prentice Hall, Englewood, NJ, 729 p.

Clough, R.W. and J. Penzien. 1993. Dynamics of structures. 2nd Edn. McGraw-Hill, New York, 738 p.

Cook, R.D., D.S. Malkus and M.E. Plesha. 2002. Concepts and applications of finite element analysis. 4th Edn. Wiley, New York, 719 p.

Dinwoodie, J.M. 2000. Timber: its nature and behaviour. 2nd Edn. E&FN SPON, London, 257 p.

Dorren, L.K.A. and F. Berger. 2006. Stem breakage of trees and energy dissipation during rockfall impacts. Tree Physiol. 26:63–71.

Dorren, L.K.A. and A.C. Seijmonsbergen. 2003. Comparison of three GIS-based models for predicting rockfall runout zones at a regional scale. Geomorphology 56:49–64.

FAO. 1998. Soil map of the world. Revised legend. *In* World Soil Resources Report, Vol. 60. FAO-UNESCO, Food and Agriculture Organisation, United Nations, Rome, 119 p.

Hakkila, P. 1972. Mechanized harvesting of stumps and roots. Commun. Inst. For. Fenn., Helsinki, 71 p.

Heidenreich, B. and V. Labiouse. 2004. Small-scale experimental study of rockfall impacts on granular slopes. Riv. Ital. Geotecnica 38:80–91.

Jonsson, M.J. 2007. Energy absorption of trees in a rockfall protection forest. Monogr. Swiss Federal Institute of Technology, Zürich, 209 p.

Jonsson, M.J., A. Foetzki, M. Kalberer, T. Lundström, W. Ammann and V. Stöckli. 2006. Root–soil rotation stiffness of Norway spruce (*Picea abies* L. Karst) growing on subalpine forested slopes. Plant Soil 285:267–277.

Jonsson, M.J., A. Foetzki, M. Kalberer, T. Lundström, W. Ammann and V. Stöckli. 2007. Natural frequencies and damping ratios of Norway spruce (*Picea abies* (L.) Karst) growing on subalpine forested slopes. Trees 21:541–548.

Kollmann, F.F.P. 1968. Principles of wood science and technology. *In* Solid Wood, Vol. 1. Springer-Verlag, Berlin, 592 p.

Krummenacher, B. and H.-R. Keusen. 1997. Steinschlag-Stutzbahnen – Modell und Realität. Proc. Société Suisse de Mécanique des sols et des roches, réunion d'automne, Montreux, pp 17–23.

Lundström, T., T. Jonas, V. Stöckli and W. Ammann. 2007*a*. Anchorage of mature conifers: resistive turning moment, root–soil plate geometry, and orientation of root growth. Tree Physiol. 27:1217–1227.

Lundström, T., M.J. Jonsson and M. Kalberer. 2007*b*. The root–soil system of Norway spruce subjected to turning moment: resistance as a function of rotation. Plant Soil 300:35–49.

Lundström, T., T. Jonas and A. Volkwein. 2008*a*. Analysing the mechanical performance and growth adaptation of Norway spruce using a nonlinear finite-element model and experimental data. J. Exp. Bot. 59:2513–2528.

Lundström, T., M. Stoffel and V. Stöckli. 2008*b*. Fresh-stem bending of silver fir and Norway spruce. Tree Physiol. 28:355–366.

Mizuyama, T. and H. Narita. 1988. Debris flow control by woods and their impact energy absorptivity. Proc. Interpraevent, Graz, pp 173–181.

Murray, Y.D. 2003. Development of a wood material model for roadside safety applications. Aptek Inc., Colorado Springs, pp 1–10.

Perret, S., M. Baumgartner and H. Kienholz. 2004. Rockfall injuries in mountain forests – a method for data collection and analysis. Proc. Interpraevent, Riva/Trient, V, pp 87–98.

Polomski, J. and N. Kuhn. 2001. Wurzelhabitus und Standfestigkeit der Waldbäume. Fortswiss. Centralbl. 120:303–317.

Stoffel, M., A. Wehrli, R. Kuhne, L.K.A. Dorren, S. Perret and H. Kienholz. 2006. Assessing the protective effect of mountain forests against rockfall using a 3D simulation model. For. Ecol. Manage. 225:113.

Stokes, A., F. Salin, A.D. Kokutse, S. Berthier, H. Jeannin, S. Mochan, L. Dorren, N. Kokutse, M. Abd Ghani and T. Fourcaud. 2005. Mechanical resistance of different tree species to rockfall in the French Alps. Plant Soil 278:107–117.

Sundström, B. 1998. Handbok och formelsamling i Hållfasthetslära, Vol. 1. Department of Solid Mechanics, Royal Institute of Technology, Stockholm, Department of Solid Mechanics, Royal Institute of Technology, 398 p.

Wessolly, L. and M. Erb. 1998. Handbuch der Baumstatik und Baumkontrolle. Patzer, Berlin, 270 p.

Zinggeler, A., B. Krummenacher and H. Kienholz. 1991. Steinschlagsimulation in Gebirgswäldern 3, Berichte und Forschungen, Geographisches Institut, Univ. Freiburg, pp 61–70.

Appendix

Table A1. List of the symbols and notations used in the study and their definitions and units.

Notation	Description	Unit
A, A_s	Cross-sectional area of the woody stem and its effective shear area	m^2
B	Double bark thickness	m, mm
β_s; β_0	Slope of the soil; angle to the horizontal of the impact direction on the tree	°
D_1, D	Stem diameter over and under bark	m, mm
DBH	Stem diameter over bark at breast height (z = 1.3 m)	m, cm
dW	Energy intensity	J s^{-1}, W, kW
ε; ε_1	Stem-bending strain (without the contribution from shear deformation); value at which the behavior changes from ideal-elastic to ideal-plastic	–
ϕ	Rotation of the root–soil system around the y-axis	rad, °
G	Modulus of shearing elasticity along the stem	MPa
γ; γ_1	Shear strain along the stem; value at which the behavior changes from ideal-elastic to ideal-plastic	–
H	Tree height	m
I	Cross-sectional moment of inertia of the woody stem	m^4
k_p	Penetration stiffness for the trolley front into the woody stem	N mm^{-1}
k_t	Translational stiffness of the root–soil system pushed along the slope (cf. Eq. (9))	N
M^0; $M^0{}_{max}$	Resistive turning moment around the y-axis of the root–soil system; maximum M^0	MPa
MOE	Modulus of bending elasticity of the stem cross section	MPa, GPa
m_{tree}	Total aboveground tree mass	kg
ρ_w	Bulk density of the fresh stem on bark	kg m^{-3}
RW; $_{i,o}$	Width of annual rings; reference to the mean of the inner 75% radial part of the stem cross section and to the mean of the remaining outer part	mm
σ, σ_{max}	Bending stress and strength of the stem cross section	MPa
t	Time after the first contact between the trolley and the tree	s, ms
T_{abs}	Period from t = 0 until the intensity of the tree's energy absorption reaches a value close to zero	s, ms
τ, τ_{max}	Shear stress and strength of the stem section in the direction along the stem	MPa
V; V_{part}	Volume of the root–soil plate; the V that effectively contributes to inertia during the impact	m^3
W	Energy	J, kJ
W_{cap}; $W_{cap,p}$	Energy absorption capacity of the tree, being the maximum W_{app0} a tree can withstand without falling over; the predicted W_{cap}	J, kJ
W_{app}; W_{app0}	Kinetic energy applied be the impact trolley on the tree; W_{app} at time zero	J, kJ
x, y, z	Tree coordinates: origin at stem base; x = horizontal stem deflection; z = height above origin (cf. Figure 3A)	m
x', y', z'	Local coordinates of the impact trolley: origin at its center of gravity; x' = impact direction; z' = upward (cf. Figure 3B)	m
I, II, …, VIII	Denominations for groups of energy absorption phenomena (cf. Table 3)	

Chapter VI

Analysing the mechanical performance and growth adaptation of Norway spruce using a non-linear finite-element model and experimental data

Journal of Experimental Botany, Vol. 59, No. 9, pp. 2513–2528, 2008 (92)
doi:10.1093/jxb/ern116

Journal of Experimental Botany
www.jxb.oxfordjournals.org

RESEARCH PAPER

Analysing the mechanical performance and growth adaptation of Norway spruce using a non-linear finite-element model and experimental data

T. Lundström[1,2,*], T. Jonas[1] and A. Volkwein[1]

[1] *WSL, Swiss Federal Institute for Snow and Avalanche Research SLF, 7260 Davos Dorf, Switzerland*

[2] *Laboratory of Dendrogeomorphology, University of Fribourg, 1700 Fribourg, Switzerland*

Received 14 December 2007; Revised 26 March 2008; Accepted 31 March 2008

Abstract

Thirteen Norway spruce [*Picea abies* (L.) Karst.] trees of different size, age, and social status, and grown under varying conditions, were investigated to see how they react to complex natural static loading under summer and winter conditions, and how they have adapted their growth to such combinations of load and tree state. For this purpose a non-linear finite-element model and an extensive experimental data set were used, as well as a new formulation describing the degree to which the exploitation of the bending stress capacity is uniform. The three main findings were: material and geometric non-linearities play important roles when analysing tree deflections and critical loads; the strengths of the stem and the anchorage mutually adapt to the local wind acting on the tree crown in the forest canopy; and the radial stem growth follows a mechanically high-performance path because it adapts to prevailing as well as acute seasonal combinations of the tree state (e.g. frozen or unfrozen stem and anchorage) and load (e.g. wind and vertical and lateral snow pressure). Young trees appeared to adapt to such combinations in a more differentiated way than older trees. In conclusion, the mechanical performance of the Norway spruce studied was mostly very high, indicating that their overall growth had been clearly influenced by the external site- and tree-specific mechanical stress.

Key words: Climate, critical load, mechanical optimisation, model performance and errors, stem taper, structural behaviour, thigmomorphogenesis.

Introduction

When a tree deflects, there is a change in the way loads, such as wind and snow, apply upon the tree. This phenomenon, which is called geometric non-linearity, is considered significant for a tree if the top deflection relative to height is larger than 20%. Until now, geometric non-linearity has rarely been fully considered in the mechanical analysis of flexible plants (Yang *et al*., 2005). In addition, trees also exhibit material non-linearity because they are composed of natural materials. This means that their mechanical properties depend on the magnitude of the load. Typically, the rotation of the root–soil system depends, in a non-linear way, on the applied turning moment of the root–soil system (Lundström *et al*., 2007*c*), just as the stem deflection due to bending depends on the applied bending stress (Lundström *et al*., 2008). These material non-linearities have never, to the author's knowledge, been considered in the analysis of tree mechanics. Consequently, it is not known which role they play in how a tree reacts to external load or under what conditions they may be mechanically advantageous for the tree, as they contribute to its flexibility.

Stresses in the tree stem and anchorage result from combinations of wind and snow load, and the overhanging weight of the leaning tree. The magnitude and frequency of such loads depend on the tree and stand characteristics, climate, and season. A sufficiently heavy load will cause the stem or the tree anchorage to fail. The type of failure depends on the stem and anchorage strengths, and on where and in which direction the load is applied. The magnitude of the failure load will, in addition, depend on how well the tree, including the crown, stem, and

* To whom correspondence should be addressed. E-mail: t.lundstroem@slf.ch

anchorage, has adapted its growth to the particular load combination (Telewski, 1995; Nicoll and Ray, 1996; Di Iorio *et al*., 2005). The most common failure mode of Norway spruce [*Picea abies* (L.) Karst.] is uprooting, but stem breakage may occur if the soil is frozen and if the crown is loaded with snow (Peltola *et al*., 1997, 2000). It is not clear to what extent a tree mutually adapts its stem and anchorage strengths to resist various types and combinations of natural loads.

Thigmomorphogenesis is the response of plants to mechanical stress (Jaffe, 1973; Telewski, 2006), with respect to their morphology and material properties (Chiatante *et al*., 2002). So far, most studies of thigmomorphogenesis have focused on isolated parts of the plant rather than on the plant as a whole (Moulia *et al*., 2006). Clearly, the spatial and temporal focus of such studies will affect how much detail they give in assessing and analysing the stress and growth histories of plants.

Wind-induced stem-bending stress has been the topic of several studies (Milne, 1991; Morgan and Cannell, 1994; Wood, 1995; Dean *et al*., 2002), where stress uniformity along the stem has been attributed to its taper. In addition to this geometric adaptation, the stem also adapts anatomically to mechanical stress through differential radial and apical growth (Meng *et al*., 2006). As the tree grows larger, this normally leads to stronger and stiffer wood forms along the lower, outer part of the stem (Ylinen, 1952; Niemz, 1993; Lundström *et al*., 2008), where the largest bending stresses due to wind are expected. Studying the thigmomorphogenesis of the stem, therefore, seems to require including both the taper and the material properties of the stem in the analysis.

This paper investigates how Norway spruce reacts to combinations of natural loading. For this purpose, a non-linear numerical tree model is provided with extensive experimental data. These data are first used to test the model performance. Then, on the basis of the model results, the stem thigmomorphogenesis is analysed with a novel method that considers both the taper and the material properties of the stem. The focus is on the mechanics of the tree as a whole, and the properties of growth were used to parameterize its mechanics. The findings are used to test three hypotheses: (i) a geometric and material non-linear analysis is required to reproduce *in situ* stem deflections and analyse critical loads; (ii) the strengths of the stem and the tree anchorage mutually adapt to the most frequent combination of seasonal tree-state and load; and (iii) the thigmomorphogenesis of the stem is the result of the prevailing combination of seasonal tree-state and load. Exploring these hypotheses should improve researchers' general understanding of how Norway spruce grows and thus contribute to the informed management of Norway spruce forests.

Materials and methods

Trees and sites

The selection of the 13 Norway spruces [*Picea abies* (L.) Karst.] analysed was intended to cover not only a range of frequent tree sizes and of typical growth conditions in the Alps (Schweingruber, 1996), but also a spectrum of different tree ages, social states, sites, and local stand densities. By taking into account these factors, it would be possible to analyse the tree growth response generally and spatiotemporally according to the mechanical loading. The site and tree characteristics relevant to this study are listed in Table 1. These, as well as all experimental data used in this study, have been obtained from plots used in winching tests (Kalberer, 2007; Lundström *et al*., 2007*b*, *c*). The standing tree is referred to with an (x, y, z)-coordinate system, with its origin (0, 0, 0) at the stem base, $z=H$ at the top of the tree, and x in the direction of the horizontal stem deflection. r is the radial distance from the pith, *DBH* the stem diameter over bark at breast height (z=1.3 m), and B the bark thickness. The symbols used in this paper are summarized in Table A1 in the Appendix.

Table 1. *Site and tree characteristics of the 13 spruces analysed*

Plot, local delimitation of the forest stand; *DBH*, stem diameter at breast height (1.3 m); H, tree height; L_C, crown length; z_{Cc}, height of the crown's area centre; AGE, cambial age; Social status (according to Dobbertin *et al*., 1997) in relation to neighbouring trees.

Plot no.	Tree no.	Elevation (m asl)	Exposition	Slope (°)	Stand density (trees ha^{-1})	*DBH* (cm)	H (m)	L_C/H (−)	z_{Cc}/H (−)	AGE at z=1.3 m (years)	Social status
1	11	1620	NE	35	1200	15	16	0.88	0.56	64	Dominated
2	12	1620	NE	35	800	15	15	0.86	0.53	47	Co-dominant
3	13	1780	ESE	31	500	22	21	0.76	0.57	103	Dominated
3	14	1780	ESE	31	500	35	26	0.80	0.56	118	Co-dominant
4	15	1650	NNW	33	500	44	32	0.57	0.68	177	Dominant
3	16	1780	ESE	31	500	52	33	0.87	0.51	267	Dominant
3	17	1780	ESE	31	500	58	35	0.82	0.52	271	Superior
5	21	460	NNW	4	350	19	17	0.82	0.56	28	Co-dominant
5	22	460	NNW	4	350	29	26	0.76	0.56	43	Co-dominant
6	23	620	NNE	5	250	40	36	0.44	0.77	85	Co-dominant
6	24	620	NNE	5	250	48	36	0.36	0.80	84	Dominant
7	25	620	NNE	5	120	65	40	0.60	0.67	83	Dominant
8	26	620	NNE	5	80	73	38	0.66	0.65	81	Dominant

The trees 11–17 (Table 1) had a mean $B(z{=}1.3\text{ m})/(DBH/2)$ of 7%. They grew at a high elevation (HE) on four closely situated plots (at about 46°46′ N, 9°49′ W) south of Davos, Switzerland. At these locations, the B-horizon (0.1 m<depth<0.4 m) is a dystric Cambisol. The 5:50:95% percentiles of daily temperature observed over the last 20 years are –8:+4:+15 °C and of 10-min-wind 0:2:6 m s^{-1}. The annual maximum 10-min-wind is 15 m s^{-1} and the annual precipitation 1100 mm. Almost half the precipitation falls as snow and there is snow cover for 6 months a year (MeteoSwiss, 2007. Climate database of the Swiss National Weather Service, http://www.meteoschweiz.ch/web/en/services/data_portal.html). The soil-frost depth generally increases from November to culminate with a mean:max depth of 0.25:0.75 m beneath the crown in April (Stadler *et al*., 1998; MeteoSwiss, 2007, http://www.meteoschweiz.ch/web/en/services/data_portal.html).

The trees 21–26 had a mean $B(z{=}1.3\text{ m})/(DBH/2)$ of 6%. They grew at a low elevation (LE) on four plots close to Zurich, Switzerland, with plots 5–6 at 47°14′ N, 8°53′ W and plots 7–8 at 47°22′ N, 8°28′ W. At these locations, the B-horizon (0.4 m<depth<1.0 m) is a dystric Cambisol with presence of Luvisol. Here, the 5:50:95% percentiles of daily temperature are –2:+10:+21 °C and of 10-min-wind 0:2:6 m s^{-1}. The annual maximum 10-min-wind is 22 m s^{-1}, and the annual precipitation 1150 mm. Almost 10% of the precipitation falls as snow and there is snow cover for about 33 d a year (MeteoSwiss, 2007, http://www.meteoschweiz.ch/web/en/services/data_portal.html). The maximum soil-frost depth beneath the crown is less than 0.10 m (Stadler *et al*., 1998; MeteoSwiss, 2007, http://www.meteoschweiz.ch/web/en/services/data_portal.html).

Attribution of mechanical properties to the tree model

The tree is divided into a sufficient number of equally long elements for which the mechanical properties are specified. In this study 100 elements are used. These elements have the idealized shape of circular cylinders, because the stem diameter on bark (D) differed little in the x- and y-directions (2% on average). Each element is attributed a stem diameter under bark $D_{ub}(z)$, according to Table 2 using the following measured data: D in the x- and y-directions every per cent of H up to $z/H{=}0.20$, and then every metre up to H; B in the x- and y-directions at $z/H{=}0.05$ and at least two additional stem heights (in stem discs). Each element is further attributed a stem weight and a crown weight and diameter, which are polynomials of z based on measurements every metre of tree height.

Table 2. *Sequential steps in the parameterization of the stem diameter as a function of stem height*

D, stem diameter over bark; D_{ub}, stem diameter under bark; B, bark thickness. Step 4 is not used by the tree model, only to analyse stem morphology.

Step	Description
1	Polynomial fit of $D_x(z)$ and of $D_y(z)$ with a polynomial degree so that the fitting error is <1% for the 2/3 lower stem and <5% for the 1/3 upper stem (the resulting degree was >16).
2	Calculation of $B_x(z)$ and $B_y(z)$ using a 5-degree polynomial of $B(z)/D(z)$ (Laasasenaho *et al*., 2005) scaled with the measured B_x and B_y at $z/H{=}0.05$. The fitting errors at the additional $B(z)$-measurements were all within the limits of the absolute values at the corresponding heights in step 1.
3	Calculation of $D_{ubx}(z) = D_x(z) – 2B_x(z)$, $D_{uby}(z) = D_y(z) – 2B_y(z)$, and the geometric mean $D_{ub}(z) = (D_{ubx}(z)D_{uby}(z))^{0.5}$.
4	Calculation of the normalized stem diameter $D_{05}(z) = D(z)/D(z/H{=}0.05)$, in the x- and y-direction, as the geometric mean, under and over bark.

Here, the crown diameter is the geometric mean of the extensions in the x- and y-directions. The stem-section elements are finally given the following deformation properties: a bending stress as a non-linear function of bending strain and stem height $\sigma(\varepsilon, z)$ (Equation 1, an approximation) and a shear stress as a non-linear function of shear strain $\tau(\gamma)$ (Equation 2, a simplification):

$$\sigma(\varepsilon, z) = \left(\overline{\frac{\sigma(\varepsilon)}{\sigma_{max}}}\right) \times \left(\overline{\frac{\sigma_{max}(z)}{\sigma_{max}(0.05H)}}\right) \times \sigma_{max}(0.05H) \quad (1)$$

$$\tau(\gamma, z) = \tau(\gamma) = \left(\overline{\frac{\sigma(\varepsilon)}{\sigma_{max}}}\right) \times \tau_{max} \quad (2)$$

where σ_{max} is the bending strength of the stem cross-section (sometimes called the modulus of rupture) and τ_{max} is the shear strength of the stem section (Table 3). The first two factors in Equation 1 are normalized mean (roof sign) curves of $\sigma(\varepsilon)$ and of $\sigma_{max}(z)$, respectively (Lundström *et al*., 2007*a*, 2008). The stem base is flexibly clamped to the ground. The lower end of the lowest element (at $z{=}0$) is therefore attributed a resistive rotational moment M^0 as a non-linear function of the rotational angle ϕ (Equations 3 and 4):

$$M^0(\phi) = M^0_{max} \times \overline{M^0_n}(\phi_n) \quad (3)$$

With

$$M^0_n = \frac{M^0}{M^0_{max}}; \phi_n = \frac{\phi}{\phi(M^0_{max})} \quad (4)$$

where $\overline{M^0_n}$ is the mean $M^0_n(\phi_n)$-curve for spruces at the two elevations (Lundström *et al*., 2007*c*), M^0_{max} is the maximum of M^0 (sometimes called the anchorage strength), and $\phi(M^0_{max})$ is the ϕ at M^0_{max} (Table 3). The idealized M^0-shape, resulting from $\overline{M^0_n}$, was used instead of the measured M^0-shape in order to simplify and systemize the modelling. This approximation was tested to make sure it had no significant effect on the results.

All the parameters in Table 3 are measured values (winching experiments), except for σ_{max} and τ_{max}. The cross-sectional σ_{max} was calculated on the basis of the annual ring width RW and the knottiness Q between the pith (radius $r{=}0$) and the bark ($r{=}D_{ub}/2$) as variables in statistical-mechanical models (Lundström *et al*., 2007*a*, 2008). RW was scanned and measured digitally (WOODSCAN 4.5, Freiburg University, Germany) in stem discs, in eight azimuthal directions as a function of r, and then averaged at the same age. Q was measured manually in digital photos of the discs and averaged accordingly. Data on $RW(r)$ and $Q(r)$ were obtained from at least four discs cut from the stem between $z{=}0$ and $z{=}H$, in addition to the disc at $z{=}0.05H$. The values of σ_{max}, calculated on the basis of the $RW(r)$ and $Q(r)$ in these additional discs, differed little from the $\sigma_{max}(z)$-values obtained with Equation 1. The latter $\sigma_{max}(z)$-curves were therefore used throughout the analysis. The cross-sectional τ_{max} was estimated (Lundström *et al*., 2008) on the basis of the mean RW of the inner 75% radial part of the stem cross-section (RW_i). RW_i was found to vary little with stem height, so $\tau_{max}(z)$ was set as a constant $= \tau_{max}(z{=}0.05H)$.

It is known that frost increases the strength and stiffness of moist wood and soil (Kollmann, 1968; Andersland and Ladanyi, 2004). Silins *et al*. (2000) showed that $MOE(z)$ of fresh wood increases by a factor ≈1.5. Trees winched in the winter at the HE-site (SLF, unpublished data) show that M^0_{max} increases by a factor ≈2.5. These factors were adopted to account for the frozen stem and soil.

Loads on the tree and combinations of tree state and snow load

In this study, intercepted snow provides the vertical load on the tree. Here, two nominal values of snow-water equivalent precipitation

Table 3. *Mechanical and growth characteristics of the trees analysed*

RW, annual ring width, where 'i' refers to the mean of the inner 75% radial part of the stem cross-section, and 'o' to the mean of the remaining outer radial part; ρ_w, bulk density, σ_{max}, bending strength, and τ_{max}, shear strength of the fresh stem. The other abbreviations are explained in the text.

Tree no.	M^0_{max} (KNm)	$\phi(M^0_{max})$ (°)	Values of the stem section at $z=0.05H$				
			RW_i (mm)	RW_o (mm)	ρ_w (kg m^{-3})	σ_{max} (MPa)	τ_{max} (MPa)
11	12	21.0	1.1	1.3	840	52.6	3.5
12	10	22.0	1.4	2.3	780	46.0	3.1
13	30	10.0	1.5	0.6	880	59.6	3.1
14	75	7.4	1.6	1.0	830	54.0	3.0
15	139	5.3	1.3	0.9	860	56.6	3.3
16	231	3.3	0.9	1.1	870	55.4	3.8
17	239	3.0	0.9	0.6	920	62.9	3.7
21	41	18.0	3.7	3.1	600	38.8	1.8
22	98	8.4	3.3	3.4	610	39.1	2.0
23	228	5.5	2.5	2.2	740	44.0	2.3
24	308	4.8	3.4	2.0	710	42.2	1.9
25	753	3.3	4.0	3.5	660	36.1	1.7
26	883	2.6	4.3	4.6	640	33.9	1.6

were first considered, $SWE_{01}=20$ and $SWE_{02}=40$ mm. The SWE effectively intercepted by the crown area projected on the ground was then calculated as $SWE = SWE_0 \times \pi/4 \times \text{atan}(\rho_{cv}/10)$, where ρ_{cv} is the vertical crown density = total crown mass/projected crown area on the ground, and 10 kg m^{-2} is the reference ρ_{cv}. This expression accounts for the fact that a denser crown has a better capacity to intercept snow (Strobel, 1978). The total snow loads on the crown, resulting from SWE_{01} and SWE_{02}, are denoted SL1 and SL2, respectively. They were distributed height-wise in proportion to the mass per height-section of the crown. This meant the top of the crown was attributed relatively more snow than its base because the crown density increased with height. SL1 was estimated to be the maximum amount of snow that can remain on the crown of a spruce of mean size when subjected to strong wind and SL2 the amount when there is almost no wind (Pomeroy and Gray, 1995; Bründl, 1997). The height-wise mean snow weight along the crown ranged between 6 kg m^{-1} and 48 kg m^{-1} for SL1 and between 12 kg m^{-1} and 95 kg m^{-1} for SL2.

The eight most significant combinations of seasonal tree state and snow load analysed are listed in Table 4, along with their probability of occurrence. Here, SL1 includes $10 \leqslant SWE_{01} < 30$ mm and SL2, $SWE_{02} \geqslant 30$ mm.

The lateral load, resulting from, for example, wind or snow pressure, was simplified and reduced to one concentrated force, $F(z)$. The next section describes how $F(z)$ was applied to the tree.

Tree model and model simulations

The tree model used is two-dimensional (Fig. 1). Since its single elements are one-dimensional, the forces and deformations along the stem, due to external forces, can be computed with the transfer matrix method. This method, which is based on the classical finite-element analysis of structural mechanics (Cook *et al*., 2002), is described in detail in Morgan and Cannell (1987) and Ancelin *et al*. (2004). In addition to the formulation in Morgan and Cannell (1987), the present method considers the geometric non-linearity and the material non-linearity of the deflecting tree.

The two non-linearities are taken into account by repeatedly performing the transfer matrixes method in its linear form, in an iterative process, until the tree model achieves static equilibrium. The geometry non-linearity is considered by redefining, at each repetition and by simple trigonometric transformation, the local coordinates (x', z') of each element in the global coordinates (x, z) in which the external forces act. Similarly, the material non-linearity is considered by redefining, at each iterative step, the secant-modulus of bending elasticity $E(\varepsilon) = \sigma(\varepsilon)/\varepsilon$ (cf. Equation 1) and of shearing elasticity $G(\gamma) = \tau(\gamma)/\gamma$ (cf. Equation 2) of the elements, to fit the $\sigma(\varepsilon)$ and the $\tau(\gamma)$ acting on the element. Here, the element deflection $dx'(z')$ due to the shear force (V, Fig. 1) is calculated with the mean shear stress of the cross section:

$$\bar{\tau}(z') = \frac{k}{A(z)} \times V(z') \tag{5}$$

as $\tau(\gamma, z')$ in Equation 2. This yields $\gamma(z')$ and thus:

$$dx'(z') = \gamma \times (z') \times dL \tag{6}$$

where $k=1.1$ is a shape factor for a circular cross-section to take into account the effective shear area, $A(z) = \pi D_{ub}(z)^2/4$ is the area of the cross-section, and dL is the length of one stem element. What is notable here is that the shear deformation of the stem due to asymmetrical stresses along the stem (dz'/dx') is very small compared to that due to the slip along the wood grain (dx'/dz'), and that therefore $\gamma \approx dx'/dz'$. The deformation along the stem is simply calculated with the stress-strain relationship in Equation 1, with the longitudinal stem stress = $N(z')/A(z)$ in place of σ and ε interpreted as the longitudinal stem strain, where N is the normal force (Fig. 1). The maximum shear stress within the cross-section is computed as $\tau(z', r=0) = 4/3 \times V(z')/A(z)$. The material non-linearity of the root–soil system is considered by redefining, at each iteration, its secant-stiffness = $M^0(\phi)/\phi$(Equation 3) to fit the M acting on the stem base. At the same time a small rotation is added or subtracted to the stem base, corresponding to a change in the stem base moment $M^0(\phi)$ to match the erroneous M at the tree top. The convergence criterion in the iteration to achieve a static equilibrium of the tree model is that the absolute values N, V, and M (Fig. 1) are all < 1E-06 (N and Nm) at the tree top.

On a second and a higher level of iteration, the critical lateral force $F_{crit}(z')$ that causes tree failure is sought. $F_{crit}(z')$ corresponds to the lower of the forces causing uprooting, i.e. $M^0 \approx M^0_{max}$, and stem breakage, i.e. $\sigma(\varepsilon, z') \approx \sigma_{max}(z')$. The corresponding static equilibriums are denoted StEq(M^0_{max}) and StEq(σ_{max}). The initial and estimated $F(z')$-value is set as a percentage of $M^0_{max}/z(F)$, to which a small value is then iteratively added or subtracted until the absolute values of $(M^0 - M^0_{max})/M^0_{max}$ or $(\sigma(\varepsilon, z') - \sigma_{max}(z'))/\sigma_{max}(z')$ are less than 5‰. To avoid model divergence, the $E=\sigma/\varepsilon$ at σ_{max} is used to calculate σ beyond σ_{max}. This is of no importance for the interpretation of the results other than that

Table 4. *Combinations of seasonal tree state and snow load in the model calculations*

HE, high elevation site; LE, low-elevation site. D_{ub} is the stem diameter under bark. SL and SWE are explained in the text.

Abbreviation		Description	Annual mean occurrence[a] (d)	
Tree state	Snow load		HE	LE
0		Normal	260	360
0	_SL1	Normal+snow load (SWE_{01})	45	5
0	_SL2	Normal+snow load (SWE_{02})	1	<0.1
FrSt		Frozen stem (depth >$0.1D_{ub}$)	40[b]	0
FrSt	_SL1	Frozen stem+snow load (SWE_{01})	18[b]	0
FrSo		Frozen soil (depth >20 cm)	10[b]	0
FrStSo		Frozen stem and soil	7[b]	0
FrStSo	_SL1	Frozen stem and soil+snow load (SWE_{01})	2[b]	0

[a] Variations of up to ten times the mean occur for the abnormal combinations.
[b] Estimation based on Stadler *et al.* (1998) and Zweifel and Hasler (2000).

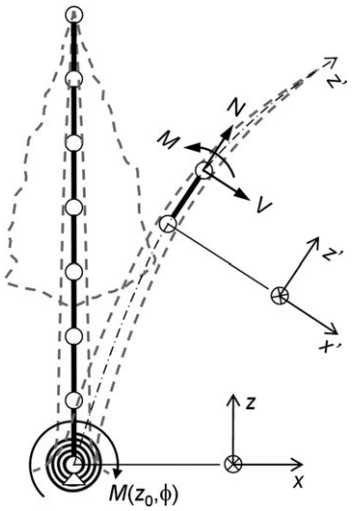

Fig. 1. The tree (grey dashed lines) and the model tree (heavy black lines) with schematic finite height segments of the tree. Each element is a one-sided clamped beam. For clarity, only one element of the deflected tree is shown with the moment (M) and forces (N, V) acting at its upper node. (x, z) refer to the global coordinate system and (x', z') to the local system of the element: z' ranges from 0 to H along the stem centre and x' is the sideway deflection of each element. $M^0(\phi)$ is the resistive moment of the root–soil system as a function of the rotational angle at the stem base.

$\sigma(z') > \sigma_{max}(z')$ indicates stem-bending failure. Figure 2 demonstrates typical model results at StEq(M^0_{max}) (Fig. 2A–D) and at StEq(σ_{max}) (Fig. 2E–H), which are here exemplified for two trees in an unfrozen state with no snow load.

Figure 2A–D shows tree no. 22 at StEq(M^0_{max}). The lateral force F is applied at z'/H=0.55 (Fig. 2A), which is close to the crown's area centre, z_{Cc} at z/H=0.56. F causes a total stem deflection (black line) and a stem deflection due to shearing only (grey line). The position of the initially applied force F_{init} (dashed line and arrow) differs from that of the converged solution F_{crit} (continuous line and arrow). Note that F is applied horizontally (in the x-direction) and at one fix z'-coordinate. For tree no. 22, uprooting occurs, i.e. the stem base moment $M^0(\phi)$ reaches M^0_{max} (Fig. 2B), before the stem fails, i.e. before the stem-bending stress $\sigma(z')$ reaches the stem-bending failure stress $\sigma_{max(z')}$ (Fig. 2C), where $\sigma(z')$ is the actual stress (solid line) and $\sigma_{max}(z')$ the failure stress (dashed line). The actual effective secant-modulus of elasticity of the stem section, $E(z') = \sigma(z')/\varepsilon(z')$ (Fig. 2D, continuous line), is, along the lower stem, lower than the modulus defined at $0.4\sigma_{max}(z')$, $MOE(z')$ (dashed line). The difference results from the non-linear $\sigma(\varepsilon,z)$ and means that the stem section softens while bending as $\sigma(z')$ approaches $\sigma_{max}(z')$, i.e. it bends more easily than $MOE(z')$ would predict.

Figure 2E–H shows tree no. 23 at StEq(σ_{max}). F is applied at z'/H=0.85 (Fig. 2E), just above z_{Cc} at z/H=0.77, and causes considerable stem deflections. In this example, the stem fails, $\sigma(z') \approx \sigma_{max}(z')$ (Fig. 2G), before the tree uproots, i.e. before $M^0(\phi)$ reaches M^0_{max} (Fig. 2F). The softening of the stem section while bending (Fig. 2H) is more extensive than in Fig. 2D.

The tree model was run for F_{crit} at the relative tree heights z'/H=0.10, 0.15, 0.20, …, 0.95, in order to determine the dependency of tree reactions on the height of the force application $z'(F_{crit})$. Here, all combinations of tree state and snow load (Table 4) were included to determine the dependency of tree reactions on the season.

To evaluate the model performance, the modelled and the measured stem deflections were compared at StEq(M^0_{max}), with F_{crit} at z'/H=0.20, for all trees in their normal state (Table 4).

Critical wind speed

The critical forces $F_{crit}(z'/H$=0.05, 0.10, …, 0.95) were interpolated every per cent of H up to 95%. F_{crit} at the height of the crown's area centre, z_{Cc} (cf. Table 1), was used to calculate the equivalent critical speed of steady wind, u_{crit}, with Equation 7:

$$F = C_D \times \frac{\rho \times u^2}{2} \times A_0;\ C_D = a + (1-a) \times e^{\alpha u} \qquad (7)$$

where C_D is the crown drag coefficient, A_0 is the horizontal projection of the undeformed crown, ρ is the density of air=1.17 kg m^{-3}, α=–0.09, and a=0.18 (Lundström *et al.*, 2007*b*). Snow on the crown is accounted for with $\alpha = \alpha/(1+\text{atan}(SWE/40))$, which is a hypothesis. Frozen branches are accounted for with $\alpha = \alpha 2/3$, as frozen wood is 50% stiffer (Silins *et al.*, 2000), which is applied when the stem is frozen (cf. Table 4). The two effects on α are multiplicative.

Stem thigmomorphogenesis

To analyse the degree to which the stem adapts its growth to mechanical stress (thigmomorphogenesis), the $\sigma(z')$ calculated by the model is compared with $\sigma_{max}(z')$. For this, a new formulation (Equation 8) was developed:

$$\eta(z'_1) = \left(SE \begin{pmatrix} z'_1 \\ z'=0 \end{pmatrix} \left(\frac{\sigma(z')}{\sigma_{max}(z')} \times \frac{\overline{\sigma_{max}(z')}}{\overline{\sigma(z')}} \right) \right)^{-1} \qquad (8)$$

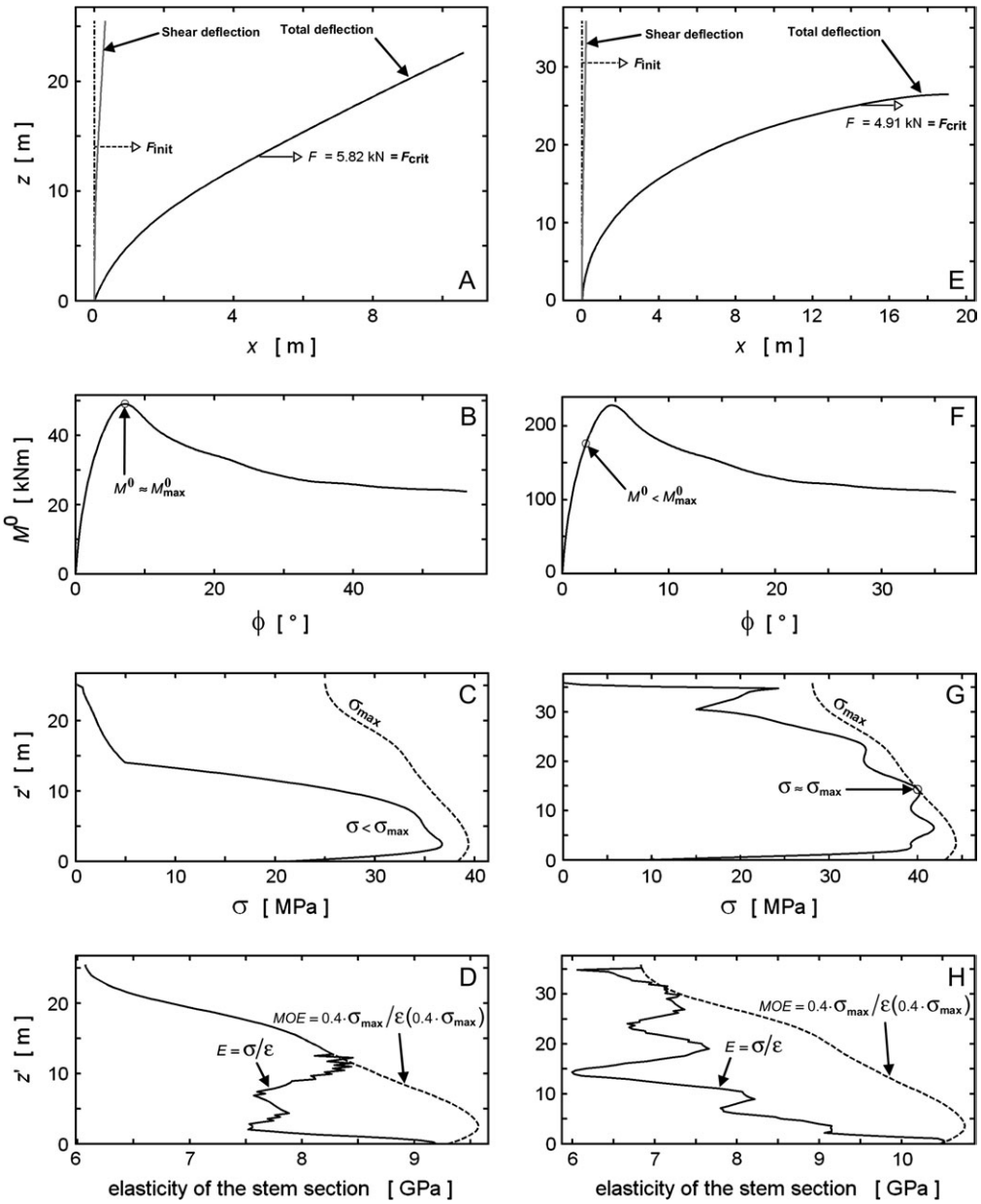

Fig. 2. Example of results with model convergence at StEq(M^0_{max}) (A–D) and at StEq(σ_{max}) (E–H). See text for explanations.

where η is the degree of uniform exploitation of bending stress capacity for the stem section between the stem base ($z'=0$) and the height of force application ($z' = z'_1$), SE is the standard error, $\sigma_{max}(z')$ is the bending strength (Table 3, Equation 1), and z'_1 is the (local) height coordinate of force application. Here, $\sigma(z')$ corresponds to the stem-bending stress at StEq(M^0_{max}) or StEq(σ_{max}). In principle, it would be more correct to use the most frequent stem stress. However, the most frequent values of $F(z'/H=0.05, 0.10, \ldots, 0.95)$, which correspond to the particular combinations of tree state and snow load, are *a priori* unknown. When the $\sigma(z')$ due to the mean wind speed was calculated and then magnified so that the shape of the $\sigma(z')$-curve could be compared with that of $\sigma(z')$ due to $F_{crit}(z_{Cc})$, it became apparent that the two $\sigma(z')$-shapes were almost identical (see the example given in the Results). The stem thigmomorphogenesis was therefore analysed using $\sigma(z')$ at StEq(M^0_{max}) or StEq(σ_{max}). It should further be noted that η is mathematically independent of the magnitude of σ_{max} and $\sigma(z')/\sigma_{max}(z')$, and that η measures the uniformity of exploitation of $\sigma_{max}(z')$ and not the magnitude of its exploitation.

Results

Model performance and potential sources of error when modelling stem deflections

The relative difference between modelled and measured horizontal tree-top deflection ranged from 1% (4 cm, tree 26) to 9% (45 cm, tree no. 22), averaging 3%. Since the exact rotation of the root–soil system was specified, these

discrepancies were due to errors in the parameterized flexibility of the stem only. Stem deflection could be modelled with very small errors up to the crown base. From here, small, local variations in flexibility accumulated or mutually balanced along the stem up to the tree top, with no sign of systematic errors. The errors in tree-top deflection were considered small and irrelevant compared to the other potential sources of errors outlined below, and the model performance was therefore fully acceptable.

Neglecting the geometric non-linearity means ignoring the additional moment resulting from the x-wise deflection of tree and snow weight, and therefore overestimating $F_{crit}(z)$. It also means ignoring the negative z-wise deflection of the leaning tree, which results in a shorter lever arm between the force application and the stem base, and therefore an underestimation of $F_{crit}(z)$. The net effect is an overestimation of $F_{crit}(z)$ if a geometric linear analysis is made. The overestimation for the trees with no snow load ranged from 5% (large tree) to 25% (small tree), averaging 14%. With snow on the crown, these values doubled and even tripled. In fact, some trees with snow-loaded crowns would have required almost no lateral force for tree failure to occur. This so-called unstable equilibrium would have been missed if the geometric non-linearity had been ignored.

Not accounting for the material non-linearity of the stem, i.e. using the stress-independent stem-bending elasticity $MOE(z)$ (the secant-modulus at $0.4\sigma_{max}$), leads to an underestimation of the stem-top deflection by between 0% and 19%, and on average by 8%. The relative softening of the stem in bending was typically a few per cent and reached locally up to 42%. If the non-linear resistive moment of the root–soil system is not taken into account, and instead a constant stiffness (the secant-stiffness at $0.4M^0_{max}$) is assumed in analogy to the stem section, then the tree-top deflection will be underestimated by a factor of between 5 and 7, and on average 6. If the tree deflections are underestimated, then $F_{crit}(z)$ will be overestimated. The net effects for material non-linearity are similar to those with geometric non-linearity. Hence, for trees with no snow load, the accumulated net effect of neglecting both material and geometric non-linearity in the analysis meant that $F_{crit}(z)$ was overestimated by between 7% (large tree) and 35% (small tree), and on average by 20%.

Tree reactions and critical loads: generalities

Figure 3 shows characteristic trends of the critical failure load F_{crit} and of tree reactions according to tree height. Up

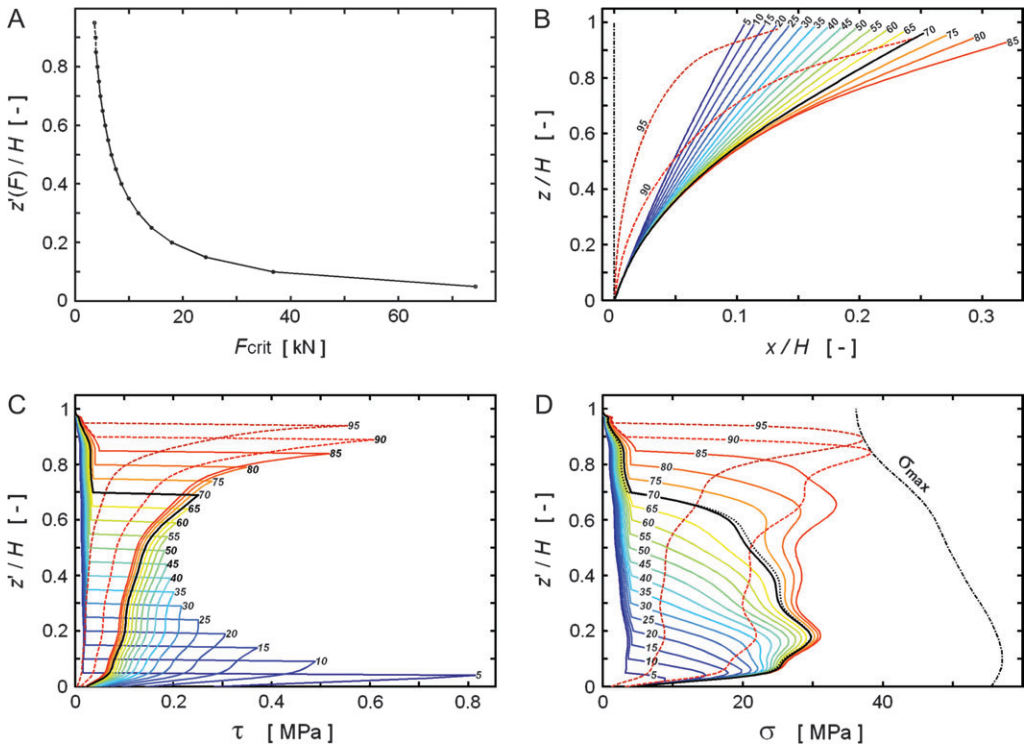

Fig. 3. (A) Values of critical lateral force F_{crit} as a function of the relative stem height of force application, $z'(F)/H$, for tree no. 15 in the unfrozen state with no snow load. Stem deflections (B), shear stress (τ) in the centre of the stem (C), and stem-bending stress (σ) (D) due to F_{crit} applied at $z'(F)/H$=5, 10, …, 95%. The dotted line indicates the σ due to the mean wind (1.7 m s^{-1}) magnified σ-wise to coincide with the $\sigma(z')$ at StEq(M^0_{max}). The dot-dash line (σ_{max}) is the stem-bending strength. Continuous lines refer to StEq(M^0_{max}) and dashed lines to StEq(σ_{max}). Heavy black lines (B–D) refer to the best 5%-multiple approximation for the relative height of the crown's area centre (z_{Cc}). Here z_{Cc}/H=68%≈70%.

to a certain height of force application (here $z'(F_{crit})/H$=87%), the tree uproots, i.e. StEq(M^0_{max}) applies (continuous lines). F_{crit} displays here a function of type $F_{crit} \sim z'^{b}$. Above this height, the tree fails in the stem, i.e. StEq(σ_{max}) applies (dashed lines), and $F_{crit}(z')$ decreases more strongly than indicated by $F_{crit} \sim z'^{b}$. The height at which this switch occurs depends on the degree of exploitation of bending stress capacity, $\sigma(z')/\sigma_{max}(z')$. The probability of shearing failure of the stem is highest when $F_{crit}(z')$ applies at the stem base (cf. Fig. 3C; Table 3). If F_{crit} applies above z'/H=0.05, the stem is more prone to bending failure than to shearing failure. Further, the $\sigma(z')$-curve due to F_{crit} and the $\sigma(z')$-curve due to the mean wind have similar shapes (Fig. 3D). The $\sigma(z')$-curve is the most similar in shape to the $\sigma_{max}(z')$-curve if F_{crit} applies just above the height of the crown's area centre, z_{Cc}. Compared with the unfrozen trees, $\sigma(z')/\sigma_{max}(z')$ was, as expected, lower if the stem was frozen, higher if both the stem and the soil were frozen, and much higher if only the soil was frozen. Furthermore, as expected, stem deflections were relatively larger for small than for big trees. For example, when F_{crit} was applied at z_{Cc}, the x- and z-wise tree-top deflections relative to H were at least 9% and 1%, respectively (tree 17, FrSt) and at most 63% and 30% (tree 11, 0_SL1), for all trees and combinations of tree state and snow load.

Stem-bending stress in relation to tree state and snow load

The spruces growing at the HE-site showed a low exploitation of their stem-bending capacity, $\sigma(z')/\sigma_{max}(z')$, when their M^0_{max} and the resulting uprooting was reached, i.e. at StEq(M^0_{max}). This is due to their relatively weak anchorage and strong stems. Consequently, the stem bending strength and the resulting stem failure, i.e. StEq(σ_{max}), was reached only if F was applied high up the stem. $\sigma(z')/\sigma_{max}(z')$ at StEq(M^0_{max}) was especially low for large trees (Fig. 4), meaning they were less likely to fail in the stem than small trees (Fig. 5). In fact, the largest trees, nos 16 and 17, were capable of achieving StEq(M^0_{max}) in all combinations of tree state and snow load even if F was applied above z_{Cc}. In contrast, the small HE-spruces in frozen soil failed in the stem if F was applied at z_{Cc} (e.g. no. 11 in Fig. 5E–G). As a consequence of the relatively weaker stem, the small HE-trees were generally more sensitive to snow load than the large trees (cf. Figs 4B, 5B). In fact, F_{crit} was very low for the trees nos 11–13 in the combination 0_SL2, independent of the height of application. This phenomenon of unstable equilibrium resulted in stem failure in the upper part of the crown at $0.70 < z'/H < 0.95$.

The spruces growing at the LE-site differed from those at the HE-site in that $\sigma(z')/\sigma_{max}(z')$ at StEq(M^0_{max}) was higher, meaning stem failure was more probable (cf. Fig. 6

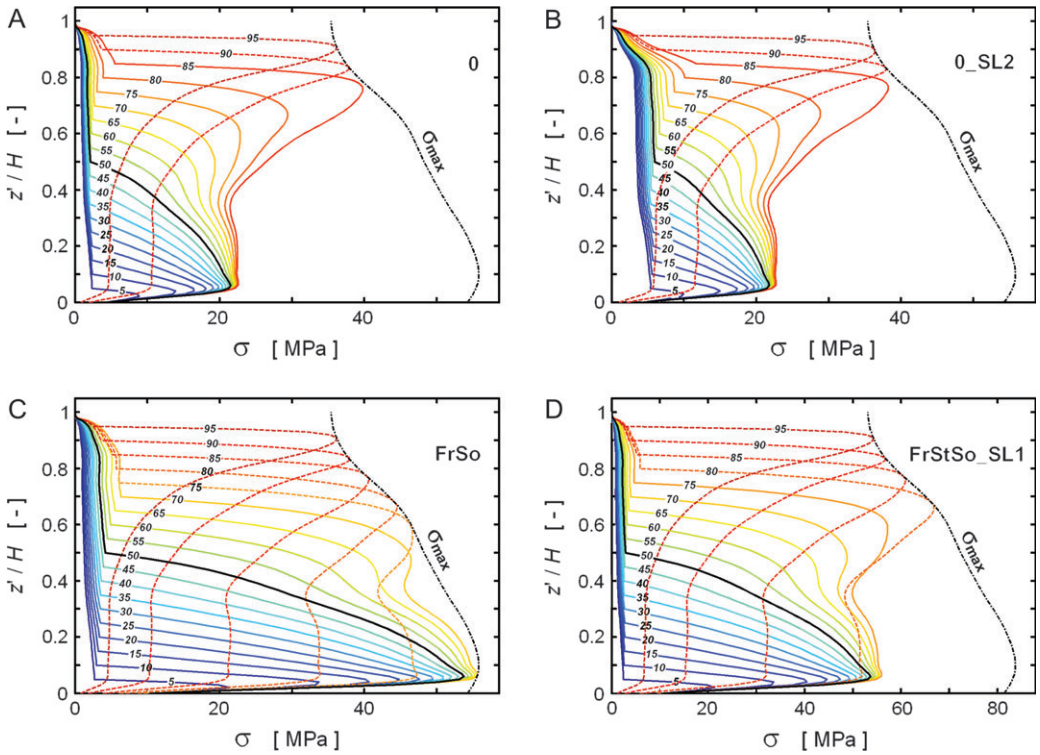

Fig. 4. Stem-bending stress (σ) due to F_{crit} for tree no. 16 in four combinations of tree state and snow load (cf. Table 4). Symbols are explained in Fig. 3.

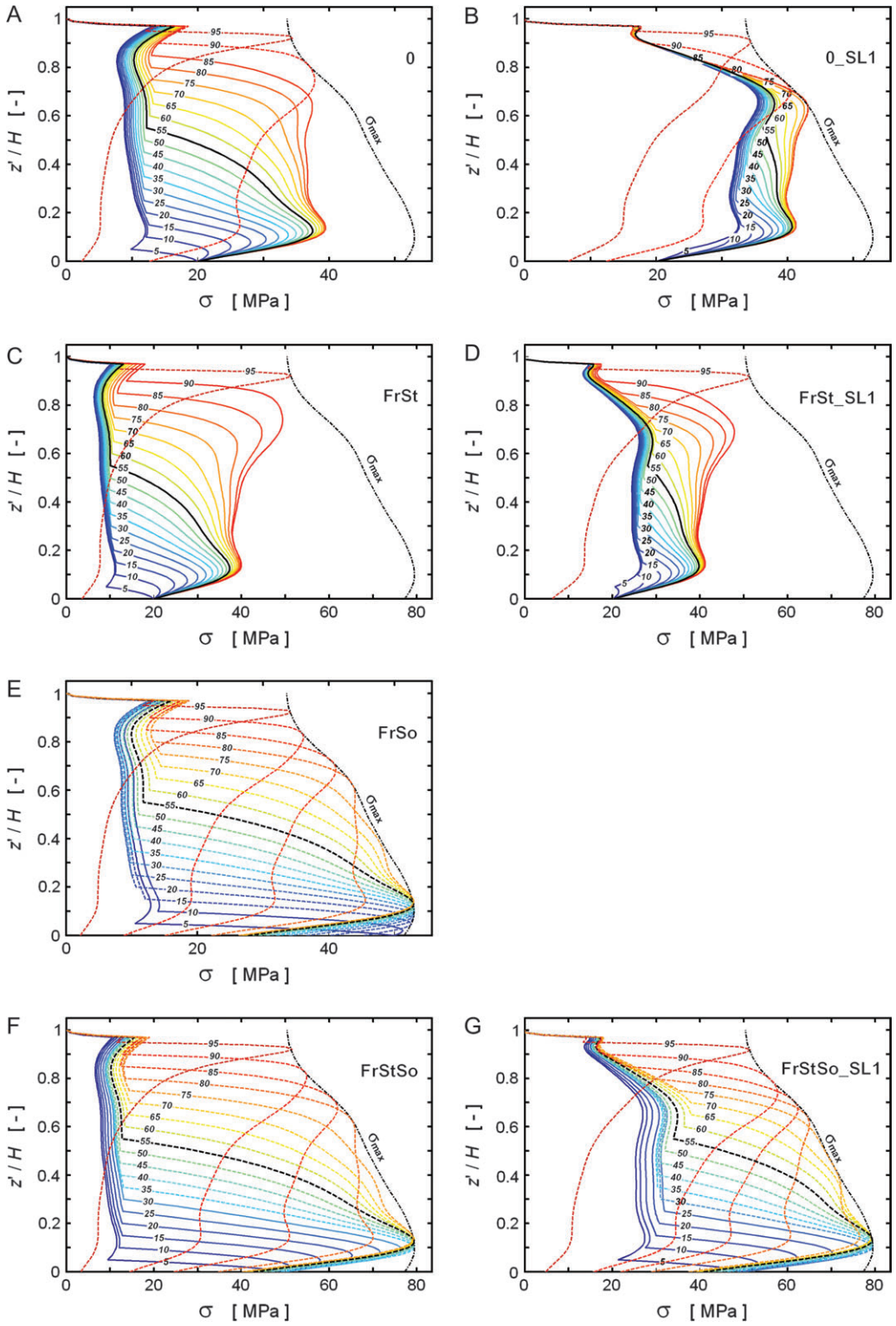

Fig. 5. Stem-bending stress (σ) due to F_{crit} for tree no. 11 in six tree-state/snow-load combinations (cf. Table 4). Symbols are explained in Fig. 3.

with Figs 4A and 5A). A further contrast with the HE-site was that the large LE-trees were more prone to stem failure than the small trees, with overall higher $\sigma(z')/\sigma_{max}(z')$ at StEq(M^0_{max}) (cf. Fig. 4B with Fig. 5B). Logically, in the tree-state and snow-load combination 0_SL1, the snow load caused overall higher $\sigma(z')/\sigma_{max}(z')$, just as it did with the HE-spruces. In the combination 0_SL2, the LE-spruces nos 22–25 failed in

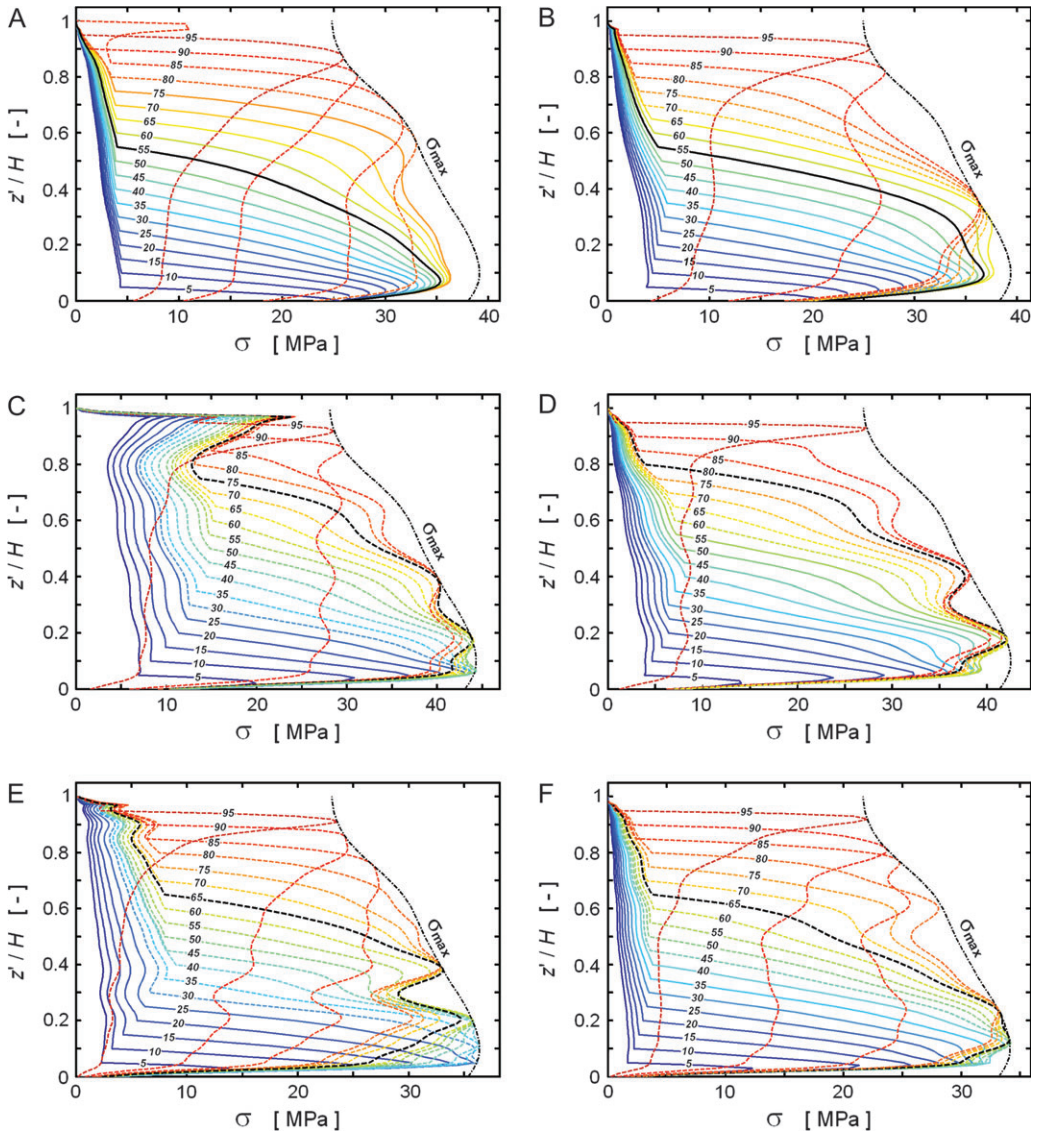

Fig. 6. Stem-bending stress (σ) due to F_{crit} in the normal tree-state/snow-load combination (0), for the trees nos 21–26 (A–F) with z_{Cc} close to z'/H=55, 55, 75, 80, 65, and 65% (heavier lines). StEq(M^0_{max} and σ_{max}) occurs with F_{crit} applied at about z'/H=77%, 66%, 29%, 56%, 25%, and 41% (A–F), where the continuous line shifts to a dashed line. Symbols are further explained in Fig. 3.

the stem at $0.50 < z'/H < 0.95$, with a very small F_{crit} required at any height (unstable equilibrium), whereas nos 21 and 26 showed simply generally higher $\sigma(z')/\sigma_{max}(z')$ at F_{crit} compared to 0_SL1.

Adaptation of stem and anchorage strengths to site-specific climate and loads

The HE-spruces displayed a well-balanced relation between the stem and the anchorage strengths when they were subjected to the combinations of tree-state and load application that can be expected during the year (Table 5). Thus, the simultaneous achievement of $M^0 = M^0_{max}$ and $\sigma(z') = \sigma_{max}(z')$, i.e. StEq($M^0_{max}$ and σ_{max}) was, for the unfrozen trees, often reached with F_{crit} at about $z' = 0.80H$ (i.e. 0.2–0.3H above z_{Cc}). This corresponds to the effective wind loading (cf. Discussion). If the soil and the stem were frozen, then $z'(F_{crit})$ at StEq(M^0_{max} and σ_{max}) was lower. With the smaller HE-trees, it shifted down towards the stem base, where, for example, pressure from gliding snow acts. In the combination 0_SL1, the HE-trees achieved StEq(M^0_{max} and σ_{max}) if F_{crit} was applied at the same z'/H-coordinate as the combination 0 or just a few per cent lower. In the combination 0_SL2 (nos 14–17), the corresponding downward shift was similar or just a few per cent more.

Most LE-trees (nos 21, 22, 24, and 26) achieved StEq(M^0_{max} and σ_{max}) with F_{crit} acting close to z_{Cc}. However, this balance was less evident than for the

Table 5. *Numerical data related to StEq(M^0_{max} and σ_{max}), i.e. the simultaneous achievement of $M^0 = M^0_{max}$ and $\sigma(z') = \sigma_{max}(z')$ due to the applied critical force F_{crit}, depending on the seasonal tree-state and snow load (cf. Table 4)*

If F_{crit} acts above the $z'(F_{crit})/H$ corresponding to StEq(M^0_{max} and σ_{max}), the stem fails. Otherwise the root–soil system fails (cf. legend in the table). M^0, turning moment acting on the root–soil system; M^0_{max}, maximum resistive M^0 of the root–soil system; $\sigma(z')$, stem-bending stress; $\sigma_{max}(z')$, stem-bending strength; z'/H, relative coordinate along the stem.

Tree no.	Seasonal tree state/snow load[a]						
	0	0 SL1	FrSt	FrSt SL1	FrSo	FrStSo	FrStSo SL1
11	0.85	0.80	0.90	0.90	0.10	0.30	0.25
	0.69	0.67	0.81	0.75	0.02	0.09	0.09
12	0.80	0.80	0.85	0.85	0.10	0.20	0.20
	0.61	0.61	0.78	0.79	0.04	0.07	0.07
13	0.85	0.80	0.85	0.85	0.15	0.75	0.75
	0.74	0.69	0.76	0.77	0.05	0.08	0.33
14	0.80	0.80	0.85	0.85	0.50	0.75	0.70
	0.69	0.69	0.75	0.75	0.23	0.62	0.30
15	0.85	0.85	0.90	0.90	0.35	0.80	0.80
	0.68	0.67	0.85	0.85	0.07	0.64	0.64
16	0.85	0.85	0.85	0.85	0.70	0.75	0.75
	0.78	0.78	0.78	0.78	0.06	0.61	0.61
17	0.80	0.80	0.85	0.85	0.70	0.75	0.75
	0.72	0.72	0.77	0.77	0.54	0.65	0.66
21	0.75	0.75					
	0.53	0.53					
22	0.65	0.55					
	0.30	0.27					
23	0.25	0.10					
	0.06	0.04					
24	0.55	0.45					
	0.17	0.17					
25	0.25	0.20					
	0.05	0.05					
26	0.40	0.35					
	0.11	0.11					

[a] Legend for each group of two numbers: $z'(F_{crit})/H \in$ StEq(M^0_{max} and σ_{max}); z'/H where $\sigma(z') = \sigma_{max}(z')$.

Table 6. *Numerical data related to the critical wind u_{crit}, depending on tree state and snow load (cf. Table 4)*

u_{crit} causes stem failure if $\max(\sigma/\sigma_{max}) = 1.00$, uprooting if $\max(\sigma/\sigma_{max}) < 1.00$, and both if the tree is in unstable equilibrium (*). σ, stem-bending stress; σ_{max}, stem bending strength (cf. legend in the table).

Tree no.	Seasonal tree state/snow load[a]						
	0	0 SL1	FrSt	FrSt SL1	FrSo	FrStSo	FrStSo SL1
11	9	4	8	5	21	18	14
	0.13	0.69	0.13	0.14	0.13	0.10	0.14
	0.71	0.90	0.47	0.50	1.00	1.00	1.00
12	15	8	13	8	33	28	21
	0.09	0.10	0.09	0.10	0.09	0.09	0.10
	0.76	0.79	0.50	0.52	1.00	1.00	1.00
13	13	8	11	8	32	28	20
	0.07	0.08	0.07	0.08	0.07	0.07	0.07
	0.57	0.59	0.38	0.38	1.00	1.00	1.00
14	15	13	14	12	38	33	25
	0.26	0.27	0.26	0.26	0.26	0.26	0.26
	0.42	0.44	0.28	0.28	1.00	0.69	0.71
15	22	16	18	15	46	42	31
	0.18	0.18	0.18	0.18	0.07	0.18	0.18
	0.53	0.54	0.35	0.35	1.00	0.87	0.89
16	19	16	17	15	45	39	30
	0.06	0.06	0.06	0.06	0.06	0.06	0.06
	0.39	0.39	0.26	0.26	0.97	0.64	0.65
17	32	24	25	20	57	53	41
	0.08	0.08	0.08	0.08	0.08	0.08	0.08
	0.27	0.27	0.18	0.18	0.68	0.45	0.45
21	22	19					
	0.07	0.07					
	0.91	0.92					
22	21	19					
	0.09	0.27					
	0.93	0.96					
23	20	11*					
	0.18	0.96					
	1.00	1.00					
24	34	24					
	0.19	0.42					
	1.00	1.00					
25	37	24					
	0.39	0.39					
	1.00	1.00					
26	41	31					
	0.14	0.23					
	1.00	1.00					

[a] Legend for each group of three numbers: u_{crit} [m s^{-1}]; z'/H for $\max(\sigma/\sigma_{max})$ [–]; $\max(\sigma/\sigma_{max})$ [–].

HE-trees, because the LE-trees sometimes lacked stem resistance. This was especially obvious with the LE-trees nos 23 and 25, which achieved StEq(M^0_{max} and σ_{max}) with F_{crit} acting at the lower part of the stem. In the combinations 0_SL1, the LE-trees achieved StEq(M^0_{max} and σ_{max}) if F_{crit} was applied at a z'/H-coordinate about 10% lower than in the combination 0. In the combination 0_SL2 (nos 21 and 26), the corresponding downward shift was 15%.

The critical speed of steady wind u_{crit} ranged between 4 m s^{-1} and 57 m s^{-1}, depending on the seasonal state of the tree and whether its crown was loaded with snow (Table 6). u_{crit} was best described by the social status of the tree in the stand (Table 1), with greater u_{crit} for more dominant trees, and then in turn by the tree size (DBH), by the site (LE or HE), or by the stand density. When described by the social status, u_{crit} was significantly higher (Wilcoxon signed-rank test, $P < 0.001$) at the LE-site than at the HE-site. Here, tree no. 23 appears weak and tree no. 12 strong in relation to their co-dominant positions. In general, the trees seem to have adapted their growth, and thus their stem and anchorage strength and crown size, reasonably well to the expected wind load. Subject to u_{crit}, the exploitation of the stem-bending stress capacity, σ/σ_{max}, was generally highest at $z' = 0.10$–$0.20H$, where the stems also exhibit their greatest $\sigma_{max}(z)$ (Fig. 3D). The LE-spruces tend to fail in the stem rather than uproot when exposed to u_{crit}, unlike the HE-spruces in unfrozen soil.

Degree of uniform exploitation of the stem-bending capacity, η

All HE- and LE-spruces display a mechanically adapted stem growth for lateral forces applied slightly above the area centre of the crown (Fig. 7). Hence, the HE-spruces exhibit high η-values if F acts on the upper crown ($0.6 < z'/H < 0.8$), similar to those of the LE-spruces ($0.6 < z'/H < 0.9$). In addition, the stems of the HE-spruces are well designed for bending due to forces acting on the lower part of the stem, up to approximately z'/H=0.20 (Fig. 7A), especially when loaded with snow (Fig. 7B). The general η-maximum along the upper stem is located higher for the LE-spruces than for the HE-spruces. Physically, this is a result of the LE-trees having relatively thicker stems along the upper half (Fig. 7D). If the crown of the HE-spruces is loaded with snow, the η-maximum is shifted downward (cf. Fig. 7A with B). A similar downward shift was observed for the LE-spruces.

The mechanically adapted stem growth is only weakly influenced by the tree states with frozen soil at the HE-site (Fig. 8), unlike those with snow load. Further, a stem's capacity (or need) to adapt its growth mechanically to different combinations of tree-state and snow load decreases with the age and size of the tree in terms of a less differentiated $\eta(z')$. The $\eta(z')$-curves of the LE-spruces with and without snow load showed a similar dependency on tree age and size.

Discussion

Model performance and potential sources of error when modelling stem deflections

There are several reasons for the differences between the parameterized and measured stem flexibility along the crown section of the stem. First, the branches induce local variations in grain orientation and stem diameter that influence the effective flexibility of the stem section. These variations were not taken into account. Second, the stem diameter was measured at larger intervals along the crown than along the stem base. Third, growth properties (*RW* and *Q*) were assessed in only two or three stem discs along the crown, which is a poor statistical base to predict the effective secant-modulus of elasticity E (governed by

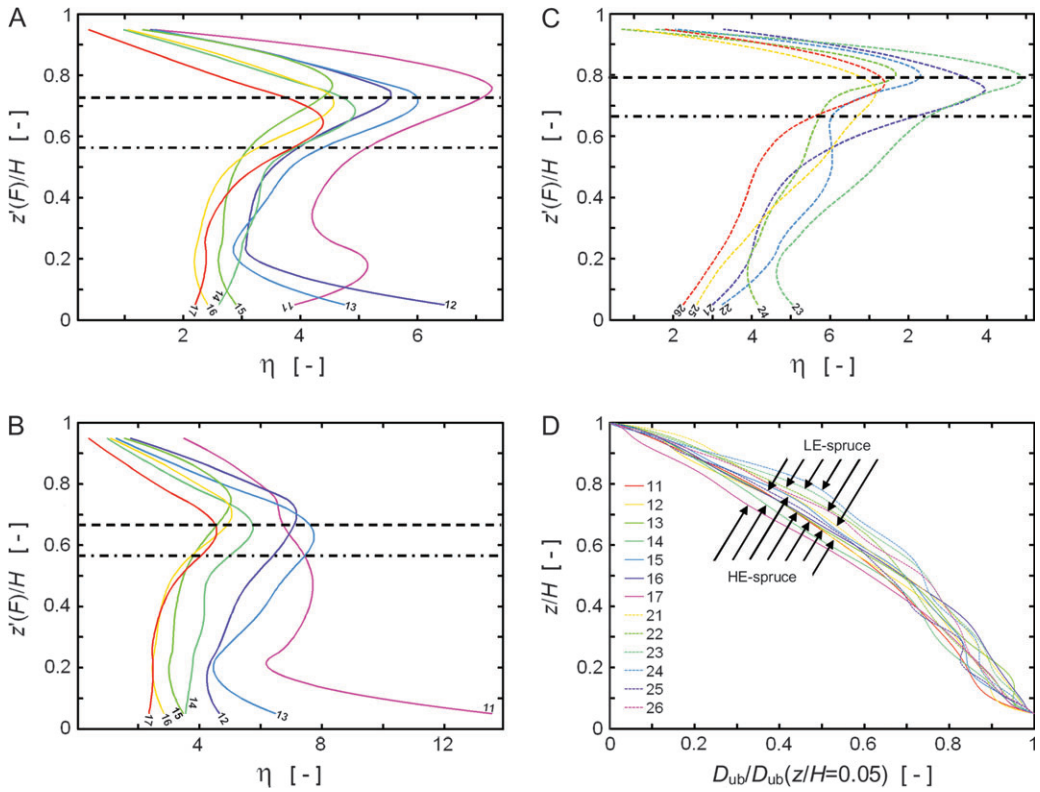

Fig. 7. (A–C) Site comparison of degrees of uniform exploitation of bending stress capacity, η, as a function of the relative coordinate along the stem z'/H at which the lateral force F acts: the HE-spruces in the tree-state/snow-load combination 0 and 0_SL1 (A, B) and LE-spruces in the combination 0 (C) (cf. Table 4). The η-maximum along the upper 80% of the tree (dashed lines) is shifted downwards if the crown is loaded with snow (A, B). The dot-dash lines indicate the location of the area centre of the crown. All horizontal lines are site medians. The inclined numbers indicate the tree no. (cf. Table 1 and Table 3). (D) The stem diameter under bark D_{ub} normalized by the D_{ub} at 5% stem height, as a function of the relative stem height z/H. The upper half of the stem is relatively thicker at the LE-site (dashed lines) than at the HE-site (continuous lines).

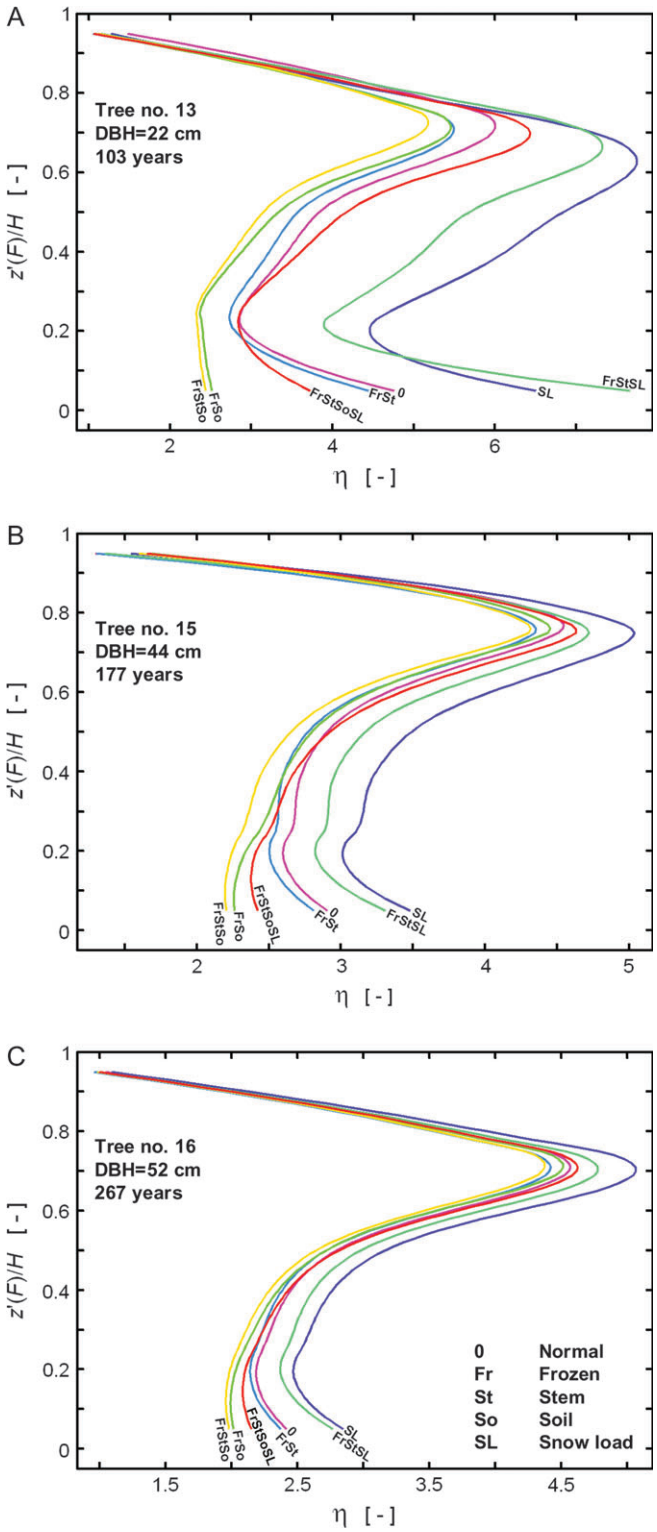

Fig. 8. Comparison of $\eta(z'(F)/H)$ among three spruces (A–C) of different sizes and cambial ages (at z=1.3 m) at the HE-site. DBH is the diameter at breast height and the axis symbols are explained in Fig. 7. Each curve corresponds to a particular combination of tree state and snow load (cf. legend in C). The snow load considered is SL1 (cf. Table 4).

Equation 1) here. Fourth, the predictive strength of E is low for the stem along the crown (Lundström *et al.*, 2008). Bending tests and investigations of the radial growth of fresh logs from the crown region are required to analyse and possibly reduce these sources of errors. However, the overall tree deflection is governed by the root–soil rotation and the bending of the stem base. The errors in flexibility along the crown section are therefore of minor importance when modelling the overall deflection of trees.

A geometric and material non-linear analysis can, unlike a linear analysis, describe *in situ* stem deflections precisely. Since this type of analysis requires non-linear experimental data, which are not always available, and more programming than if the analysis is made linear, it may be of interest to know when such precision is useful. When estimating critical lateral forces, a strict linear analysis will always overestimate the critical force (in the present case by up to 35%), especially if the crown is loaded with snow (possibly no additional force required for tree failure). A non-linear approach therefore seems adequate here as well as for failure analysis in general, for example when investigating the balance between the stem and anchorage strengths. As a comparison, the streamlining of the crown subject to wind, which is also a non-linear effect, reduces the effective drag force by up to 75% in strong wind (Equation 4). Unless the crown is loaded with heavy snow, crown streamlining is therefore the most important non-linear effect to consider in analysing tree reactions to wind. It is apparent that the spruces analysed are normally mechanically favoured by their overall flexibility, as demonstrated here by a 75%–35% = 40% higher F_{crit}.

Adaptation of stem and anchorage strength to tree states and loads

The strengths of the stem and the anchorage appear, in general, to be mutually best adapted to the prevailing combination of seasonal tree state and load, which at both sites is the wind on the unfrozen tree. The stem and anchorage strengths were also in balance for the HE-spruces in frozen soil subject to gliding or creeping snow (Table 5), especially for the smaller trees. The LE-spruces nos 23 and 25 were two exceptions to this pattern. Their growth seems to have been more strongly influenced by other criteria than the balance between the stem and anchorage strengths. Even so, the overall signs of mechanically adapted stem and anchorage strengths, which mean an adaptation of tree growth to acute loading, should be kept in mind when changes in the forest structure are planned.

The social status of the tree in the stand, the tree size, the site, and to some extent, the stand density seem, in turn, to govern the critical values of steady wind, u_{crit} (Table 6). This indicates that the tree adapts, through appropriate growth allocation, its stem and anchorage

strengths as well as its crown size to the wind pressure. In this study, the steady wind and a uniform wind pressure on the entire crown were used as a basis for comparing the u_{crit} of the trees. Evidently, a tree will also experience (i) gusts due to the wind turbulence (Holbo *et al*., 1980), (ii) dynamic, structural amplification due to tree-wind resonance (Peltola, 1996; SIA, 2006), (iii) varying types of wind profile in the canopy (Raupach, 1994; Lo, 1995) depending on the local topology and stand structure, and possibly (iv) torsion (Mayer, 1985). When relating u_{crit} to standard 10-min-wind measurements, the two first effects tend to counterbalance the third. It is, however, obvious that predictions of wind-induced tree failure will require additional and more specific measurements than those made in the present study. Nevertheless, this analysis clearly shows that the studied trees in frozen soil will never fail due to wind load alone, and that the trees with unfrozen stem and soil and snow-loaded crowns are at greatest risk of wind failure. The HE-trees are accustomed to frost (note that light frost is more frequent than 'Fr' in Table 4) and appear to allocate growth to the anchorage and the stem in accordance. In fact, they seem to rely on their anchorage and stem strengthening when the crown is loaded with snow, which is another sign of site-specific mechanical growth adaptation.

Field observations at the HE-site over the last few decades (H Hefti, municipal forester at the HE site, personal communication) reveal only a few tree failures. These were mainly due to local Foehn-storms, small slabs of gliding snow, and rare tree-top failure due to snow-loaded crowns. In comparison, more frequent tree failures due to winter storms were observed at the LE-site, of which about one-third were stem and two-thirds root–soil failure (B Blöchliger, municipal forester at the LE-site, personal communication). These observations are in line with the model simulations in this study.

Degree of uniform exploitation of the stem-bending capacity, η

Stem thigmomorphogenesis reflects the local prevailing seasonal combination of tree state and load. In fact, the degree of uniform exploitation of bending stress capacity $\eta(z')$ (Equation 8) shows that both the taper and the material properties of the stem mechanically adapt to frequent complex loading, independent of the growth situation. This is especially true for young trees (Fig. 8). The general maxima of $\eta(z')$ of about 0.75 (Fig. 7) shows that the stem adapts its growth to the effectively induced wind load, just like the strengths of the stem and of the root–soil system. Actually, the effective height of equivalent wind-force application $z'(F)$ on the crown could be estimated to 20–25% above the crown's area centre if the crown's area was considered by segments of height in Equation 7 and an approximate mean wind profile in the canopy was assumed (on the basis of Zoumakis, 1993; Raupach, 1994).

In terms of stem thigmomorphogenesis, the thicker stems of the LE-spruces along the crown section of the stem, and thus the slightly higher located $\eta(z')$-maxima for the LE- compared to the HE-spruces, could be a result of differences in the wind pressure profiles, with relatively higher pressures close to the tree tops at the LE-site. Concerning the observed response in stem growth to the prevailing load combination, the snow load SL1 is an exception. Although the tree crown is mostly not covered with snow, the stem seems to 'remember' this critical additional load and adapts its growth accordingly. The downward shift in general $\eta(z')$-maxima for trees with snow-loaded crowns seems natural, since the equivalent wind force acting on the crown is likely to shift downward if the branches are loaded with snow. This interpretation is supported by the fact that the application height of F_{crit} at StEq($M^0_{max}$and σ_{max}) was also shifted downward if the crown was loaded with snow.

It is known that trees also exhibit stem failure due to shearing (Mattheck and Breloer, 1994), but no signs of stem thigmomorphogenesis due to shear stresses were found. To ascertain this will require a shear-stress modelling with more detail than could be included in this study. Nevertheless, the formulation of the degree of uniform exploitation of a tree's stem-bending stress capacity presented here provides further strong evidence that tree stems are able to adapt their growth mechanically.

This study covers numerous tree and climate parameters, with an emphasis on drawing general conclusions rather than doing a detailed analysis of the spatiotemporal growth response of spruce to mechanical stress. For more insight into the thigmomorphogenesis of Norway spruce, it would be worthwhile analysing how specific growth processes develop in detail under the influence of variable mechanical stress and climatic conditions.

Acknowledgements

We thank Silvia Dingwall for revising the text and the anonymous reviewer for constructive comments.

Appendix

List of symbols and notations and their definitions and units used in the study

Notation	Description	Unit
A	Area of the stem cross-section	m^2
B	Bark thickness	m, mm
D, $D_{ub;\ x,\ y,\ 05}$	Stem diameter over and under bark; reference to x-direction, y-direction, and to 5% tree height (cf. Table 2)	m, mm
DBH	Stem diameter over bark at breast height (z=1.3 m)	m, cm
E	Secant-modulus of stem bending elasticity $= \sigma/\varepsilon$	GPa
ε	Stem-bending strain (without the contribution from shear deformation)	–

Continued

Continued

Notation	Description	Unit
F ; F_{init}; F_{crit}	Force applied on the tree in the x-direction; F initially applied; critical F, causing stem-bending failure ($\sigma=\sigma_{max}$), or tree uprooting ($M^0 \approx M^0_{max}$), or both ($M^0_{max}$and σ_{max}) simultaneously	N
ϕ	Rotation around the y-axis of the root-soil system	rad, °
G	Secant-modulus of shearing elasticity along the stem	MPa
γ	Stem-shear strain along the stem	–
H	Tree height	m
η	Degree of uniform exploitation of the stem-bending capacity (cf. Equation 8)	–
HE, LE	High-elevation site, low-elevation site	
M	Turning moment around the y-axis of the stem section	MPa
M^0; M^0_{max}	Turning moment around the y-axis of the root–soil system; maximum resistive M^0	MPa
MOE	Secant-modulus of stem bending elasticity defined at $\sigma=0.4\sigma_{max}$	GPa
N	Normal force (along the stem)	N
Q	Knottiness (relative frequency of knots) in the stem cross-section	–
r	Radial coordinate of the stem, ranging from the stem centre to the bark ($D_0/2$)	m
RW; $_{i,o}$	Width of annual rings; reference to the mean of the inner 75% radial part of the stem cross-section and to the mean of the remaining outer part	mm
σ, σ_{max}	Bending stress and strength of the stem cross-section	MPa
SL1, SL2	Snow load on the crown m^{-1} height (1= moderate; 2=heavy, cf. Table 4 and the text)	kg m^{-1}
StEq	Static equilibrium for the tree model when subjected to F_{crit} (cf. explanation of F_{crit} above)	
SWE	Snow-water equivalent precipitation relating to the amount of snow	mm
τ, τ_{max}	Shear stress and strength of the stem section in the direction along the stem	MPa
u; u_{crit}	Wind speed; critical u causing stem-bending failure ($\sigma=\sigma_{max}$) or tree uprooting ($M^0 \approx M^0_{max}$)	m s^{-1}
V	Shear force (across the stem)	N
x, y, z	Global (Cartesian) coordinates of the tree: origin at stem base; x=horizontal stem deflection; z=height above origin (cf. Fig. 1)	m
x', z'	Local coordinates of the deflecting stem; x'=sideway deflection of each stem element; z'=coordinate along the deflecting stem, ranging from 0 to H (cf. Fig. 1).	m
z_{Cc}	Height of the crown's area centre	m

References

Ancelin P, Fourcaud T, Lac P. 2004. Modelling the biomechanical behaviour of growing trees at the forest stand scale. Part 1. Development of an incremental Transfer Matrix Method and application to simplified tree structures. *Annals of Forest Science* **61,** 263–275.

Andersland OB, Ladanyi B. 2004. *Frozen ground engineering*. 2. Hoboken, NJ: Wiley.

Bründl M. 1997. *Snow interception and meltwater transport in subalpine forests*. Monograph 12271. Zürich: ETH.

Chiatante D, Scippa SG, Di Iorio A, Sarnataro M. 2002. The influence of steep slopes on root system development. *Journal of Plant Growth Regulation* **21,** 247–260.

Cook RD, Malkus DS, Plesha ME. 2002. *Concepts and applications of finite element analysis*. 4. New York: Wiley.

Dean TJ, Roberts SD, Gilmore DW, Maguire DA, Long JN, O'Hara KL, Seymour RS. 2002. An evaluation of the uniform stress hypothesis based on stem geometry in selected North American conifers. *Trees—Structure and Function* **16,** 559–568.

Di Iorio A, Lasserre B, Scippa GS, Chiatante D. 2005. Root system architecture of *Quercus pubescens* trees growing on different sloping conditions. *Annals of Botany* **95,** 351–361.

Dobbertin M, Hug C, Schwyzer A. 1997. *Sanasilva Inventory Field Manual*. WSL, 18(57).

Holbo HR, Corbett TC, Horton PJ. 1980. Aeromechanical behavior of selected Douglas-Fir. *Agricultural Meteorology* **21,** 81–91.

Jaffe MJ. 1973. Thigmomorphogenesis: The response of plant growth and development to mechanical stimulation. *Planta* **114,** 143–157.

Kalberer M. 2007. *Quantification and optimization of the forest protection against rock falls*. Monograph. Freiburg: University of Freiburg.

Kollmann FFP. 1968. *Principles of wood science and technology* Vol. 1 *Solid wood*. Berlin: Springer.

Laasasenaho J, Melkas T, Alden S. 2005. Modelling bark thickness of *Picea abies* with taper curves. *Forest Ecology and Management* **206,** 35–47.

Lo AKF. 1995. Determination of zero-plane displacement and roughness length of a forest canopy using profiles of limited height. *Boundary-Layer Meteorology* **75,** 381–402.

Lundström T, Heiz U, Stoffel M, Stöckli V. 2007*a*. Fresh-wood bending: linking the mechanical and growth properties of a Norway spruce stem. *Tree Physiology* **27,** 1229–1241.

Lundström T, Jonas T, Stöckli V, Ammann W. 2007*b*. Anchorage of mature conifer: resistive turning moment, root–soil plate geometry and orientation of root growth. *Tree Physiology* **27,** 1217–1227.

Lundström T, Jonsson MJ, Kalberer M. 2007*c*. The root–soil system of Norway spruce subjected to turning moment: resistance as a function of rotation. *Plant and Soil* **300,** 35–49.

Lundström T, Stoffel M, Stöckli V. 2008. Fresh-stem bending of silver fir and Norway spruce. *Tree Physiology* **28,** 355–366.

Mattheck C, Breloer H. 1994. *The body language of trees: a handbook for failure analysis*. London: HMSO.

Mayer H. 1985. *Baumschwingungen und Sturmgefährdung des Waldes*. München: 51: Universität München, Meteorologisches Institut.

Meng SX, Lieffers VJ, Reid DEB, Rudnicki M, Silins U, Jin M. 2006. Reducing stem bending increases the height growth of tall pines. *Journal of Experimental Botany* **57,** 3175–3182.

Milne R. 1991. Dynamics of swaying of *Picea sitchensis*. *Tree Physiology* **9,** 383–399.

Morgan J, Cannell MGR. 1987. Structural analysis of tree trunks and branches: tapered cantilever beams subject to large deflections under complex loading. *Tree Physiology* **3,** 365–374.

Morgan J, Cannell MGR. 1994. Shape of tree stems: a reexamination of the uniform stress hypothesis. *Tree Physiology* **14,** 49–62.

Moulia B, Coutand C, Lenne C. 2006. Posture control and skeletal mechanical acclimation in terrestrial plants: implications for mechanical modeling of plant architecture. *American Journal of Botany* **93,** 1477–1489.

Nicoll BC, Ray D. 1996. Adaptive growth of tree root systems in response to wind action and site conditions. *Tree Physiology* **16,** 891–898.

Niemz P. 1993. *Physik des Holzes und der Holzwerkstoffe Holz: Anatomie, Chemie, Physik* Vol. III. DRW-Verlag.

Peltola H. 1996. Swaying of trees in response to wind and thinning in a stand of Scots pine. *Boundary-Layer Meteorology* **77,** 285–304.

Peltola H, Kellomäki S, Hassinen A, Granander M. 2000. Mechanical stability of Scots pine, Norway spruce and birch: an analysis of tree-pulling experiments in Finland. *Forest Ecology and Management* **135,** 143–153.

Peltola H, Nykanen ML, Kellomaki S. 1997. Model computations on the critical combination of snow loading and windspeed for snow damage of Scots pine, Norway spruce and Birch sp. at stand edge. *Forest Ecology and Management* **95,** 229–241.

Pomeroy JW, Gray DM. 1995. *Snowcover accumulation, relocation and management*. National Hydrology Research Institute science report. Saskatoon, Saskatchewan, Canada: National Hydrology Research Institute.

Raupach MR. 1994. Simplified expressions for vegetation roughness length and zero-plane displacement as functions of canopy height and area index. *Boundary-Layer Meteorology* **71,** 211–216.

Schweingruber FH. 1996. *Tree rings and environment. Dendroecology*. Bern: Haupt.

SIA. 2006. *Wind*. D 0188, Zurich: Schweizerischer Ingenieur- und Architektenverein (SIA).

Silins U, Lieffers VJ, Bach L. 2000. The effect of temperature on mechanical properties of standing lodgepole pine trees. *Trees–Structure and function* **14,** 424–428.

Stadler DC, Bründl M, Schneebeli M, Meyer-Grass M, Flühler H. 1998. *Hydrologische Prozesse im subalpinen Wald im Winter*. Schlussbericht/NFP 31. Zürich VDF; Hochschulverlag an der ETH.

Strobel T. 1978. *Schneeinterzeption in Fichtenbeständen in den Voralpen des Kantons Schwyz*. Davos, Switzerland: International Seminar on Mountain, Forests and Avalanches, 63–79.

Telewski FW. 1995. Wind-induced physiologial and developmental responses in trees. In: Coutts M, Grace J, eds. *Wind and trees*. Cambridge: Cambridge University Press, 241–263.

Telewski FW. 2006. A unified hypothesis of mechanoperception in plants. *American Journal of Botany* **93,** 1466–1476.

Wood CJ. 1995. Understanding wind forces on trees. In: Coutts MP, Grace J, eds. *Wind and trees*. Cambridge: Cambridge University Press, 133–164.

Yang YB, Yang YT, Su HH. 2005. Behavior of the tree branches, trunk, and root anchorage by non-linear finite element analysis. *Advances in Structural Engineering* **8,** 1–14.

Ylinen A. 1952. Über die mechanische Schaftformtheorie der Bäume. *Silva Fennica* **76,** 1–52.

Zoumakis NM. 1993. Estimating the zero-plane displacement and roughness length for tall vegetation and forest canopies using semi-empirical wind profiles. *Journal of Applied Meteorology* **32,** 574–579.

Zweifel R, Hasler R. 2000. Frost-induced reversible shrinkage of bark of mature subalpine conifers. *Agricultural and Forest Meteorology* **102,** 213–222.

Summary discussion and conclusions

In general

Tree stability

A strong tree that is only subject to minor forces has a high level of tree stability. Such trees do not exist in nature and are difficult to produce because trees are intelligent plants that allocate their growth according to mechanical stress. In contrast, a low level of tree stability may occur if the natural development of a tree is subject to a sudden biological or physical disturbance, induced by nature or by humans through forest management. Here, tree stability has an important ecological, social and economical dimension.

Tree loads in nature

The loads prone to act on trees vary greatly in time and space due to the turbulent nature of winds (Gardiner 1994) and the punctual nature of mass movements (e.g. rockfall and snow avalanches). Clearly, these variations therefore govern the level of tree stability to a larger extent than the mechanical properties of the tree, but these variations are generally more difficult and less cost efficient to influence than the mechanical properties of trees.

Tree structure

A tree is a heterogeneous structure. It adapts its growth to the environment in various ways, and is especially responsive to mechanical stress. Knowledge about the load applications on trees will therefore contribute to our knowledge about the mechanical structure of trees. The mechanical properties of the wood in a tree depend on the wood's anatomical properties, and the mechanical properties of the tree anchorage depend on the ground conditions. Information about wood anatomy and the ground will therefore greatly contribute to a better assessment of a tree's mechanical structure.

The trees selected for investigation in this PhD thesis were growing under different climatic, ground, and forest conditions. This allowed the influence of the soil and the radial stem growth on the mechanical properties of the tree to be assessed. This range of trees also made it possible to highlight the influence of mechanical stress on the mechanical properties of trees, because the different growth conditions induced natural loads of different kinds and properties on the trees.

To better understand the mechanics of the tree structure, the heterogeneous tree structure was arranged into a pattern of mechanical functions. The root-soil system was identified as one major structural element, with mechanical properties that depend on the tree size and the environment. The stem and the crown were identified as being the second and the third major structural elements. The stem was investigated in most detail because: (1) the stem governs the stability of the tree in its interaction with many natural hazards; (2) relatively little is know about the mechanical properties of fresh stem wood and their relationships to properties of growth; and (3) the stem is easier to investigate in detail with respect to its morphology and anatomy than the two other major structural elements. As expected, the mechanical properties of the stem were found to depend on the tree size and the environment.

The tree in interaction with loads in nature

The mechanical reaction of the tree to most natural loads is dynamic, which means that the load and the tree interact during load application. The highly dynamic tree reaction was particularly striking in the rock-tree experiments of this study. Tree dynamics also play an important role for trees subject to wind (e.g. Gardiner 1995). Investigations of the swaying pattern of the entire tree subject to wind show that the rotational deflection of the crown may reduce tree deflection (Sellier et al. 2008), and that this damping of the tree swaying by the crown is important (Moore and Maguire 2005). In fact, the rotation of the crown lessens the effectively applied load on the tree crown and the branches provide the tree with mass dampers that are relatively well tuned with the two first swaying frequencies of the tree. Therefore, the crown strongly reduces the effect of load amplification at tree-wind resonance, and hence lessens the relative importance of resonance for tree stability. Structural damping has, however, little influence on the reaction of the tree during more high frequent dynamic interactions, e.g. when subjected to a rock impact. Nonetheless, when analyzing tree stability, it is important to elucidate the role of tree and load dynamics, and whether they can be simplified and described in a static approach or not.

The anatomical reaction of trees, i.e. the adaptation of growth, does not seem to depend on the dynamic reaction of the tree because growth adaptation was found to depend more strongly on the average load than on the maximum load (papers I and VI). This aspect is difficult, though, to investigate and will need more detailed studies to be better understood.

Mechanical performance of tree growth

The role of mechanical stress is important in the adaptation of tree growth (Jaffe 1973, Mickovski and Ennos 2003, Moulia et al. 2006), as was further confirmed in this study. Clearly, the focus was on the mechanical aspects rather than the anatomical. Direct proofs of the adaptation of tree growth to mechanical stress would require simultaneous measurements of mechanical stress and growth on the anatomical level. This would be very difficult to perform on the scale of the entire tree. By selecting trees of different age and social status and by analyzing the radial growth of tree stems, this study was able to identify strong signs of growth adaptation to mechanical stress.

This is a major issue in tree stability, and was therefore discussed in all six papers in this PhD thesis.

Aims and approach of this study

New allometric relationships for the mechanical properties of the root-soil system and the stem

The mechanical properties of the two major structural elements, the root-soil system and the stem, of the Norway spruce and silver fir investigated were obtained on the basis of curves describing the resistance as a function of deformation. The tilting of the root-soil system subject to turning moment and the deflection of the stem subject to bending could be very well described with properties of tree growth and size (allometry). As the particular deformations approached their limits of failure, the predictions were still quite precise for the root-soil system but only approximate for the stem. This means that the overall flexibility of the tree subject to frequent loads, i.e. of low and intermediate magnitude, could be well predicted by allometry. In contrast, the overall tree deformations that occur during rare exceptional natural loadings of large magnitude, like heavy storms and exceptional snowfalls, are more difficult to predict because of the approximate predictions of stem bending at high stress levels.

The allometry studied involves two types of growth parameters: morphology (size, taper, and form) and anatomy (properties of radial growth and health). Morphology had a greater influence on the mechanical properties of the stem than anatomy. In fact, the impact of the cross-sectional anatomy on the cross-sectional mechanics was weak compared to the impact of the stem diameter (papers III and IV). Typically, the lowering effect of the wider annual ring width on the stem bending strength (approximately power 0.3) was much weaker than the increasing radial growth (diameter in the third power). Among the anatomical properties of radial growth studied, only the knottiness close to the stem periphery had an impact (knottiness squared), comparable to the diameter of the stem section, i.e. to the geometric radial growth. In an unpublished work on stem-failure stress in winching experiments (Appendix 3), it is shown that mechanical damage and decay in the stem may significantly reduce its bending strength, as may the knots of old pruned branches. However, these factors do not have an impact of the same order of magnitude as that of the stem diameter.

The mechanical properties of the root-soil system subject to turning moment (papers I and II) could be well described by the variables tree and stem weight, stem diameter at breast height, and tree height. This is understandable, as aboveground tree size is related to the cross-sectional sum of roots (Bolenikus 2001). The anatomy of the roots was not studied explicitly. Nonetheless, it is improbable that the anatomical variables of the roots would significantly influence the mechanical properties of the root-soil system unless the roots are rotten (cf. paper I) or mechanically damaged.

In conclusion, tree size and stem taper are the most important variables for predicting the mechanics of the root-soil system and the stem of healthy and undamaged Norway spruce and silver fir. The growth properties of the stem cross-section can be used to more precisely predict the mechanics of the stem.

Influence of environmental abiotic stress on mechanical properties of the tree

The investigations in this PhD thesis of the tree's growth allocation to lessen concentrations of mechanical stress focused on some parts of the entire tree, including: azimuthal orientation of root-growth (paper I), resistance of the root-soil anchorage to uprooting (papers I and II), stem taper (paper VI), growth properties of the stem (papers III and IV), and to some extent, size of the crown (paper VI). The results relating to these topics have one thing in common: The way the growth adapts, in terms of mechanical performance to environmental abiotic stress, depends on the accumulated stress in time. In other words, the mechanical perception of cell growth in Norway spruce and silver fir depends on the integrated stress in time according to direction. The most thorough study of this topic (paper VI) also showed signs of growth adaptation to acute loads, but this became much less apparent with increasing age of the tree.

Because the growth adaptation to mechanical stress of the trees studied includes the entire tree, it seems probable that the information transmitted to the cell division in the various tree elements is centralized or organized in a manner so that most, if not all, cells are "aware" of the needs elsewhere in the tree. Further, for a tree to develop an optimal mechanical performance, it will need some decades of mechanically high-performing growth. This is important to keep in mind when changes in forest structure occur or are planned. Clearly, the growth optimization of the tree as a whole to lessen concentrations of mechanical stress greatly governs the mechanical behavior of the whole tree subject to mechanical stress in nature.

Mechanical behavior of the whole tree subject to mechanical stress in nature

The deformation properties of the stem and the root-soil system of all trees investigated allow the trees considerable flexibility. This flexibility may contribute to higher tree stability, but it can also impair stability. The flexibility allows the tree to deflect and thus avoid loading, but under some extreme load conditions it may also trigger stem buckling and contribute to tree uprooting (paper VI). Tree flexibility also governs how a tree reacts to dynamic loads, i.e. most loads in nature. For these three reasons, an adequate description of tree flexibility is important for analyzing tree stability.

The spruce trees investigated for critical combinations of load and tree state (paper VI) display no predominant type of failure when subjected to the most common combinations of load and tree state. For example, neither stem failure nor uprooting were more likely to occur at high winds for the unfrozen trees at low elevation. This is also true for the trees growing at high elevation in their average state. On the basis of the results related to tree reactions to steady winds in paper VI and of experimental investigations of tree-wind dynamics in the literature (given in the same paper), the consideration of dynamic effects was limited here to the discussion. The new data on tree flexibility and the models to predict tree flexibility described in this PhD thesis should contribute to more precise prediction models of the interaction between turbulent wind flow and trees, because a tree's flexibility governs the effective load application and amplification due to resonance.

The investigation of trees subject to rock impact (paper V) shows that inertia is key factor affecting the mechanical behavior of the whole tree subject to dynamic loading. In fact, the energy absorption related to inertia forces represented up to a third of the total energy absorption during the impact loading of a rock, and about a fifth at the end of the loading, when the tree's energy absorption capacity was reached. It is probable that inertia would also play a significant role in the tree's reaction to other rapid mass movements, like snow avalanches and debris flow.

Study approach

The approach to this PhD-study was mainly experimental, because the mechanical properties of the tree required for a numerical analysis of mechanical tree stability were unknown at the beginning of the study. The experimental results of tree deflection (winching tests and impact tests) can be fairly well predicted numerically (paper VI and Jonsson 2007). This suggests that future investigations of tree stability may be made with numerical help provided that the mechanical properties of the tree are well described. Nonetheless, experimental data are important for the validation of numerical tree models. Fortunately, there are now and efficient experimental set-ups to assess tree reactions to several types of loadings, for example those developed in this study.

Future research

This study provides insight in the following three topics: (1) allometric relationships for the mechanical properties of the main structural elements of the tree, the root-soil system and the stem; (2) the influence of mechanical stress in nature on such properties; and (3) the mechanical behavior of the whole tree subject to mechanical stress in nature, originating from wind, snow, and rockfall. Clearly, the work described here has not completely filled all the relevant knowledge gaps, but the results and the experiences gained during the PhD thesis have allowed better insights into the biomechanical function of trees. These should contribute to making the co-existence of trees and humans mutually beneficial. Further research drawing on the findings of this study would be worthwhile.

In (1), the allometric relationships developed depend not only on the site but probably also on the species (Peltola et al. 2000, Stokes et al. 2005). Therefore, the same type of relationships need be developed for additional sites and tree species in order to develop provide a versatile and useful basis for tree stability analyses and forest management. The species and sites of particular interest will depend upon the full value of the forest, i.e. the wood and pulp produced, and the protection and recreation offered (cf. *Background*).

In (2), it would be useful to investigate whether other species like Norway spruce adapt their growth to mechanical stress in nature. Then, important biomechanical aspects of forest management could be compared and taken into account in the management strategies.

In (3), additional sites and tree species should be emphasized as in (1). Further, experimentally based analyses of tree reactions to snow avalanche and debris flow are lacking. Finally, experimentally based analyses of tree-wind interactions would contribute to the knowledge built up in this field during recent decades.

Future research related to the topics (1) - (3) with a focus on the Alpine countries should concentrate on the species beech and larch growing at representative sites. These two species are frequent in forests providing protection against rockfall and avalanches, but their mechanical properties are still relatively unknown.

Working on this PhD thesis has generated data and results not yet published. Two papers on the tree-rock interactions have recently been submitted for publication (Jonsson et al.) and others could be soon ready for submission with some additional work. One topic is how trees react to snow avalanche flow and the amounts of energy they can absorb and another is described in Appendix 3. The findings about the mechanics of single trees are being incorporated in numerical models on the scale of the forest at the WSL-SLF. Of great interest for forest management, hazard mapping, and risk analysis would be combining such mechanical models and growth models on the scale of the protection forest.

Appendices

Appendix 1

Study sites

The 136 trees included in this study were located in twelve different plots (Table A1- 1). The detailed locations of these plots are given in Table A1- 2 and in Fig. A1- 1 to 10. The photos of the location of the sites were taken from Google Earth (earth.google.com) and the map segments from Swisstopo (www.swisstopogeodata.ch/geodaten-viewer).

Table A1- 1: Number of trees according to study, site, plot (a-l), and species. Abbreviations: LE=low elevation (below 650 m asl); HE=high elevation (above 1600 m asl); S=Norway spruce; Fir=silver fir; and Pine=Scots pine.

Study/	Plots															
Paper	LE-site									HE-site						
	a			b		c		d	e	f	g	h	i	j	k	l
No.	S	Fir	Pine	S	Fir	S	S	S	S	S	S	S	S	S	S	S
I	25	5	4	2	7	31	10	-	-	-	-	-	-	-	-	-
II	19	-	-	18	-	-	-	4	4	1	4	3	4	4	1	4
III	-	-	-	1	-	-	-	-	-	-	-	-	-	-	-	-
IV	-	-	-	3	4	-	-	-	-	-	-	-	-	-	-	-
V	-	-	-	-	-	-	-	-	-	-	-	-	-	-	5	10
VI	-	-	-	2	-	-	-	2	2	-	-	2	-	-	1	4

Table A1- 2: Coordinates of the centre of the plots (cf. Fig. A1- 2 to 10) on which the trees investigated originate. CH1903+ is the Swiss local reference system, relating (+) to the reference point Zimmerwald. WGS84 is the World Geodetic System using the ellipsoid model of 1984 (rigorous coordinate transformation, FOT 2006).

Reference	Coor-	Unit	Plots											
system	dinates		a	b	c	d	e	f	g	h	i	j	k	l
CH1903+	y	m	707490	709610	710400	677920	677980	781710	781760	782280	781940	780730	783300	780580
	x	m	233520	231520	231710	246780	246780	182940	182700	182380	181640	181590	185450	183920
	h	m asl	455	455	470	625	625	1770	1820	1860	1650	1730	1680	1760
WGS84	W	°	8	8	8	8	8	9	9	9	9	9	9	9
		'	51	53	53	28	28	49	49	49	49	48	50	48
		"	35	14	51	17	20	10	12	36	19	22	28	18
	N	°	47	47	47	47	47	46	46	46	46	46	46	46
		'	14	13	13	22	22	46	46	46	45	45	47	46
		"	43	37	42	7	7	27	19	8	45	44	47	60

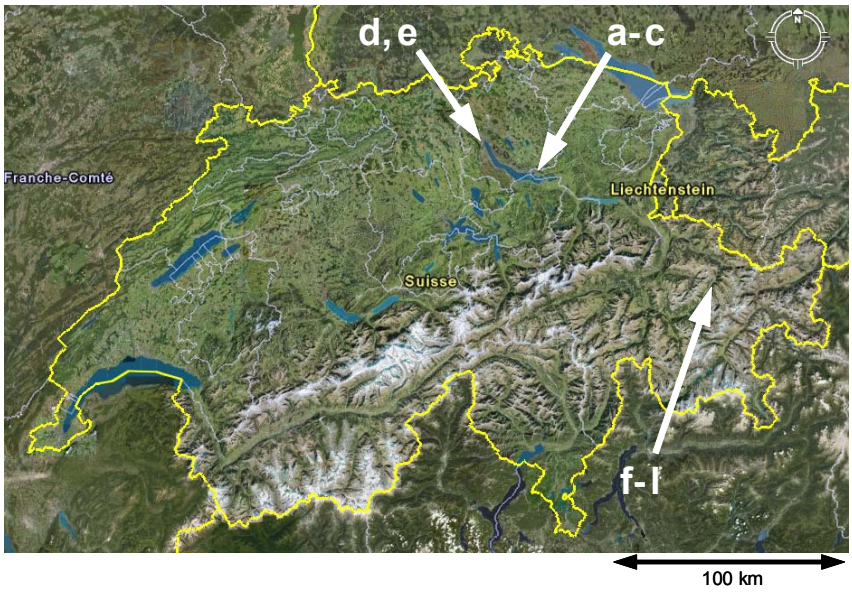

Fig. A1- 1: Location of all study plots (letters from a to l.) on the scale of Switzerland (Suisse).

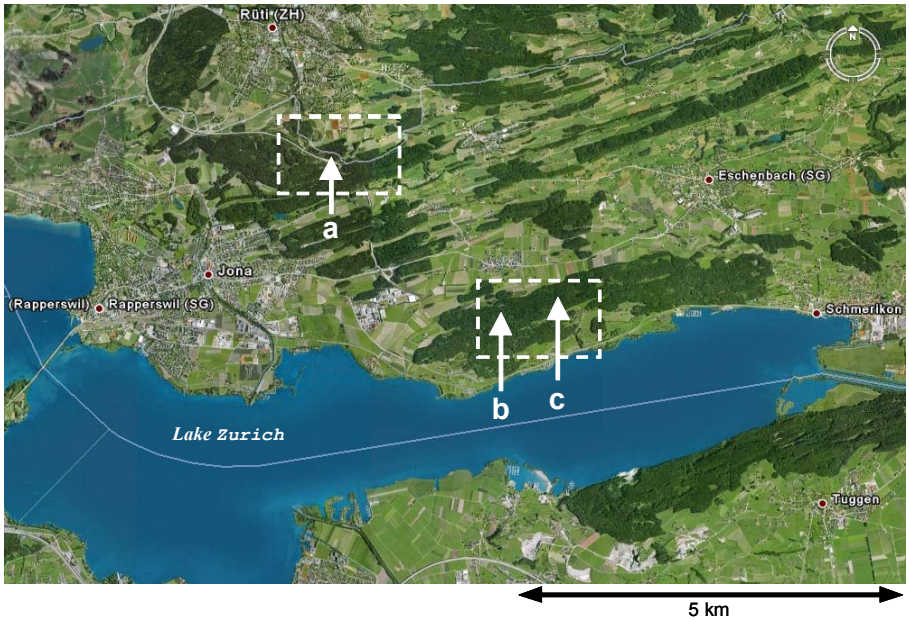

Fig. A1- 2: Location of the three study plots a-c, north of the Lake Zurich and about 30 km ESE of Zurich.

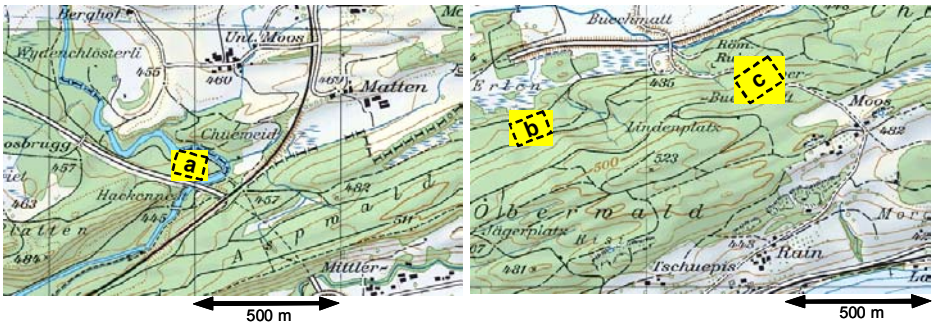

Fig. A1- 3: Details of Fig. A1- 2 with the plots a, b and c.

Fig. A1- 4: The study plots d and e are located in the research forest of the ETHZ (Swiss Federal Institute of Technology Zurich), on a hill 5 km W from the centre of Zurich.

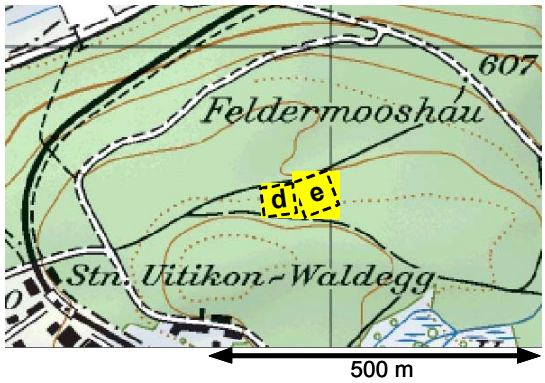

Fig. A1- 5: Detail of Fig. A1- 4 with the plots d and e.

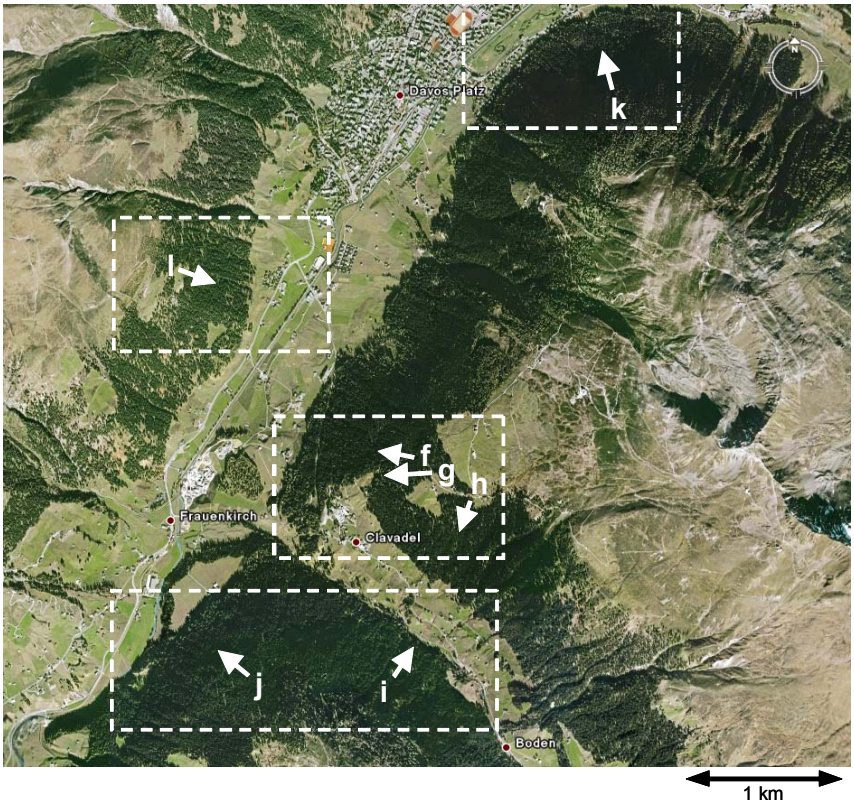

Fig. A1- 6: The plots f-l are located south of Davos, on the forested slopes that sideways border the “Landwasser” valley (light green band from centre-top to left-bottom).

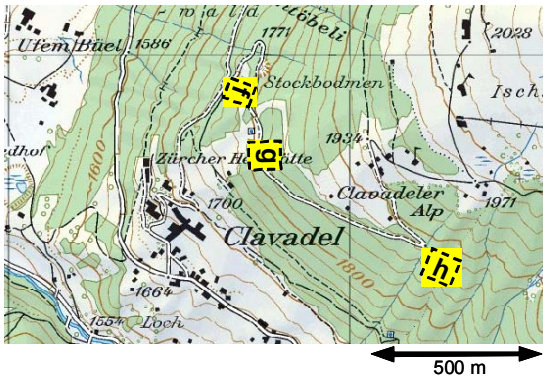

Fig. A1- 7: Detail of Fig. A1- 6 with the plots f, g and h.

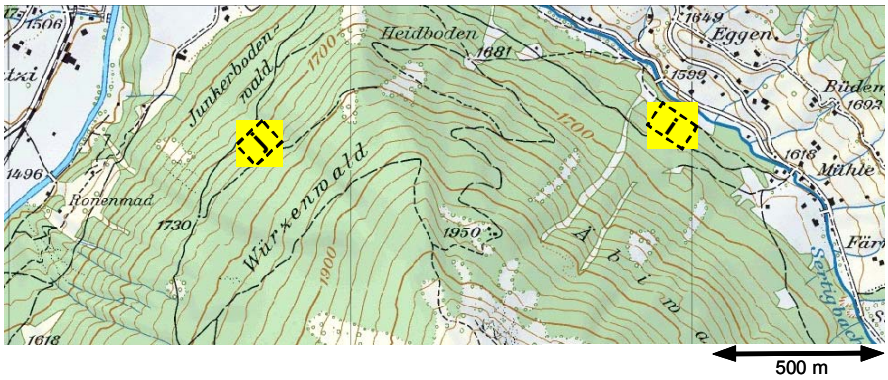

Fig. A1- 8: Detail of Fig. A1- 6 with the plots i and j.

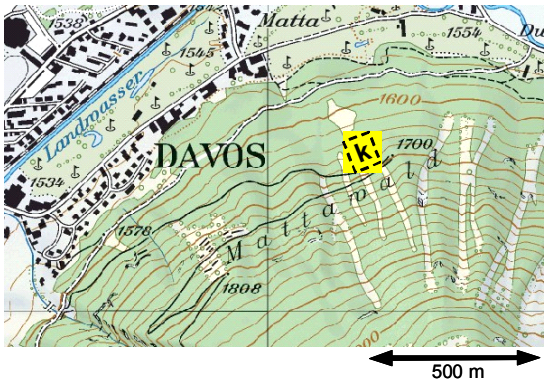

Fig. A1- 9: Detail of Fig. A1- 6 with the plot k.

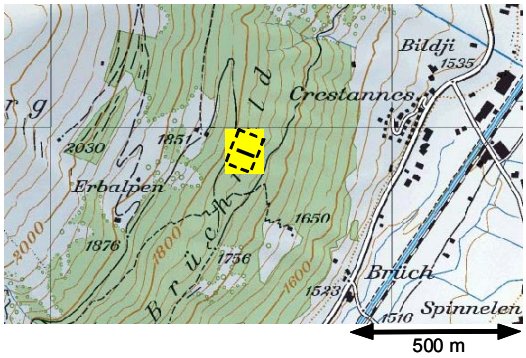

Fig. A1- 10: Detail of Fig. A1- 6 with the plot l.

Appendix 2

Stemtrack - digital image analysis as tool to detect the stem deflection in tree stability experiments

Tobias Jonas[1] and Tor Lundström[1]

[1] Tree Stability Research Group, Swiss Federal Institute for Snow and Avalanche Research SLF, 7260 Davos Dorf, Switzerland

Available in www.wsl.ch/forschung/forschungsprojekte/Treestability/Stemtrack.pdf [accessed October 2008]

Date: September 2006 (first access)

Introduction

This is a technical annex to the piece of software STEMTRACK. The annex provides detailed information about the data processing methods incorporated in the software, with particular focus on the image referencing procedure. The annex also describes the measurements in the field required for the camera set-up. Our ambition is to enable the reader to reproduce and apply our approach to "Digital image analysis as tool to detect the stem deflection in tree stability experiments". The software has been used since 2004 at the Swiss Federal Institute for Snow and Avalanche Research SLF.

Tree stability research at the Swiss SLF focuses on mechanical response of trees to natural hazards, i.e. wind, rockfall and avalanches. The experimental approach includes series of rock impact simulations (Fig. A2- 1), swaying and winching tests. A common feature of these experiments is to investigate the stem line deflection in response to external forcing.

We identified image analysis techniques as a tracking tool that could potentially cover all requirements at once for the different types of experiments. In particular we needed; (1) a spatially continuous recording of the stem line deflection; (2) an adjustable temporal resolution from static (winching test) up to 250 records/second (rock impact simulations); and (3) a spatial resolution on the order of 10^{-2} m. Additional advantages of image analysis techniques were identified with no expensive equipment required and remote data capture, not sensitive to enormous stem accelerations.

These arguments gave us motivation to set-up image analyses technique for our purposes. This in particular meant to overcome many practical problems from recording stem deflection dynamics to spatially referencing the images to true-world coordinates. With this technical annex we would like to share the experiences made and the developed methods.

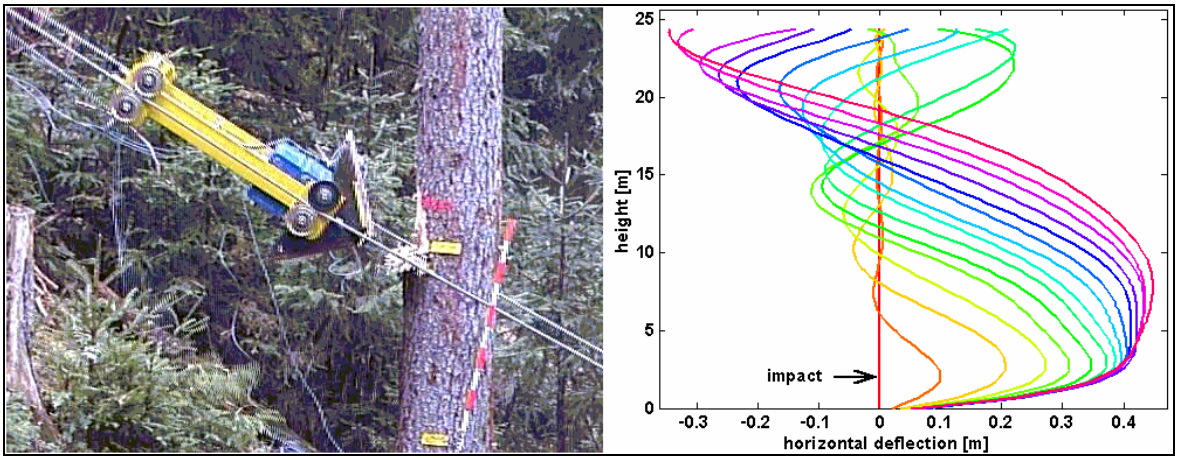

Fig. A2- 1: In situ rock-tree impact simulations: A trolley, guided by pre-constrained steel wires mounted on the slope, simulates the rock (left panel). Weighing 592 kg, it hits the tree stem at a height of 1.95 m with a speed of 21.5 m/s. Images were taken at 250 Hz; Deflection response of the tree, tracked by means of image analysis technique using our software package STEMTRACK (right panel). The curves from red to ruby show time steps of 20 ms

Short description of the software package

In order to apply image analysis technique in an efficient and operational mode, we decided to develop an own tailor-made software solution instead of using a combination of commercially available image manipulation software. The resulting software package STEMTRACK has been implemented in Matlab 7 (Mathworks Inc., USA) and features a graphical user interface (Fig. A2- 2). STEMTRACK allows: (1) image handling and basic image manipulation; (2) spatially referencing and rectifying images; (3) edge detection of the stem; (4) calculation of the center stem line and its polynomial parameterization; (5) basic analysis of center stem line data; and (6) data export for more sophisticated analysis.

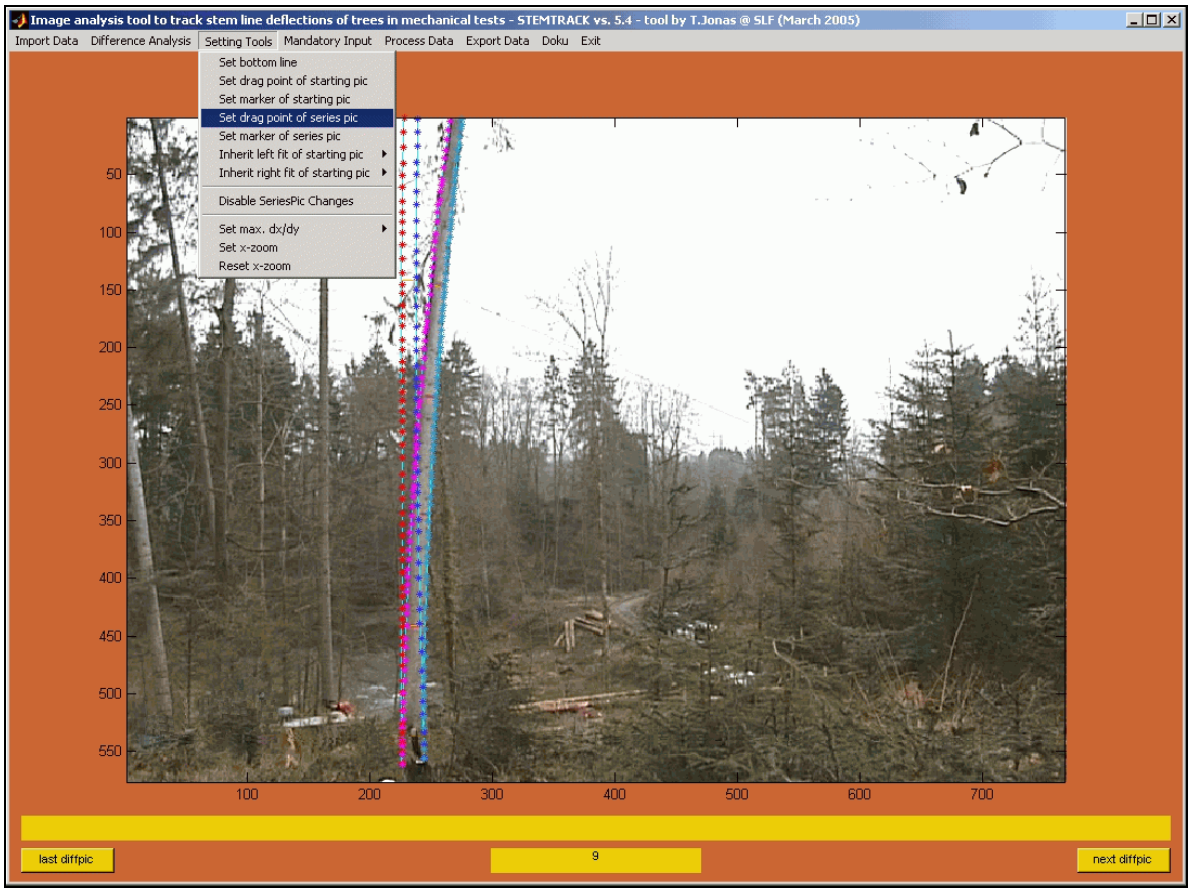

Fig. A2- 2: Screenshot of the graphical user interface of STEMTRACK, here with an image of a winching experiment

To start, the user can assemble a sorted series of images for the later analysis and apply simple picture manipulation filters, such as grayscale, contrast enhancement, left-right flip, etc. The first image of the series will be interpreted as the initial tree position (i.e. zero deflection). Upon confirming the final set of images, STEMTRACK calculates image differences of each picture in the series to the first reference picture. These will be used for stem edge detection (see inset I, Fig. A2- 3). The Software offers several modes that allow edge detection of the stem. For automated detection the user is required to give a starting point upon the stem edge. Given a sufficient image quality the stem edge is followed automatically. The user can manipulate the automatic result by cropping or adding fit points. If the contrast is critically low, the edges may also be determined by selecting all fit points manually. As the edge lines are parameterized by a polynomial, a few dozen fit points typically suffice.

When all edge lines are determined STEMTRACK calculates the center stem lines. Therefore, orthogonal opposite points are identified, the mid positions of which are taken to determine the center stem line (see inset II, Fig. A2- 3). We also parameterize this line by least-squares fitting a polynomial to the determined mid points.

The software allows to spatially reference the images, by re-projecting them onto an orthogonal and metric coordinate system in the plane of the tree deflection (cf. *Image referencing*). This procedure requires the user to enter some spatial information about the set up in the field, i.e. the spatial relationship between camera and deflection plane (cf. *Measurements in the field*). With this referencing procedure, the stem line pixel data is transformed into spatial data in metric coordinates of the deflection plane. This spatial data of the stem line dynamics is basis for any further analysis of e.g. rock impact experiments.

A helpful feature of STEMTRACK is that it allows saving work sessions. This option allows the user to interrupt the work at any step during the analysis and to continue later without loss of data. At present only basic analysis features are implemented, that operate on the referenced stem line data, e.g. curvature, etc. For complex analysis, the stem line data is exported and evaluated against external data separately. However, the modular structure of STEMTRACK source code enables to integrate more analysis features as plug-in tools.

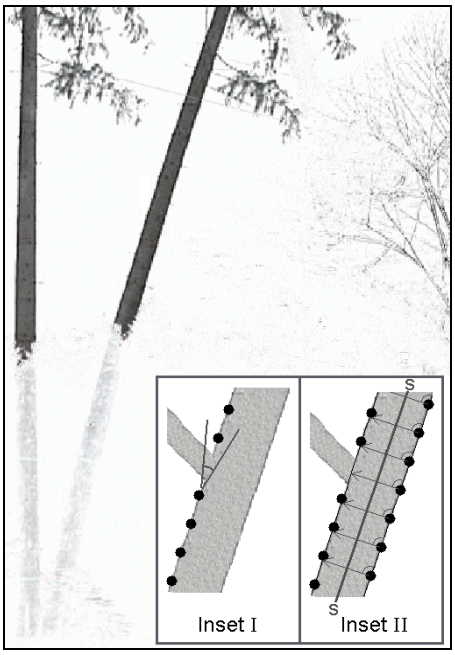

Fig. A2- 3: Difference image of a picture from a deflected tree in a winching experiment and the reference picture at the begin of the experiment, that illustrate two possible problems for the automatic edge detection: a) Part of the tested tree is obstructed by bushes; b) the tree in the upper right corner has apparently moved due to winds. This may perturb the edge detection procedure if in the proximity of the edge line. The angle-restricted edge detection bypasses branches (Inset I, upward edge detection). The center stem line is estimated from the two edge lines by identifying points halfway between pairs of orthogonal opposite points on the edge lines (Inset II).

Image referencing

The basis for our image analysis approach to track stem line deflections consists of a photographic technique that allows spatially referencing the resulting images. In typical applications (e.g. winching or swaying experiments) we face a quasi 2-dimensional deflection response of the tree to external forces. We will refer to the in this way spanned 2-d plane, as the deflection plane ***D*** (cf. Fig. A2- 9).

The image referencing shall be understood as the vertical analogon to rectifying / geo-reference maps in GIS to a given coordinate system. I.e., we retrace the position from where in the deflection plane pixels on the image sensor have been projected.

Measurement of the lens distortion

We intended to develop a method that would not have to rely on expensive photographic equipment such as quasi-metric camera-lens systems designed for photogrammetry. Thus we had to accept, the camera optics to display a normal level of radial lens distortion (barrel distortion). This effect especially matters as working in forests requires the use of wide-angle zoom lenses, which are especially susceptible to considerable distortion. Uncorrected, the projected length on images of identical lines may vary by a few percents from the image center to the outer edges. Therefore it is imperative to include the actual lens projection when spatially referencing images.

To assess the distortion of the camera-zoom lens system, we conducted systematic performance tests. For ten zoom settings we photographed a rectangular point grid pattern, mounted parallel to the image sensor surface at a distance of 5 m (Fig. A2- 4). The optical origin of an pixel can be directly read out by locating its position on the grid's image. Doing so for each pixel, the lens projection is directly measured. This procedure results in a projection matrix, the entries of which contain the position from where in an object plane at 5 m distance each pixel on the image sensor has been projected. The positions are given in coordinates of the camera-inherent coordinate system ***CP*** (Fig. A2- 5). The figure gives an example of the projection matrix $\underline{\boldsymbol{M}}_{\boldsymbol{P}}$ for a Nikon Coolpix 4300 camera at a focal length ***f***=10 mm, and a resolution of 90 x 60 pixels. $\underline{\boldsymbol{M}}_{\boldsymbol{P}}(x_i,z_j)$ is to be understood as the vector containing the ***x***-, ***y***-, and ***z***-coordinates (in ***CP***) from where the pixel $[x_i,z_j]$ has been projected given an object plane at 5 m distance.

Actually, a projection matrix would be needed for each factor combination of focal length settings x pixel resolution settings. For practical reasons, we parameterize the matrix as a function of ***f***. The parameterization assumes pure radial lens distortion, the compensation of which can be described by a radius correction function ***rc***,

$$(1)\quad rc = \left(k \cdot r^2 + 1 - k\right) \cdot r \text{ , with } k = k_1 \cdot f^{-k_2},$$

where k_1 and k_2 are parameters that are obtained from a best fit to the lens performance tests (Fig. A2- 4). The correction factor rc is applied by shifting the pixel towards the image center by multiplying its radius with rc (Fig. A2- 6).

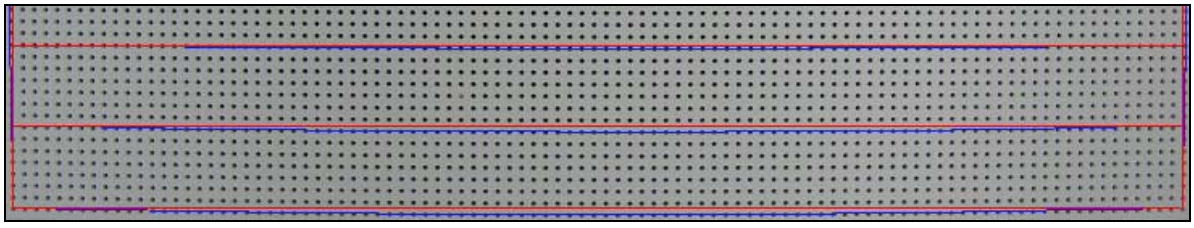

Fig. A2- 4: Measurement of the lens performance. The figure shows the lower part of an image of a rectangular point grid pattern. The curvature of the image of a straight row of points (blue line) is the effect of radial distortion (offset from the straight red line).

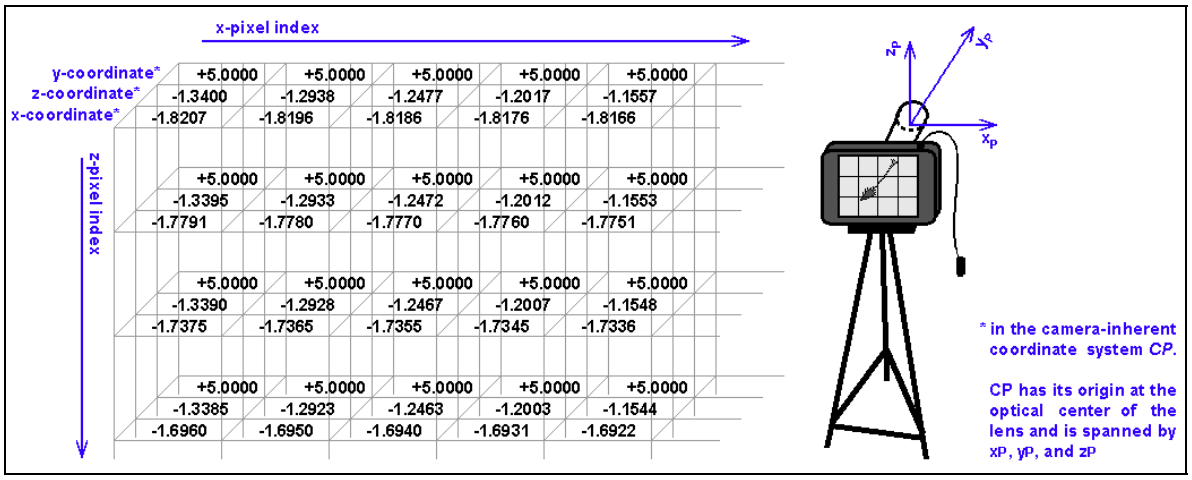

Fig. A2- 5: Projection matrix $\underline{\boldsymbol{M}}_P$ for a Nikon Coolpix 4300 camera at a focal length f=10 mm, and a low resolution of 90 x 60 pixels. The matrix contains the position from where in an object plane at 5 m distance each pixel on the image sensor has been projected. The positions are given in coordinates of the camera-inherent coordinate system ***CP***.

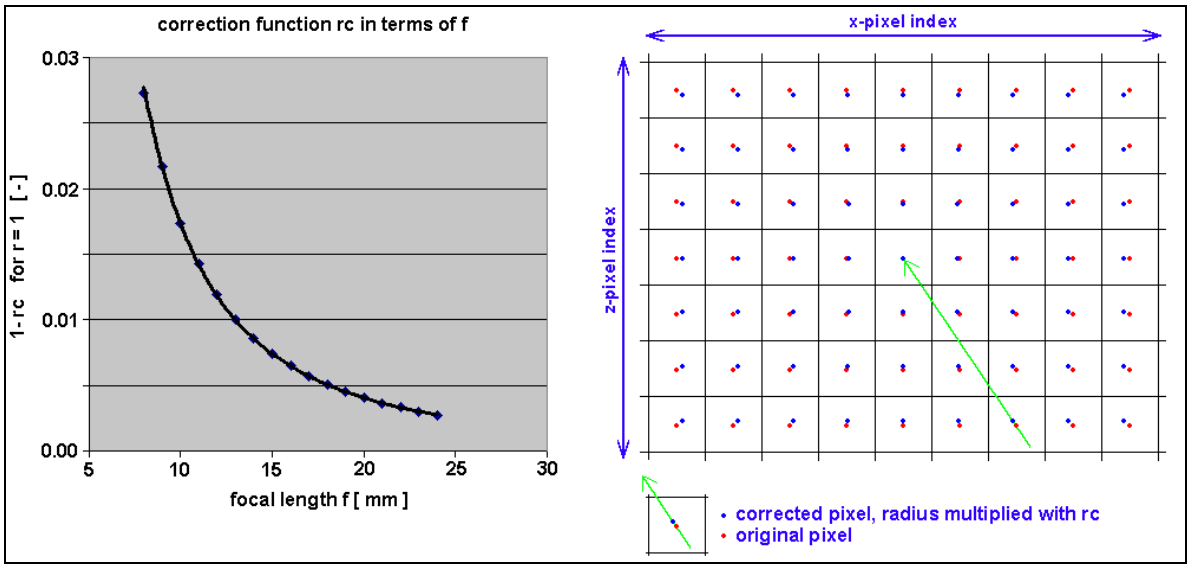

Fig. A2- 6: Description of the parameterized form of radial lens distortion. Left panel: radius correction function rc according to eq(1) fitted to measurements of the lens system of a Nikon Coolpix 4300 camera; Right panel: schematic (exaggerated) of a rectangular grid (red pixels) that the correction function has been applied to (blue pixels). The corrected grid is used to calculate parameterized projection matrices.

In a next step the so far parameterization needs to be scaled and discretized for the selected pixel resolution. For scaling purposes, the maximum horizontal and vertical aperture angles $\boldsymbol{ap}_{horz}$ and $\boldsymbol{ap}_{vert}$ have to be known from measurements and parameterized by a polynomial in terms of focal length $\boldsymbol{f}$ (Fig. A2- 7).

The parameterized raw projection matrix in the right panel of Fig. A2- 6 is remapped to meet $\boldsymbol{ap}_{horz}$ and $\boldsymbol{ap}_{vert}$, given an object plane at 5 m distance. Discretized for the appropriate pixel resolution the resulting matrix corresponds to a parameterized form of the projection matrix $\underline{\boldsymbol{M}}_P$ in Fig. A2- 5.

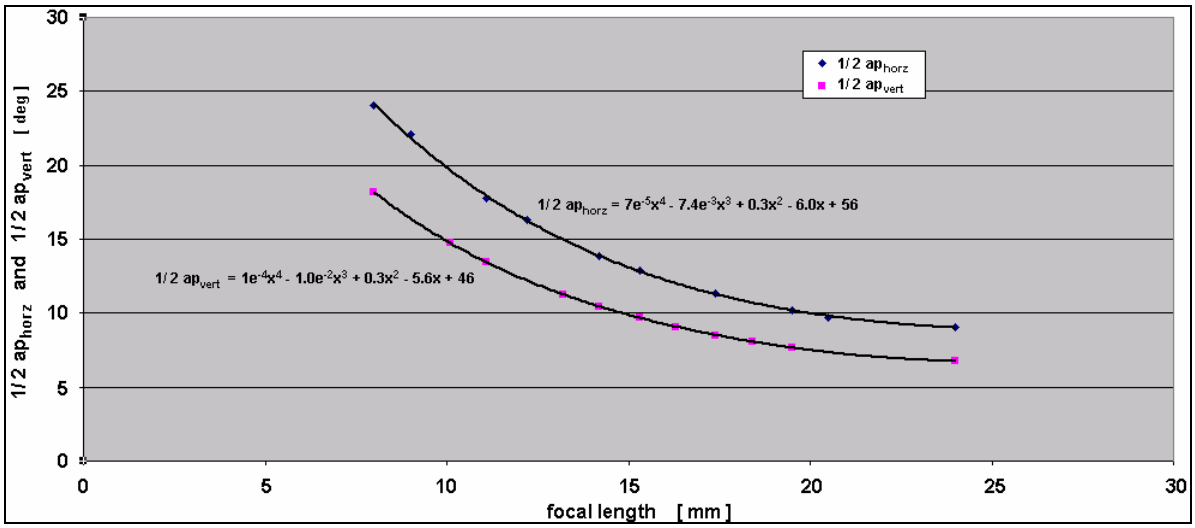

Fig. A2- 7: Measurements (points) and parameterization (lines) of horizontal and vertical aperture angles of the lens system of a Nikon Coolpix 4300 camera.

Measurements in the field

The camera set-up in the field is important to the referencing procedure of images. In order to allow accurate image referencing results, the camera's image sensor should be oriented approximately parallel to deflection plane (Fig. A2- 9). The digital image analysis presented here is used to track the position of the center stem line of trees in mechanical tests (Fig. A2- 8). Therefore, we need to retrace the position from where pixels on the image sensor have been projected. The accuracy of this procedure can benefit from a thorough camera set-up in the field. That is why we shortly address how to optimize the experimental set-up.

Most mechanical tests will lead to tree deflections in a quasi 2-dimensional plane, referred to as the deflection plane *D* in the following. In order to keep the projection of the tree onto the image sensor's surface geometrically as simple as possible, the camera's image sensor in the pixel plane *P* should be oriented approximately parallel to the deflection plane (Fig. A2- 8). This might require a camera position at about half of the trees' heights. Typically, zoom lens systems achieve best optical performance in the center bulk of the image and for middle zoom ranges. Correspondingly, border areas of the image and wide angle shots may be subject to considerable distortion effects and should be avoided. However, to exclude obstacles between camera and test tree, wide angle recordings may be necessary.

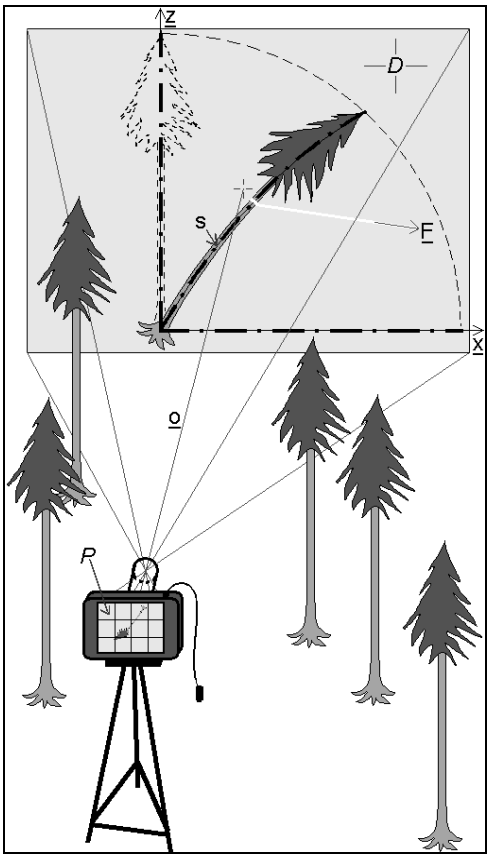

Fig. A2- 8: Experimental set-up (1), illustrated for a winching experiment. The horizontal component of the drag force F defines the x-axis and spans the deflection plane D with the vertical z-axis. The optical axis is denoted by o, s is the center stem line. An important requirement for accurate data analysis is to position the camera's image sensor in the pixel plane P approximately parallel to D. Heavy tripod gear and a remote release keeps the camera still during the experiment.

For the identification of the stem edges a sufficient image contrast is needed. Markers, tape or paint on the stem improve contrast in poor light conditions. Of great importance is to keep the camera completely still during the tests, as otherwise fix points would be erroneously interpreted as being moved. This can be achieved by mounting the camera onto a heavy tripod, by using a remote release and by locking the auto-focus.

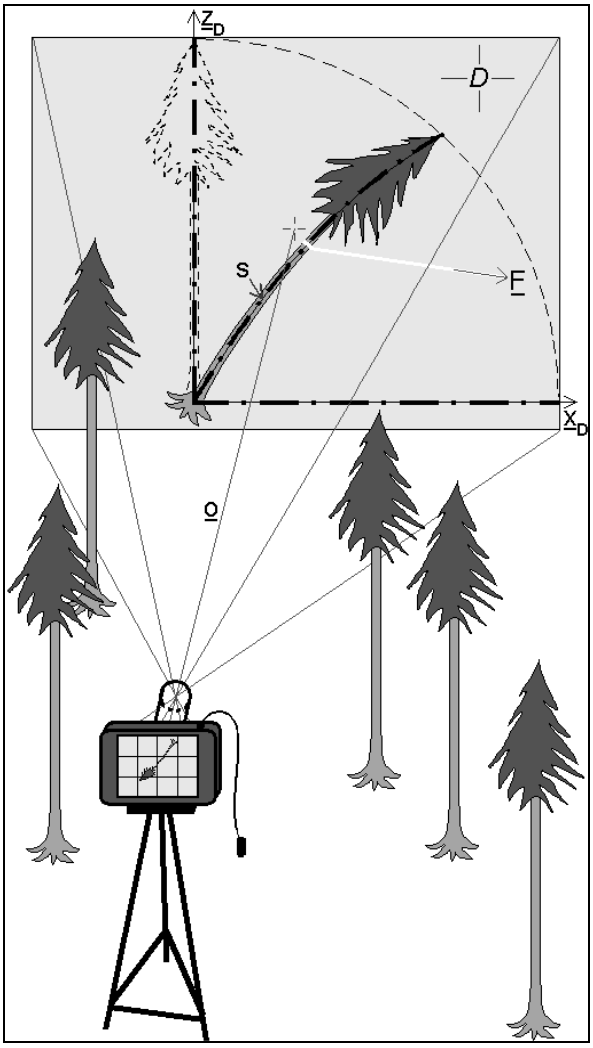

Fig. A2- 9: Experimental set-up (2), illustrated for a winching experiment. The horizontal component of the winching force ***F*** defines the x_D-axis and spans the deflection plane ***D*** with the vertical z_D-axis. The optical axis of the lens is denoted by ***o***, ***s*** is the center stem line. An important requirement for accurate data analysis is to position the camera's image sensor approximately parallel to ***D***. Heavy tripod gear and a remote release keeps the camera still during the experiment.

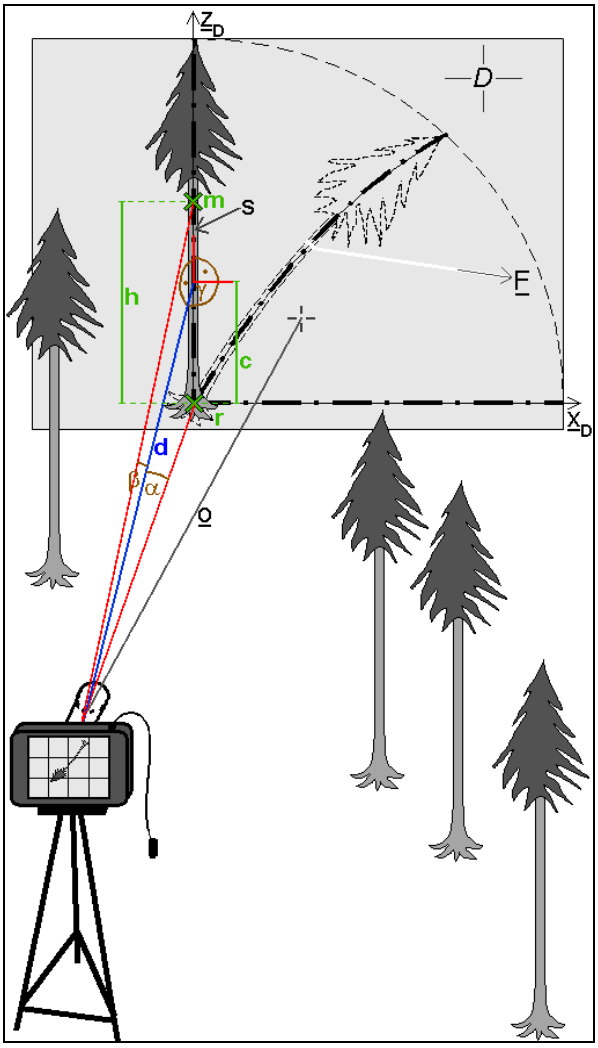

Fig. A2- 10: Distance and angle measurements of the camera set-up in order to describe the spatial relationship between the camera's images sensor and the deflection plane ***D***. Note, that the optical axis ***o*** of the camera's lens system is not necessarily orthogonal to the deflection plane ***D***. The horizontal distance from the lens to the stem is denoted by ***d***. The intersection of the center stem line ***s*** with the ground ***r*** is taken as origin for the coordinate system associated with ***D***.

In experiments with no need for high temporal resolutions, e.g. in winching experiments, we used Nikon Coolpix 4300 (Nikon Corporation, Japan) cameras at a low resolution profile of 724x512 pixel, a Nikon MC-EU1 cable release and a Manfrotto tripod additionally fixed to a neighboring tree. The auto-focus was locked and images were saved without compression. For dynamic tests the digital cameras were replaced by high-speed video cameras, which were synchronized with other measuring devices. For swaying tests we deployed a 25 Hz Sony DCR-TRV900E (Sony Corporation, Japan), while rock impact simulations were recorded with a 250 Hz Redlake MotionScope-PCI (DEL Imaging Systems, LLC, USA).

An essential requirement for the image referencing procedure is that the spatial relationship between the camera-inherent coordinate system ***CP*** (Fig. A2- 5) and the deflection plane can be described. Using a set of

distance and angle measurements of the camera set-up (Fig. A2- 10), we parameterize origin and spanning vectors of the coordinate system associated with ***D*** using ***CP***-coordinates. In particular we need to measure the cameras horizontal distance ***d*** and height offset ***c*** relative to the root, and two angles α and γ that characterize the relative rotation of the deflection plane ***D*** against the optical axis $\underline{o}$ (Fig. A2- 10). Moreover we utilize a marker ***m*** on the tree (localized by ***h*** or β) in order to have an in situ vertical length scale.

Description of the spatial relationship between the camera's images sensor and the deflection plane

The length and angle measurements obtained in the field are utilized to characterize the spatial relationship between the camera-inherent coordinate system ***CP*** and the deflection plane ***D***, i.e. expressing origin and spanning vectors of the coordinate system associated with ***D*** in coordinates of ***CP*** (eq. 2 to 6 below). The origin ***r*** of ***D*** is found using the projection matrix entry at the image pixel of the root $\underline{\boldsymbol{M}}_{\boldsymbol{P}}(\boldsymbol{x}_{root},\boldsymbol{z}_{root})$:

$$(2)\qquad \text{distance}[\text{lens} \leftrightarrow \text{root}] = \sqrt{d^2 + c^2} = g_{root} \cdot \sqrt{\underline{M}_p(x_{root}, z_{root})^2}$$

where $\boldsymbol{g}_{root}$ is a scaling factor of $\underline{\boldsymbol{M}}_{\boldsymbol{P}}$, and $\boldsymbol{g}_{root} \cdot \underline{\boldsymbol{M}}_{\boldsymbol{P}}(\boldsymbol{x}_{root},\boldsymbol{z}_{root})$ is the origin of ***D*** in coordinates of ***CP***. In the same way we determine the position of the marker ***m***,

$$(3)\qquad \text{distance}[\text{lens} \leftrightarrow \text{marker}] = \sqrt{d^2 + (h-c)^2} = g_{mar\,ker} \cdot \sqrt{\underline{M}_p(x_{mar\,ker}, z_{mar\,ker})^2}$$

with $\boldsymbol{g}_{marker} \cdot \underline{\boldsymbol{M}}_{\boldsymbol{P}}(\boldsymbol{x}_{marker},\boldsymbol{z}_{marker})$ yield the ***CP***-coordinates of marker ***m***. The vector difference of the positions of marker ***m*** and root ***r*** is used as vertical spanning vector $\underline{\boldsymbol{z}}_{\boldsymbol{D}}$ of ***D***.

$$(4)\qquad \underline{y}_D = g_{mar\,ker} \cdot \underline{M}_p(x_{mar\,ker}, z_{mar\,ker}) - g_{root} \cdot \underline{M}_p(x_{root}, z_{root})$$

The horizontal spanning vector $\underline{x}_D$ of ***D*** is found by rotating a vector corresponding to the blue line in Fig. A2- 10 around axes $\underline{\boldsymbol{z}}_{\boldsymbol{D}}$ with angle γ.

$$(5)\qquad \underline{x}_D = \underline{R} \cdot \left(g_{root} \cdot \underline{M}_p(x_{root}, z_{root}) + \frac{c}{h} \underline{z}_D \right)$$

$$\underline{R} = \begin{bmatrix} z_1^2(1-\cos\gamma) + \cos\gamma & z_1 z_2(1-\cos\gamma) - z_3 \sin\gamma & z_1 z_3(1-\cos\gamma) + z_2 \sin\gamma \\ z_1 z_2(1-\cos\gamma) + z_3 \sin\gamma & z_2^2(1-\cos\gamma) + \cos\gamma & z_2 z_3(1-\cos\gamma) - z_1 \sin\gamma \\ z_1 z_3 \cdot (1-\cos\gamma) - z_2 \sin\gamma & z_2 z_3 \cdot (1-\cos\gamma) + z_1 \sin\gamma & z_3^2(1-\cos\gamma) + \cos\gamma \end{bmatrix}$$

$$\begin{pmatrix} z_1 \\ z_2 \\ z_3 \end{pmatrix} = \frac{\underline{z}_D}{|\underline{z}_D|}$$

where $\underline{\boldsymbol{R}}$ is the rotation matrix corresponding to a 3d-rotation by γ around axes $\underline{\boldsymbol{z}}_{\boldsymbol{D}}$. Given the origin and the spanning vectors of ***D*** in ***CP***-coordinates, each point $\underline{\xi}$ in the deflection plane can be expressed as a linear combination

$$(6)\qquad \underline{\xi} = g_{root} \cdot \underline{M}_p(x_{root}, z_{root}) + \xi_x \cdot \frac{\underline{x}_D}{|\underline{x}_D|} + \xi_z \cdot \frac{\underline{z}_D}{|\underline{z}_D|}$$

where ξ_x and ξ_z are the coordinates of $\underline{\xi}$ in ***D***-coordinates.

Final re-projection of the pixel grid onto the deflection plane

In a next step of the image referencing process, the projection matrix is re-projected onto the deflection plane, using a central (optical center of the lens) projection, Fig. A2- 11. In order to find the central projection of a pixel image in the projection matrix, we need to solve the vector equation

$$(7) \qquad h \cdot \underline{M}_p\left(x_i, z_j\right) = g_{root} \cdot \underline{M}_p\left(x_{root}, z_{root}\right) + \xi_{x,i} \cdot \frac{\underline{x}_D}{\left|\underline{x}_D\right|} + \xi_{z,i} \cdot \frac{\underline{z}_D}{\left|\underline{z}_D\right|}$$

yielding the intersection of the line [***CP***-origin ↔ pixel $\underline{\boldsymbol{M}}_{\boldsymbol{P}}(\boldsymbol{x}_i,\boldsymbol{z}_i)$] with the deflection plane. This 3-dimensional vector equation can be solved for the three scalar parameter $\boldsymbol{h}$, $\boldsymbol{\xi}_{x,i}$, $\boldsymbol{\xi}_{z,i}$. With $\boldsymbol{\xi}_{x,i}$ and $\boldsymbol{\xi}_{z,i}$ being the ***D***-coordinates of the pixel's $\underline{\boldsymbol{M}}_{\boldsymbol{P}}(\boldsymbol{x}_i,\boldsymbol{z}_i)$ re-projection, we can compute the final reference matrix $\underline{\boldsymbol{M}}_{\boldsymbol{R}}$, that contains for each pixel the optical origin in the deflection plane in ***D***-coordinates. The final reference matrix re-projects images onto deflection plane coordinates and thus enables any spatial analysis.

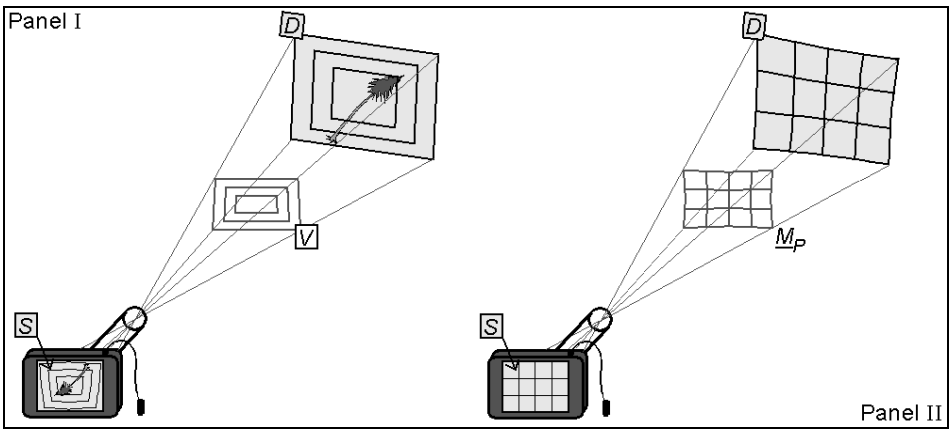

Fig. A2- 11: Projection of objects in the deflection plane ***D*** onto the camera's image sensor ***S***, with ***D*** is not parallel to ***S*** (Panel I). This projection can be split up into two steps: First, a central (optical center of the lens) projection of objects in ***D*** onto a virtual plane ***V***, which is parallel to ***S***. And second, a distorted projection of the image in ***V*** onto ***S***; To spatially reference the digital images, the pixel grid in ***S*** is re-projected onto ***D*** (Panel II). This allows assigning to each pixel its originating position in ***D***. Note that the re-projection of the pixel grid upon ***V*** yields the entries of the Projection matrix $\underline{\boldsymbol{M}}_{\boldsymbol{P}}$, provided ***V*** is positioned 5 m in front of the lens.

Validation of the image referencing procedure

In order to validate the spatial image referencing procedure under realistic conditions we took pictures of a building with zoom settings, from distances, and under angles typical for tree experiments in the forest. A grid of markers on the buildings surface allowed testing the markers real position against the position estimation from the referenced image of the building.

The test set-up is shown in Fig. A2- 12. The positions of 42 marker points in a 7x6 grid design upon the building's surface were measured using a laser tracker, a plumb-line, and a level. The positions of the three camera locations were determined correspondingly. We calculated the positioning error of any of the in this way obtained 3d coordinates to be smaller than 3 cm. Images were taken from three locations, using different zoom settings per location.

We evaluated the positions of the markers in the spatially referenced images (Fig. A2- 13) and tested these coordinates against the known position from the measurements directly upon the wall (Table A2- 1). The tests resulted in a mean positioning error of 1.0 cm per 10 m distance (camera – building), a maximum positionning error of 2.0 cm per 10 m, respectively. These excellent results let us believe that image analysis technique is capable of accurate stem deflection tracking. We hope to contribute with this Annex to more easily access the advantages of image analysis for tree stability sciences.

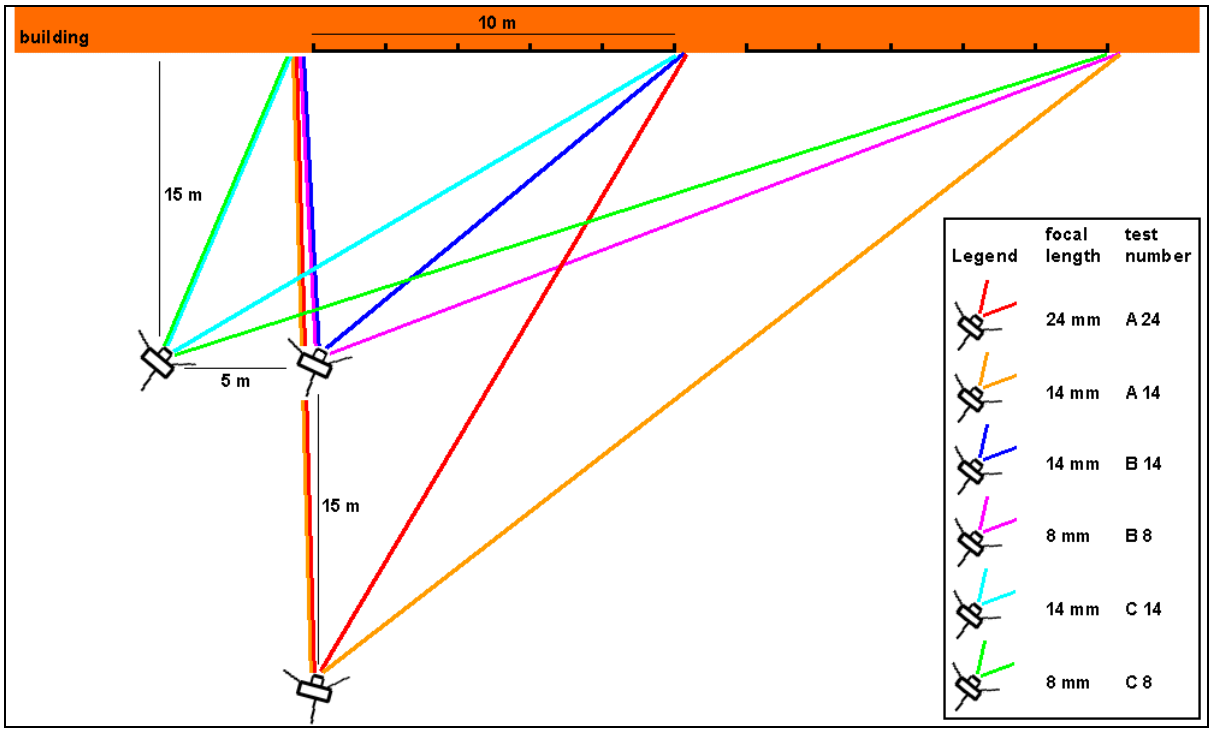

Fig. A2- 12: Top view of the test set-up.

Fig. A2- 13: Spatial referencing/rectification of image: original photo (left panel); referenced images (right panel). The image, which was taken with set-up B 14 in Fig. A2- 12, includes 16 visible red markers.

Table A2- 1: Validation of image referencing procedure, difference of known position of markers and position estimated from spatially referenced images.

	test A 24	test A 14	test B 14	test B8	test C 14	test C 8
mean positioning difference	1.7 cm	3.3 cm	1.1 cm	n.n., later	2.1 cm	n.n., later
mean positioning difference per distance [camera – building]	0.6 cm / 10 m	1.2 cm / 10 m	0.7 cm / 10 m	n.n., later	1.4 cm / 10 m	n.n., later.
maximum positioning difference	2.8 cm	7.5 cm	2.1 cm	n.n., later	4.9 cm	n.n., later
maximum positioning difference per distance [camera – building]	1.0 cm / 10 m	2.7 cm / 10 m	1.4 cm / 10 m	n.n., later	3.2 cm / 10 m	n.n., later

Appendix 3

Rot, knots from old branches, and wind-induced mechanical damage reduce the stem-bending strength of living Norway spruce and silver fir

Tor Lundström

Swiss Federal Institute for Snow and Avalanche Research SLF, 7260 Davos Dorf, Switzerland

Date: June 2006 (unpublished)

One hundred and five mature trees, including 71 Norway spruce, 28 silver fir, four Scots pine, one European beech, and one ash, growing in plots a-c, were pulled sideways with a winch until the tree failed in the root-soil system or in the stem. The stem-bending stress σ in the outermost wood fiber of the living trees was calculated, according to Lundström et al. (2008a), when the maximum applied force was applied, corresponding to tree failure.

Eighty-six of the 105 winching tests led to failure in the root-soil system. The anchorage properties of 84 of these 86 trees are reported in Lundström et al. (2007b). The remaining 19 trees (13 Norway spruce and six silver fir) failed in the stem. The locations of failure, in terms of relative stem height *z*/*H*, and the magnitude of bending stress there, σ, are shown in Fig. A3- 1. Out of these 19 trees, 13 had "normal" stems ("reference trees") and six trees showed signs of mechanical damage (most likely wind-induced compression failure), of knots from old pruned branches, or of rot on the outer stem. Otherwise the properties of radial growth were similar among the trees. Clearly, the rot, knots from old branches, and the wind-induced mechanical damage reduce the bending strength of the stem (P=0.002). In fact, the affected trees had a 33% lower mean bending strength than the reference trees. Naturally, rot reduces the resistance of stem wood as it does that of root wood (cf. Lundström et al. 2007b) and the reduction due to knots is in line with that described in the literature (Kucera 1973, Lundström et al. 2008b), as is the reduction due to stem-wood compression (Arnold and Steiger 2007).

In conclusion, the prediction of the stem-bending strength of living Norway spruce and silver fir requires knowledge about whether the stem-wood is healthy, contains knots, and has experienced strong winds resulting in compression failures along the stem.

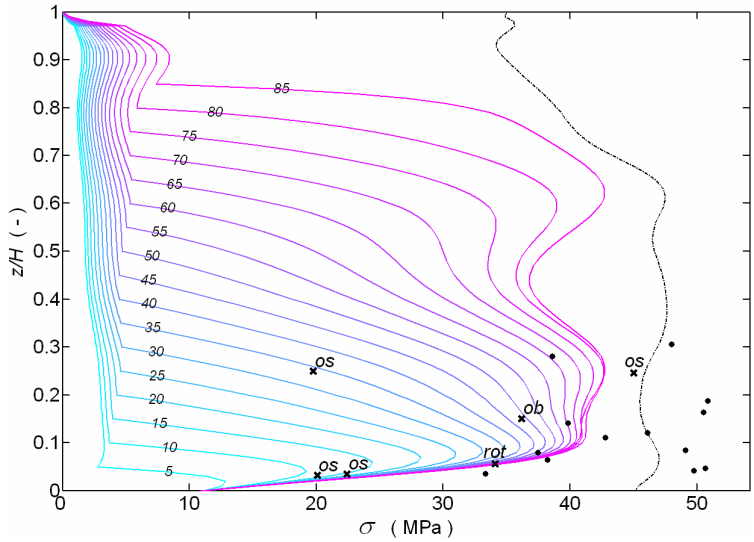

Fig. A3- 1: Calculated stem-bending stress σ (according to Lundström et al. 2008a) as a function of the relative tree height *z*/*H* of load application (from cyan to magenta) ranging from 5 to 85%. The applied load corresponds to tree uprooting. If the load is applied above *z*/*H*=85%, the stem-bending stress reaches the stem-bending strength (black dash-dot line) predicted by the properties of radial growth according to Lundström et al. (2007a, and 2008b). All lines refer to one Norway spruce growing in plot c. This spruce was pulled at an average relative stem height *z*/*H*=0.4 and was of average size (DBH=0.44 m, *H*=31 m) in relation to the other study trees growing on the plots a-c. The 13 dots correspond to the bending stress at stem failure of clearly healthy Norway spruce (9) and silver fir (4), and the six crosses to Norway spruce (3) and silver fir (3) with signs of mechanical damage ("os" = old scars obviously due to the stem-wood compression occasioned by wind), of wood rot ("rot"), and of knots from old pruned branches ("ob").

References

A

Achim A, Nicoll BC, Mochan S, Gardiner BA. 2003. Wind stability of trees on slopes. In: B Ruck, C Kottmeier, C Mattheck, C Quine and G Wilhelm, eds. *Wind Effects on Trees*. University of Karlsruhe, Karlsruhe, 231-237.

Adjanohoun G, Guillot J-L, Lanvin J-D, Cholat R. 1998. Small roundwood grading by non destructive x-rays and ultrasonic waves methods. 5th world conference on timber engineering. Presses polytechniques et universitaires romandes, Lausanne, Switzerland. Available in www .ndt.net/article/v04n11/adjanoh/adjanoh.htm

Aitken SN, Yeaman S, Holliday JA, Wang T, Curtis-McLane S. 2008. Adaptation, migration or extirpation: climate change outcomes for tree populations. *Evolutionary Applications* **1,** 95 - 111.

Amtmann R. 1986. Dynamische Windbelastung von Nadelbäumen. *Forstliche Forschungsberichte* **74**.

Ancelin P, Fourcaud T, Lac P. 2004. Modelling the biomechanical behaviour of growing trees at the forest stand scale. Part 1: Development of an incremental Transfer Matrix Method and application to simplified tree structures. *Annals of Forest Science* **61,** 263-275.

Andersland OB, Ladanyi B. 2004. Frozen ground engineering. 2: Hoboken, NJ Wiley.

Arnold M, Steiger R. 2007. Relevance of wind-induced compression failures regarding bending strength and stiffness of Spruce structural timber. COST E 53 Conference - Quality Control for Wood and Wood Products, Warsaw.

Azzoni A, Defreitas MH. 1995. Experimentally gained parameters, decisive for rock fall analysis. *Rock Mechanics and Rock Engineering* **28,** 111-124.

B

BAFU. 2002a. Die genützte Umwelt: Waldwirtschaft. *Umwelt Schweiz 2002. Politik und Perspektiven*, Vol. 1. BAFU, previously BUWAL Bundesamt für Umwelt, Wald und Landschaft, Bern, 203-215.

BAFU. 2002b. Ohne Schutzwald - Kein Lebensraum in den Alpen. *Umwelt* 1/2002, 18-21.

BAFU. 2005. Der Waldboden – ein optimaler Filter. *Umwelt* 3/2005, 31-35.

BAFU. 2008. Inventaire forestier national: Les bûchers sont pleins. *Environnement* 4/2008, 29.

Blackwell PG, Rennolls K, Coutts MP. 1990. A root anchorage model for shallowly rooted Sitka spruce. *Forestry* **63,** 73-92.

Bolenikus D. 2001. Zur Wurzelausbildung von Fichte (*Picea abies* L. Karst) und Weisstanne (*Abies alba* Mill.) in gleich- und ungleichaltrigen Beständen. *Berichte Freiburger Forstliche Forschung* **35**.

Bragov A, Lomunov AK. 1997. Dynamic properties of some wood species. *Journal De Physique IV* **7,** 487-492.

Bräker OU. 1981. Der Alterstrend bei Jahrringdichten und Jahrringbreiten von Nadelhölzern und sein Ausgleich. *Mitteilungen der Forstlichen Bundes-Versuchsanstalt Wien* **142,** 75-102.

Brang P, Bachofen H. 2002. Kleiner Wurzelballen – grosser Lotharschaden? *Informationsblatt Forschungsbereich Wald* **11,** 3.

Brang P, Schönenberger W, Frehner M, Schwitter R, Thormann J-J, Wasser B. 2006. Management of protection forests in the European Alps: an overview. *Forest Snow and Landscape Research* **80,** 23-44.

Brassel P, Brändli U-B. 1999. Inventaire forestier national suisse. Résultats du deuxième inventaire 1993-1995. Berne: Haupt.

Brauner M, Weinmeister W, Agner P, Vospernik S, Hoesle B. 2005. Forest management decision support for evaluating forest protection effects against rockfall. *Forest Ecology and Management* **207,** 75–85.

Brüchert F, Becker G, Speck T. 2000. The mechanics of Norway spruce [*Picea abies* (L.) Karst]: mechanical properties of standing trees from different thinning regimes. *Forest Ecology and Management* **135,** 45-62.

Bründl M. 1997. Snow interception and meltwater transport in subalpine forests. Monograph 12271. Zürich: ETH.

BSI. 2001. Timber poles for overhead lines - Test methods - Determination of modulus of elasticity, bending strength, density and moisture content. BS EN 12509 2001. London: BSI.

C

Cannell MGR, Morgan J. 1987. Youngs modulus of sections of living branches and tree trunks. *Tree Physiology* **3,** 355-364.

CEN. 2003. EN 408: Timber structures - Structural and glued laminated timber - Determination of some physical and mechanical properties. Brussels.

Chau KT, Wong RHC, Wu JJ. 2002. Coefficient of restitution and rotational motions of rockfall impacts. *International Journal of Rock Mechanics and Mining Sciences* **39,** 69-77.

Chiatante D, Scippa SG, Di Iorio A, Sarnataro M. 2002. The influence of steep slopes on root system development. *Journal of Plant Growth Regulation* **21,** 247-260.

Chopra AK. 1995. Dynamics of structures : theory and applications to earthquake engineering. International series in civil engineering and engineering mechanics Vol. 1. London: Prentice Hall.

Clough RW, Penzien J. 1993. Dynamics of structures. International Editions 1993. 2. New York.

Cook RD, Malkus DS, Plesha ME. 2002. Concepts and applications of finite element analysis. 4. New York: Wiley.

Core HA, Côté WA, Day AC. 1979. Wood: Structure and identification. 2. Syracuse - N.Y.: Syracuse University Press.

Coutts MP. 1983. Root architecture and tree stability. *Plant and Soil* **71,** 171-188.

Coutts MP. 1986. Components of tree stability in Sitka spruce on peaty gley soil. *Forestry* **59,** 173-198.

Coutts MP, Nielsen CCN, Nicoll BC. 1999. The development of symmetry, rigidity and anchorage in the structural root system of conifers. *Plant and Soil* **217,** 1-15.

Crook MJ, Ennos AR. 1996. The anchorage mechanics of deep rooted larch, *Larix europea x L-japonica*. *Journal of experimental botany* **47,** 1509-1517.

Cucchi V, Meredieu C, Stokes A, Berthier S, Bert D, Najar M, Denis A, Lastennet R. 2004. Root anchorage of inner and edge trees in stands of Maritime pine (*Pinus pinaster* Ait.) growing in different podzolic soil conditions. *Trees-Structure and Function* **18,** 460-466.

D

Daniel D, Wood FS, Gorman JW. 1980. Fitting equations to data: computer analysis of multifactor data. Wiley series in probability and mathematical statistics. Applied probability and statistics Vol. XVIII. 2. N. Y.

Danjon F, Fourcaud T, Bert D. 2005. Root architecture and wind-firmness of mature *Pinus pinaster*. *New Phytologist* **168,** 387-400.

Dean TJ, Roberts SD, Gilmore DW, Maguire DA, Long JN, O'Hara KL, Seymour RS. 2002. An evaluation of the uniform stress hypothesis based on stem geometry in selected North American conifers. *Trees-Structure and Function* **16,** 559-568.

Deresse T, Shepard RK. 1999. Wood properties of red pine (*Pinus resinosa* Ait.). CFRU Information Report 42, Orono, Maine: Department of Forest Management, College of Natural Sciences, Forestry, and Agriculture, University of Maine.

Di Iorio A, Lasserre B, Scippa GS, Chiatante D. 2005. Root system architecture of Quercus pubescens trees growing on different sloping conditions. *Annals of Botany* **95,** 351-361.

DIN. 1992. Normen über Holz. Deutsches Institut für Normung. DIN-Taschenbuch Vol. 31. 6. Berlin; Köln: Beuth.

DIN. 2000. Normen über Holz. Deutsches Institut für Normung. DIN-Taschenbuch Vol. 31. 7. Berlin; Köln: Beuth.

Dinwoodie JM. 1961. Tracheid and fibre length in timber. A review of literature. *Forestry* **34,** 125-144.

Dinwoodie JM. 2000. Timber: its nature and behaviour. 2. London: E&FN SPON.

Dobbertin M, Hug C, Schwyzer A. 1997. Sanasilva Inventory Field Manual. WSL.

Dorren LKA, Berger F. 2006. Stem breakage of trees and energy dissipation during rockfall impacts. *Tree Physiology* **26,** 63-71.

Dorren LKA, Seijmonsbergen AC. 2003. Comparison of three GIS-based models for predicting rockfall runout zones at a regional scale. *Geomorphology* **56,** 49-64.

Dupuy L, Fourcaud T, Stokes A. 2005. A numerical investigation into the influence of soil type and root architecture on tree anchorage. *Plant and Soil* **278,** 119-134.

E

Einspahr DW, Vaneperen RH, Fiscus ML. 1984. Morphological and bark strength characteristics important to wood-bark adhesion in hardwoods. *Wood and Fiber Science* **16,** 339-348.

Ennos AR. 1993. The scaling of root anchorage. *Journal of Theoretical Biology* **161,** 61-75.

F

FAO. 1998. Soil map of the world. Revised legend. World soil resources report Vol. 60. Rome: FAO-Unesco, Food and Agriculture Org. of the United Nations.

Fioravanti M. 2001. The influence of age and growth factors on microfibril angle of wood. First international conference of European society for wood mechanics, Lausanne, Switzerland, 47-54.

FOT. 2006. Formulas and constants for the calculation of the Swiss conformal cylindrical projection and for the transformation between coordinate systems. Wabern: FOT, Federal Office of Topography.

Fourcaud T, Blaise F, Lac P, Castera P, de Reffye P. 2003a. Numerical modelling of shape regulation and growth stresses in trees II. Implementation in the AMAPpara software and simulation of tree growth. *Trees-Structure and Function* **17,** 31-39.

Fourcaud T, Danjon F, Dupuy L. 2003b. Numerical analysis of the anchorage of maritime pine trees in connection with root structure. In: B Ruck, C Kottmeier, C Mattheck, C Quine and G Wilhelm, eds. *Wind Effects on Trees*. University of Karlsruhe, Karlsruhe, 323-330.

Fourcaud T, Ji JN, Zhang ZQ, Stokes A. 2008. Understanding the impact of root morphology on overturning mechanisms: A modelling approach. *Annals of Botany* **101,** 1267-1280.

Fraser AI. 1962. The soil and roots as factors in tree stability. *Forestry* **35(2),** 117-127.

Fraser AI, Gardiner JBH. 1967. Rooting and stability in Sitka spruce. For. Comm. Bull. Vol. 40. London: HMSO.

Fredericksen TS, Hedden RL, Williams SA. 1993. Testing Loblolly-pine wind firmness with simulated wind stress. *Canadian Journal of Forest Research* **23,** 1760-1765.

Friml J. 2003. Auxin transport - shaping the plant. *Current Opinion in Plant Biology* **6,** 7-12.

FSS. 1997. Nordic timber-grading rules. Grading rules for pine (*Pinus sylvestris*) and spruce (*Picea abies*) sawn timber. Commercial Grading Based on Evaluation of the Four Sides of Sawn Timber. 2. Sweden/Finland/Norway: Föreningen Svenska Sågverksmän (FSS)/Suomen Sahateollisuusmiesten Yhdistys (STMY)/-Treindustriens Tekniske Forening (TTF).

G

Gardiner BA. 1989. Mechanical characteristics of Sitka spruce. Edinburgh: For. Comm.

Gardiner BA. 1994. Wind and wind forces in a plantation spruce forest. *Boundary-Layer Meteorology* **67,** 161-186.

Gardiner BA. 1995. The interactions of wind and tree movements in forest canopies. In: MP Coutts and J Grace, eds. *Wind and Trees*. Cambridge University Press, Cambridge, 41-59.

Gardiner BA, Peltola H, Kellemäki S. 2000. Comparison of two models for predicting the critical wind speeds required to damage coniferous trees. *Ecological Modelling* **129,** 1-23.

Gardiner BA, Stacey GR, Belcher RE, Wood CJ. 1997. Field and wind tunnel assessments of the implications of respacing and thinning for tree stability. *Forestry* **70,** 233-252.

Gerber W, Schnyder D. 1998. Attention, chutes de pierres. Des ouvrages de protection plus efficaces. *Arguments de la recherche* **14,** 12-17.

Green DW, Winandy JE, Kretschmann DE. 1999. Mechanical properties of wood. Dep. of Agriculture, For. Serv., Forest Products Lab., Madison, Wisc., U.S. Available in www.fpl-.fs.fed.us/documnts/fplgtr/fplgtr113/ch04.pdf

H

Hakkila P. 1972. Mechanized harvesting of stumps and roots. *Communicationes Instituti Forestalis Fenniae* **77**:1 Helsinki.

Hassinen A, Lemettinen M, Peltola H, Kellomaki B, Gardiner B. 1998. A prism-based system for monitoring the swaying of trees under wind loading. *Agricultural and Forest Meteorology* **90,** 187-194.

Heidenreich B, Labiouse V. 2004. Small-scale experimental study of rockfall impacts on granular slopes. *Rivista Italiana di Geotecnica* **38,** 80-91.

Holbo HR, Corbett TC, Horton PJ. 1980. Aeromechanical Behavior of Selected Douglas-Fir. *Agricultural Meteorology* **21,** 81-91.

Huang YS, Chen SS, Kuo-Huang LL, Lee CM. 2005. Growth strain in the trunk and branches of *Chamaecyparis formosensis* and its influence on tree form. *Tree Physiology* **25,** 1119-1126.

I

Ikonen VP, Kellomäki S, Peltola H. 2003. Linking tree stem properties of Scots pine (*Pinus sylvestris* L.) to sawn timber properties through simulated sawing. *Forest Ecology and Management* **174,** 251-263.

IPCC. 2007. Summary for policymakers. In: ML Parry, Canziani, O.F., Palutikof, J.P., van der Linden, P.J. & Hanson, C.E., ed. *Climate change 2007: Impacts, adaptation and vulnerability. Contribution of Working Group II to the Fourth Assessment Report of the Intergovernmental Panel of Climate Change (IPCC)*. Cambridge University Press, Cambridge, UK, 7-22.

J

Jaffe MJ. 1973. Thigmomorphogenesis: The response of plant growth and development to mechanical stimulation. *Planta* **114,** 143-157.

James KR, Haritos N, Ades PK. 2006. Mechanical stability of trees under dynamic loads. *American Journal of Botany* **93,** 1522-1530.

Johnson RC, Ramey GE, Ohagan DS. 1982. Wind Induced Forces on Trees. *Journal of Fluids Engineering-Transactions of the ASME* **104,** 25-30.

Jonsson MJ. 2007. Energy absorption of trees in a rockfall protection forest. Monograph. Zürich: Swiss federal institute of technology.

Jonsson MJ, Foetzki A, Kalberer M, Lundström T, Ammann W, Stöckli V. 2006. Root-soil rotation stiffness of Norway spruce (*Picea abies* L. Karst) growing on subalpine forested slopes. *Plant and Soil* **285,** 267-277.

Jonsson MJ, Foetzki A, Kalberer M, Lundström T, Ammann W, Stöckli V. 2007. Natural frequencies and damping ratios of Norway spruce (Picea abies (L.) Karst) growing on subalpine forested slopes. *Trees-Structure and Function* **21,** 541-548.

K

Kalberer M. 2007. Quantification and optimization of the forest protection against rockfall. Monograph. Freiburg, D: University of Freiburg.

Kollmann FFP. 1968. Principles of wood science and technology. Solid Wood. Vol. 1. Berlin: Springer.

Köstler JN, Brückner E, Bibelriether H. 1968. Die Wurzeln der Waldbäume. Vol. Ill. Hamburg Berlin: Verlag Paul Parey.

Krummenacher B, Keusen H-R. 1997. Steinschlag-Stutzbahnen - Modell und Realität. Proceedings, Société Suisse de Mécanique des sols et des roches, réunion d'automne, Montreux, 17-23.

Kucera B. 1973. Holzfehler und ihr Einfluss auf die mechanischen Eigenschaften der Fichte und Kiefer. *Holztechnologie* **14,** 8-17.

Kucera LJ, Gfeller B. 1994. Einheimische und fremdländische Nutzhölzer. Zürich: Professur Holzwissenschaften, ETHZ.

L

Laasasenaho J, Melkas T, Alden S. 2005. Modelling bark thickness of *Picea abies* with taper curves. *Forest Ecology and Management* **206,** 35-47.

Lindstrom H. 1996. Basic density of Norway spruce. Part II. Predicted by stem taper, mean growth ring width, and factors related to crown development. *Wood and Fiber Science* **28,** 240-251.

Lindstrom H. 1997. Fiber length, tracheid diameter, and latewood percentage in Norway spruce: Development from pith outwards. *Wood and Fiber Science* **29,** 21-34.

Lo AKF. 1995. Determination of zero-plane displacement and roughness length of a forest canopy using profiles of limited height. *Boundary-Layer Meteorology* **75,** 381-402.

Lohou F, Lopez A, Druilhet A, Brunet Y, Irvine MR, Lamaud E. 2003. Response of a homogenous forest canopy to wind stress through the analysis of accelerometer measurements. In: B Ruck, C Kottmeier, C Mattheck, C Quine and G Wilhelm, eds. *Wind Effects on Trees*. University of Karlsruhe, Karlsruhe, 109-116.

Lundström T, Heiz U, Stoffel M, Stöckli V. 2007a. Fresh-wood bending: linking the mechanical and growth properties of a Norway spruce stem. *Tree Physiology* **27,** 1229–1241.

Lundström T, Jonas T, Stöckli V, Ammann W. 2007b. Anchorage of mature conifers: resistive turning moment, root-soil plate geometry, and orientation of root growth. *Tree Physiology* **27,** 1217–1227.

Lundström T, Jonas T, Volkwein A. 2008a. Analysing the mechanical performance and growth adaptation of Norway spruce using a nonlinear finite-element model and experimental data. *Journal of Experimental Botany* **59,** 2513-2528.

Lundström T, Jonsson MJ, Kalberer M. 2007c. The root-soil system of Norway spruce subjected to turning moment: resistance as a function of rotation. *Plant and Soil* **300,** 35-49.

Lundström T, Stoffel M, Stöckli V. 2008b. Fresh-stem bending of silver fir and Norway spruce. *Tree Physiology* **28,** 355–366.

M

Madsen B. 1975. Duration of load test for wet lumber in bending. *Forest products journal* **25,** 33-40.

Märki C, Niemz P, Mannes D. 2005. Vergleichende Untersuchungen zu ausgewählten mechanischen Eigenschaften von Eibe und Fichte. *Schweizerische Zeitschrift für Forstwesen* **3-4,** 85-91.

Mattheck C. 1998. Design in nature: learning from trees. Berlin: Springer.

Mattheck C, Bethge K, Erb D. 1993. Failure criteria for trees. *Allgemeine Forst und Jagdzeitung* **164,** 9-12.

Mattheck C, Breloer H. 1994. The body language of trees: a handbook for failure analysis. London: HMSO.

Mayer H. 1985. Baumschwingungen und Sturmgefährdung des Waldes. 51, München: Universität München; Meteorologisches Institut.

Meng SX, Lieffers VJ, Reid DEB, Rudnicki M, Silins U, Jin M. 2006. Reducing stem bending increases the height growth of tall pines. *Journal of Experimental Botany* **57,** 3175-3182.

MeteoSwiss. 2005 and 2006. Climate database. Swiss National Weather Service. Available in: www-.meteoschweiz.ch/web/en/services/data_portal.html.

Meunier S, Ruel JC, Laflamme G, Achim A. 2002. Comparative resistance of white spruce and balsam fir to overturning. *Canadian Journal of Forest Research* **32,** 642-652.

Mickovski SB, Ennos AR. 2003a. Anchorage and asymmetry in the root system of *Pinus peuce*. *Silva Fennica* **37,** 161-173.

Mickovski SB, Ennos AR. 2003b. The effect of unidirectional stem flexing on shoot and root morphology and architecture in young *Pinus sylvestris* trees. *Canadian Journal of Forest Research* **33,** 2202-2209.

Milne R. 1991. Dynamics of swaying of *Picea sitchensis*. *Tree Physiology* **9,** 383-399.

Milne R, Blackburn P. 1989. The elasticity and vertical distribution of stress within stems of *Picea sitchensis*. *Tree Physiology* **5,** 195-205.

Mizuyama T, Narita H. 1988. Debis flow control by woods and their impact energy absorptivity. Proceedings Interpraevent, Graz, 173-181.

Moore JR. 2000. Differences in maximum resistive bending moments of *Pinus radiata* trees grown on a range of soil types. *Forest Ecology and Management* **135,** 63-71.

Moore JR, Maguire DA. 2004. Natural sway frequencies and damping ratios of trees: concepts, review and synthesis of previous studies. *Trees-Structure and Function* **18,** 195-203.

Moore JR, Maguire DA. 2005. Natural sway frequencies and damping ratios of trees: influence of crown structure. *Trees-Structure and Function* **19,** 363-373.

Morgan J, Cannell MGR. 1987. Structural analysis of tree trunks and branches: tapered cantilever beams subject to large deflections under complex loading. *Tree Physiology* **3,** 365-374.

Morgan J, Cannell MGR. 1994. Shape of tree stems - a reexamination of the uniform stress hypothesis. *Tree Physiology* **14,** 49-62.

Morse AP, Brunet Y, Devalance M, Gamboa-Marrufo M, Irvine MR, Marshall BJ, Paw KT, Shaw RH, Wood C, Yang B, Gardiner BA. 2003. The role of forest edges in the pattern of turbulence development - Findings from a field experiment, wind tunnel experiment and a large eddy simulation model experiment. In: B Ruck, C Kottmeier, C Mattheck, C Quine and G Wilhelm, eds. *Wind Effects on Trees*. Univ. of Karlsruhe, Karlsruhe, 33-38.

Moulia B, Coutand C, Lenne C. 2006. Posture control and skeletal mechanical acclimation in terrestrial plants: Implications for mechanical modeling of plant architecture. *American Journal of Botany* **93,** 1477-1489.

Murray YD. 2003. Development of a wood material model for roadside safety applications. 6, Colorado Springs: Aptek Inc.

N

Natterer J, Sandoz JL. 1997. Construire en bois. Notions de base. Publication IBOIS 97:16. 3. Lausanne, Switzerland: Reprographie Ecole polytechnique fédérale de Lausanne.

Natterer J, Sandoz JL, Martial R. 2000. Construction en bois. Traité de Génie Civil Vol. 13. Lausanne: Presses Polytechniques et Universitaires Romandes.

Neild SA, Wood CJ. 1999. Estimating stem and root-anchorage flexibility in trees. *Tree Physiology* **19,** 141-151.

Newlin JA, Trayer GW. 1956. Deflection of beams with special reference to shear deformations. Report 1309, Madison, Wisconsin, U.S.: Department of Agriculture, Forest Service, Forest Products Laboratory.

Nicoll BC, Achim A, Mochan S, Gardiner BA. 2005. Does steep terrain influence tree stability? A field investigation. *Canadian Journal of Forest Research* **35,** 2360-2367.

Nicoll BC, Easton EP, Milner AD, Walker C, Coutts MP. 1995. Wind stability factors in tree selection: distribution of biomass within root systems of Sitka spruce clones. In: MP Coutts and J Grace, eds. *Wind and Trees*. Cambridge University Press, Cambridge, 276-292.

Nicoll BC, Gardiner BA, Rayner B, Peace AJ. 2006. Anchorage of coniferous trees in relation to species, soil type, and rooting depth. *Canadian Journal of Forest Research* **36,** 1871-1883.

Nicoll BC, Ray D. 1996. Adaptive growth of tree root systems in response to wind action and site conditions. *Tree Physiology* **16,** 891-898.

Niemz P. 1993. Physik des Holzes und der Holzwerkstoffe. Holz: Anatomie, Chemie, Physik Vol. Ill. DRW-Verlag.

O

OcCC. 2008. Das Klima ändert – was nun? Der neue UN-Klimabericht (IPCC 2007) und die wichtigsten Ergebnisse aus Sicht der Schweiz. Bern: OcCC - Advisory Body on Climate Change Research and Policy / Organe consultatif sur les changements climatiques.

O'Neill GA, Hamann A, Wang TL. 2008. Accounting for population variation improves estimates of the impact of climate change on species' growth and distribution. *Journal of Applied Ecology* **45,** 1040-1049.

P

Papesch AJG, Moore JR, Hawke AE. 1997. Mechanical stability of *Pinus radiata* trees at eyrewell forest investigated using static tests. *New Zealand Journal of Forestry Science* **27,** 188-204.

Peltola H. 1995. Studies on the mechanism of wind-induced damage of Scots pine. University of Joensuu.

Peltola H. 1996. Swaying of trees in response to wind and thinning in a stand of Scots pine. *Boundary-Layer Meteorology* **77,** 285-304.

Peltola H, Kellomäki S. 1993. A mechanistic model for calculating windthrow and stem breakage of Scots pine at stand edge. *Silva Fennica* **27,** 99-111.

Peltola H, Kellomäki S, Hassinen A, Granander M. 2000. Mechanical stability of Scots pine, Norway spruce and birch: an analysis of tree-pulling experiments in Finland. *Forest Ecology and Management* **135,** 143-153.

Peltola H, Nykanen ML, Kellomaki S. 1997. Model computations on the critical combination of snow loading and windspeed for snow damage of Scots pine, Norway spruce and Birch sp. at stand edge. *Forest Ecology and Management* **95,** 229-241.

Perret S, Baumgartner M, Kienholz H. 2004. Rockfall injuries in mountain forests - a method for data collection and analysis. Proceedings Interpraevent, Riva/Trient, V / 87-98.

Polomski J, Kuhn N. 1998. Wurzelsysteme. Bern Stuttgart Wien: Haupt.

Polomski J, Kuhn N. 2001. Wurzelhabitus und Standfestigkeit der Waldbäume. *Forstwissenschaftliches Centralblatt* **120,** 303-317.

Pomeroy JW, Gray DM. 1995. Snowcover accumulation, relocation and management. National Hydrology Research Institute science report. Saskatoon, Saskatchewan, Canada: National Hydrology Research Institute.

R

Raupach MR. 1994. Simplified Expressions for Vegetation Roughness Length and Zero-Plane Displacement as Functions of Canopy Height and Area Index. *Boundary-Layer Meteorology* **71,** 211-216.

Ray D, Nicoll BC. 1998. The effect of soil water-table depth on root-plate development and stability of Sitka spruce. *Forestry* **71,** 169-182.

Rudnicki M, Mitchell SJ, Novak MD. 2004. Wind tunnel measurements of crown streamlining and drag relationships for three conifer species. *Canadian Journal of Forest Research* **34,** 666-676.

S

Sakamoto Y, Ishiguro M, Kitagawa G. 1986. Akaike information criterion statistics. Vol. XIX. Tokyo: KTK Scientific Publishers.

Saren MP, Serimaa R, Andersson S, Paakkari T, Saranpaa P, Pesonen E. 2001. Structural variation of tracheids in Norway spruce (*Picea abies* L. Karst.). *Journal of Structural Biology* **136,** 101-109.

Saunderson SET, England AH, Baker CJ. 1999. A dynamic model of the behaviour of sitka spruce in high winds. *Journal of Theoretical Biology* **200,** 249-259.

Schiesser HH, Pfister C, Bader J. 1997. Winter storms in Switzerland north of the Alps 1864/1865-1993/1994. *Theoretical and Applied Climatology* **58,** 1-19.

Schmidt-Vogt H. 1991. Die Fichte: ein Handbuch in zwei Bänden. Waldbau, Ökologie, Urwald, Wirtschaftswald, Ernährung, Düngung, Ausblick Vol. 2/3. Hamburg und Berlin: Verlag Paul Parey.

Schweingruber FH. 1996. Tree Rings and Environment. Dendroecology. Bern: Haupt.

Sellier D, Brunet Y, Fourcaud T. 2008. A numerical model of tree aerodynamic response to a turbulent airflow. *Forestry* **81,** 279-297.

SIA. 2003. Timber structures - supplementary specifications. 265/1, Zurich: Schweizerischer Ingenieur- und Architektenverein (SIA).

SIA. 2006. Wind. D 0188, Zurich: Schweizerischer Ingenieur- und Architektenverein (SIA).

Siau JF. 1995. Wood: Influence of moisture on physical properties. Keene, NY: Department of Wood Science and Forest Products, Virginia Polytechnic Institute and State University.

Silins U, Lieffers VJ, Bach L. 2000. The effect of temperature on mechanical properties of standing lodgepole pine trees. *Trees-Structure and Function* **14,** 424-428.

Sirviö J. 2001. The effects of age and growth rate on wood basic density in Scots pine and Norway spruce. First international conference of European society for wood mechanics, Lausanne, Switzerland, 13-22.

SLF. 2000. Der Lawinenwinter 1999: Ereignisanalyse. Davos: Swiss Federal Institute for Snow and Avalanche Research, SLF.

Soethe N, Lehmann J, Engels C. 2006. Root morphology and anchorage of six native tree species from a tropical montane forest and an elfin forest in Ecuador. *Plant and Soil* **279,** 173.

Sovilla B, Schaer M, Rammer L. 2008. Measurements and analysis of full-scale avalanche impact pressure at the Vallee de la Sionne test site. *Cold Regions Science and Technology* **51,** 122-137.

Stadler DC, Bründl M, Schneebeli M, Meyer-Grass M, Flühler H. 1998. Hydrologische Prozesse im subalpinen Wald im Winter. Schlussbericht / NFP 31. Zürich VDF, Hochschulverlag an der ETH.

Stoffel M, Wehrli A, Kuhne R, Dorren LKA, Perret S, Kienholz H. 2006. Assessing the protective effect of mountain forests against rockfall using a 3D simulation model. *Forest Ecology and Management* **225,** 113.

Stokes A, Fitter AH, Coutts MP. 1995. Responses of young trees to wind and shading - effects on root architecture. *Journal of Experimental Botany* **46,** 1139-1146.

Stokes A, Fourcaud T, Berthier S. 2001. How trees stand up and fall down: Tree resistance to wind, or strange things that happen under stress. International conference: Tree structure and mechanics, Savannah, Georgia, U.S., 21-37.

Stokes A, Salin F, Kokutse AD, Berthier S, Jeannin H, Mochan S, Dorren L, Kokutse N, Abd Ghani M, Fourcaud T. 2005. Mechanical resistance of different tree species to rockfall in the French Alps. *Plant and Soil* **278,** 107-117.

Strobel T. 1978. Schneeinterzeption in Fichtenbeständen in den Voralpen des Kantons Schwyz. International Seminar on Mountain, Forests and Avalanches, Davos, Switzerland, 63-79.

Sundström B. 1998. Handbok och formelsamling i Hållfasthetslära. Vol. 1. Stockholm: Department of Solid Mechanics, Royal Institute of Technology.

T

Telewski FW. 1995. Wind-induced physiologial and developmental responses in trees. In: M Coutts and J Grace, eds. *Wind and Trees*. Cambridge University Press, Cambridge, 241-263.

Telewski FW. 2006. A unified hypothesis of mechanoperception in plants. *American Journal of Botany* **93,** 1466-1476.

Trendelenburg R, Mayer-Wegelin H. 1955. Das Holz als Rohstoff. 2. München: J.F. Lehmanns Verlag.

U

USDA. 1972. The Moisture Content and Specific Gravity of the Bark and Wood of Northern Pulpwood Species. Res. Note NC-141. Minnesota: North Centr. For. Exp. Stn., For. Serv., U.S. Dep. of Agric. (USDA).

V

Vanomsen P. 2006. Der Einfluss der Durchforstung auf die Verankerung der Fichte hinsichtlich ihrer Sturmresistenz. Monograph. Zürich: Swiss federal institute of technology.

W

Wessolly L, Erb M. 1998. Handbuch der Baumstatik und Baumkontrolle. Berlin: Patzer.

Wood CJ. 1995. Understanding wind forces on trees. In: MP Coutts and J Grace, eds. *Wind and Trees*. Cambridge university press, Cambridge, 133-164.

WSL, BUWAL. 2001. Lothar der Orkan 1999 Ereignisanalyse. Birmensdorf, Bern: Eidg. Forschungsanstalt WSL, Bundesamt für Umwelt, Wald und Landschaft BUWAL.

Y

Yang YB, Yang YT, Su HH. 2005. Behavior of the tree branches, trunk, and root anchorage by nonlinear finite element analysis. *Advances in Structural Engineering* **8,** 1-14.

Ylinen A. 1952. Über die mechanische Schaftform-theorie der Bäume. *Silva Fennica* **76,** 1-52.

Z

Zinggeler A, Krummenacher B, Kienholz H. 1991. Steinschlagsimulation in Gebirgswäldern. 3: Geographisches Institut, Univ. Freiburg (CH).

Zoumakis NM. 1993. Estimating the zero-plane displacement and roughness length for tall vegetation and forest canopies using semi-empirical wind profiles. *Journal of Applied Meteorology* **32,** 574–579.

Zweifel R, Hasler R. 2000. Frost-induced reversible shrinkage of bark of mature subalpine conifers. *Agricultural and Forest Meteorology* **102,** 213-222.

Curriculum Vitae

Tor Lundström

Bielstrasse 5, 3912 Termen, Switzerland

Born on 26 April, 1966 in Sweden

Citizen of Puidoux (VD), Servion (VD), and Sweden

EMPLOYMENT

07-	**Consultant engineer**, Schneller, Ritz und Partner engineers SRP, Brig: design of buildings and other civil engineering works, especially with regard to earthquake hazards. Environment quality analysis of habitations.
02-06	**Project manager**, Swiss federal institute for snow and avalanche research, SLF–WSL, Davos: interdisciplinary research project on biomechanical processes of trees subject to natural hazards and strategies of forest management.
99-02	**Research assistant** (75%), Institute of wood constructions IBOIS – Swiss federal institute of technology of Lausanne EPFL, in collaboration with the Laboratory of building technology – Royal institute of technology KTH, Stockholm, Sweden: Indoor climate comfort in buildings of massive wood, material life cycle assessment analysis, wood structure design. Industry missions, research project management, teaching, and supervision of students.
	Consultant engineer (25%), Concepts bois technologies CBT engineers, Saint-Sulpice: wood technologies, project promotion in the Nordic countries.
97-98	**Consultant engineer**, Bjerking engineers, Uppsala, Sweden: wood structure design, building physics, public wood information, exportation of houses to Germany.
95-96	**Project manager**, National institute for testing and research of materials SP, Wood laboratory of applied research, Borås, Sweden: bending tests of tree trunks, re-use of structural timber, wood structure design.
93-94	**Assistant**, Laboratory of energy systems LASEN–EPFL: coordinator for an interdisciplinary project of distance heating, fed by heat pumps.

EDUCATION

88-93	Master in civil engineering EPFL (91-93) and KTH (88-91)
86-87	Military service, Sweden

CONTINUED EDUCATION

06-09	PhD, Laboratory of Dendrogeomorphology, University of Fribourg: Mechanical stability and growth performance of trees.
00-01	Postgraduate course « Les Constructions en bois », EPFL
98-99	Physics and chemistry of the atmosphere, Department of meteorology, University of Uppsala, Sweden (two semesters)

PUBLICATIONS

Lundström T, Jonsson MJ, Volkwein A, Stoffel M. 2009. Reactions and energy absorption of trees subject to rockfall: a detailed assessment using a new experimental method. *Tree Physiology* **29**, 345-359.

Lundström T, Jonas T, Volkwein A. 2008. Analysing the mechanical performance and growth adaptation of Norway spruce using a nonlinear finite-element model and experimental data. *Journal of Experimental Botany* **59**, 2513-2528.

Lundström T, Stoffel M, Stöckli V. 2008. Fresh-stem bending of silver fir and Norway spruce. *Tree Physiology* **28**, 355–366.

Lundström T, Jonsson MJ, Kalberer M. 2007. The root-soil system of Norway spruce subjected to turning moment: resistance as a function of rotation. *Plant and Soil* **300**, 35-49.

Lundström T, Heiz U, Stoffel M, Stöckli V. 2007. Fresh-wood bending: linking the mechanical and growth properties of a Norway spruce stem. *Tree Physiology* **27**, 1229–1241.

Lundström T, Jonas T, Stöckli V, Ammann W. 2007. Anchorage of mature conifers: resistive turning moment, root-soil plate geometry, and orientation of root growth. *Tree Physiology* **27**, 1217–1227.

Jonsson MJ, Foetzki A, Kalberer M, Lundström T, Ammann W, Stöckli V. 2007. Natural frequencies and damping ratios of Norway spruce (Picea abies (L.) Karst) growing on subalpine forested slopes. *Trees-Structure and function* **21,** 541-548.

Jonsson MJ, Foetzki A, Kalberer M, Lundström T, Ammann W, Stöckli V. 2006. Root-soil rotation stiffness of Norway spruce (*Picea abies* L. Karst) growing on subalpine forested slopes. *Plant and Soil* **285,** 267-277.

Hameury S, Lundstrom T. 2004. Contribution of indoor exposed massive wood to a good indoor climate: in situ measurement campaign. *Energy and Buildings* **36,** 281-292.